COMMUNICATIONS

COMMUNICATIONS

Dear Readers,

This issue of the Communications – Scientific Letters of the University of Zilina is devoted to the three important technologies – mainly to electronics, power electronics and partly to mechatronics due to motion control. Electronics has substituted low and medium voltage vacuum electrotechnics and has caused stormy development of transistor- and computational techniques on the one hand and industrial high voltage and high power applications as controlled converter drives, applications in electric traction and photovoltaic plants on the other hand. Today, there is no technology branch without power electronics, control electronics or without any mechatronic system.

This issue brings original reviewed scientific papers belonging to mentioned scientific areas as well as some supporting papers. It is pleasure of the guarantees to thank all authors, coauthors and reviewers, especially foreign contributors, for their effort in this selected technological field.

Branislav Dobrucky, Pavol Spanik

COMMUNICATIONS

Dudrik Jaroslav – Bodor Marcel – Trip Nistor Daniel *

OPERATION ANALYSIS OF SOFT SWITCHING PWM DC-DC CONVERTER WITH SECONDARY SNUBBER

The paper deals with analysis of operation of a soft switching PWM DC-DC full-bridge converter with new energy recovery turn-off snubber on secondary side of high frequency power transformer.

Principal equations are derived for individual operation states. On the basis of them the diagrams are made out. The diagrams give complex image on the converter behaviour during whole period of operation at nominal load. Theoretical waveforms are compared with simulation results.

Keywords: *Snubber, soft switching, zero voltage zero current switching, PWM, DC-DC converter.*

1. Introduction

DC-DC converter is the main and most important part of voltage or current switching power supplies. Full bridge pulse-width modulated (PWM) DC-DC converters have been often used in high power high frequency applications because they have several advantages over resonant converters [1]–[17]. Diode output rectifier is mostly employed on the secondary side of the power transformer to rectify high frequency secondary voltage [1]–[8]. Various snubbers, clamps and auxiliary circuits are often added on secondary side to ensure soft switching of the main switches and suppression of converter circulating currents [4]-[10]. The features of these configurations are quite well known and widely described in many papers. Very effective way, how to decrease circulating currents in the converter and simultaneously achieve reduction of switching losses, is to utilize a controlled output rectifier [18]–[21]. According to control algorithm it is either zero-voltage or zero current turn off achieved at inverter transistors. The ZVZCS PWM DC-DC converter with secondary controlled rectifier, novel turn-off energy recovery snubber and new method of control is shown in Fig. 1.

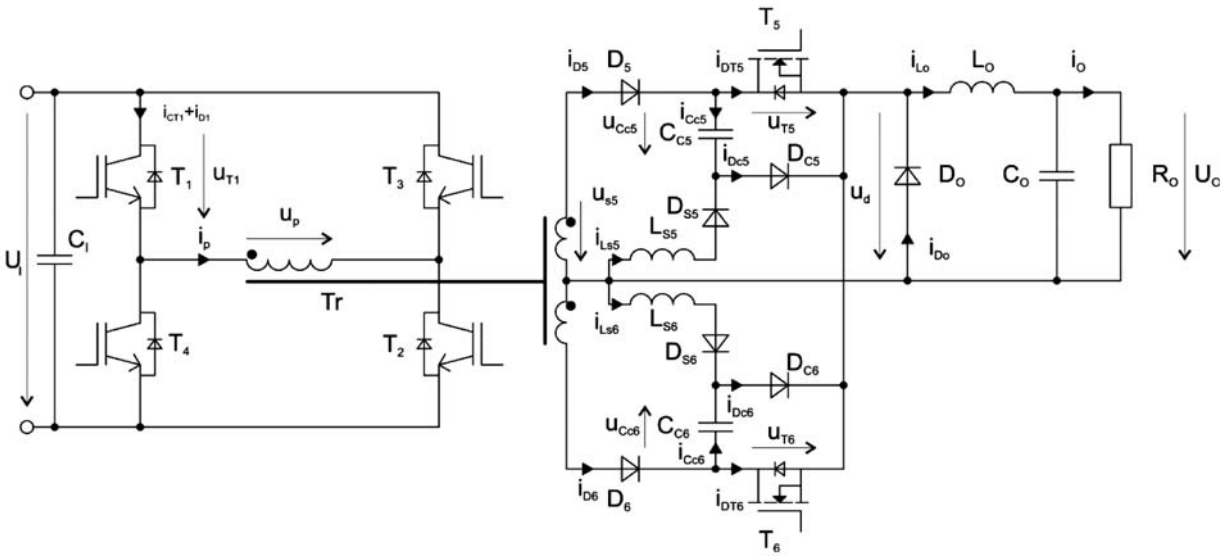

Fig. 1 Scheme of the proposed converter

* **Dudrik Jaroslav[1], Bodor Marcel[2], Trip Nistor Daniel[3]**
[1] Technical University of Kosice, Kosice, Slovakia, E-mail: jaroslav.dudrik@tuke.sk
[2] Johnson Controls Innotec Technologies, Lucenec, Slovakia
[3] University of Oradea, Oradea, Romania

The proposed converter in Fig. 1 consists of high frequency full-bridge inverter (T_1 – T_4), high frequency centre tapped power transformer T_r, controlled output rectifier (T_5, D_5; T_6, D_6), free-wheeling diode D_O, output filter (L_O, C_O) and novel type of secondary turn-off snubber (C_{C5}, C_{C6}, L_{S5}, L_{S6}, D_{S5}, D_{S6}, D_{C5}, D_{C6}).

The converter is controlled by new algorithm of pulse-width modulation (Fig. 2). The secondary switches are turned-off earlier than primary switches and thus zero-voltage turn-on and zero-current turn-off all of the transistors T_1 – T_4 in the inverter are reached.

The new snubber circuit eliminates the turn off losses of the secondary transistors. The semiconductor switches T_5, T_6 in the secondary side are used to reset secondary and simultaneously also primary circulating current. The energy stored in the leakage inductance of the power transformer is transferred to the load.

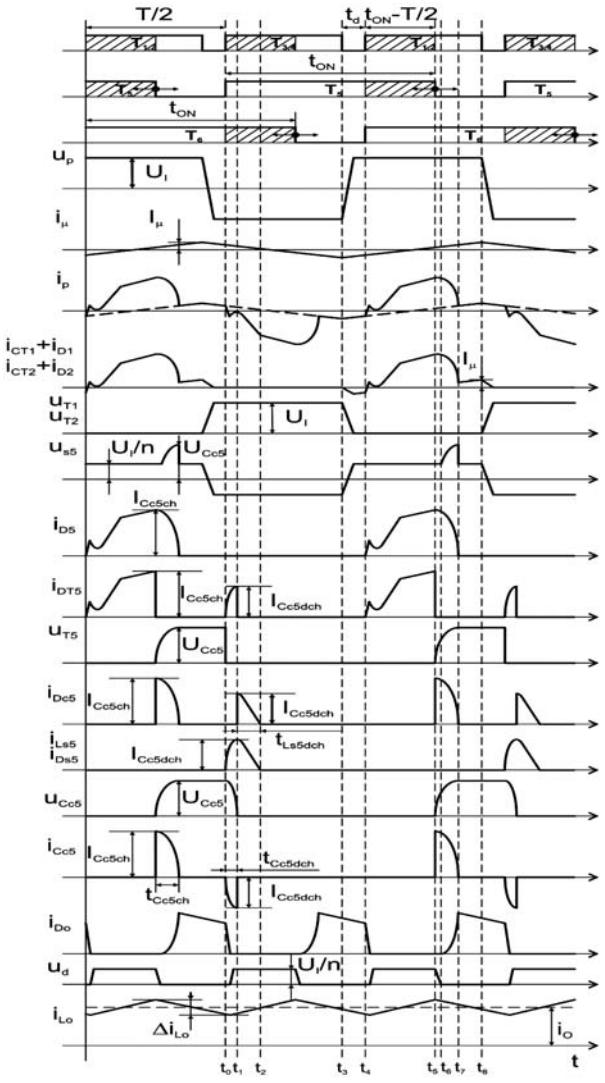

Fig. 2 Operation waveforms

2. Converter operation

The switching diagram and operation waveforms are shown in Fig. 2. DC/DC converter is controlled by novel modified pulse width modulation with variable phase shift between primary and secondary switches. The transient time analysis is done in distinctive intervals with help of Laplace-Carson transform. It is assumed that all components and devices are ideal.

Interval (t_0 – t_1):

Operation of the converter in interval t_0 – t_1 is shown in Fig. 3. The secondary transistor T_5 is turned on at t_0 half period earlier than primary transistors T_1 and T_2. The capacitor C_{C5} starts discharging through T_5, L_O, R_O, L_S, and D_{S5}. The rate of rise of discharging current of this capacitor C_{C5} is limited by the snubber circuit inductance L_{S5}, and thus zero current turn on for the MOSFET transistor T_5 is achieved. In the same time transistors T_3, T_4 are turned on. Because the transistor T_6 is already in on-state, so the output voltage of the rectifier u_p is equalled U_I/n (where $n = u_p/u_s$ is transformer turn's ratio). The current of the primary transistors T_3, T_4 and the current of the secondary transistor T_6 are reduced by the discharging current of capacitor C_{C5}.

For mathematical analysis the equivalent operator circuit in each interval of converter operation was created as it is present in Fig. 4 for interval t_0 – t_1.

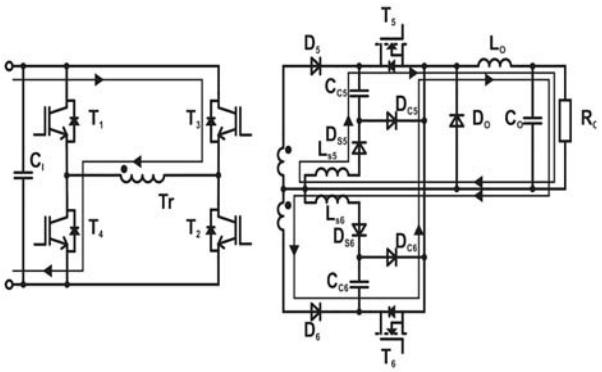

Fig. 3 Operation of the converter in interval t_0 – t_1

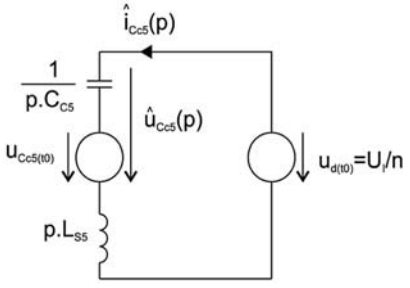

Fig. 4 Equivalent operator circuit for interval t_0 – t_1

Capacitor C_{C5} voltage and current image can be found from operator scheme in Fig. 4 as follows

$$\hat{i}_{Cc5}(p) = \frac{u_{d(t_0)} - u_{Cc5(t_0)}}{\frac{1}{pC_{C5}} + pL_{S5}} \quad (1)$$

$$\hat{u}_{Cc5}(p) = \hat{i}_{Cc5}(p)\frac{1}{pC_{C5}} + u_{Cc5(t_0)} \quad (2)$$

Initial conditions are

$$u_{d(t_0)} = \frac{U_I}{n} \quad (3)$$

$$u_{Cc5(t_0)} = U_{Cc5} \quad (4)$$

Voltage and current time waveforms are

$$i_{Cc5}(t) = \sqrt{\frac{C_{C5}}{L_{S5}}}\left(\frac{U_I}{n} - U_{Cc5}\right)\sin\left(\frac{t - t_0}{\sqrt{L_{S5}C_{C5}}}\right) \quad (5)$$

$$u_{Cc5}(t) = \frac{U_I}{n} + \left(U_{Cc5} - \frac{U_I}{n}\right)\cos\left(\frac{t - t_0}{\sqrt{L_{S5}C_{C5}}}\right) \quad (6)$$

From equation (6) follows that total discharging of the capacitor occurs only in the case if its initial voltage U_{Cc5} is higher than double rectified voltage $u_d = U_I/n$

$$\frac{U_I}{n} + \left(U_{Cc5} - \frac{U_I}{n}\right)(-1) \le 0 \rightarrow U_{Cc5} \ge 2\frac{U_I}{n} \quad (7)$$

If condition (7) is valid, capacitor discharging time (when $u_{Cc5}(t) = 0$) can be obtained from equation (6)

$$_{Cc5dch} = t_1 - t_0 = \sqrt{L_{S5}C_{C5}}\arccos\left(\frac{\frac{U_I}{n}}{\frac{U_I}{n} - U_{Cc5}}\right) \quad (8)$$

Discharging time is from interval

$$\frac{\pi}{2}\sqrt{L_{S5}C_{C5}} < t_{Cc5dch} \le \pi\sqrt{L_{S5}C_{C5}} \quad (9)$$

As discharging time is greater than quarter of resonance period, the magnitude of the discharging current of the capacitor can be calculated from equation (5)

$$I_{Cc5dch} = \left|\sqrt{\frac{C_{C5}}{L_{S5}}}\left(\frac{U_I}{n} - U_{Cc5}\right)\right| = \sqrt{\frac{C_{C5}}{L_{S5}}}\left(U_{Cc5} - \frac{U_I}{n}\right) \quad (10)$$

Interval (t_1 – t_2):

The energy stored in snubber inductance L_S is now flowing through D_{S5}, D_{C5}, L_O, R_O, L_S. At t_2 the whole load current flows through the transistor T_6 as it is seen in Fig. 5. The indispensable equations for this interval can be derived from equivalent operator circuit shown in Fig. 6.

The snubber inductor current decays to zero according to

$$i_{Ls5}(t) = \sqrt{U_{Cc5}\left(U_{Cc5} - 2\frac{U_I}{n}\right)}\sqrt{\frac{C_{C5}}{L_{S5}}} - \frac{U_I}{n}\frac{t - t_1}{L_{S5}} \quad (11)$$

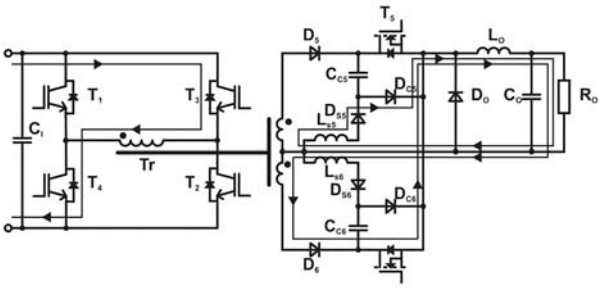

Fig. 5 Operation of the converter in interval t_1 - t_2

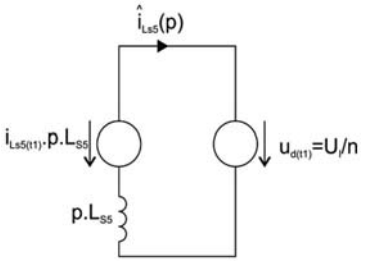

Fig. 6 Equivalent operator circuit for interval t_1 - t_2

From this equation decay time of the inductor current can be determined

$$t_{Ls5dch} = t_2 - t_1\frac{\sqrt{U_{Cc5}\left(U_{Cc5} - 2\frac{U_I}{n}\right)}\sqrt{\frac{C_{C5}}{L_{S5}}}}{\frac{U_I}{n}}L_{S5} \quad (12)$$

Interval (t_3 – t_4):

This interval starts with the turn off of the primary transistors T_3 and T_4. The magnetizing current of the transformer T_r discharges the output capacitances C_{OSS} of the transistors T_1, T_2 and charges the output capacitances of the transistors T_3, T_4 (Fig. 7).

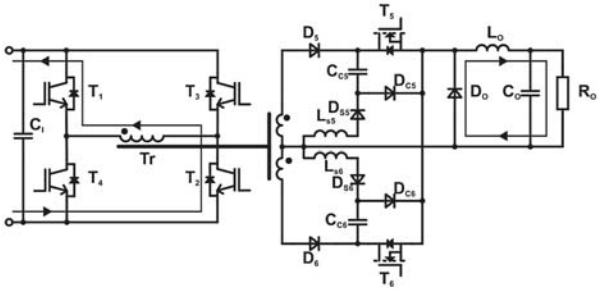

Fig. 7 Operation of the converter in interval t_3 - t_4

If we assume that magnetizing inductance of power transformer and output smoothing inductance are much smaller than leakage inductances (L_{1H}, $L_O << L_{16}$, L'_{26}), then simplified equations for

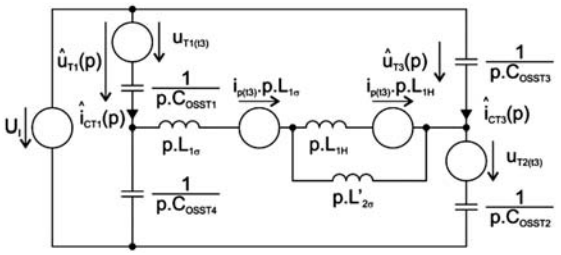

Fig. 8 Equivalent operator circuit for interval t_3 - t_4

collector-emitter voltages of the primary transistors T_1, T_2, and T_3, T_4 are obtained from Fig. 8 as follows

$$u_{T1}(t) = u_{T2}(t) = \frac{1}{2}U_I\left(1 + \cos\left(\sqrt{\frac{1}{C_{OSS}}}(t - t_3)\right)\right) - \\ - \frac{1}{2}I_\mu\sqrt{\frac{L_\sigma}{C_{OSS}}}\sin\left(\sqrt{\frac{1}{C_{OSS}L_\sigma}}(t - t_3)\right) \tag{13}$$

$$u_{T3}(t) = u_{T4}(t) = \frac{1}{2}U_I\left(1 - \cos\left(\sqrt{\frac{1}{C_{OSS}L_\sigma}}(t - t_3)\right)\right) + \\ + \frac{1}{2}I_\mu\sqrt{\frac{L_\sigma}{C_{OSS}}}\sin\left(\sqrt{\frac{1}{C_{OSS}L_\sigma}}(t - t_3)\right) \tag{14}$$

Where $L_\sigma = L_{1\sigma} + L'_{2\sigma}$

The minimum (transistors T_1, T_2) or maximum (transistors T_3, T_4) collector-emitter voltages are achieved during following interval

$$t_4 - t_3 = t_d \approx \pi\sqrt{C_{OSS}\left(L_{1\sigma} + L'_{2\sigma}\right)} \tag{15}$$

Interval (t_4 - t_5):

The turn on of the transistors T_1, T_2 and T_6 commutation from freewheeling diode to T_5 transistor occur at t_4 (Fig. 2). The current of transistor T_5 is reduced by the discharge current of the capacitor C_{C6} and later by the current of the inductance L_{S6} (Fig. 9).

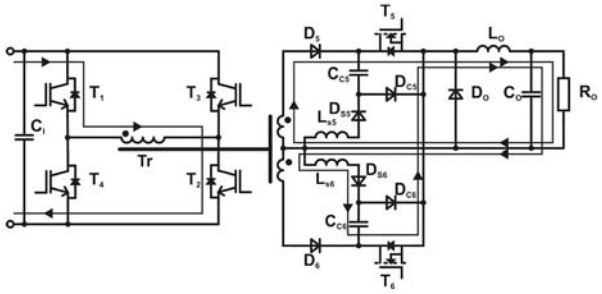

Fig. 9 Operation of the converter in interval t_4 - t_5

Rate of rise of collector current of the secondary transistor T_5 is

$$\frac{di_{DT5}}{dt} = \frac{U_I}{n}\frac{1}{\left(L'_{1\sigma} + L_{2\sigma}\right)} \tag{16}$$

Rate of rise of collector current of the primary transistors T_1, T_2 is a little higher

$$\frac{di_{CT1,CT2}}{dt} = \frac{U_I}{\left(L_{1H} + L_{1\sigma}\right)} + \frac{U_I}{\left(L_{1\sigma} + L'_{2\sigma}\right)} \tag{17}$$

Interval (t_5 - t_6):

At t_5 transistor T_5 turns off. Its current commutates on capacitor C_{C5} and diode D_{C5} and consequently zero voltage turn off of this transistor is ensured. The energy of the leakage inductance of the power transformer is absorbed by the snubber capacitance and then transferred to the load. The situation is displayed in Fig. 10.

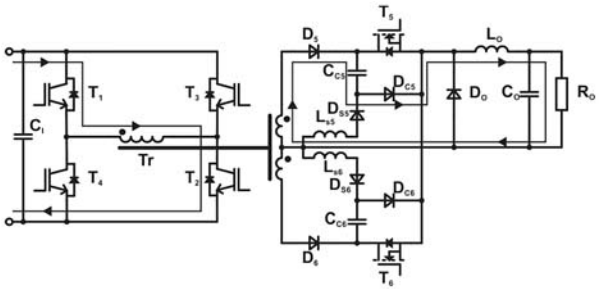

Fig. 10 Operation of the converter in interval t_5 - t_6

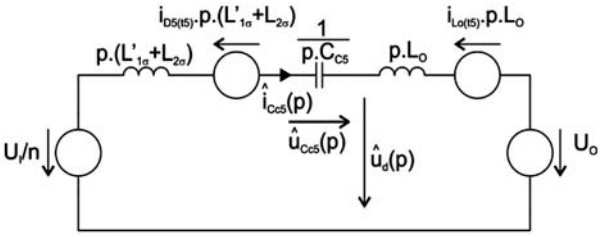

Fig. 11 Equivalent operator circuit for interval t_5 - t_6

When assuming that Lo >> L′16, L26, then capacitor current and capacitor voltage are described by the next simplified equations according to Fig. 11

$$i_{Cc5}(t) \approx I_{Cc5ch}\cos\left(\frac{t - t_5}{\sqrt{C_{C5}L_O}}\right) + \\ + \left(\frac{U_I}{n} - U_O\right)\sqrt{\frac{C_{C5}}{L_O}}\sin\left(\frac{t - t_5}{\sqrt{C_{C5}L_O}}\right) \tag{18}$$

$$u_{Cc5}(t) \approx I_{Cc5ch}\sqrt{\frac{L_O}{C_{C5}}}\sin\left(\frac{t - t_5}{\sqrt{C_{C5}L_O}}\right) + \\ + \left(U_O - \frac{U_I}{n}\right)\cos\left(\frac{t - t_5}{\sqrt{C_{C5}L_O}}\right) + \frac{U_I}{n} - U_O \tag{19}$$

The rectified secondary voltage drops to zero according to equation

$$u_d(t) \approx U_O\left(\frac{U_I}{n} - U_O\right)\cos\left(\frac{t-t_5}{\sqrt{C_{C5}L_O}}\right) - \\ - I_{Cc5ch}\sqrt{\frac{L_O}{C_{C5}}}\sin\left(\frac{t-t_5}{\sqrt{C_{C5}L_O}}\right) \quad (20)$$

The time needed to decreasing the rectified voltage to zero during this interval can be calculated from (20) and it is approximately

$$t_6 - t_5 \approx \sqrt{C_{C5}L_O}\arcsin\left(\frac{U_O}{I_{Cc5ch}}\sqrt{\frac{C_{C5}}{L_O}}\right) \quad (21)$$

Interval (t_6 - t_7):

Operation of the converter in this interval is shown in Fig. 12. At t_6 (Fig. 2) the rectified voltage ud reached zero and afterwards the waveform of the charging process of the C_{C5} capacitance are changed. In this interval the whole energy of the leakage inductance is absorbed by the capacitor C_{C5}.

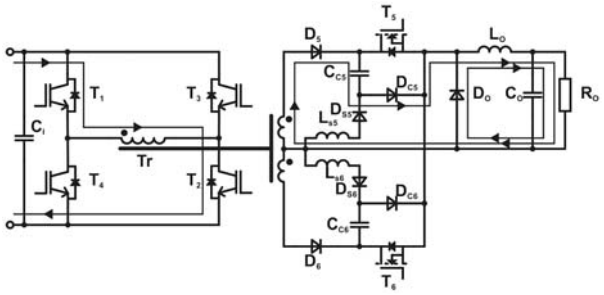

Fig. 12 Operation of the converter in interval t_6 - t_7

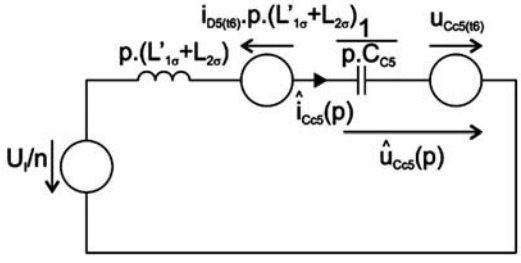

Fig. 13 Equivalent operator circuit for interval t_6 - t_7

At t_7 the current of the rectifier diode D_5 falls to zero, and the primary current that flows through the transistor T_1 and T_2 drops on value of the magnetizing current.

Charging current of the capacitor can be expressed from Fig. 13 as

$$i_{Cc5}(t) = i_{Cc5(t_6)}\cos\left(\frac{t-t_6}{\sqrt{C_{C5}L'_\sigma}}\right) + \\ + \left(\frac{U_I}{n} - u_{Cc5(t_6)}\right)\sqrt{\frac{C_{C5}}{L'_\sigma}}\sin\left(\frac{t-t_6}{\sqrt{C_{C5}L'_\sigma}}\right) \quad (22)$$

where $L'_\sigma = L'_{1\sigma} + L'_{2\sigma}$

The capacitor voltage rises according to equation

$$u_{Cc5}(t) = \frac{U_I}{n} + \left(u_{Cc5(t_6)} - \frac{U_I}{n}\right)\cos\left(\frac{t-t_6}{\sqrt{C_{C5}L'_\sigma}}\right) + \\ + i_{Cc5(t_6)}\sqrt{\frac{L'_\sigma}{C_{C5}}}\sin\left(\frac{t-t_6}{\sqrt{C_{C5}L'_\sigma}}\right) \quad (23)$$

In t_7 the current flowing through rectifying diode D_5 decays to zero and current of the transistors T_1, T_2 drops to value of magnetizing current of the transformer, because capacitor absorbed all the leakage inductance energy. This time interval is expressed by

$$t_7 - t_6 = \sqrt{C_{C5}L'_\sigma}\arctan\left(\frac{i_{Cc5(t_6)}}{\sqrt{\frac{C_{C5}}{L'_\sigma}}\left(u_{Cc5(t_6)} - \frac{U_I}{n}\right)}\right) \quad (24)$$

Where $u_{Cc5(t_6)} \approx \frac{U_I}{n}$ and $i_{Cc5(t_6)} \approx I_{Cc5ch} = i_o + \frac{\Delta i_{Lo}}{2}$

Charging time of the capacitor is approximately sum of equations (21) and (24)

$$t_{Cc5ch} = t_7 - t_5 \approx \frac{\pi}{2}\sqrt{C_{C5}\left(L'_{1\sigma} + L_{2\sigma}\right)} \quad (25)$$

Voltage of the capacitor after charging is

$$U_{Cc5} \approx \frac{U_I}{n} + \left(i_o + \frac{\Delta i_{Lo}}{2}\right)\sqrt{\frac{\left(L'_{1\sigma} + L_{2\sigma}\right)}{C_{C5}}} \quad (26)$$

Interval (t_7 - t_8):

Only the magnetizing current flows through the primary winding of the power transformer in this interval (Fig. 14). This small magnetizing current is turned off by primary switches and thus zero current turn off is achieved. The current of the smoothing inductance L_O is flowing through the freewheeling diode.

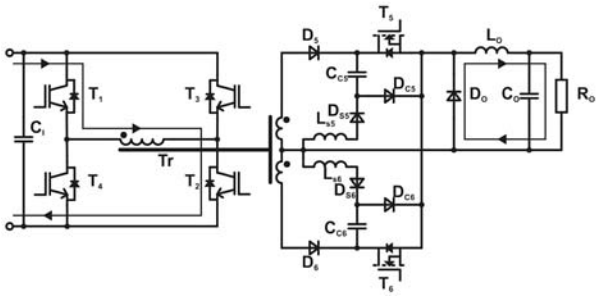

Fig. 14 Operation of the converter in interval t_7 - t_8

At t_8 the primary transistors turn-off only magnetizing current, whose magnitude is given by

$$I_{\mu} = \frac{U_I}{2(L_{1H} + L_{1\sigma})}\frac{T}{2} \tag{27}$$

The smoothing inductance current ripple is

$$\Delta i_{Lo} = \frac{U_O}{L_O}\frac{T}{2}(1-d) \tag{28}$$

Where $d = \dfrac{\left(t_{ON} - \dfrac{T}{2}\right)}{\dfrac{T}{2}}$ is duty cycle

Output voltage can be determined as

$$U_O = \frac{\left(t_{ON} - \dfrac{T}{2}\right)}{\dfrac{T}{2}}\frac{U_I}{n} = d\frac{U_I}{n} \tag{29}$$

Then smoothing inductance current ripple can be expressed as

$$\Delta i_{Lo} = \frac{T}{2L_O}\left(U_O - \frac{U_O^2}{U_I}n\right) = \frac{U_I T}{2nL_O}(d - d^2) \tag{30}$$

The output voltage ripple is given by

$$\Delta U_O = \frac{1}{C_O}\int_0^{d\frac{T}{2}} \frac{\Delta i_{Lo}}{d\dfrac{T}{2}} t dt = \\ = \frac{T^2}{8C_O L_O}\left(\frac{U_O^2}{U_I}n - \frac{U_O^3}{U_I^2}n^2\right) = \frac{U_I T^2}{8nC_O L_O}(d^2 - d^3) \tag{31}$$

3. Simulation results

The theoretical analysis was verified by simulation of the proposed converter in program OrCad. The results confirm zero voltage turn-on and zero current turn-off of primary switches (Fig. 15) and zero current turn-on and zero voltage turn-off of the secondary switches (Fig. 16).

The secondary turn-off snubber works also in compliance with theoretical assumptions as it is shown in Fig. 17. The circulating current is totally depressed as can be seen in Fig. 18, where the primary current decays to value of magnetizing current of the transformer.

4. Conclusion

Detail mathematical description of the proposed converter allows understanding individual dependences and gives the complex view on converter behaviour. On the basis of this analysis it is possible to make optimization of the converter devices from the point of their own operation as well as the converter operation. The present analysis can also help at calculation and optimization of the converter efficiency. By using the new secondary energy recovery turn-off snubber and used control algorithm the turn-off losses of the primary switches are considerably reduced. Moreover, the circulating current is suppressed by controlled rectifier and thus efficiency of the converter is increased.

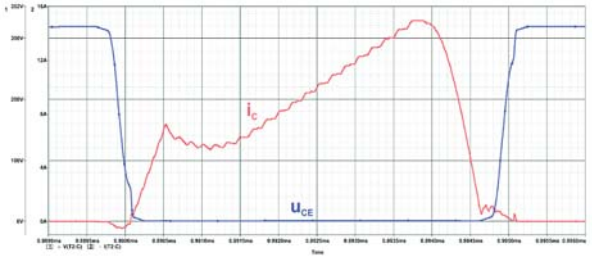

Fig. 15 Collector current i_C and collector-emitter voltage u_{CE} of the inverter transistor T_2 at turn-on and turn-off

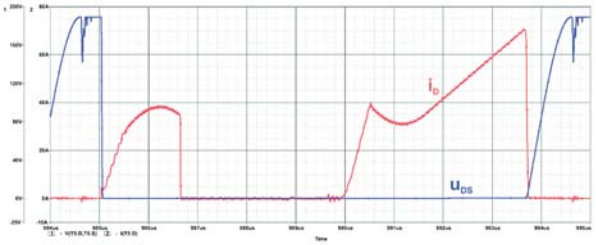

Fig. 16 Collector current i_D and collector-emitter voltage u_{DS} of the output rectifier transistor T_5 at turn-on and turn-off

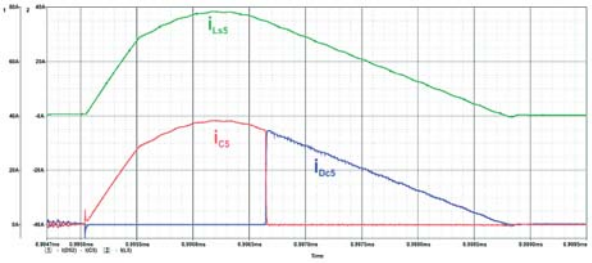

Fig. 17 Current of the snubber inductor L_{S5}, capacitor C_{C5} and diode D_{C5}

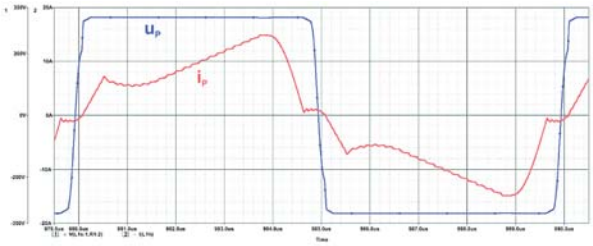

Fig. 18 Primary voltage u_P and current i_P of the power transformer

Acknowledgement

This work was supported by the Slovak Research and Development Agency under the contract No. APVV-0185-10 and R&D operational program Centre of excellence of power electronics systems and materials for their components No. OPVaV-2008/2.1/01-SORO, ITMS 26220120003 funded by European regional development fund (ERDF).

References

[1] CHOI, H. S., KIM, J. W., CHO, B. H.: Novel Zero-voltage and Zero-current-switching (ZVZCS) Full-bridge PWM Converter Using Coupled Output Inductor, *IEEE Transactions on Power Electronics,* vol. 17, No. 5, 2002, pp. 641–648.

[2] JEON, S. J. , CHO, G. H.: A Zero-Voltage and Zero Current Switching Full Bridge DC-DC Converter With Transformer Isolation, *IEEE Trans. on Power Electronics,* vol.16, No. 5, 2001, pp. 573–580.

[3] BOJOI, R., GRIVA, G., KOVACEVIC, G., TENCONI, A.: *ZVS-ZCS Full-Bridge DC-DC Converter for Voltage Step-up in Fuel Cell Distributed Generation Systems,* Record, European Conference on Power Electronics and Applications, 2–5 Sept. 2007, pp. 1–8.

[4] MOISSEEV, S. SATO, S. HAMADA, S., NAKAOKA, M.: *Full Bridge Soft-Switching Phase-Shift PWM DC-DC Converter Using Tapped Inductor Filter,* Record, PESC 2003, pp. 1826–1831.

[5] DUDRIK, J.: *High Frequency Soft Switching DC-DC Power Converters (in Slovak),* Monograph, Elfa: Kosice, Slovakia, 2007.

[6] CHLEBIS, P.: *Soft Switching Converters (in Czech),* Monograph, VSB-TU Ostrava, Ostrava, 2004, ISBN 80-248-0643-6, 148 p.

[7] TEREN, A., FENO, I., SPANIK. P.: *DC/DC Converters with Soft (ZVS) Switching,* Record, Elektro 2001, section – Electrical Engineering, Zilina, 2001, pp. 82–90.

[8] DUDRIK, J., SPANIK, P., TRIP, D. N.: Zero Voltage and Zero Current Switching Full-Bridge DC-DC Converter with Auxiliary Transformer, *IEEE Trans. on Power Electronics,* vol. 21, No. 5, 2006, pp. 1328–1335.

[9] LIU, R.: Comparative Study of Snubber Circuits for DC-DC Converters Utilized in High Power Off-line Power Supply Applications, Record, *IEEE APEC '99*, pp. 821–826.

[10] HIMMELSTOSS, F. A., VOTZI, H. L.: Combined Forward-Flyback-Converter with Only Two Diodes – Function And Modelling, *Communications - Scientific Letters of the University of Zilina,* No. 2a, 2011, pp. 6–12.

[11] SPANIK, P. KANDRAC, J., FRIVALDSKY, M., DRGONA, P.: Verification of Operation Modes of Designed LLC Resonant Converter, *Communications - Scientific Letters of the University of Zilina,* No. 2a, 2011, pp. 67–3.

[12] HAMAR, J., NAGY, I., STUMPF, P., OHSAKI, H,. MASADA, E.: New Dual Channel Quasi Resonant DC-DC Converter Topologies for Distributed Energy Utilization, Record, *EPE -PEMC 2008*, pp.1778–1785.

[13] PETROV, S.: Expectations of Resonant Converters Utilization as Welding Power Sources, *Schematics* No. 7, 2006, pp. 30–33 (in Russian).

[14] HAMAR, J., BUTI, B., NAGY. I.: Dual Channel Resonant DC-DC Converter Family, *EPE J.*, vol. 17, No. 3, 2007, pp. 5–15.

[15] DOBRUCKY, B., BENOVA, M. FRIVALDSKY, M. PRAZENICA, M.: Choosing Modulation Strategies for 2-Stage Combine LLC- and Direct Converter–Modelling, Simulation, Application, *Communications Scientific Letters of the University of Zilina,* No. 2a, 2011, pp. 25–31.

[16] PAVLOVSKY, M., DE HAAN, S. W. H., FERREIRA, J. A.: Reaching High Power Density in Multikilowatt DC-DC Converters with Galvanic Isolation, *IEEE Transactions on Power Electronics,* vol. 24, No. 3–4, 2009, pp. 603–612.

[17] PAUL, A. K., SINGH, S., CHINOY, S.: *Quality Engineering Aspects of Series Resonant Induction Heating Power Supply with Wide Coil Range,* PCIM Europe, Nurnberg, 2008, pp. 173–178.

[18] HARADA, K., ISHARA, Y., TODAKA, T.: *Analysis and Design of ZVS-PWM Half-Bridge Converter with Secondary Switches,* Record, IEEE power Electronics Specialists Conference, PESC 95, vol. 1, June, 1995, pp. 280–285.

[19] DUDRIK, J., TRIP, D. N.: Soft-Switching PS-PWM DC-DC Converter for Full-Load Range Applications, *IEEE Transactions on Industrial Electronics,* vol. 57, No. 8, 2010, pp. 2807–2814.

[20] DUDRIK, J.: Soft Switching Full-Bridge PWM DC/DC Converter Using Secondary Snubber, in: *Journal of Electrical and Electronics Engineering,* vol. 2, No. 1, 2009, pp. 147–150.

[21] DUDRIK, J., RUSCIN, V., BODOR, M.: *Soft Switching DC/DC Converter Using Controlled Output Rectifier with Secondary Turn-off Snubber,* EDPE 2009: Abstracts & CD Proc. of 15th Intern. Conference on Electrical Drives and Power Electronics : 4th Joint Croatia-Slovakia Conference, October, 2009, Dubrovnik: Zagreb, KoREMA, 2009, pp. 1–5.

Yvonne Flicker – Felix A. Himmelstoss *

ANALYSIS OF A POSSIBLE BATTERY CHARGERTOPOLOGY

Battery chargers are very important, especially for handhelds and cars. In this paper a converter is analyzed which enables us to control the voltage across the battery for a high input voltage range. Using the converter as a battery charger, the load current has to be controlled. Consequently, a two-point controller can be used. Therefore, a draft of a two-point controller is given. In addition, the weighted state differential equations are linearized in order to use the possibilities of the linear control theory. A basic analysis of the charger topology is given, the losses are approximated, and some experimental results are presented.

Keywords: *Battery charger, DC/DC converter, modelling.*

1. Introduction

The basic converter is shown in Fig. 1 [1] and consists of an inductor L, an inductor L_B, a capacitor C, an active switch S and a passive switch D. The positive pole of the output voltage is the cathode of the diode. The battery is modelled by a voltage source U_B. Due to the additional capacitor C and the additional inductor L, the classical converter, which is only a step-down converter, is transferred into a step-up-down converter. The mean value of the output voltage U_2, with the duty ratio of the active switch d (the on-time of the active switch referred to the switching period) and neglecting the losses is

$$U_2 = \frac{d}{(1-d)} \cdot U_1 . \qquad (1)$$

The converter is a step-up step-down converter, which also enables us to drive a DC motor in one direction (one-quadrant drive), controlled braking is not possible with this circuit. For other concepts, control applications, and detail about the electrical machine refer to the references [2] till [7].

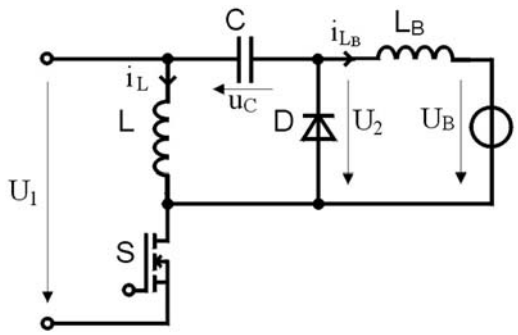

Fig. 1 Step-up-down converter

2. Basic analysis

The basic analysis has to be done with idealized components (that means no parasitic resistors, no switching losses) and for the continuous mode in steady (stationary) state. A good way to start is to consider the voltage across the inductors.

Since for the stationary case the absolute values of the voltage-time-areas of the inductors have to be equal (the voltage across the inductor has to be zero in the average), we can easily draw the shapes according to Figs. 2 and 3. (Here the capacitor is assumed to be so large that the voltage can be regarded constant during a pulse period.)

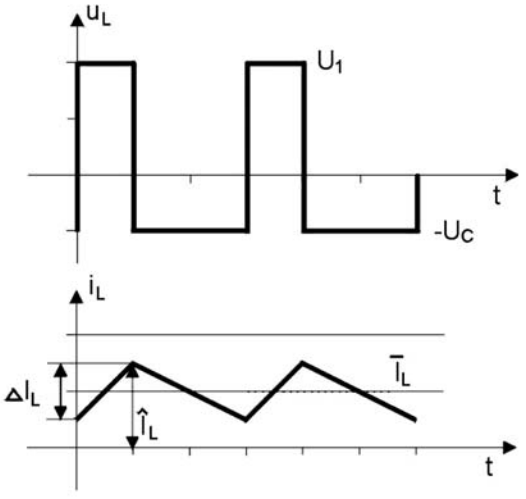

Fig. 2 Voltage across and current through the inductor L

* **Yvonne Flicker, Felix A. Himmelstoss**
University of Applied Science Technikum Wien, E-mail: Felix.Himmelstoss@technikum-wien.at

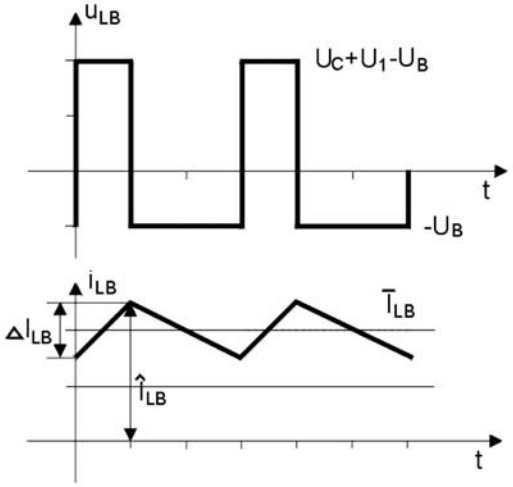

Fig. 3 Voltage across and current through the inductor L_B

Figure 2 shows the current through and the voltage across inductor L. The current rate of rise of course depends on the values of L and U_1. Figure 3 shows the current through and the voltage across inductor L_B. Based on the equality of the voltage-time-areas in the stationary case, it is easy to give the transformation relationship for the battery voltage U_B as a function of the input voltage U_1 and the duty ratio d. From Fig. 3 we get

$$(U_C + U_1 - U_B)\cdot d = U_B\cdot(1-d) \tag{2}$$

and from Fig. 2

$$U_1\cdot d = U_C\cdot(1-d)\,. \tag{3}$$

After a few steps we get the voltage transformation law

$$M = \frac{U_B}{U_1} = \frac{d}{(1-d)}\,. \tag{4}$$

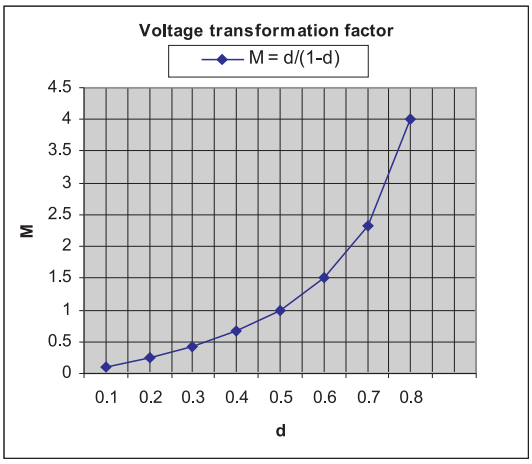

Fig. 4 Voltage transformation factor in dependence on the duty cycle

Figure 4 shows the voltage transformation factor $M = \frac{U_B}{U_1}$ (the ratio of mean value of the output voltage of the converter to input voltage) which is dependant on the duty cycle d. The converter is a step-up-down converter.

In the same manner a relationship for the currents through the inductors can be derived based on the equality of the absolute values of the current-time-areas of the capacitor during on- and off-times of the active switch. From Fig. 5, which shows the current through the capacitor C, we get

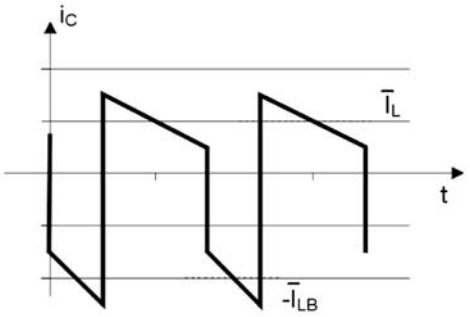

Fig. 5 Current through the capacitor C

$$\bar{I}_L\cdot(1-D) = \bar{I}_{LB}\cdot d\,, \tag{5}$$

$$\bar{I}_L = \bar{I}_{LB}\cdot\frac{d}{(1-d)}\,. \tag{6}$$

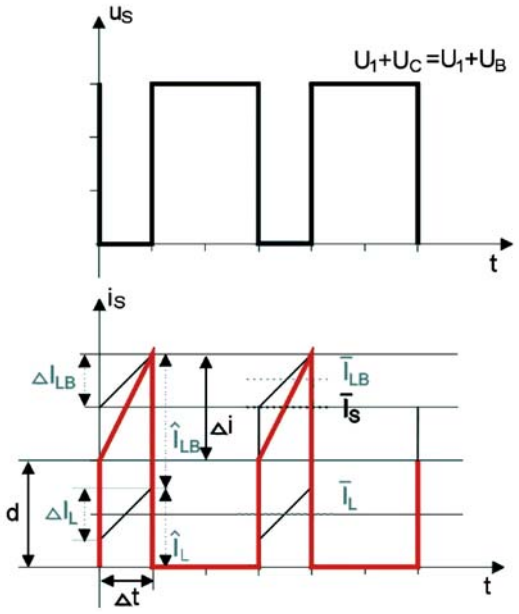

Fig. 6 Voltage across and current through the switch S

From the schematic Fig. 1 one can immediately see that the current through the semiconductor devices is the sum of the inductor currents i_L and i_{LB} (through the switch S during $T_{on} = d \cdot T$ through the diode D during $T_{off} = (1 - \mathrm{d}) \cdot T$. Therefore, the current maximum values for the semiconductor devices are approximately

$$\tilde{I}_{S,\max} = \tilde{I}_{D,\max} = \bar{I}_L + \bar{I}_{LB} \,. \tag{7}$$

Figure 6 shows the current through the active switch and Fig. 7 through the passive switch (diode).

From Fig. 6 one can see that the correct current through the switch S is

$$\begin{aligned} i_S &= i_L + i_{LB} = \frac{\Delta i}{\Delta t} \cdot t + d = \\ &= \frac{(\Delta I_L + \Delta I_{LB}) \cdot t}{d \cdot T} + \bar{I}_L + \bar{I}_{LB} - \frac{\Delta I_L + \Delta I_{LB}}{2}. \end{aligned} \tag{8}$$

The *rms* values are important for the calculation of the on-state losses. One can calculate the exact *rms* value for switch S according to

$$I_{S,rms} = \sqrt{\frac{1}{T} \cdot \int_0^{d \cdot T} (i_S)^2 \cdot dt} \,. \tag{9}$$

After a few steps we get the exact *rms* value for the switch S to

$$I_{S,rms} = \sqrt{\left[\begin{aligned} &\frac{(\Delta I_L + \Delta I_{LB})^2}{3} + \\ &+ (\Delta I_L + \Delta I_{LB}) \cdot \left(\bar{I}_L + \bar{I}_{LB} - \frac{\Delta I_L + \Delta I_{LB}}{2} \right) + \\ &+ \left(\bar{I}_L + \bar{I}_{LB} - \frac{\Delta I_L + \Delta I_{LB}}{2} \right)^2 \end{aligned} \right] \cdot d} \,. \tag{10}$$

The current *rms* value in the middle for the transistor S with the current mean value of the inductors is approximately

$$\bar{I}_{S,rms} = (\bar{I}_L + \bar{I}_{LB}) \cdot \sqrt{d} \,. \tag{11}$$

The conduction losses for the switch S with $R_{DS(on)}$ as on-resistance of the transistor S can be calculated according to

$$P_{v,S} = \frac{1}{T} \int_0^{d \cdot T} u_{DS} \cdot i_S \cdot dt = \frac{1}{T} \int_0^{d \cdot T} R_{DS(on)} \cdot (i_S)^2 \cdot dt \,. \tag{12}$$

After a few steps we get for the conduction losses of the active switch S

$$P_{v,S} = R_{DS(on)} \cdot \left[\begin{aligned} &\frac{(\Delta I_L + \Delta I_{LB})^2}{3} + \\ &+ (\Delta I_L + \Delta I_{LB}) \cdot \left(\bar{I}_L + \bar{I}_{LB} - \frac{\Delta I_L + \Delta I_{LB}}{2} \right) + \\ &+ \left(\bar{I}_L + \bar{I}_{LB} - \frac{\Delta I_L + \Delta I_{LB}}{2} \right)^2 \end{aligned} \right] \cdot d \,. \tag{13}$$

$$P_{v,S} = R_{DS(on)} \cdot I_{S,rms}^2$$

The conduction losses of transistor S with (11) are approximately

$$\begin{aligned} P_{v,S} &= R_{DS(on)} \cdot I_{S,rms}^2 = R_{DS(on)} \cdot \left[(\bar{I}_L + \bar{I}_{LB}) \cdot \sqrt{d} \right]^2 \\ P_{v,S} &= R_{DS(on)} \cdot (\bar{I}_L + \bar{I}_{LB})^2 \cdot d \end{aligned} \,, \tag{14}$$

which could be supplemented by the current ripple by using the exact equation (10).

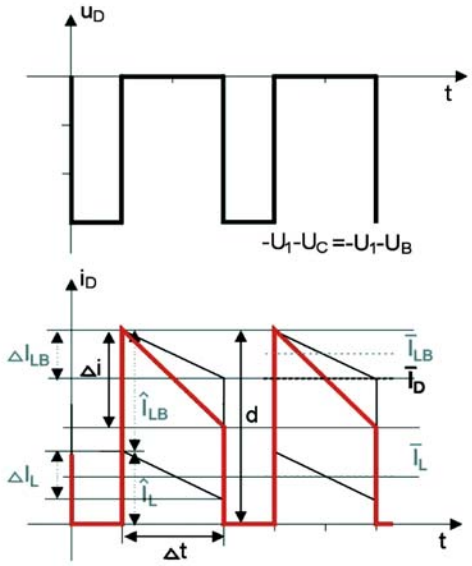

Fig. 7 Voltage across and current through the diode D

From Fig. 7 one can see that the current through the passive switch D is

$$\begin{aligned} i_D &= i_L + i_{LB} = -\frac{\Delta i}{\Delta t} \cdot t + d = \\ &= -\frac{(\Delta I_L + \Delta I_{LB}) \cdot t}{(1 - d) \cdot T} + \bar{I}_L + \bar{I}_{LB} + \frac{\Delta I_L + \Delta I_{LB}}{2} \cdot \end{aligned} \tag{15}$$

Therefore, one can calculate the exact *rms* value for diode D according to

$$I_{D,rms} = \sqrt{\frac{1}{T} \cdot \int_0^{(1-d) \cdot T} (i_D)^2 \cdot dt} \,. \tag{16}$$

After a few steps we get the exact *rms* value for the diode

$$I_{D,rms} = \sqrt{\left[\begin{aligned} &\frac{(\Delta I_L + \Delta I_{LB})^2}{3} + \\ &+ (\Delta I_L + \Delta I_{LB}) \cdot \left(\bar{I}_L + \bar{I}_{LB} - \frac{\Delta I_L + \Delta I_{LB}}{2} \right) + \\ &+ \left(\bar{I}_L + \bar{I}_{LB} - \frac{\Delta I_L + \Delta I_{LB}}{2} \right)^2 \end{aligned} \right] \cdot (1 - d)} \,. \tag{17}$$

The current *rms* value in the middle for the diode D with the current mean value of the inductors is approximately

$$\bar{I}_{D,rms} = (\bar{I}_L + \bar{I}_{LB}) \cdot \sqrt{(1-d)}\,. \tag{18}$$

The conduction losses for the diode D with R_D as differential resistor of the diode and U_{VD} as the fixed forward voltage can be calculated according to

$$\begin{aligned} P_{v,D} &= \frac{1}{T}\int_0^{(1-d)\cdot T} u_D \cdot i_D \cdot dt = \\ &= \frac{1}{T}\int_0^{(1-d)\cdot T} \left[U_{VD}\cdot i_D + R_D \cdot (i_D)^2\right]\cdot dt \end{aligned}\,. \tag{19}$$

After a few steps we get the conduction losses for the passive switch D

$$\begin{aligned} P_{v,D} &= U_{VD}\cdot\left[-\frac{\Delta I_L + \Delta I_{LB}}{2} + \right.\\ &\left.+\left(\bar{I}_L + \bar{I}_{LB} - \frac{\Delta I_L + \Delta I_{LB}}{2}\right)\right]\cdot(1-d) + \\ &+ R_D \cdot \left[\begin{array}{l} \frac{(\Delta I_L + \Delta I_{LB})^2}{3} - \\ -(\Delta I_L + \Delta I_{LB})\cdot\left(\bar{I}_L + \bar{I}_{LB} - \frac{\Delta I_L + \Delta I_{LB}}{2}\right) + \\ +\left(\bar{I}_L + \bar{I}_{LB} - \frac{\Delta I_L + \Delta I_{LB}}{2}\right)^2 \end{array}\right]\cdot(1-d) \end{aligned}$$

$$\begin{aligned} P_{v,D} &= U_{VD}\cdot\left[-\frac{\Delta I_L + \Delta I_{LB}}{2} + \right.\\ &\left.+\left(\bar{I}_L + \bar{I}_{LB} - \frac{\Delta I_L + \Delta I_{LB}}{2}\right)\right]\cdot\\ &\cdot(1-d) + R_D \cdot I_{D,rms}^2 \end{aligned}\,. \tag{20}$$

The conduction losses of diode D with (18) are approximately

$$\begin{aligned} P_{v,D} &= U_{VD}\cdot(\bar{I}_L + \bar{I}_{LB})\cdot(1-d) + R_D \cdot I_{D,rms}^2 \\ P_{v,D} &= \left[U_{VD}\cdot(\bar{I}_L + \bar{I}_{LB}) + R_D\cdot(\bar{I}_L + \bar{I}_{LB})^2\right]\cdot(1-d) \end{aligned}\,, \tag{21}$$

which omits the current ripple.

So one can calculate the total conduction losses according to

$$P_v = P_{v,S} + P_{v,D}\,. \tag{22}$$

We can calculate a rough approximation of the total conduction losses according to (22) and get

$$\begin{aligned} P_v &= \left[R_{DS(on)}\cdot d + R_D\cdot(1-d)\right]\cdot(\bar{I}_L + \bar{I}_{LB})^2 + \\ &+ U_{VD}\cdot(\bar{I}_L + \bar{I}_{LB})\cdot(1-d) \end{aligned}\,. \tag{23}$$

One can calculate the efficiency of the converter (taking only the semiconductor conduction losses into account) according to

$$\eta = \frac{P_{out}}{P_{in}} = \frac{(U_B\cdot\bar{I}_{LB})}{(U_B\cdot\bar{I}_{LB}) + P_v}\,. \tag{24}$$

It is therefore easy to calculate a rough approximation of the efficiency of the converter for continuous operation mode and we get

$$\eta = \frac{1}{1 + \frac{\left[R_{DS(on)}\cdot d + R_d\cdot(1-d)\right]\cdot(\bar{I}_L + \bar{I}_{LB}) + U_{VD}\cdot(\bar{I}_L + \bar{I}_{LB})\cdot(1-d)}{U_B\cdot\bar{I}_{LB}}}\,. \tag{25}$$

3. Converter model

The state variables are the inductor current i_L, the charging inductor current i_{LB}, and the capacitor voltage u_C. The input variables are the input voltage u_1 and the voltage u_B. The fixed forward voltage of the diode (the diode is modelled as a fixed forward voltage U_{VD} and an additional voltage drop depending on the differential resistor of the diode R_D) is included as an additional vector. The parasitic resistances are the on-resistance of the active switch R_S, the series resistance of the converter coil R_L, the series resistance of the charging coil R_{LB}, the series resistor of the capacitor R_C, and the differential resistor of the diode R_D.

In continuous inductor current mode there are two states. In state one the active switch is turned on and the passive switch is turned off. Figure 8 shows this switching state one.

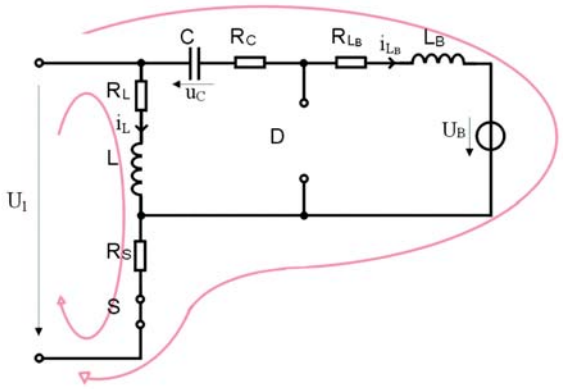

Fig. 8 Equivalent circuit for state one of the converter

The state space equations are now

$$\frac{di_L}{dt} = \frac{-i_L\cdot(R_L + R_S) - i_{LB}\cdot R_S + u_1}{L} \tag{26}$$

$$\frac{di_{LB}}{dt} = \frac{-i_L\cdot R_S - i_{LB}\cdot(R_{LB} + R_C + R_S) + u_C + u_1 + u_B}{L_B} \tag{27}$$

$$\frac{du_C}{dt} = \frac{-i_{LB}}{C} \tag{28}$$

leading to the state space description

$$\frac{d}{dt}\begin{pmatrix} i_L \\ i_{LB} \\ u_C \end{pmatrix} = \begin{bmatrix} \frac{-(R_L+R_S)}{L} & \frac{-R_S}{L} & 0 \\ \frac{-R_S}{L_B} & \frac{-(R_{LB}+R_C+R_S)}{L_B} & \frac{1}{L_B} \\ 0 & \frac{-1}{C} & 0 \end{bmatrix} \cdot \begin{pmatrix} i_L \\ i_{LB} \\ u_C \end{pmatrix} + \begin{bmatrix} \frac{1}{L} & 0 \\ \frac{1}{L_B} & \frac{-1}{L_B} \\ 0 & 0 \end{bmatrix} \cdot \begin{pmatrix} u_1 \\ u_B \end{pmatrix}. \tag{29}$$

In state two the active switch is turned off and the passive switch is turned on. Figure 9 shows this switching state two.

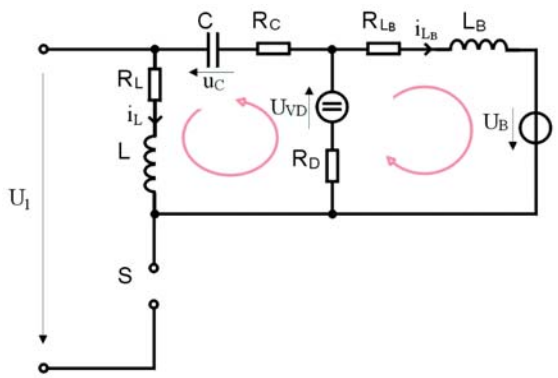

Fig. 9 Equivalent circuit for state two of the converter

The describing equations are

$$\frac{di_L}{dt} = \frac{-i_L \cdot (R_L + R_C + R_D) - i_{LB} \cdot R_D - U_{VD} - u_C}{L} \tag{30}$$

$$\frac{di_{LB}}{dt} = \frac{-i_L \cdot R_D - i_{LB} \cdot (R_{LB} + R_D) - U_{VD} - u_B}{L_B} \tag{31}$$

$$\frac{du_C}{dt} = \frac{i_L}{C} \tag{32}$$

leading to the state space description (33)

When using two active switches in push-pull mode (a second active switch instead of the diode), the diode is shunted and U_{VD} can be set to zero. R_D is then the on-resistance of the second switch. Combining the two systems by the state-space averaging method leads to a model, which describes the converter in the mean. We can combine these two sets of equations, providing that the system time constants are large compared to the switching period.

Weighed by the duty ratio, the combination of the two sets yields to (34)

The dynamic behavior of the idealized converter is described correctly in the average by the given system of equations, thus quickly giving us a general view of the dynamic behavior of the converter. The superimposed ripple (which appears very pronounced in the coils) is of no importance for qualifying the dynamic behavior. This model is also appropriate as large-signal model, because no limitations with respect to the signal values have been made.

$$\frac{d}{dt}\begin{pmatrix} i_L \\ i_{LB} \\ u_C \end{pmatrix} = \begin{bmatrix} \frac{-(R_L+R_C+R_D)}{L} & \frac{-R_D}{L} & \frac{-1}{L} \\ \frac{-R_D}{L_B} & \frac{-(R_{LB}+R_D)}{L_B} & 0 \\ \frac{1}{C} & 0 & 0 \end{bmatrix} \cdot \begin{pmatrix} i_L \\ i_{LB} \\ u_C \end{pmatrix} + \begin{bmatrix} 0 & 0 \\ 0 & \frac{-1}{L_B} \\ 0 & 0 \end{bmatrix} \cdot \begin{pmatrix} u_1 \\ u_B \end{pmatrix} + \begin{bmatrix} \frac{-1}{L} \\ \frac{-1}{L_B} \\ 0 \end{bmatrix} \cdot u_{VD}. \tag{33}$$

$$\frac{d}{dt}\begin{pmatrix} i_L \\ i_{LB} \\ u_C \end{pmatrix} = \begin{bmatrix} \frac{-[d \cdot R_S + (1-d) \cdot (R_C + R_D) + R_L]}{L} & \frac{-[d \cdot R_S + (1-d) \cdot R_D]}{L} & \frac{(d-1)}{L} \\ \frac{-[d \cdot R_S + (1-d) \cdot R_D]}{L_B} & \frac{-[d \cdot (R_C + R_S) + R_{LB} + (1-d) \cdot R_D]}{L_B} & \frac{d}{L_B} \\ \frac{(1-d)}{C} & \frac{-d}{C} & 0 \end{bmatrix} \cdot$$

$$\cdot \begin{pmatrix} i_L \\ i_{LB} \\ u_C \end{pmatrix} + \begin{bmatrix} \frac{d}{L} & 0 \\ \frac{d}{L_B} & \frac{-1}{L_B} \\ 0 & 0 \end{bmatrix} \cdot \begin{pmatrix} u_1 \\ u_B \end{pmatrix} + \begin{bmatrix} \frac{(d-1)}{L} \\ \frac{(d-1)}{L_B} \\ 0 \end{bmatrix} \cdot u_{VD} \tag{34}$$

Linearizing this system around the operating point enables us to calculate transfer functions for constructing Bode plots.

The weighed matrix differential equation representing the dynamic behavior of the converter is a nonlinear one. A linearization is necessary to use the possibilities of the linear control theory. We can calculate the linearized small signal model of the converter with capital letters for the operating point values and small letters for the disturbance around the operating point

$$i_L = I_{LO} + \hat{i}_L$$

$$i_{LB} = I_{LB0} + \hat{i}_{LB} \qquad u_1 = U_{10} + \hat{u}_1 . \tag{35}$$

$$u_C = U_{C0} + \hat{u}_C \qquad d = D_0 + \hat{d}$$

The following equations can be specified for the stationary (working point) values

$$\begin{aligned} 0 = {} & I_{L0}\cdot\left[-D_0\cdot R_S + (R_C + R_D)\cdot(D_0 - 1) - R_L\right] + \\ & + I_{LB0}\cdot\left[-D_0\cdot R_S + R_D\cdot(D_0 - 1)\right] + \\ & + U_{C0}\cdot(D_0 - 1) + D_0\cdot U_{10} + U_{VD}\cdot(D_0 - 1) \end{aligned} \tag{36}$$

$$\begin{aligned} 0 = {} & I_{L0}\cdot\left[-D_0\cdot R_S + (D_0 - 1) - R_D\right] + \\ & + I_{LB0}\cdot\left[-D_0\cdot(R_C + R_S) - R_{LB} + R_D\cdot(D_0 - 1)\right] + \\ & + U_{C0}\cdot D_0 - U_{B0} + D_0\cdot U_{10} + U_{VD}\cdot(D_0 - 1) \end{aligned} \tag{37}$$

$$I_{LB0} = I_{L0}\frac{(1 - D_0)}{D_0} . \tag{38}$$

The same results as derived from the section basic analysis can be achieved in the ideal case (assuming ideal devices with no losses)

$$0 = U_{C0}\cdot(D_0 - 1) + D_0\cdot U_{10} \tag{39}$$

$$0 = U_{C0}\cdot D_0 - U_{B0} + D_0\cdot U_{10} \tag{40}$$

leading again to

$$_B = \frac{D_0}{(1 - D_0)}\cdot U_{10} . \tag{41}$$

One can calculate the linearized small signal model of the converter according to (eq. 42)

4. Experimental model of the converter

A small converter model was built. The coils L and L_B have about 43 µH and a resistor of about 5.6 mΩ, the capacitor (implemented with an electrolyte capacitor and a film capacitor) has about 100 µF and a resistor of about 21mΩ. A pulse capacitor is shunted parallel to the electrolyte capacitor for the high frequency component of the capacitor current. The diode has a current rating of 30 A, a differential on-resistance of 30mΩ, and a forward voltage of 730 mV. The transistor can carry a current of 26 mΩ at a maximum drain source voltage of 100 V. The on-resistance is 26 mV.

Figure 10 shows the control signal of the active switch for a duty cycle of 50% (generated by the arbitrary pulse generator),

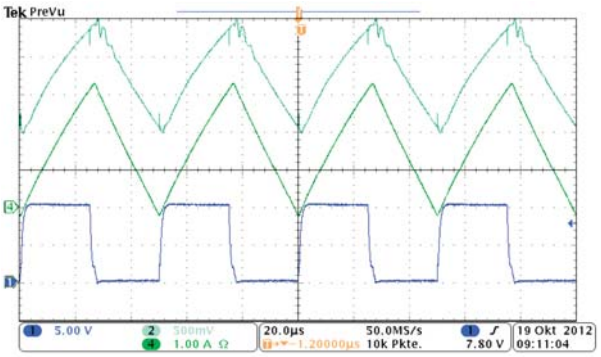

Fig. 10 Gate-source voltage (blue) of the active switch by a duty cycle of 50%, measurement signal of the LEM current sensor (turquoise) and current through the inductor LB measured by a current probe (green)

$$\frac{d}{dt}\begin{pmatrix}\hat{i}_L\\ \hat{i}_{LB}\\ \hat{u}_C\end{pmatrix} = \begin{bmatrix} \frac{-D_0\cdot R_S + (D_0 - 1)\cdot(R_C + R_D) - R_L}{L} & \frac{-\left[D_0\cdot R_S + (1 - D_0)\cdot R_D\right]}{L} & \frac{(D_0 - 1)}{L} \\ \frac{-D_0\cdot R_S + (D_0 - 1)\cdot R_D}{L_B} & \frac{-D_0\cdot(R_C + R_S) + R_{LB} + (1 - D_0)\cdot R_D}{L_B} & \frac{D_0}{L_B} \\ \frac{(1 - D_0)}{C} & \frac{-D_0}{C} & 0 \end{bmatrix} \cdot \begin{pmatrix}\hat{i}_L\\ \hat{i}_{LB}\\ \hat{u}_C\end{pmatrix} + \begin{bmatrix} \frac{D_0}{L} & \frac{I_{L0}\cdot(-R_S + R_C + R_D) + I_{LB0}\cdot(-R_S + R_D) + U_{C0} + U_{10} + U_{VD}}{L} \\ \frac{D_0}{L_B} & \frac{I_{L0}\cdot(-R_S + R_D) + I_{LB0}\cdot(-R_C - R_S + R_D) + U_{C0} + U_{10} + U_{VD}}{L_B} \\ 0 & \frac{-I_{L0} - I_{LB0}}{C} \end{bmatrix} \cdot \begin{pmatrix}\hat{u}_1\\ \hat{d}\end{pmatrix} \tag{42}$$

which is measured at the active switch (blue), the measurement signal of a LEM current sensor (turquoise and triangular shaped) and the current through the inductor L_B (green and triangular shaped).

5. Two-point control

The two-point control is another control method for controlling the output current of the battery charger. In comparison with the pulse width modulation, the two-point control operates with variable periodic time as well as with variable pulse width. The activation and deactivation of the active switch depends on the instantaneous values of the current to be controlled. The active switch has to be turned off when the current reaches the upper limit and has to be turned on again when the current reaches the lower limit. The difference between the switching points is called hysteresis.

Figure 11 shows the non-inverting Schmitt-trigger. The parallel positive feedback creates the needed hysteresis. The hysteresis voltage is controlled by the proportion between the resistances of R_1 and R_2. The resistor R_1 can be calculated from resistor R_2, upper threshold voltage u_{T+}, lower threshold voltage u_{T-}, higher supply voltage u_{sat+} and lower supply voltage u_{sat-} according to

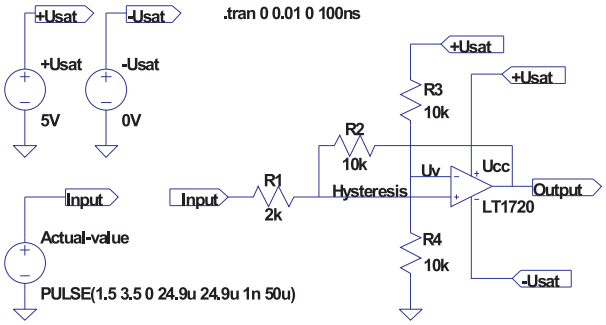

Fig. 11 Non-inverting Schmitt-trigger

$$R_1 = \frac{(u_{T+} - u_{T-}) \cdot R_2}{u_{sat+} - u_{sat-}}. \tag{43}$$

The inverting input makes the reference point. The reference voltage is obtained from the voltage divider R_3 and R_4. One can calculate the offset voltage u_V according to

$$u_V = \frac{u_{T+} \cdot u_{sat+} - u_{T-} \cdot u_{sat-}}{u_{sat+} - u_{sat-} + u_{T+} - u_{T-}}. \tag{44}$$

The resistor R_4 can be calculated from resistor R_3, offset voltage u_V and supply voltage usat according to

$$R_1 = \frac{u_V \cdot R_3}{\pm u_{sat} - u_V}. \tag{45}$$

6. Results of two-point control

A DC-DC converter with two-point control and current measurement was built for the evaluation of the two-point control in the circuit.

Figure 12 shows the concept. The DC-DC converter with parasitic resistances of the components and fixed forward voltage of the diode as well as the two-point control and current measurement are indicated. A so-called "shunt resistor" RS is indicated for the current measurement. A LEM-current sensor in series with the output inductor is used in the real circuit for current sensing. A driver stage is used in order to turn on or block the MOSFET as quickly as possible.

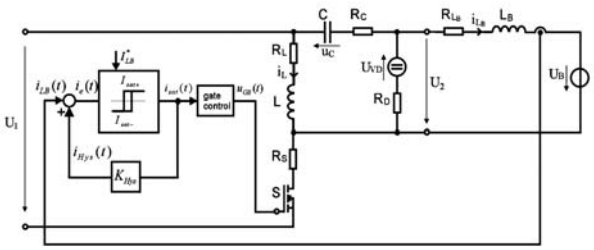

Fig. 12 Converter with two-point control and current measurement

The circuit of the non-inverting Schmitt-trigger is dimensioned so that the upper threshold voltage u_{T+} is and the lower threshold voltage u_{T-} is 2.2 V. The offset voltage u_V is 2.4 Vin this case. The supply voltage of the LEM-converter and the gate driver is 10 V. The input voltage of the converter can be up to 36 V.

Figure 13 shows that the control signal (orange) turns to "high", when the measurement signal of the LEM current sensor (red) reaches the lower threshold and it turns to "low", when the measurement signal of the LEM current sensor reaches the upper threshold. The on-time is 6 µs and the off-time is 17 µs. This corresponds to a frequency of 59 kHz.

Fig. 13 Measurement signal of the LEM current sensor (red), hysteresis (blue), offset voltage (green) and gate-source voltage (orange)

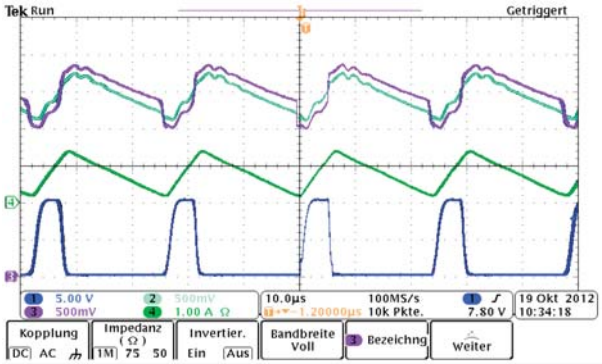

Fig. 14 Measurement signal of the LEM current sensor (turquoise), hysteresis (pink), current through the inductor LB (green) and gate-source voltage (blue)

Figure 14 shows the measurement signal of the LEM current sensor (turquoise), the hysteresis (pink), the current through the inductor L_B (green) and the gate-source voltage (blue). From Fig. 10 one can immediately see that the current through the inductor L_B (green) is between –2.2 A and 3.3 V. With the two-point control, the current through the inductor L_B (green) is limited between 0.2 A to 1.4 A now.

7. Conclusion

Battery chargers are very important, especially for low and medium voltages and low and medium power (e.g. handhelds, cars [8], solar applications [9]). The here treated converter is similar to the basic step-down converter. Due to a simple *LC* element which is added, the converter generates now a mean voltage across the diode, which can be higher or lower than the input voltage. This is especially useful when only low input voltages are available. The system can be described as a three order system. A two-point control with a non-inverting two-point controller is useful to control the output voltage or output current. In this way, the active switch is turned on and off. Therefore, it is possible to keep the load current i_{LB} in a defined range by stopping the rise of the coil current via the active switch. The converter is especially applicable for solar and small fuel cell applications. It can be designed also for medium power applications e.g. for charging car batteries out of a solar generator.

References

[1] HIMMELSTOSS, F.: *Ein- und Zweiqudrantenstellglieder*, Austrian Patent Office AT 507203 B1 filed 2008.10.30.
[2] HIMMELSTOSS, F. A., FLICKER, Y., RABL, M.: *A Simple Two-Quadrant DC Motor Controller,* OPTIM 2010.
[3] ZACH, F.: *Leistungselektronik,* 4. Aufl, Wien : Springer, 2010.
[4] MOHAN, N., UNDELAND, T., ROBBINS, W.: *Power Electronics, Converters, Applications and Design* (2nd Ed.), New York: W. P. John Wiley & Sons, 2003.
[5] BOLDEA, I., TUTELEA, L.: *Electric Machines: Steady State, Transients, and Design with MATLAB,* Boca Raton, FL: CRC Press Taylor and Francis Group, 2010.
[6] SCOTARU, P., NICOLAEI, D. V., CERNAT, M., PUKLUS, Z.: *Reversible DC-to-DC Converter for a Dual Voltage Automotive System Using Zero Voltage Switching Technique,* OPTIM 2008
[7] MARCHESONI, M., VACCA, C.: New DC–DC Converter for Energy Storage System Interfacing in Fuel Cell Hybrid Electric Vehicles, *IEEE Trans. On Power Electronics*, vol. 54, No. 2, 2007, pp. 301–308.
[8] EMADI, A.: *Handbook of Automotive Power Electronics and Motor Drives,* Marcel Dekker, 2005.
[9] TURCEK, J., HRASKO, M., ALTUS, J.: Photovoltaics in Present Days and their Coexistence with Power Systems, *Communications – Scientific Letters of the University of Zilina,* No. 2a, 2011, pp.109–113.

Michal Frivaldsky – Branislav Dobrucky – Giacomo Scelba – Pavol Spanik – Peter Drgona *

BIDIRECTIONAL STEP-UP/STEP-DOWN DC-DC CONVERTER WITH MAGNETICALLY COUPLED COILS

The paper is focused on bidirectional up/down DC-DC converter with magnetically coupled coils (MCC), which can be utilized as a part of power semiconductor system in traction, automotive, or industrial applications like renewable energy sources. Proposed solution of main circuit of bidirectional converter should serve for energy transfer from source to load, and vice versa, whereby parameters of electrical variables like voltage, current and power are able to be adapted based on the current requirements of application. Their values can be increased or decreased in first (energy transfer from source to load) or in third (energy transfer from load to source) quadrant of converter's operation. The boost effect of output voltage can be increased - if it is not sufficient one - by appropriate ratio of number of inductor windings.

Keywords: *DC-DC power converter, bidirectional step-up/step-down converter, duty cycle factor, transfer function, parasitic parameters, steady-state operation.*

1. Introduction

Process of energy recuperation is well known phenomena, especially in the field of traction applications. Nowadays, the recuperation of energy is used in the industrial, commercial and also in the consumer sector. The main factor, which allows this breakthrough, was development of technology in production of power semiconductor structures and research of new topologies of main circuit of switched mode power supplies (SMPS), which are working in two-quadrant (2Q bi-directional) operation [1]–[3]. Although, there are now a variety of schemes of DC/DC bidirectional converters, the disadvantage of these solutions is high complexity, or lack of versatility, which is associated with limited utilization of mentioned topologies. The main reason for this are specific requirements for their properties, particularly possibility of change of electrical values as wide as possible. Another disadvantage of existing solutions in terms of universal utilization is relatively high material costs.

Nowadays, the existing solutions of bidirectional converters can by divided as follows: The first group includes cascade DC/DC converters in buck-boost topology, second group are non-isolated half-bridge topologies, in another group the multi-tank non-isolated Cuk and Sepic topologies are presented and last group involves so-called split topologies, using pi-filters at the input and output of converter. The mentioned drawback in the comparison with proposed solution is considerably higher number of components in the system resulting in higher complexity of topology, lack of versatility and insufficient dynamical range of input and output parameters

2. Bidirectional step-up/step-down converter with MCC

The main circuit of proposed converter, based on boost DC-DC converter [4]-[6], is composed of three main parts (Fig. 1). The first is given by primary capacitive filter together with primary transistor T1. Second part consists of the most important part of converter – bifilar wound coil, whose windings are connected in order to create auto-transformer with common ground on the primary and secondary side. If target application requires total galvanic isolation between primary and secondary side, it is possible to realize the proposed converter as an isolated bidirectional converter. This approach can also be done by simple modification of the main circuit with the use of auxiliary switch. The last, third part of the proposed converter is composed of secondary transistor T2, of a filter and of load/appliance.

It can be seen from Fig. 1 that the primary as well as secondary part of converter have in principle the same functionality. Based on this property both parts can behave as input or output of the converter (the secondary side is dissymmetrical to the primary side), and, therefore, the energy transfer from source to load and vice versa can be simply and effectively realized. Simultaneously the modification of the electrical variables magnitudes (increase or decrease) can be done in a wide regulation range. Based on the operating conditions, the converter functionality is held in the first- or third quadrant of operating characteristic.

The main advantages compared to other solution of bidirectional DC/DC converters are:

- extra-wide regulation range of electrical variables at given output (step-up/step-down)

* **Michal Frivaldsky[1], Branislav Dobrucky[1], Giacomo Scelba[2], Pavol Spanik[1], Peter Drgona[1]**
[1] Department of Mechatronics and electronics, University of Zilina, Slovakia, E-mail: michal.frivaldsky@fel.uniza.sk
2 Dipartimento di ingegneria, Universita degli studi di Catania, Italy

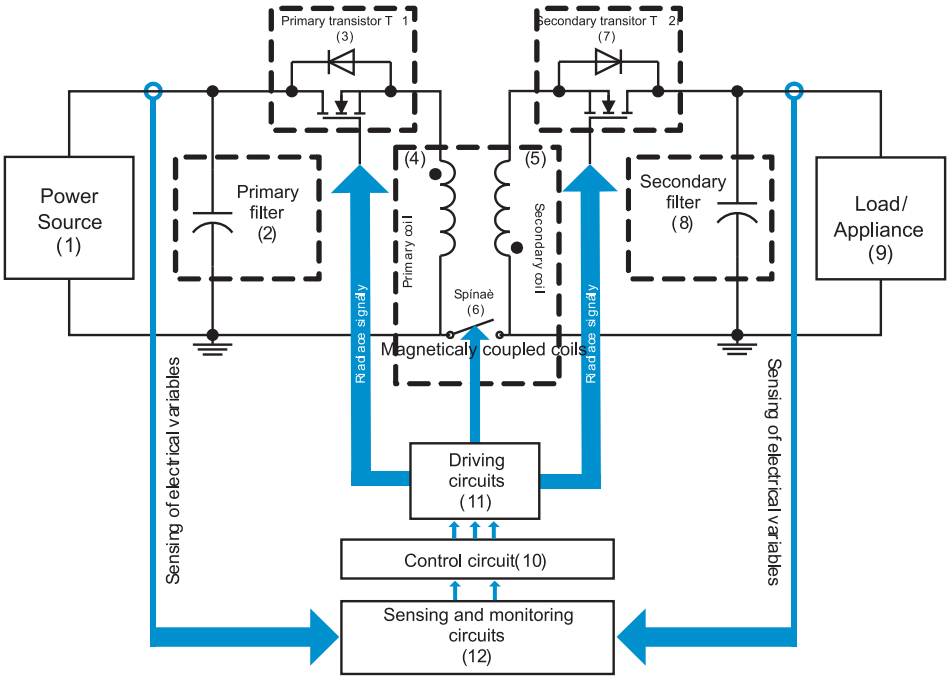

Fig. 1 Block scheme of proposed bidirectional DC-DC converter with MCC [7]

- low complexity of the main circuit within achievement of high universality
- possibility of isolated and non-isolated version

The analysis of proposed converter

The proposed converter, whose principal schematic is shown in Fig. 1 is classified as DC-DC converter. The following analysis is oriented on the determination of state space variables and on the investigation of voltage-transfer characteristic in both direct and recuperative mode of operation.

The operation of converter both for directions (energy transfer from source into load) and for recuperative (energy transfer from load into source) mode can be divided into two operating intervals:

- interval $I\langle t_0 - t_1\rangle$: transistor T_1 (T_2) closed, transistor T_2 (T_1) open;
- interval $II\langle t_1 - T\rangle$: transistor T_1 (T_2) open, transistor T_2 (T_1) closed.

Fig. 2 shows schematics of the proposed converter, whereby parasitic resistances are considered, and due to fact that their presence is influencing voltage transfer characteristic. This impact is negative and, therefore, must be accepted during state space model setting and its consequent derivation.

The state space model for the proposed converter is derived for the operating condition when the converter operates at direct mode. Here, it must be noted that considering recuperative operating mode the state space will be the same, whereby only one change applies specifically for the input/output arguments in the case of voltages and currents (input will act as output and vice versa).

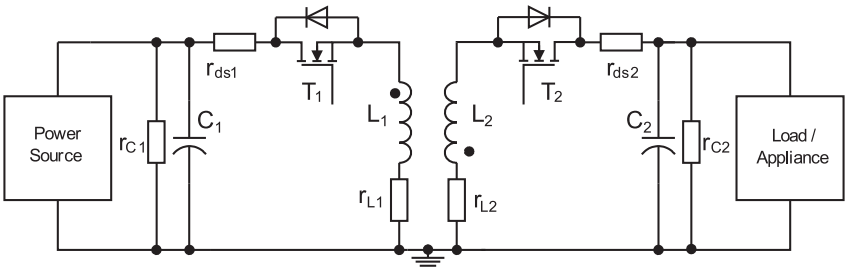

Fig. 2 Block scheme of proposed bidirectional DC-DC converter with MCC

Interval $I\langle t_0 - t_1\rangle$

$$\frac{d}{dt}\begin{pmatrix} i_{L1} \\ u_{C2} \end{pmatrix} = \begin{pmatrix} -r_s/L_1 & 0 \\ 0 & -(1/r_2 + 1/R_2)1/C \end{pmatrix}\begin{pmatrix} i_{L1} \\ u_{C2} \end{pmatrix} + \\ + \begin{pmatrix} 1/L_1 & 0 \\ 0 & 0 \end{pmatrix}\begin{pmatrix} u_1 \\ 0 \end{pmatrix}, \quad (1)$$

where:
i_{L1} is the current in the primary side
u_{C2} isoutput capacitor voltage
r_s is the sum of series parasitic resistances
r_2 is the parallel parasitic resistances
L_1 is value of primary inductance
U_1 is input voltage
R_2 is load resistance

Interval $II\langle t_1 - T\rangle$

$$\frac{d}{dt}\begin{pmatrix} i_{L2} \\ u_{C2} \end{pmatrix} = \begin{pmatrix} -r_s/L_2 & -1/L_2 \\ 1/C_2 & -(1/r_2 + 1/R_2)1/C \end{pmatrix}\begin{pmatrix} i_{L1} \\ u_{C2} \end{pmatrix} + \\ + \begin{pmatrix} 1/L_2 & 0 \\ 0 & 0 \end{pmatrix} * \begin{pmatrix} 0 \\ 0 \end{pmatrix} \quad (2)$$

The voltage transfer characteristic can be derived from the comparison of ripple current during the first and second interval. The analysis outgoes from the equation of inductor's voltage:

$$u_L = L \cdot \frac{di_L}{dt} \quad (3)$$

After linearization, the next formula is valid for ripple current:

$$\Delta I_L = \frac{U \cdot D \cdot T}{L}, \quad (4)$$

where:
D is duty cycle,
T is switching period of converter.

Comparing the value of ripple current during interval when transistor T1 is closed with the ripple current from the interval when transistor T1 is open leads to:

$$\frac{U_1 \cdot D \cdot T}{L_1} = \frac{U_2 \cdot (1 - D) \cdot T}{L_2}. \quad (5)$$

When $L_1 = L_2$, thus $N_1 = N_2$, where N_1 and N_2 are numbers of primary or secondary turns and all parasitic resistances are neglected, then the next equation for approximate computation of voltage transfer function can be written:

$$\frac{U_2}{U_1} = \frac{D}{(1 - D)}. \quad (6)$$

Figure 3 shows graphical interpretation of voltage transfer characteristic with ideal waveform (without parasitic ones), and voltage transfer waveform when parasitic resistances are being considered.

3. Simulation investigations of proposed converter's properties

In this chapter we would like to investigate the voltage transfer functions of the proposed converter based on parametrical simulations from OrCAD/Pspice. Based on this, and after comparisons with theoretical assumptions it is possible to demonstrate existing deviations in voltage transfer function.

Next figure shows voltage transfer function of the proposed converter whose input/output parameters are as follows:

$U_{IN} = 24$ V, $f_{SW} = 50$ kHz, $L_1 = L_2 = 300$ µH($N_1 = N_2$),
$U_{OUT} =$ var, $I_{OUT} =$ var, $P_{OUT} =$ max. 25 W,
load resistance $R_2 = 48$ Ω,
Parasitics $r_s = 0.24$, 0.48, 0.96 and 1.44 Ω:

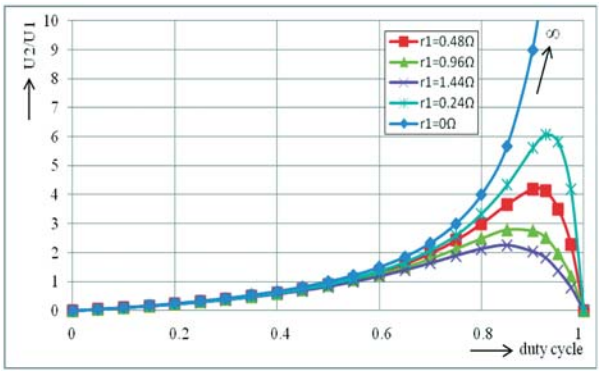

Fig. 3 Voltage transfer function of proposed converter at 100% power loading and various parasitic resistances from 0 to 1.44 Ohm

Load 100, 200 and 20%, $R = 48$, 24 and 240 Ω:

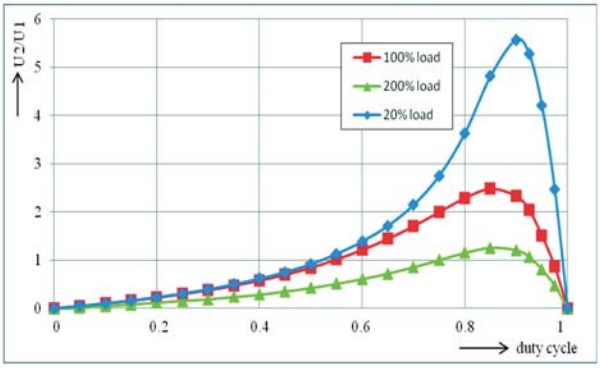

Fig. 4 Voltage transfer function of proposed converter at 20, 100 and 200 % of power loading

It is evident from Figs. 3 and 4 that
- idealized relation of voltage transfer ration U_2/U_1 on duty cycle D (i.e. $= D/1 - D$) is not valid for entire range of duty cycle ($\in \langle 0;1 \rangle$;
- consequently, voltage transfer characteristic is not monotonic one but it has a local extreme at which derivative of the transfer is changing; it is a critical point of characteristic;
- control system used should be acting just in 'secure' range from 0 to a critical value of duty cycle D_{crit}, otherwise it must have a variable structure.

4. Experimental verification of bidirectional step-up/step-down converter with MCC

The experimental set/up was built (Fig. 5) with parameters: $U_{IN} = 24$ V, $f_{SW} = 50$ kHz, $L_1 = L_2 = 300$ μH($N_1 = N_2$), C load resistance $R_2 = 48$, 24, 240 Ω, $P_{OUT} =$ var. 25 W as maximum, depending on load resistance.

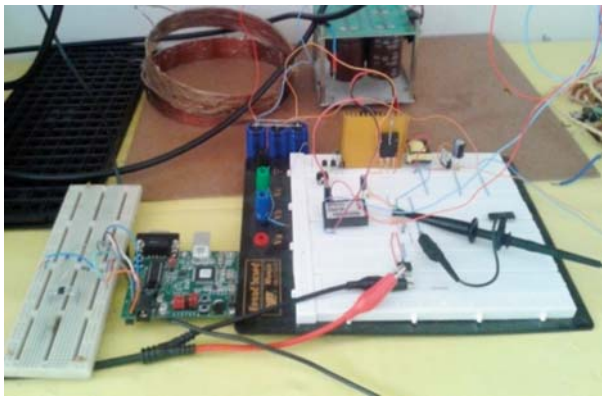

Fig. 5 Experimental set-up of proposedbidirectional step-up/step-down converter

There are results carried-out by measurement on experimental set-up of the converter at 20-, 100-, and 200 % of the load under resistive loading.

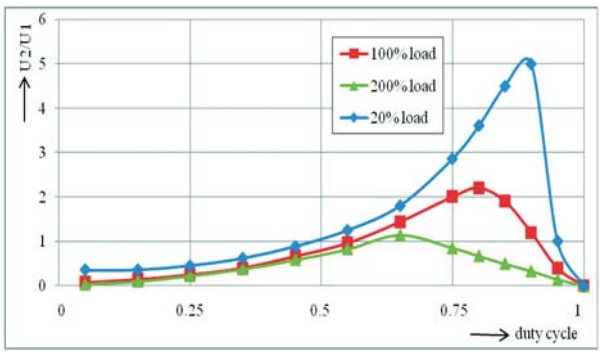

Fig. 6 Experimental voltage transfer functions of proposed converter at 20–200 % load

Output power can be calculated from the carried-out transfer characteristics in Fig. 6

$$P_{OUT} = \frac{U_2^2}{R_2}: \; P_{48\Omega} = \frac{(2 \cdot 24)^2}{48} = \frac{4}{2}\frac{24^2}{24} = 48 \; W$$

at $D = 0.75$;

$$P_{48\Omega} = \frac{(1 \cdot 24)^2}{48} = \frac{14}{2}\frac{24^2}{24} = 12 \; W$$

at duty cycle $D = 0.50$;

$$P_{48\Omega} = \frac{(1.41 \cdot 24)^2}{48} = \frac{2}{2}\frac{24^2}{24} = 24 \; W$$

at duty cycle $D = 0.625$;

It is possible to calculate the requested power (24 W) also under 24 Ω load resistance

$$P_{24\Omega} = \frac{(1 \cdot 24)^2}{24} = \frac{1}{1}\frac{24^2}{24} = 24 \; W$$

at duty cycle $D = 0.65$.

So, for a fair design of the converter elements it is necessary to determine at what output voltage we want the requested power. Possible improvements of operation and efficiency of the converter are to be reached by works [8]–[10].

5. Conclusion

The bidirectional step-up/step-down converter was presented in the paper. Simulation experiment results worked-out using OrCAD/PSpice programming environment showed that voltage transfer characteristics feature two parts: the first one with positive derivative part, and the second one with negative derivative part. Maximal output voltage doesn't depend only on a duty cycle of electronic switches but also on the parasitic parameter values of the converter circuit elements. The experimental set/up measurements verified results of simulation and theoretical assumptions.

Presented solution of bidirectional converters based on buck-boost DC/DC topologyconsists of substantial lesser components than classical cascade DC/DC converters or non-isolated half-bridge topologies, and features: an extremely wideregulation range of output voltage, low complexity of main circuit within achievement of high universality, and possibility of isolated and non-isolated versions. Such a converter system can be utilized as a part of power semiconductor system in traction, automotive, or industrial applications like renewable energy sources.

As future work we suppose the investigation of transient behavior –, efficiency analysis- and control system design of that type of bidirectional step-up/step-down converter.

Acknowledgement

The authors wish to thank for the financial support to Slovak Research and Development Agency project No. APVV-0138-10 and R&D operational program Centre of excellence of power electronics systems and materials for their components No. OPVaV-2008/2.1/01-SORO, ITMS 26220120046 funded by European regional development fund (ERDF).

References

[1] LUO, F.L., YE, H.: *Power Electronics - Advanced Conversion Technologies.* CRC Press: Boca Raton, 2010, ISBN 978-1-4200-9429-9.

[2] SZYCHTA, E.: *Multi-Resonant ZVS Converter of DC/DC Voltage Type(in Polish).* Monograph, Oficyna Wydawnicza Uniwersytetu Zielonogorskiego, 2006.

[3] BERES, T., DUDRIK, J., EOTVOS E.: Bidirectional Step-up/step-down DC-DC Converter for Hybrid Battery (in Slovak). *EE-Journal for Electrical Engineering and Electro-Energetics,* vol. 17, No. 1, 2011, pp. 31-32, ISSN 1335-2547.

[4] HIMMELSTOSS, F. A., VOTZI, H. L.: Combined Forward-Flyback-Converter with Only Two Diodes - Function and Modelling. *Communications - Scientific Letters of the University of Zilina ZU,* pp. 6-12, 2a/2011.

[5] LUFT, M., SZYCHTA, E., SZYCHTA, L.: *Method of Designing ZVS Boost Converter,* 13th Power Electronics and Motion Control Conference - EPE-PEMC, Poznan, pp. 463-467, 2008.

[6] DOBRUCKY, B., HRABOVEC, L., POPRENDA, J.: *Power Supply of Increased Exciting Voltage of Static Exciter for Traction Generator GPA-600 (in Slovak),* Research Report No. V-0767/88, EVPU a.s., Nova Dubnica, March 1988.

[7] FRIVALDSKY, M., DOBRUCKY, B., SPANIK, P.: *Bidirectional Step-up/step-down DC-DC Converter with Magnetically Coupled Coils (in Slovak),* Application on Industrial TemplatePUV No. N/A, submitted: Apr. 8, 2013.

[8] DUDRIK, J., TRIP, N. D.: Soft- Switching PS-PWM DC-DC Converter for Full-load Range Applications, *IEEE Transactions on Industrial Electronics,* vol. 57, No. 8, pp. 2807-2814, 2010.

[9] DOBRUCKY, B., SPANIK, P., SUL, R.: Improvement of Power Electronic Structure Characteristics Using SiC Technology - An Overview. *Communications - Scientific Letters of ZU*, No.1, pp. 34-38, 2006

[10] SPANIK, P., DOBRUCKY, B., FRIVALDSKY, M., DRGONA, P.: Experimental Analysis of Commutation Process of Power Semiconductor Transistor Structures, *ActaTechnica CSAV,* vol. 52, No. 4, 2007, pp. 399-413, ISSN 0001-7043.

Elzbieta Szychta – Grzegorz Krawczyk – Jozef Buday – Jozef Kuchta – Jan Michalik *

SIMULATION STUDIES OF THE UNDERGROUND DC TRACTION SUBSTATION WITH AND WITHOUT ENERGY STORAGE DEVICE

This paper presents the results of the underground DC traction substation simulation studies for two versions: the substation equipped with the ESD (Energy Storage Device) and without the ESD. In these studies Supercapacitors Energy Storage System of energy capacity 10 kWh and voltage 900 V is used. Simulation studies were performed in the Simscape/Simulink.

Keywords: *Traction substation, underground, energy storage device, supercapacitor, simulation model, energy, power, Simscape/Simulink.*

1. Introduction

Continuous increase in the cost of electricity requires the use of modern technology to reduce power consumption, including electricity storage devices known as (ESD – Energy Storage Device). Energy storage is used to compensate for the demand and supply of energy in stationary and mobile applications.

To the group of these devices accumulating energy we can include, among others ESD such as: Electrochemical Energy Storage Devices, Superconducting Magnetic Energy Storage Devices and Supercapacitors (also known as Ultracapacitors and Double Layer Supercapacitors) and Flywheels.

The possibility of a large number of charging and discharging cycles of supercapacitors (10000 ÷ 500000) without degradation, distinguishing them clearly from the typical electrical energy storage, such as batteries. Double-layer capacitors combine, the advantages of traditional batteries and capacitors that is: the ability to quickly adapt to changes in loading and a high value of accumulated energy.

Ultracapacitors are used in: electric and rail vehicles, industrial applications, supplementing, or even replacing the batteries as a source of guaranteed supply voltage to the control, automation, etc.

The use of the ESD in underground traction substation could cause lower demand for electricity, which in turn is associated with its lower production, so as to limit carbon dioxide emissions into the environment. It is estimated that the production of 1 MWh is associated with the emission of one ton of CO_2 [1]. Another equally important aspect arising from the use of these devices is to stabilize the voltage in the traction line and the reduction of peak power consumption.

The analysis of the literature [2] shows that the greatest opportunity for practical application of traction substations described types of ESD has supercapacitors. Therefore, in simulation studies Supercapacitors Energy Storage System is included.

2. The underground substation simultation studies in two versions with and without energy storage devices

Simulation studies were carried out using Simscape package, which is an extension of simulation environment from Mathworks Simulink. Simscape is used for modeling and simulation of physical

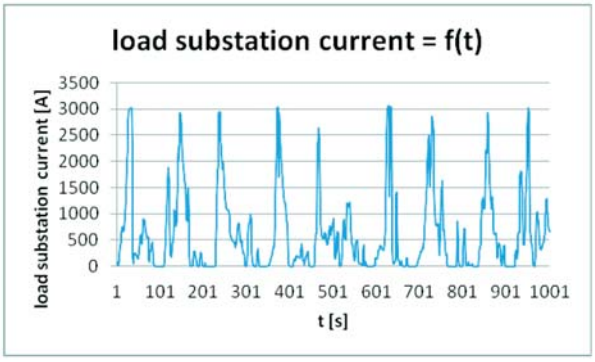

Fig. 1 The course of the instantaneous value of the load current substation (part of – the first 1000 values) beyond communication peak driving metro for the time period 12.00.00 – 13.00.00

* **Elzbieta Szychta[1], Grzegorz Krawczyk[1], Jozef Buday[2], Jozef Kuchta[2], Jan Michalik[2]**
[1] Faculty of Transport and Electrical Engineering, Kazimierz Pulaski University of Technology and Humanities in Radom, Poland, E-mail: e.szychta@uthrad.pl
[2] EVPU, Electrotechnical research and projecting company Nova Dubnica, Slovakia

systems, such as: mechanical, electrical and hydraulics systems. Continuous process simulation studies are performed with a variable time step of the simulation.

Substation model input data are real DC substation load current obtained during the measurement on one of the Warsaw underground traction substation at a frequency of every 4–5 minutes (beyond communication peak driving metro trains – Fig. 1).

2.1 The underground substation simulation studies without energy storage device

The traction substation simulation model (Fig. 2) consists of a *DC Substation* subsystem block in series with the *Load* block.

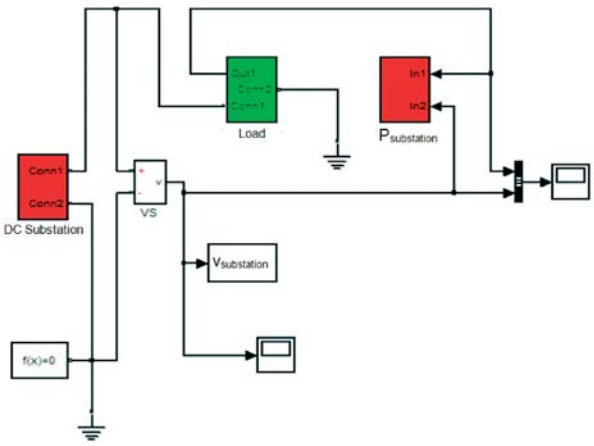

Fig. 2 The underground substation simulation model implemented in the Simscape

DC substation subsystem was modeled as a series connection of a voltage source, reflecting the substation load voltage U_0 = = 900 V, resistor with a resistance $R_{internal}$ = 0.0234 Ω corresponding to the internal resistance of the substation [2]. However, substations load was modeled as a receiver controlled substation load current (Fig. 1) obtained on the basis of measurements carried out on the real underground traction substation (subsystem *Load* – Fig. 2). Instantaneous power substation waveform values are determined in $P_{substation}$ block (Fig. 2). Figs. 3 and 4 show the waveforms obtained from the simulation tests beyond communication peak driving metro.

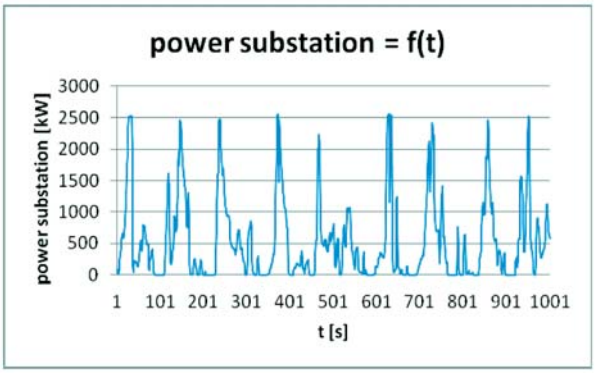

Fig. 4 Fragment course of instantaneous peak power substation beyond communication peak driving metro trains

2.2 Simulation studies metro traction substations equipped with energy storage system (supercapacitors energy storage system)

Supercapacitors are described by the same laws of physics as traditional capacitors, but the first one have a larger surface area to allow the storage of a larger charge and less space between the electrodes than conventional capacitors. The result is an increase of capacity and energy that can be stored in double-layer capacitors. Depending on the research approach double-layer capacitors are variously modeled. The variety of theoretical models describing supercapacitors, due to the fact that they are used in different areas, and that each model provides different accuracy of the processes described in these devices. Based on the analysis of the available literature of theoretical models describing the superca-

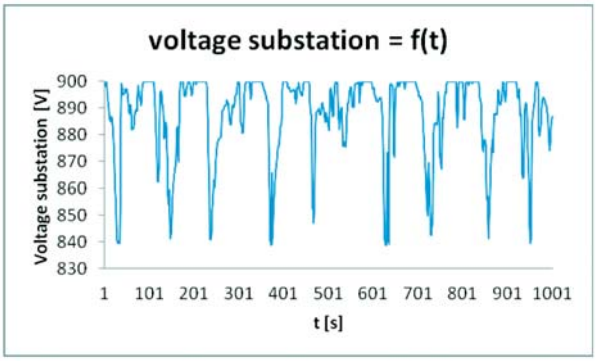

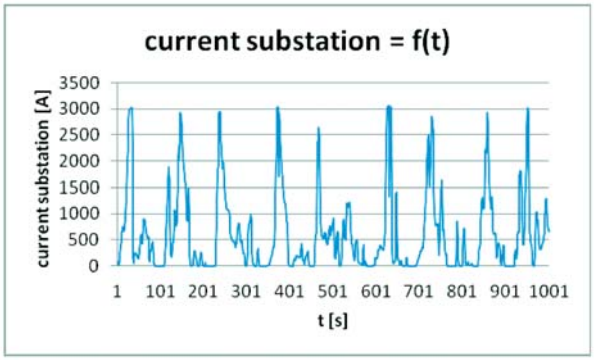

Fig. 3 The fragment of a course of the instantaneous values of voltage and current substation beyond communication peak driving metro trains

pacitors [2, 3, 4], a model of supercapacitor (Fig. 5a) has been selected to the simulation studies.

The simulation studies take into account the following substitute parameters ESD (Fig. 5b): $C = 93$ F, $E = 10$ kWh, $U = 900$ V, $R_s = 124.22\ \Omega$ (resistance responsible for losses in supercapacitor), $R_p = 6.440$ kΩ (resistance reflecting supercapacitor self-discharge) [2, 5].

It was created with the appropriate combination of series-parallel single-supercapacitors. For the calculation of substitute parameters ESD LS Mtron supercapacitor rated voltage of 2.8 V and a rated capacity of 3000 F were adopted.

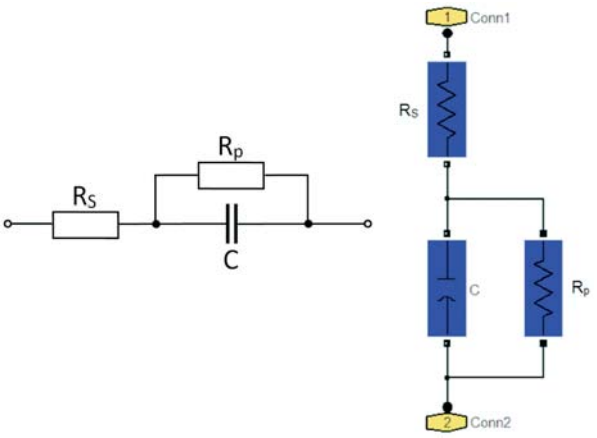

a) classical physical model capacitor without considering inductance terminals

b) computer model of supercapacitor

Fig. 5 A model of Supercapacitors Energy Storage System: a) and b)

Underground substation simulation model equipped with the energy accumulation system (Fig. 6) were tested assuming an initial voltage ESD (initial conditions) of 900 V. In this case, the voltage on the ESD in moment before commutation was equal to the value of the resultant voltage, which has been dimensioned Supercapacitors Energy Storage System.

Sequences on and off switches in the *System charge and discharge* ESD ("charging" and "dischaging") are performed by the control algorithm (Fig. 7) located in block S-function called *Control* (Fig. 6).

Symbols used in Fig. 7:

v_{ESD} – instantaneous value of the voltage at the terminals of the power ESD;

V_{MAX_ESD} – nominal voltage ESD;

V_{MIN_ESD} – minimal (acceptable) voltage ESD (equation 1);

$$V_{MIN\_ESD} = \frac{V_{MAX\_ESD}}{2} \tag{1}$$

v_{sub} – instantaneous value of the voltage at the terminals of the substation;

V_s – switching voltage which is defined by the average voltage substations, above which the ESD is charging and discharging below this value;

V_a – voltage, which is to be charged ESD. Based on the equation 2 the user can define the value range from 900 V to 500V.

$$V_a = \frac{\left(V_{MAX\_ESD} - V_{MIN\_ESD}\right)}{g} \tag{2}$$

where:

g – a numerical value containing in the range of 0.5 ÷ 0.9.

Operating regimes of substation control system with ESD are shown in Table 1.

Figures 8 – 11 contain waveforms obtained during the simulation studies with ESD.

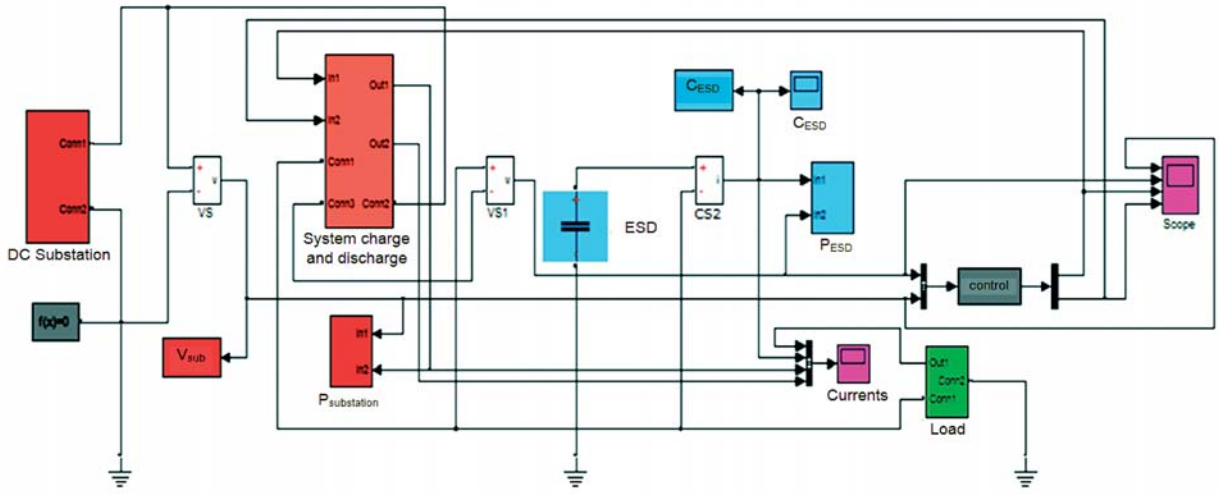

Fig. 6 A simulation of underground substation with ESD model

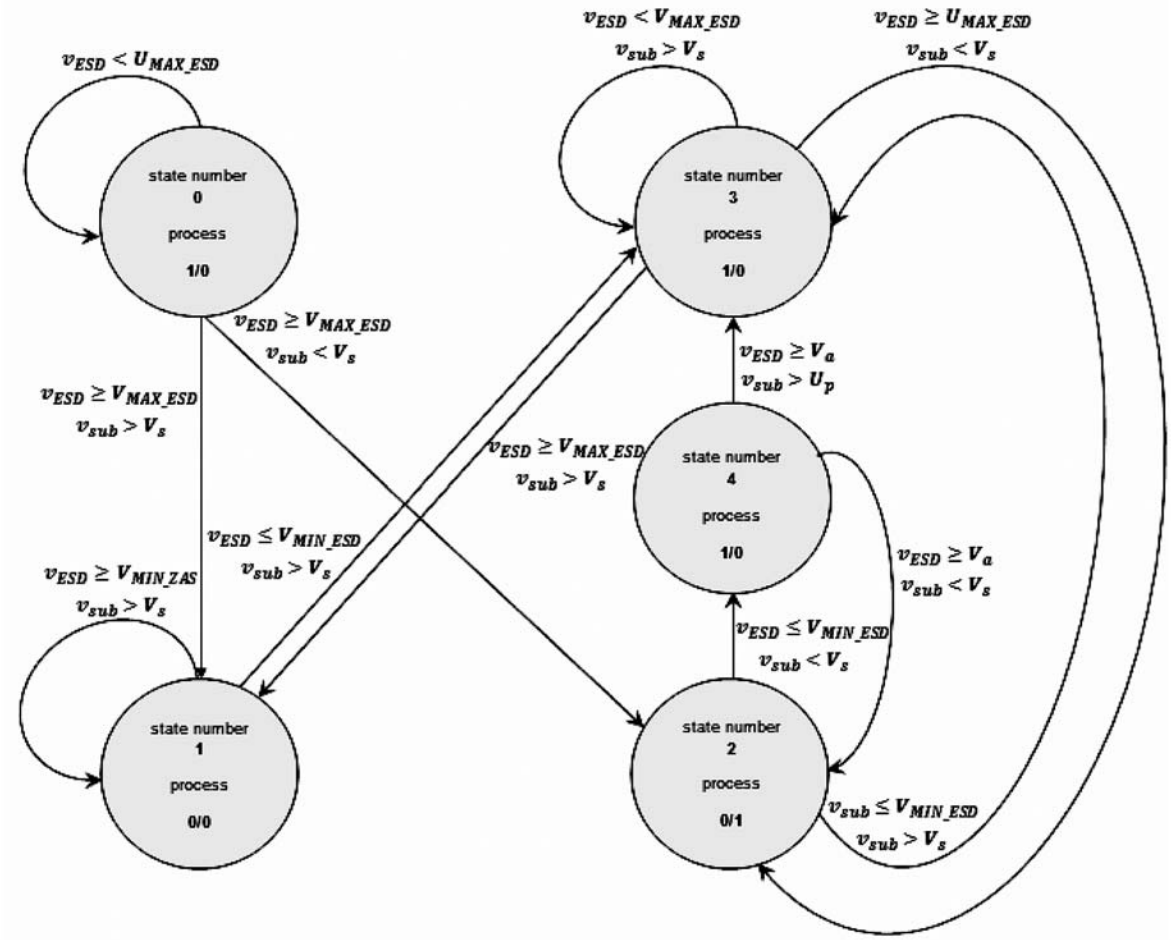

Fig. 7 A simulation model of the substation control system ESD

Operating regimes of substation control system with ESD — Table 1

Operating regimes of substation control system with ESD		
1/0	0/1	0/0
Value "1" on the left side shows the charging state, and the value "0" to the right the discharge state.	Value "0" to the left side means no charging status, and the number "1" to the right side means the state of discharge.	This means the system idle state that there is neither charging nor discharging state.

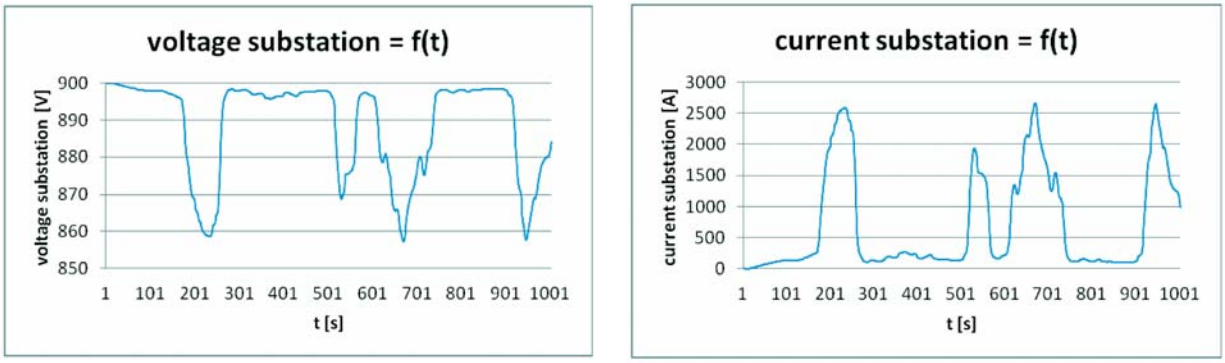

Fig. 8 The fragment of a course of the instantaneous values of voltage and current substation beyond communication peak driving metro trains

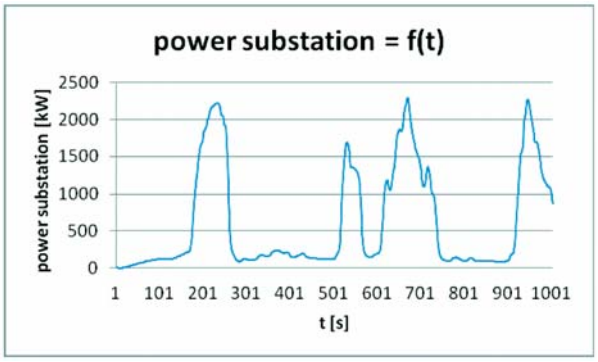

Fig. 9 The fragment of a course of the instantaneous values of power substation beyond communication peak driving metro trains

3. The results of calculations of statistical parameters characterizing the voltage and power substation

In the next part of this article the results of calculations of statistical parameters (arithmetic mean values and standard deviations) obtained during the simulation for variants: with and without Supercapacitors Energy Storage System were summarized.

Graphs presented in Fig. 12 show the results of calculations of the parameters characterizing the voltage traction substation for the course of the instantaneous values of load current substation beyond communication peak driving metro trains.

The average value of the same voltage substation beyond communication peak driving metro trains is lower by 0.06% as compared to a substation of an electrical energy storage device. The standard deviation is by 23.22% higher than beyond communication peak driving metro trains. The graph contains the values of average power substation, beyond communication peak driving metro trains obtained for variants: with and without ESD is shown in Fig. 13.

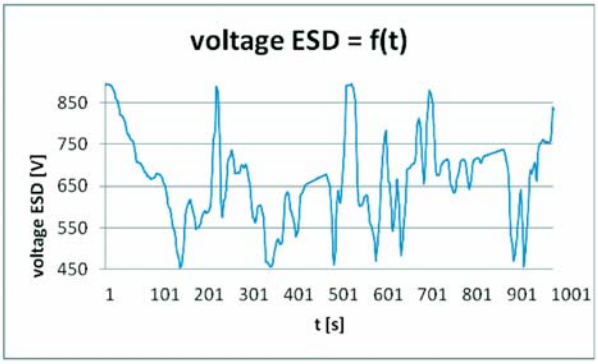

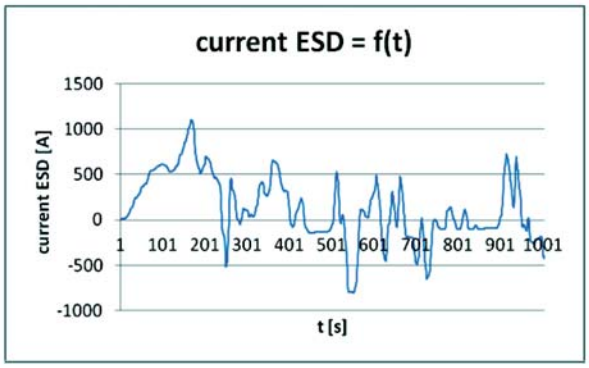

Fig. 10 The fragment of a course of the instantaneous values of voltage and current ESD in communication beyond peak driving metro trains

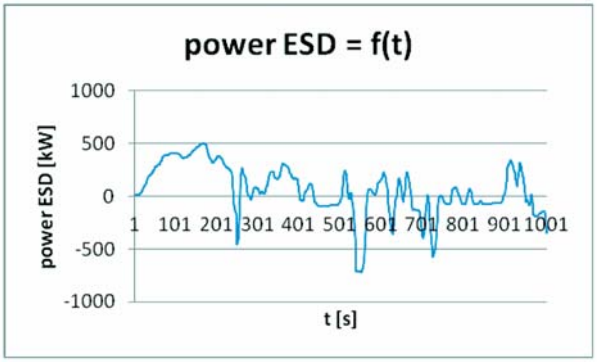

Fig. 11 The fragment of a course of the instantaneous values of power ESD in communication beyond peak driving metro trains

Based on the above waveforms (Figs. 3 – 4 and Figs. 8 – 11) it can be concluded that the application of ESD with appropriate parameters (93 F, 10 kWh and 900 V) resulted in smoothing of voltage at the terminals of the substation as well as reducing the value of the current drawn from the substation, in relation to the same substation model version.

Comparing the values of power substations in the system without and with ESD (energy capacity of 10 kWh) beyond peak driving metro trains, reduction of the power consumption of: 13.63 % for the version of the substation not equipped with a system of accumulation was received.

4. Conclusions

Analysis of simulation results leads to the conclusion that the use of the substation equipped with energy storage device reduces the power consumed by the substation, in relation to the substation not fitted with ESD. In addition, electrical energy storage is beneficial for stabilizing the voltage substations. The more stable voltage, the more predictable movement of trains of the metro line, the better conditions for both accelerating trains, as well as the return of recuperative braking energy [6, 7]. In this case, it is possible to discharge ESD in the moment of the increased

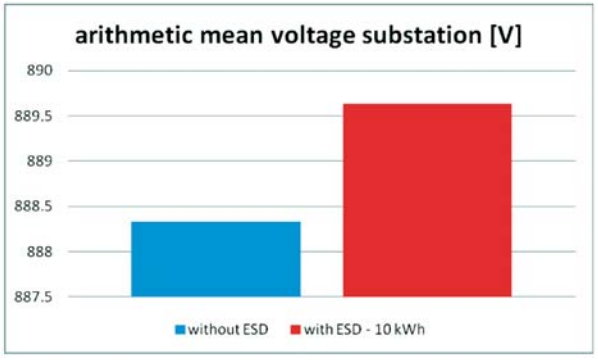

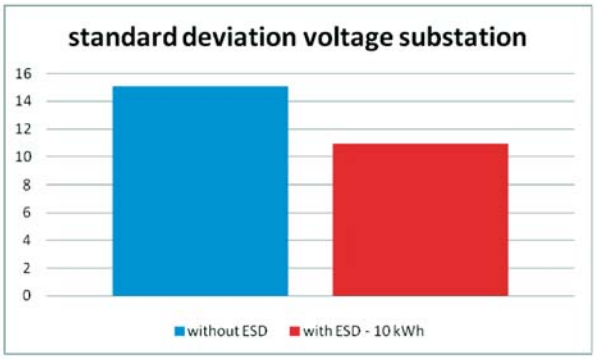

Fig. 12 The average values of voltage at the terminals of the substation and the standard deviation of the voltage without and with ESD (E = 10 kWh) beyond communication peak driving metro trains

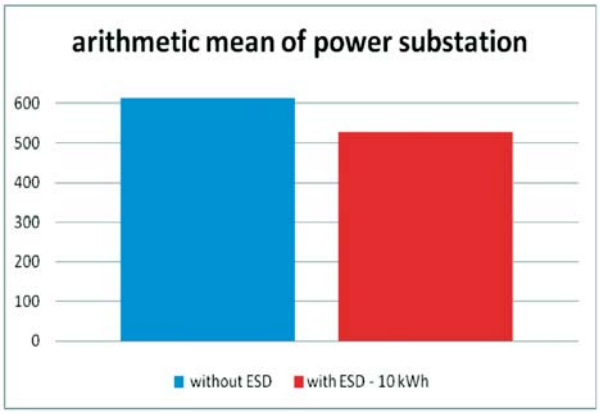

Fig. 13 The average values of power substation without and with ESD (E = 10 kWh) beyond communication peak driving metro trains

demand for power and accumulate in the ESD overcapacity present in the traction network.

ESD is more efficiently used in beyond communication peak driving metro trains than in the communication peak. This is due to the fact that in beyond communication peak distances between trains are larger, and so there are more variations of currents and voltages, therefore ESD will be used more efficiently than in the peak hours. The intensity of the train is greater at the peak of the metro trains running and therefore, it is more likely to exchange energy between adjacent trains. Substation load is more steady than in beyond communication peak driving metro trains.

The use of ESD reduces the phenomenon of surge voltage causing damage to the power system components. At the time when the vehicle goes into regenerative braking mode, and the power section is not a train that would be able to pick up the energy from braking, the voltage in the traction network rises to the level defined as the maximum allowable.

In addition, ESD can also be used as an additional source of energy supply in emergency situations, so that for example, it can result in a metro train to the nearest station, which is important from the point of view of safety of passengers.

References

[1] SZELAG, A.: Increasing the Energy Efficiency of Railway Transport. *Rail Transport Technology,* No. 12, 2008, ISSN 1232-3829.
[2] KRAWCZYK, G.: *Assessment of Effectiveness of the Application of Energy Storage Devices in the Underground Supply System.* The doctoral dissertation. Technical University of Radom, 2012.
[3] GUERRERO, M., ROMERO, E., BARRERO, F., MILANES, M., GONZALEZ, E.: *Overview of Medium Scale Energy Storage Systems.* Prof. of conference IEEE 6th Intern. Conference-Workshop Compatibility in Power Electronics, CPE2009, Badajoz, 2009, ISBN 978-1-4244-2856-4.
[4] SHI, L., CROW, M.: *Comparison of Ultracapacitor Electric Circuit Models,* IEEE Power and Energy Society General Meeting. Conversion and Delivery of Electrical Energy in the 21st Century, pp. 1–6, July, 2008, ISSN 1932-5517.
[5] PAWEŁCZYK, M., KRAWCZYK, G.: A Method of the Determination of the Energy Storage Device Basic Parameters in the DC Electric Traction. *Logistics,* No. 3, 2007, ISSN 1231-5478.
[6] DOBRUCKY, B., OTCENASOVA, A., POKORNY, M., TABACEK, R.: The New Possibilities of Dynamic Compensation and Regeneration of Energy in Electric Traction. *Communications - Scientific Letters of the University of Zilina,* ISSN 1335-4205, Content 1/1999.
[7] DOBRUCKY, B., ALTUS, J., SPANIK, P.: Synergic Influence of Power Electronics, Electric Traction and Electro-energetics. *Communications - Scientific Letters of the University of Zilina,* No. 2–3, 2001, ISSN 1335-4205.

Jan Perdulak – Dobroslav Kovac – Irena Kovacova – Matus Ocilka
– Andrii Gladyr – Dmytro Mamchur – Iurii Zachepa – Tibor Vince – Jan Molnar *

EFFECTIVE UTILIZATION OF PHOTOVOLTAIC ENERGY USING MULTIPHASE BOOST CONVERTER IN COMPARISON WITH SINGLE PHASE BOOST CONVERTER

The paper presents a novel concept of multiphase boost converter (MPBC) with high efficiency of energy conversion. The new topology of MPBC is compared with conventional single-phase boost converter (SPBC). It is shown that almost whole input energy from photovoltaic module entering to the proposed MPBC is utilized more effectively in comparison with conventional SPBC. This effective energy utilization is ensured by suitable algorithm of switches control. Modeling, simulation and experimental results are given. Subsequently the laboratory models of SPBC and MPBC were built and experimental results were obtained to confirm the simulation results. Also the control module of MPBC was designed, simulated and built to ensure the correct operation of proposed converter.

Keywords: *Multiphase boost converter, single phase boost converter, efficiency of energy conversion, photovoltaic.*

1. Introduction

Photovoltaic is the direct conversion of light into electricity in form of direct current electricity. Usually the *DC/DC* converters are used to convert this direct electrical power from one level to another.

There are many types of materials which are used to make of the PV modules. The main problem of these materials is low conversion efficiency which is usually moving from 5% (*a-Si*) to 25% – 30% (*GaAs*) [1]. Nowadays, the efficiency of the soft switching *DC/DC* converters is very high and it is moving around the 97%. But, on the other hand, the efficiency of energy conversion is not good in comparison with abovementioned converter efficiency.

This paper presents the novel concept of *MPBC* with high efficiency of energy conversion. The high efficiency of energy conversion is ensured by adding five more parallel legs to the conventional *SPBC*. The suitable algorithm of switches control in particular legs ensures that the almost whole *PV* output energy from the *PV* module is effective utilized.

2. Efficiency of energy conversion

Figure 1 explains the problem of efficiency of energy conversion. The impinging sun energy P_{IN_sun} is converted by *PV* module direct to the electric energy. According to the material from which *PV* module is built this conversion efficiency is moving from 5% (*a-Si*) to 30% (*GaAs*) [1] and [2]. The output *PV* energy P_{OUT_PV} is equal to the input energy to the converter P_{IN_con}.

Let us assume that *SPBC* is used to adjustment of input energy P_{IN_con} from one level to another.

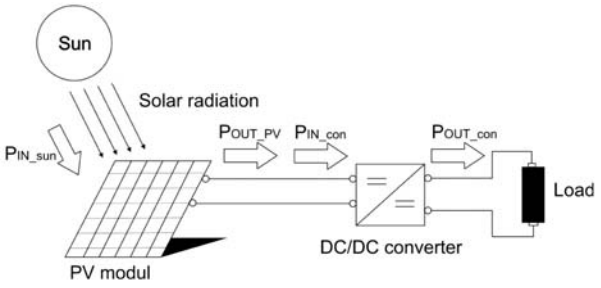

Fig. 1 Overview at efficiency of energy conversion

The function principle of conventional *SPBC* is well known. When the switch *S* is turned on the input energy starts to accumulate in form of magnetic field in the inductor *L*. This accumulated inductor energy with input energy (source energy) are delivered to the output *Z* after switch *S* is turned off. The average value of the output voltage $U_{Z(AV)}$ in continuous conduction mode (*CCM*) is:

* **Jan Perdulak[1], Dobroslav Kovac[1], Irena Kovacova[1], Matus Ocilka[1], Andrii Gladyr[2], Dmytro Mamchur[2], Iurii Zachepa[2], Tibor Vince[1], Jan Molnar[1]**
[1] Department of Theoretical Electrical Engineering and Electrical Measurement, Technical University of Kosice, Slovakia
[2] Department of Automatic Management and Electrical Drive, Kremenchuk Mykhailo Ostrohradskyi National University, Ukraine
E-mail: jan.perdulak@tuke.sk

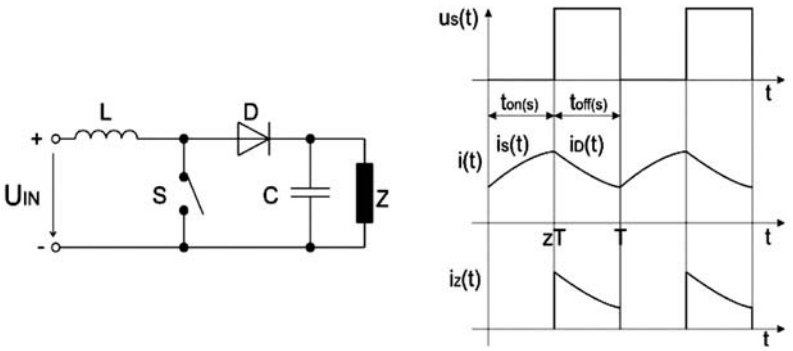

Fig. 2 Topology and theoretical waveforms of SPBC

$$U_{Z(AV)} = \frac{1}{1-z} U_{IN} \tag{1}$$

where duty cycle "z" is ratio between time when the switch S is turned on and the period T, $z = t_{on(s)}/T$. The theoretical waveforms and topology of conventional *SPBC* are shown in Fig. 2.

It can be seen that there exists a time interval within the period T when the energy delivered to the load Z is equal to zero. This is the main problem of conventional *SPBC* – effective utilization of input energy. We have to ensure that the input energy will be delivered to the load Z over the whole period T. We have to remove the time interval within the period T where the energy delivered to the load Z is zero. The another important fact is, that in case of unfavorable operating conditions of *PV* module, the *SPBC* is unable to obtain ist maximum power point (*MPP*)

It stands to reason that the efficiency of energy conversion is very low because we are unable to utilize the whole potential of input energy.

This is done by using the proposed *MPBC*, [3] and [4].

The three different efficiencies can be defined as:

The conversion efficiency of *PV* module η_{PV}:

$$\eta_{PV} = \frac{P_{OUT\_PV}}{P_{INsun}} \tag{2}$$

The converter efficiency η_{con}:

$$\eta_{con} = \frac{P_{OUTcon}}{P_{INcon}} \tag{3}$$

The efficiency of energy conversion η_E:

$$\eta_E = \frac{P_{OUTcon}}{P_{OUT\_PV(MPP)}} \tag{4}$$

where $P_{OUT\_PV(MPP)}$ is the instantaneous maximal output power of *PV* module for its certain operating conditions.

3. The proposed concept of MPBC

The proposed topology of *MPBC* is in Fig. 3a. The *MPBC* has, in comparison with the conventional *SPBC*, five more parallel legs with five inductors (L_2 – L_6), five rectifier diodes (D_2 – D_6) and five switches (S_2 – S_6).

This *MPBC* allows the effective utilization of energy delivered form the *PV* module. Appropriate control algorithm of switches allows converter to take the *PV* output energy by cooperation of all six parallel legs in every moment.

4. Principle of operation

The principle of operation of *SPBC* was mentioned above. This described process can be repeated six times because six parallel legs are presented in proposed *MPBC* which allows effective utilization of delivered energy from *PV* module.

The proposed *MPBC* has 6 operating cycles within each period. The corresponding operation waveforms are shown in Fig. 3b.

***Mode 1* (t_0 – t_1):** The switch S_1 (*leg A*) is turned on at the time t_0. The energy in form of magnetic field begins to accumulate in inductor L_1. The input current is closed in loop $+U_{IN} - L_1 - S_1 - -U_{IN}$. In this mode the switches S_5 (*leg E*) and S_6 (*leg F*) are in on-state. The input energy is delivered to the inductor L_5 and L_6 in particular legs, too. The switches S_2 and S_3 (leg C) are in off-state. The inductor energy W_{L2} and W_{L3} is delivered through diodes D_2 and D_3 to the load Z. The equivalent equations are:

The inductor voltages $u_{L1}(t)$, $u_{L5}(t)$ and $u_{L6}(t)$ are:

$$u_{L1}(t) = u_{L5}(t) = u_{L6}(t) = U_{IN} = L_{1(5,6)} \frac{di_{L1(5,6)}(t)}{dt} \tag{5}$$

The inductor voltage $u_{L2}(t)$, $u_{L3}(t)$ and $u_{L4}(t)$ are:

$$u_{L2}(t) = u_{L3}(t) = u_{L4}(t) = U_{IN} - U_{out} = \\ = L_{2(3,4)} \frac{di_{L2(3,4)}(t)}{dt} \tag{6}$$

The currents flow through inductors L_1, L_5, L_6 and switches S_1, S_5, S_6 are

$$i_{L1}(t) = i_{L5}(t) = i_{L6}(t) = i_{S1}(t) = i_{S5}(t) = \\ = i_{S6}(t) = \frac{1}{L_{1(5,6)}}\int_{t0}^{t1} u_{L1(5,6)}(t)dt + I_{L1(5,6)}(t_0) = \\ = \frac{U_{IN}}{L_{1(5,6)}}(t_1 - t_0) + I_{L1(5,6)}(t_0) \quad (7)$$

The currents flow through inductors L_2, L_3, L_4 and diodes D_2, D_3, D_4 are:

$$i_{L2}(t) = i_{L3}(t) = i_{L4}(t) = i_{D2}(t) = i_{D3}(t) = \\ = i_{D4}(t) = \frac{1}{L_{2(3,4)}}\int_{t0}^{t1} u_{L2(3,4)}(t)dt + I_{L2(3,4)}(t_0) = \\ = \frac{U_{IN} - U_{OUT}}{L_{2(3,4)}}(t_1 - t_0) + I_{L2(3,4)}(t_0) \quad (8)$$

The inductor current $i_{L1}(t)$ exponentially increases from the initial value I_{L1} to the maximum value I_{L1max} (reached at the time t_3) with time constant $\tau_1 = L_1/R$.

Mode 2* (t_1 - t_2)** and ***mode 3* (t_2 - t_3)** are the same as ***mode 1. Only other switches S_2 (*leg B*, *mode 2*) and S_3 (*leg C*, *mode 3*) are turned on, on-state S_1, S_6 (*leg A* and *leg F*, *mode 2*) and S_1, S_2 (*legs A* and *B*, *mode 3*) and off-state S_3, S_4 (*leg D* and *leg C*, *mode 2*) and S_4, S_5 (*legs D* and *E*, *mode 3*). The corresponding equations are the same. Only subscripts are changed.

***Mode 4* (t_3 - t_4):** The switch S_1 is turned off and S_4 is turned in the beginning of this mode at the time t_3. The inductor energy W_{L1} begins to deliver through diode D_1 to the load Z. The output current $i_Z(t)$ is enclosed in the loop L_1 - D_1 - Z - $-U_{IN}$ - $+U_{IN}$. The switches S_2 (leg B) and S_3 (leg C) are on-state and the input energy is delivered to the inductor L_2 and L_3. The switches S_5 (leg E) and S_6 (leg F) are in off-state. The inductor energy W_{L5} and W_{L6} is delivered through diodes D_5 and D_6 to the load Z. The equivalent equations are:

The inductor voltages $u_{L4}(t)$, $u_{L2}(t)$ and $u_{L3}(t)$ are

$$u_{L4}(t) = u_{L2}(t) = u_{L3}(t) = U_{IN} = L_{4(2,3)}\frac{di_{L4(2,3)}(t)}{dt} \quad (9)$$

The inductor voltages $u_{L1}(t)$, $u_{L5}(t)$ and $u_{L6}(t)$ are

$$u_{L1}(t) = u_{L5}(t) = u_{L6}(t) = U_{IN} - U_{out} = \\ = L_{1(5,6)}\frac{di_{L1(5,6)}(t)}{dt} \quad (10)$$

The currents flow through inductors L_4, L_2, L_3 and switches S_4, S_2, S_3 are

$$i_{L4}(t) = i_{L2}(t) = i_{L3}(t) = i_{S4}(t) = i_{S2}(t) = \\ = i_{S3}(t) = \frac{1}{L_{4(2,3)}}\int_{t3}^{t4} u_{L4(2,3)}(t)dt + I_{L4(2,3)}(t_0) = \\ = \frac{U_{IN}}{L_{4(2,3)}}(t_3 - t_4) + I_{L4(2,3)}(t_3) \quad (11)$$

The currents flow through inductors L1, L5, L6 and couple of diodes D1, D5, D6 are

$$i_{L1}(t) = i_{L5}(t) = i_{L6}(t) = i_{D1}(t) = i_{D5}(t) = \\ = i_{D6}(t) = \frac{1}{L_{1(5,6)}}\int_{t3}^{t4} u_{L1(5,6)}(t)dt + I_{L1(5,6)}(t_3) = \\ = \frac{U_{IN} - U_{OUT}}{L_{1(5,6)}}(t_4 - t_3) + I_{L1(5,6)}(t_3) \quad (12)$$

The inductor current $i_{L4}(t)$ exponentially increases with time constant $\tau_4 = L_4/R$.

Mode 5* (t_4 - t_5)** and ***mode 6* (t_5 - t_6)** are the same as ***mode 4. Only other switches S_5 (*leg E, mode 5*) and S_6 (*leg F, mode 6*) are turned on, on-state S_3, S_4 (*leg C* and *leg D, mode 5*) and S_4, S_5 (*legs D* and *E*, *mode 6*) and off-state S_1, S_2 (*legs A* and *B*, *mode 6*) and S_1, S_6 (*leg A* and *leg F, mode 5*). The corresponding equations are the same. Only subscripts are changed.

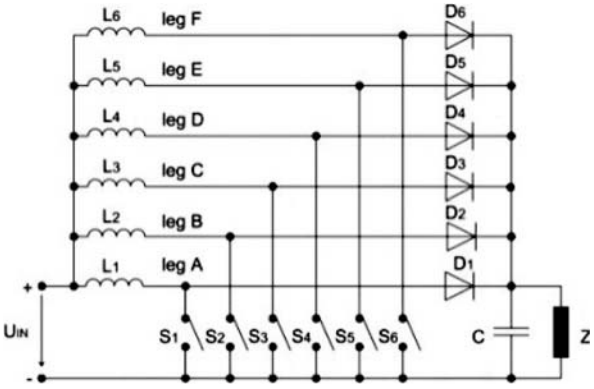

a)

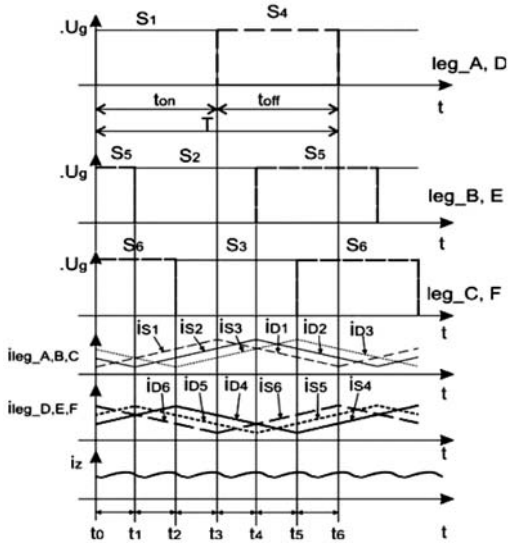

b)

Fig. 3 The proposed topology and theoretical waveforms of MPBC

5. Simulation Results

The simulation models of *MPBC* and *SPBC* shown in Fig. 4 were created in simulation environment OrCAD Capture CSI to verify its theoretical properties. The power MOSFET transistors were used as switches. The two *DC* voltage sources were used to simulate output photovoltaic voltage *UPV* and battery voltage U_{bat}. Parameters:

switching frequency $f_S = 50$ kHz,
output voltage $U_{bat} = 14$ V,
inductance $L = L_1 = L_2 = L_3 = L_4 = L_5 = L_6 = 100$uH

Three different levels of input voltage U_{PV} were set to compare the properties of simulation models of *MPBC* and *SPBC*. The tested values of input voltage were $U_{PV} = \{2\text{ V}, 6\text{ V}, 12\text{ V}\}$.

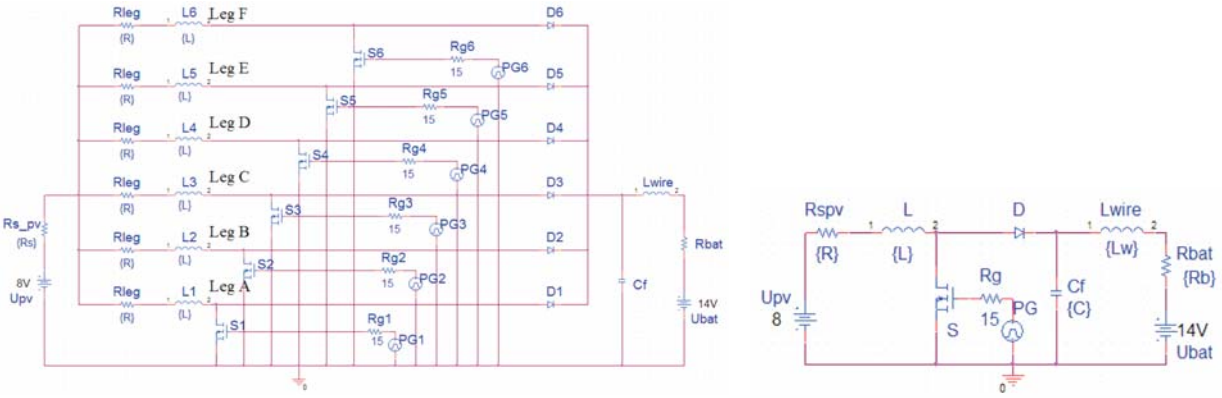

Fig. 4 Simulation models of proposed MPBC a) and conventional SPBC b)

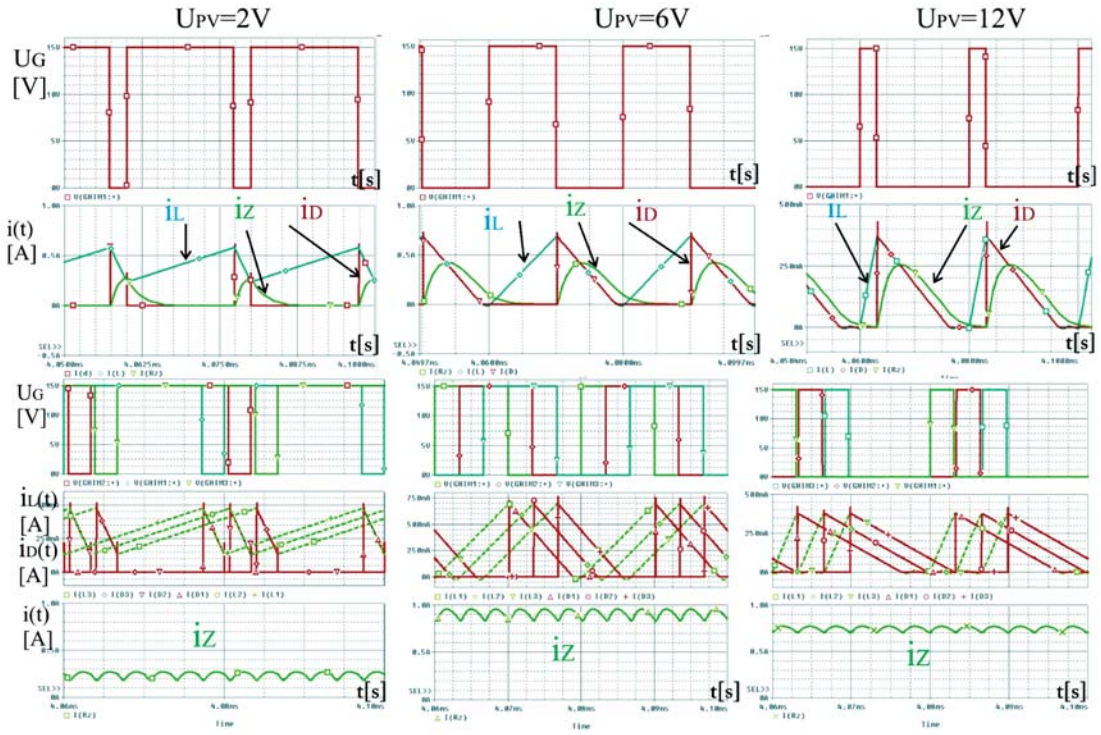

Fig. 5 Simulation comparison of basic properties of SPBC (upper part) and MPBC (lower part)

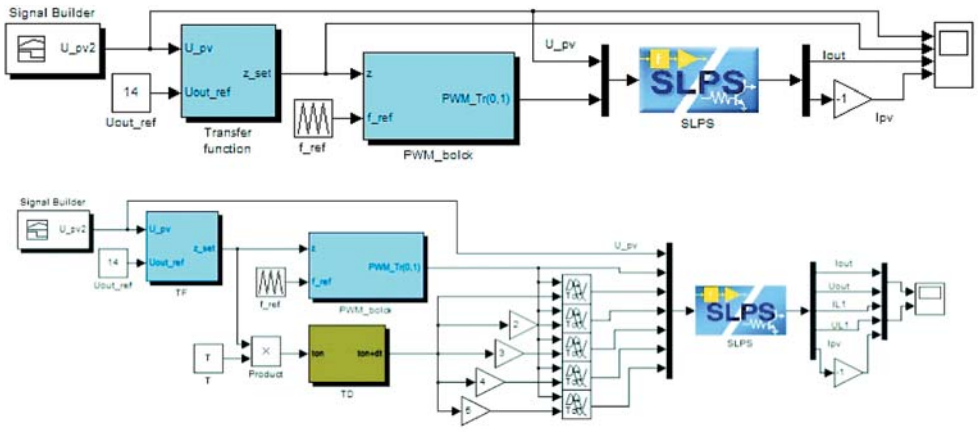

Fig. 6 Simulink models of control structure of SPBC (upper part) and conventional MPBC (lower part)

Figure 5 shows gate voltage U_G, inductor current $i_L(t)$, diode current $i_D(t)$, and load current $i_Z(t)$ at the different value of input voltage U_{PV}. In can be seen that the *MPBC* works in comparison with *SPBC* in *CCM* for whole range of input voltage U_{PV} except the minimum value $U_{PVmin} = 2$ V. The load current $i_Z(t)$ is sum of currents in particular legs which delivers its energy to the load *Z*. The waveforms of three legs of *MPBC* are displayed for lucidity.

Control structures created in Simulink environment are shown in Fig. 6, [5]–[7]. For this purpose the *PSpice SLPS* (SimuLink PSpice) simulation environment was used. This environment supports the substitution of an actual Simulink block with an equivalent analog PSpice electrical circuit. The simulation models of *SPBC* and *MPBC* are completely included to the simulink model control design by means of *SLPS* block.

Figures 7a and 8a show overall view of load current $i_Z(t)$, inductor current $i_L(t)$, input voltage U_{PV} and duty cycle z of *SPBC* and *MPBC*. From the detailed analysis (Figs. 7b, 7c and 8b) it is clear that the *MPBC* works in comparison with SPBC in *CCM* for the whole range of input voltages U_{PV} except the minimum value $U_{PVmin} = 2$ V.

6. Experimental results

The laboratory models of *SPBC* and proposed *MPBC* were built and tested to verify the theoretical assumptions and simulation results. The laboratory model of control structure of *MPBC* was built and connected to the converter to generate corresponding gate signals for transistors in particular legs. Figure 9 shows the overall view connection of converter with designed control.

The *DC* regulated voltage source was used to simulate different operating conditions and thus different levels of output *PV* voltage U_{PV}. The battery was used as a load *Z*.

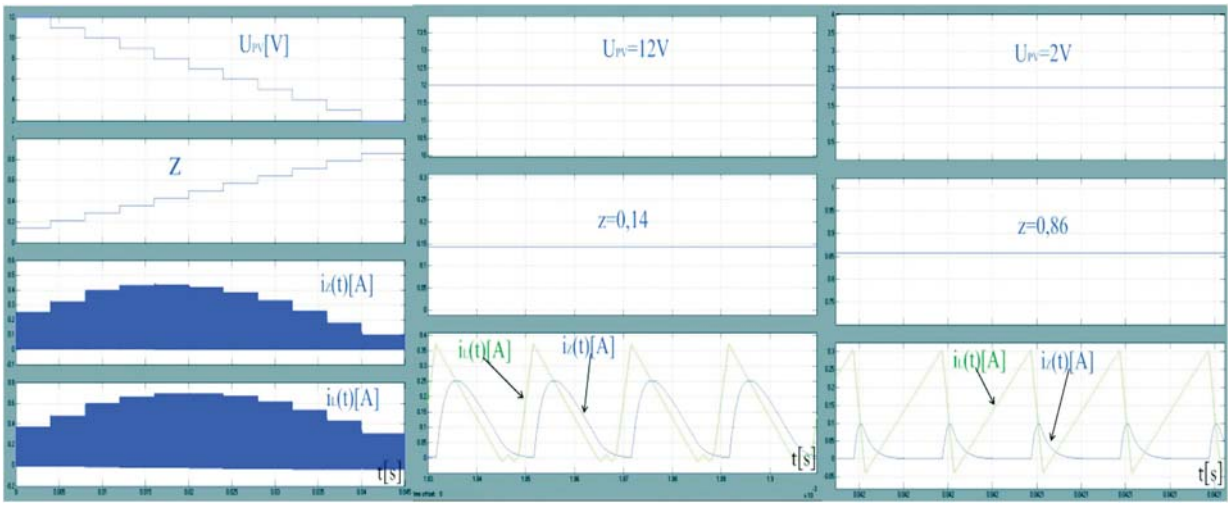

a) *b)* *c)*

Fig. 7 Waveforms of photovoltaic voltage UPV, duty cycle z, inductor current iL(t) and load current iZ(t) of SPBC

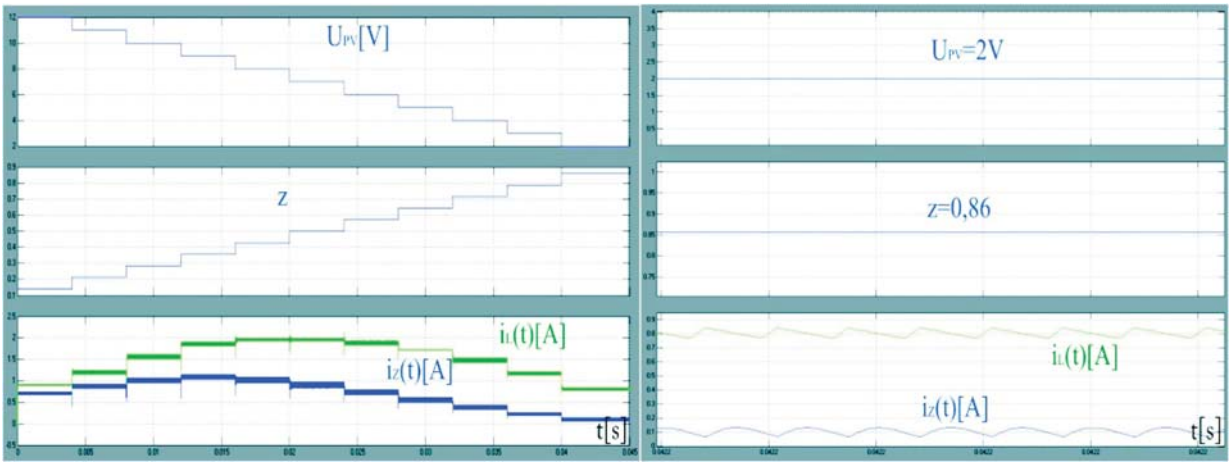

a) *b)*

Fig. 8 Waveforms of photovoltaic voltage U_{PV}, duty cycle z, inductor current $i_L(t)$ (leg A) and load current $i_Z(t)$ of MPBC

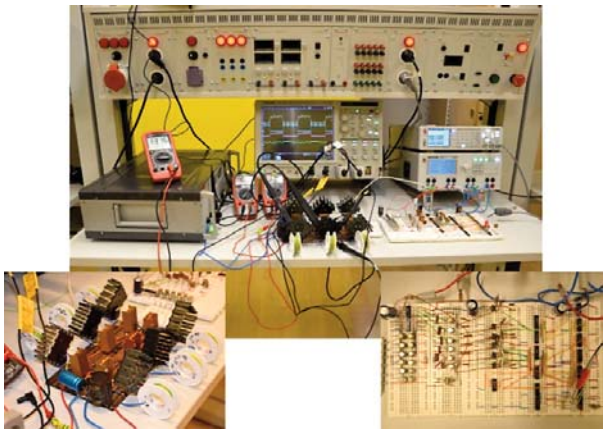

Fig. 9 Laboratory model of MPBC with control

Figures 10 and 11 show input voltage U_{PV}, gate voltage U_G, input current I_{PV} and load current $i_Z(t)$, of *SPBC* and *MPBC*. It is clear that the load current $i_Z(t)$ is continually delivered to the load *Z*. Even if input voltage U_{PV} is set to the minimum value 4 V the maximum input current I_{PV_max} is taken from the input voltage source. This is another important fact in comparison with *SPBC*. The laboratory model of proposed *MPBC* works in discontinuous conduction mode at the U_{PV} = 4V in comparison with simulation model. This is because the real components were used in comparison with the simulation model where many of parasitic and physical properties cannot be taken into account.

7. Comparison of efficiency of energy conversion

Efficiency of energy conversion η_E can be defined as a ratio of output converter energy P_{OUTcon} to the maximum output energy $P_{OUT\_PV(MPP)}$, of *PV* module which it is able to deliver under the given operating conditions. It is evident, that the efficiency of energy conversion η_E of *MPBC* is several times higher in comparison with *SPBC*, Fig. 12, for the whole range of operating conditions. The low efficiency of energy conversion η_E of *SPBC* results from its principle of operation. The *SPBC* operates in pulse mode so only a portion of its input energy is delivered to output. The *PV* module operates

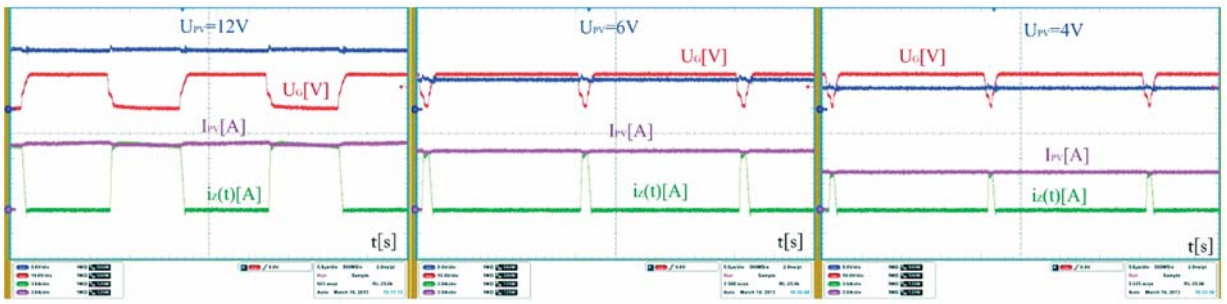

Fig. 10 Waveforms of photovoltaic voltage U_{PV}, duty cycle z, photovoltaic current $i_Z(t)$ and load current $i_Z(t)$ of SPBC

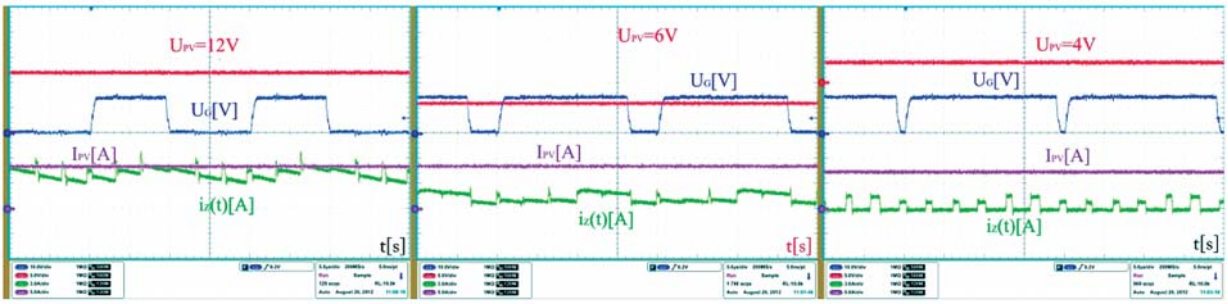

Fig. 11 Waveforms of photovoltaic voltage U_{PV}, duty cycle z, photovoltaic current $i_Z(t)$ and load current $i_Z(t)$ of MPBC

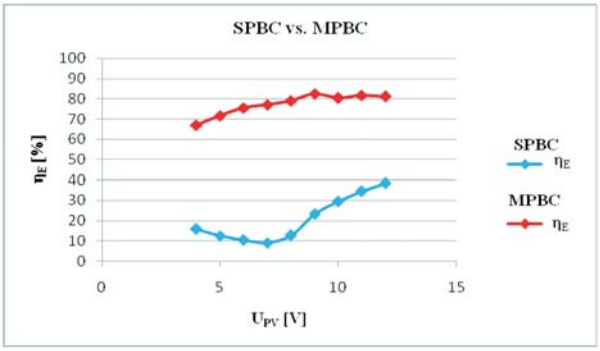

Fig. 12 Comparison of efficiency of energy conversion

in *MPP* point for whole range of operating conditions, or more precisely, for the whole range of input photovoltaic voltage U_{PV} when the *MPBC* is used.

8. Conclusion

The most popular material used to make the solar cell is silicium (*Si*). The *Si* is also one of major factors in long-term energy recovery and high cost of *PV* modules. One way to reduce the long –term energy and financial recovery is to use the proposed *MPBC*. The *MPBC* works with high efficiency of energy conversion in comparison with *SPBC*. The *MPBC* continually delivers the input source energy to the load Z using six parallel phases. In this case, the time interval when the output energy is equal to zero is removed. The *MPBC* ensures that the PV module is operating in the maximum power point for whole range of its operating conditions, so we can effectively utilize the output *PV* energy.

Acknowledgement

The paper has been prepared under the support of the Slovak grant project KEGA No. 005TUKE-4/2012.

References

[1] MAH, O.: *Fundamentals of Photovoltaic Materials.* National Solar Power Research Institute, Inc., 1998, pp.10.
[2] TURCEK, J., HRASKO, M., ALTUS, J.: Photovoltaics in Present Days and their Coexistence with Power System. *Communications - Scientific Letters of the University of Zilina*, No. 2A, pp.109–113, 2011.
[3] KOVAC, D., KOVACOVA, I.: Patent application No. 00150-2010.
[4] KOVAC, D., KOVACOVA, I.: Patent application No. 00001-2011.
[5] DOBRUCKY B., BENOVA, M., FRIVALDSKY, M., PRAZENICA, M.: Choosing Modulation Strategies for 2-Stage Combine LLC - and Direct Converter - Modelling, Simulation, Application. *Communications - Scientific Letters of the University of Zilina,* No. 2A, pp. 25–31, 2011.
[6] KOVAC, D., KOVACOVA, I., PERDULAK, J., VINCE, T., MOLNAR, J.: Patent app. No. 00097-2011.
[7] KOVAC, D., KOVACOVA, I., PERDULAK, J., VINCE, T., MOLNAR, J.: Patent app. No. 00008-2012.

Stepan Janous – Jozef Sedlak – Michal Prazenica – Jozef Kuchta *

IMPLEMENTATION OF THREE PHASE-DISCONTINUOUS SPACE VECTOR MODULATION USING SINGLE DSC-PWM MODULE

The paper presents an implementation of a discontinuous space vector modulation of three phase inverter. The modulation is implemented in a DSC (Digital Signal Controller) using only one PWM module. Phases of the inverter work in a complementary mode. This implementation gives an assumption to use one DSC for simultaneous controlling of several three phase inverters. Furthermore, a simulation comparison of discontinuous and continuous space vector modulation is made.

Keywords: *Three-phase inverter, space vector modulation, discontinuous space vector modulation, pulse width modulation.*

1. Introduction

Thanks to its simplicity and ability to supply three phase load by a voltage with variable frequency and magnitude, three phase voltage inverters have a wide use. Control of these inverters plays a big role. The simplest and the most widely used control method is the carrier-based sine-triangle PWM. Its drawback is low use of DC-bus voltage. Next method with very good preferences is a Space Vector Modulation (SVM). It has also a lot of variants and improvements. Discontinuous Space Vector Modulation (marked as DPWM) is one of them. It suffers from worst properties of voltage and current waveforms, but also it allows the control to be simpler and also leads to less switching losses.

2. Space Vector Modulation

We can look at the Three-phase voltage, created by inverter like at a single voltage vector in a vector space. It is rotating by an angular speed of electric field and is stated by its amplitude. The idea of SVM is to create this vector using switching elements of the inverter. The inverter can create six voltage vectors (U_0, U_{60}, U_{120}, U_{180}, U_{240}, U_{300}) and two zero vectors (0000, 0111), which set in by switching on all of the top or bottom transistors.

It is obvious from Fig. 1 that voltage vectors divide a space into six sectors. Approximation of a desired voltage vector is done by creating two vectors that border actual sector within every PWM period. According to desired magnitude of the voltage vector, both zero vectors are applied as well. Mathematical consideration is shown bellow.

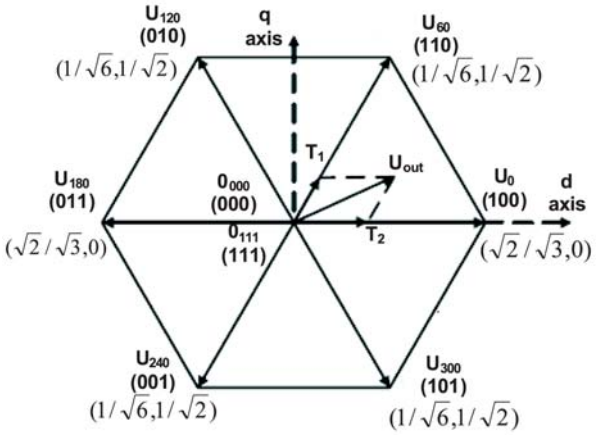

Fig. 1 Voltage vectors of the inverter [1]

$$\frac{1}{T}\int_{nT}^{(n+1)T} U_{out}\,dt = \frac{1}{T}\left(T_1 U_x + T_2 U_{x\pm 60}\right) \qquad (1)$$

Where:
T [s] is the period of PWM signal,
U_{out} [V] is the magnitude of the reference voltage vector
U_x [V] and $U_{x\pm 60}$ [V] are the magnitudes of the inverter voltage vectors
T_1 [s] and T_2 [s] are the durations of the respective voltage vectors

* **Stepan Janous[1], Jozef Sedlak[2], Michal Prazenica[3], Jozef Kuchta[4]**
[1] Department of Electromechanics and Power Electronics, Faculty of Electrical Engineering, University of West Bohemia, Czech Republic
[2] Department of Mechatronics and Electronics, Faculty of Electrotechnical Engineering, University of Zilina, Slovakia,
E-mail: jozef.sedlak@fel.uniza.sk
[3] Department of Mechatronics and Electronics, Faculty of Electrotechnical Engineering, University of Zilina, Slovakia
[4] EVPU, a.s. Nova Dubnica, Slovakia

Equation 1 doesn't deal with zero vectors. Therefore, it is valid only if sum of U_x and $U_{x\pm60}$ gives a vector with the same amplitude as vector Uout has. If we assume that the change of Uout within one period is small, we can rewrite Eq. 1 as:

$$U_{out}(nT) = \frac{1}{T}(T_1 U_x + T_1 U_{x\pm60}) \tag{2}$$

And if we take zero vectors into account, we get:

$$T_{pwm} U_{out} = T_1 U_x + T_2 U_{x\pm60} + \frac{T_0}{2}(0_{000}) + \frac{T_2}{2}(0_{111}) \tag{3}$$

, where
0_{000} [V] and 0_{111} [V] are the zero vectors of the inverter.

These zero vectors have a strong influence on a shape of inverter voltage. If we know a magnitude of desired voltage vector and an angle between this vector and the closest inverter voltage vector, we can calculate times T_1, T_2 and T_0 as follows:

$$T_2 = \frac{2 \cdot U_{out} T_{pwm} \cdot \sin\alpha}{U_{vect} \cdot \sqrt{3}} \tag{4}$$

$$T_1 = \frac{\cos\alpha U_{out} T_{pwm} - 0.5 U_{vect} T_2}{U_{vect}} \tag{5}$$

$$T_0 = T_{pwm} - (T_1 + T_2) \tag{6}$$

α is the angle between the respective inverter vector and the reference voltage vector,
T_0 [s] is the duration of both zero vectors
U_{vect} [V] is a magnitude of inverter voltage vectors, and U_{dc} [V] is an inverter supply voltage.

$$U_{vect} = \frac{2}{3} U_{dc} \tag{7}$$

In Fig. 1, the combination of upper transistors in a conducting state is listed next to every inverter-voltage vector. As an example for vector U_{60}, (110) means that upper transistors in first and second branch are in the conducting state. Transistors are switched complementary in every branch. Based on knowledge of creating respective vectors it is easy to define the switching times of upper transistors in terms of every PWM period. Composition of the switching states is different for every sector. In Fig. 2 we have an example for 1st sector. a, b and c are the respective branches.

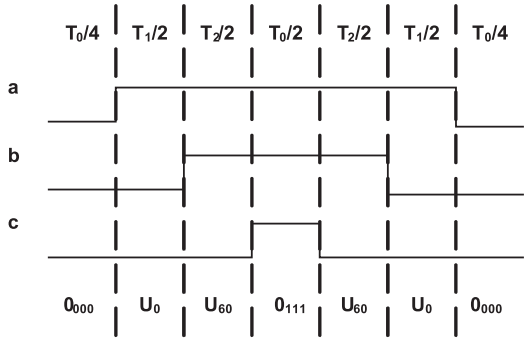

Fig. 2 Switching times assignment of the upper transistors in first sector during PWM period [1]

Thanks to appropriate arrangement of the voltage vectors it is achieved that every transistor is once switched on and once switched off in every PWM period. It is obvious from Fig. 2 that a switchover in c branch is made only because of change from one zero vector to another zero vector. It leads us to one possible simplification of the switching scheme. This is in literature called Discontinuous Space Vector Modulation. Its switching scheme is in Fig. 3 [2], [3], [1].

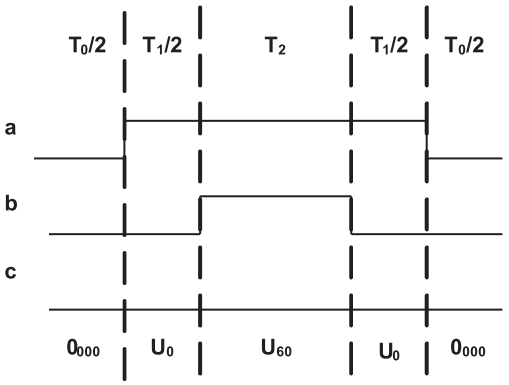

Fig. 3 Switching times assignment of the upper transistors in first sector during PWM period for Discontinuous Space Vector Modulation [1]

3. Implementation of Discontinuous Space Vector Modulation in a Digital Signal Processor

Exactly, the fact that in the terms of every PWM period transistors in one branch don't change their state gives an assumption to drive the whole three-phase inverter with only one PWM module. Digital Signal Controller by Texas Instruments TMS320F28335 has six PWM modules. Every module has its own register to set up a PWM period and also has two compare registers, as we can see in Fig.4. If we are going to use a DPWM, we can use these two registers for controlling two branches.

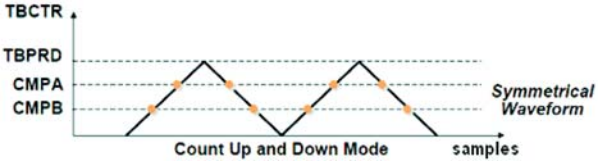

Fig. 4 Principle of the PWM module function [4]

In Fig. 5 we have a reference waveform for one branch of the inverter calculated by an algorithm of DPWM in Code Composer Studio v4. TBPRD is a register that defines the length of the PWM

period. TBCTR is a counter that is incrementing until it reach the TBPRD value and then starts to decrement until zero. We can set up some events during PWM period with CMPA and CMPB registers. Mainly switching of a PWM output.

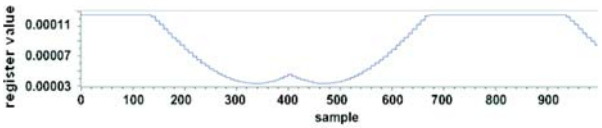

Fig. 5 Reference for one branch of the inverter

It is necessary to switchover a dispatching of the compare registers to the inverter branches due to an actual sector of the reference vector [4].

4. Simulation comparison of continuous and discontinuous SVM

We used MatLab-Simulink software in order to compare these two types of control with regard to quality of output parameters. The proposed simulated layout is in Fig. 6. In Fig. 7 reference waveforms for continuous SVM and in Fig. 8 for DPWM are shown.

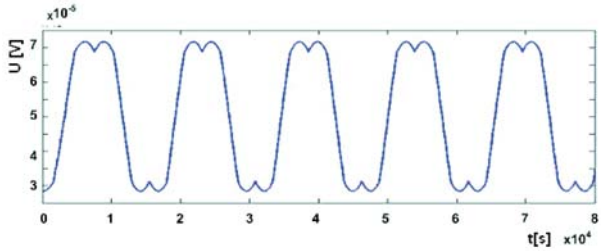

Fig. 7 Reference waveform for single phase in a case of continuous SVM

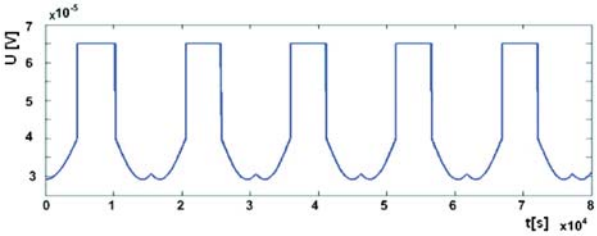

Fig. 8 Reference waveform for single phase in a case of DPWM

Currents were simulated with the use of mathematical model of an ideal three-phase inverter, which supplied RL load. Waveforms of currents were shown in Figs. 9 and 10 respectively.

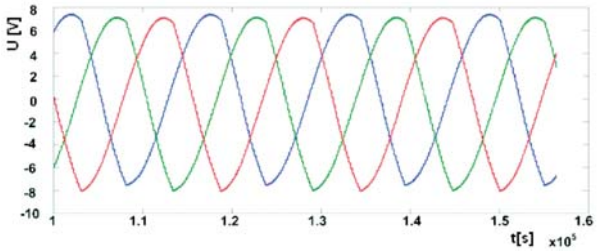

Fig. 9 Currents in a case of DPWM

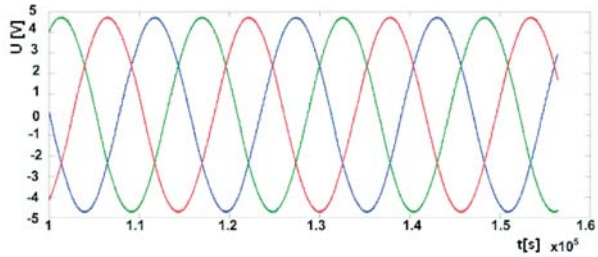

Fig. 10 Currents in a case of continuous SVM

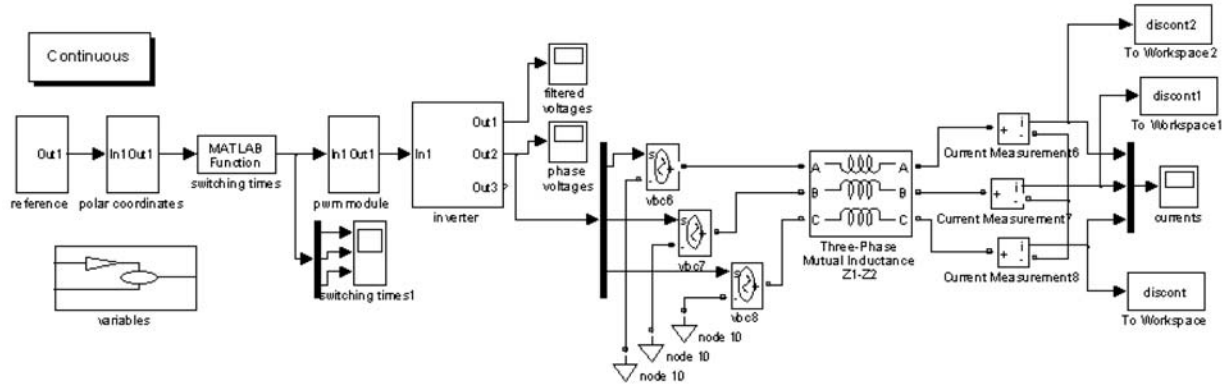

Fig. 6 Simulating scheme

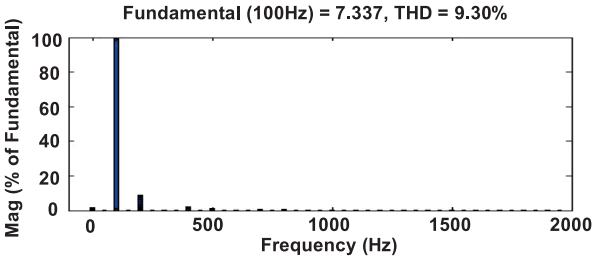

Fig. 11 Amplitude spectrum of harmonic components (DPWM)

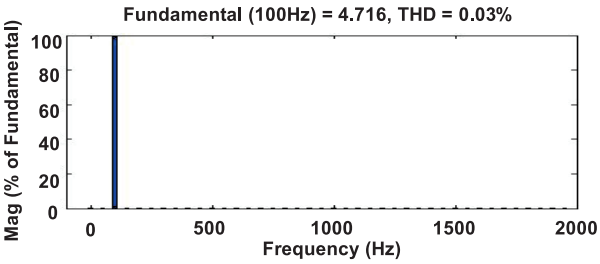

Fig. 12 Amplitude spectrum of harmonic components (continuous SVM)

Finally, a comparison of FFT analysis and currents THD is made [5, 6, 7, 8]. Amplitude spectrums of harmonic components for respective PWM methods are shown in Figs. 11 and 12.

5. Conclusion

The principle of space vector modulation was introduced in this paper. Then we dealt with discontinuous space vector modulation. We showed that DPWM can be implemented in DSP using only one PWM module. It means a great opportunity to save control accessories in some three-phase power systems, such as motor drives. However, a quality of current waveforms is worst in case of DPWM.

Acknowledgement

This paper was created thanks to the project ITMS 26220220078.

References

[1] Space-Vector PWM With TMS320C24x/F24x Using Hardware and Software Determined Switching Patterns, [27.03.2013], available on website: http://www.ti.com/lit/an/spra524/spra524.pdf

[2] DORIN O. NEACSU: *Space Vector Modulation – An Introduction,* ICEON'01

[3] IQBAL, A., AHMED, M., KHAN M.: Abu-Rub H.: Generalised Simulation and Experimental Implementation of Space Vector PWM Technique of a Three-phase Voltage Source Inverter, *Intern. J. of Engineering, Science and Technology,* vol. 2, No. 1, pp. 1 12, 2010.

[4] TMS320x280x, 2801x, 2804x Enhanced Pulse Width Modulator (ePWM) Module [27.03.2013], available on website: http://www.ti.com/lit/ug/spru791f/spru791f.pdf

[5] DRGONA, P., PRIKOPOVA, A., FRIVALDSKY, M., PRIECINSKY, M.: Simulation Based Method for Design and Application of Digital Control System, *Communications - Scientific Letters of the University of Zilina,* No. 2a, 2011, ISSN 1335-4205.

[6] BRANDT, M., RAFAJDUS, P., PENIAK, A., MICHALIK, J.: *Diagnostics System of Power Transformers Supported by Finite Element Analysis,* SPEEDAM 2012, ISBN 978-1-4673-1300-1.

[7] ZASKALICKA, M., ZASKALICKY, P., BENOVA, M., ABDALMULA, M. A. R., DOBRUCKY, B.: Analysis of Complex Time Function of Converter Output Quantities Using Complex Fourier Transform/Series. *Communications - Scientific Letters of the University of Zilina,* No. 1(12), pp. 23–30, 2010.

[8] ZASKALICKY, P., DOBRUCKY, B.: Complex Fourier–series Mathematical Model of a Three-Phase Inverter with Improved PWM Output Voltage Control; *Elektronika ir Elektrotechnika,* Kaunas, No. 7 (123), pp. 65–68, 2012.

Branislav Dobrucky – Michal Pokorny – Mariana Benova – Mahmud Ali Rzig Abdalmula *

MODELLING OF POWER CONVERTERS USING Z-TRANSFORM

The paper introduces a novel method of analysis and modelling of power electronic converters. Z-transform, numerical series (sequences) are used for both steady and transient states investigation of converters. The new impulse switching functions are created which are used as exciting functions of one- and multidimensional state-space models. Theoretical waveforms are compared with simulation results.

Keywords: *Power converter, impulse switching function, Z-transform, inverse Z-transform, modelling and simulation, steady state operation.*

1. Introduction – Impulse switching functions

There are many methods of analyses of power converters. Classical analytic methods, Laplace transform or/and Fourier analysis are suitable mainly for steady state operation [1], [2]. Transient analysis uses dynamic state-space modeling and/or Z-transform method. One of the fastest methods is that, which uses impulse switching functions (ISF). This method is used in signal theory, lesser in electrical engineering. Obviously, caused by power converters nature, those ISFs are strongly non-harmonic; sometime piece wise constant with zero spaces between pulses [3]. Then, it deals with power series of time pulses. From those series the impulse switching functions can be derived which are again orthogonal ones. Derived relations for voltages sequences can be used for current sequences calculations in electrical engineering system using impulse transfer function of the used plant and its time discretization. Similarly, one can derive relation for continuous time functions of voltages and currents. They are often grouped in two orthogonal α and β axes [4], [5].

Examples of impulse switching functions belonging to output voltage of single- and three-phase inverters are shown in Fig. 1a and 1b, respectively.

2. Mathematical description of ISFs using Z-transform

Converter output phase voltages in Z-domain

Using basic definition of Z-transform (linearity-, shift right, index exchanging theorems) – and taking into account Z-images of constant- and alternating series [6] we can write

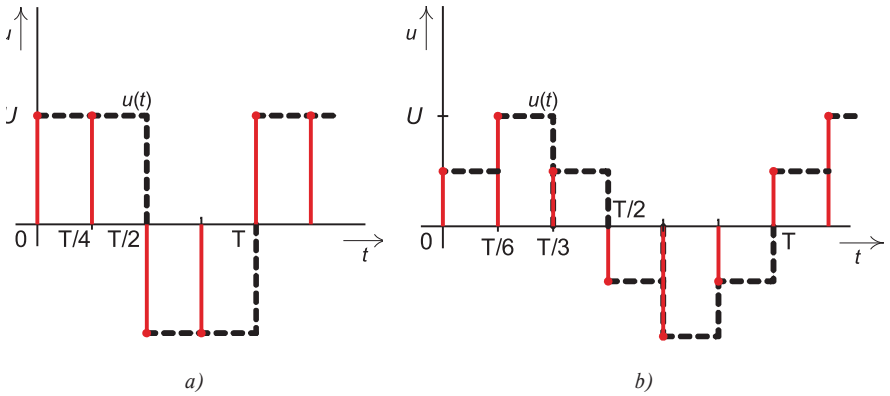

Fig. 1 Impulse switching functions of single a)- and three phase b) voltage source inverters (VSI)

* **Branislav Dobrucky[1], Michal Pokorny[1], Mariana Benova[1], Mahmud Ali Rzig Abdalmula[2]**
[1] Faculty of Electrical Engineering, University of Zilina, Slovakia, E-mail: branislav.dobrucky@fel.uniza.sk
[2] University of Zawia, Libya

– for single/two-phase α, β-system

$$U_\alpha(z) = U\frac{z^2+z}{z^2+1} \text{ and} \tag{1a}$$

$$U_\beta(z) = -U\frac{z^2+z}{z^2+1}, \tag{1b}$$

where $U_\alpha(z)$, $U_\beta(z)$ are voltages in orthogonal axes and roots of polynomial of denominator are

$$z_{1,2} = \pm j = \pm(-1)^{\frac{1}{2}} = e^{\pm j\frac{\pi}{2}},$$

placed on boundary of stability in unit circle [6], [7] see Fig. 2,

– for three-phase α,β-system (i.e. transformed, orthogonal system)

$$U_\alpha(z) = \frac{z^3+2z^2+z}{z^3+1} \text{ and} \tag{2a}$$

$$U_\beta(z) = -U\frac{z^3+z^2}{z^3+1} \tag{2b}$$

where roots of polynomial of denominator are

$$z_{1,2} = \frac{1}{2} \pm j\frac{\sqrt{3}}{2} = e^{\pm j\frac{\pi}{3}}; z_3 = -1;$$

placed again on boundary of stability in unit circle [6], [7], Fig. 2.

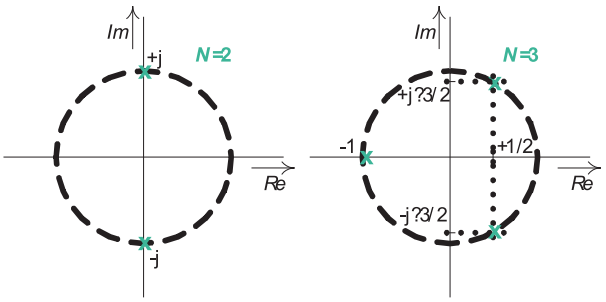

Fig. 2 Denominator poles placement of single a) – and three-phase z-form voltages in unit circle

Applying inverse Z-transform for converter output phase voltages in Z-domain we can create orthogonal impulse switching functions.

For inverse Z-transform $U_{(\alpha,\beta)}(z) \leftrightarrow [u_n]$ one can use the residua theorem [7], [8]

$$\sum_{i=1}^{N} res_{z=z_i} U(z)z^{n-1} = \sum_{i=1}^{N} \lim_{z\to z_i}(z-z_i)U(z)z^{n-1} \tag{3a}$$

where $n = 0, 1, 2, ...$; N is number of poles.

or, if $U(z)$ can be expressed as ratio of polynomials of z-variable

$$\sum_{i=1}^{N} res_{z=z_i} U(z)z^{n-1} = \sum_{i=1}^{N} \frac{A(z_i)}{B'(z_i)} z_i^{n-1}, \tag{3b}$$

where $B'(z)$ is the derivative of $B(z)$

$$\frac{dB(z)}{dz}(at\ z = z_i).$$

Applying inverse Z-transform for single/two-phase α,β-system

$$U_\alpha(z) = U\frac{z^2+z}{z^2+1} \leftrightarrow \{u_n\} = \left\{u_\alpha\left(n\frac{T}{4}\right)\right\} = \\ = \sum_{i=1}^{N} \lim_{z\to z_i}(z-z_i)U\frac{z+1}{z^2+1}z^n \tag{4}$$

after adapting

$$u_\alpha\left(n\frac{T}{4}\right) = U\frac{1}{2}(-1)^{\frac{n}{2}}\left\{1+(-1)^n - \right. \\ \left. -(-1)^{\frac{1}{2}}\left[1-(-1)^n\right]\right\}, \tag{5}$$

or

$$u_\alpha\left(n\frac{T}{4}\right) = U\sqrt{2}\sin\left(n\frac{\pi}{2}+\frac{\pi}{4}\right). \tag{5a}$$

By similar way for β-axis

$$u_\beta\left(n\frac{T}{4}\right) = -U\frac{1}{2}(-1)^{\frac{n}{2}}\left\{1+(-1)^n - \right. \\ \left. -(-1)^{\frac{1}{2}}\left[1-(-1)^n\right]\right\} = -U\sqrt{2}\cos\left(n\frac{\pi}{2}+\frac{\pi}{4}\right). \tag{6}$$

Applying inverse Z-transform for three-phase α,β-system

$$U_\alpha(z) = U\frac{z^3+2z^2+z}{z^3+1} \leftrightarrow \{u_n\} = \left\{u_\alpha\left(n\frac{T}{6}\right)\right\} = \\ = \sum_{i=1}^{N} \lim_{z\to z_i}(z-z_i)U\frac{z^2+2z+z}{z^3+1}z^n \tag{7}$$

after adapting

$$u_\alpha\left(n\frac{T}{6}\right) = U\frac{1}{2}\left[\left(1-j\sqrt{3}\right)\left(1+j\sqrt{3}\right)^n + \right. \\ \left. +\left(1+j\sqrt{3}\right)\left(1-j\sqrt{3}\right)^n\right] \tag{7a}$$

or

$$u_\alpha\left(n\frac{T}{6}\right) = U_{DC}\frac{2}{3}\sin\left(n\frac{T}{3}+\frac{T}{6}\right). \tag{7b}$$

By similar way for β-axis of three-phase converter

$$u_\beta\left(n\frac{T}{6}\right) = -U_{DC}\frac{2}{3}\cos\left(n\frac{T}{3}+\frac{T}{6}\right). \tag{8}$$

Taking discrete state-space model for three-phase converter output current as state-variable considering the 1st order load (resistive-inductive or resistive-capacitive)

$$x_{n+1} = \boldsymbol{F}_{T/6}x_n + \boldsymbol{G}_{T/6}\left\{u\left(n\frac{T}{6}\right)\right\} \tag{9}$$

where $\boldsymbol{F}_{T/6}$, $\boldsymbol{G}_{T/6}$ are fundamental and transition matrices (in general) of system parameters.

Applying Z-transform and considering the 1st order load

$$zX(z) = F_{T/6}X(z) + G_{T/6}Y_\infty(z) \rightarrow X(z) = X_\infty G_{T/6}\frac{z^3 + 2z^2 + z}{(z - F_{T/6})(z^3 + 1)}, \quad (10)$$

where $X(z)$ is image of founded state-variable (inductor current or capacitor voltage), and $Y_\infty(z)$ is maximum of steady state value (U/R or U, respectively).

And after adaption and simplification

$$X(z) = X_\infty G_{T/6}\frac{z(z+1)}{(z - F_{T/6})(z^2 - z + 1)} = X_\infty G_{T/6}\frac{z(z+1)}{(z - z_0)(z - z_1)(z - z_2)}, \quad (11)$$

where

$$z_0 = F_{T/6},\ z_{1,2} = \frac{1}{2} \pm j\frac{\sqrt{3}}{2} = e^{\pm j\frac{\pi}{3}}$$

Applying inverse Z-transform

$$x\left(n\frac{T}{6}\right) \equiv \{x_n\} = X_\infty G_{T/6} \cdot \lim_{z \to z_i} \cdot \left\{\sum_{i=0}^{2}(z - z_i)\frac{z_i(z_i+1)}{(z_i - z_0)(z_i - z_1)(z_i - z_2)}z_i^n\right\} \quad (12)$$

Finally we get discrete form of state variable (converter output state variable – inductor currents or capacitor voltages)

$$x\left(n\frac{T}{6}\right) \equiv \{x_n\} = X_\infty \frac{G_{T/6}(1 + F_{T/6})}{F_{T/6}^2 - F_{T/6} + 1} \cdot \left[F_{T/6}^n + \sqrt{3}\frac{1 - F_{T/6}}{1 + F_{T/6}}\sin\left(n\frac{T}{3}\right) - \cos\left(n\frac{T}{3}\right)\right], \quad (13)$$

where $n = 0, 1, 2, \ldots$

3. Calculation of ISF function values using series and sequences

The ISF functions presented above are numerical series (sequences) or trigonometric ones, respectively.

At first it is necessary to determine the $\boldsymbol{F}_{T/6}$, $\boldsymbol{G}_{T/6}$ functions values which are the state-variable values in 1/6-instant of time period (i.e. they are state- and transition responses). These can be obtained e.g. by using recursive relation for one-pulse solution:

$$\frac{dx(t)}{dt} = A \cdot x(t) + BY_\infty(t) \quad (14)$$

thus recursive relation

$$x(k+1) = \mathrm{F}_\Delta x_k + G_\Delta X_\infty, (t) \quad (15)$$

where $i_{k=0} = I_0 = 0$. Solution in z-domain yields

$$X(z) = X_\infty \frac{G_\Delta}{(z - F_\Delta)}\frac{1 - (rz^{-1})^{60}}{(1 - rz^{-1})}, \quad (16)$$

where F_Δ a G_Δ are discrete impulse responses of state-variables gained by some of identification methods. The second fraction term is z-image of the partial sum of voltage impulses (1 ÷ 60) [6], since $r^{an} \cdot z^{-n}$; $a < 0$ is geometrical series, see Fig. 3.

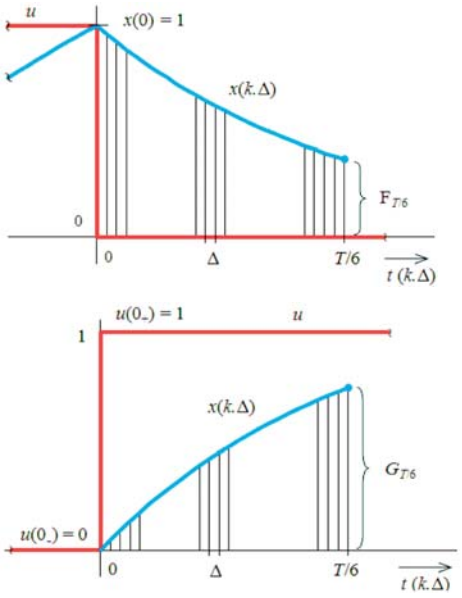

Fig. 3 To determination of $F_{T/6}$, $G_{T/6}$

After choosing $\Delta = T/360$, k will be the in the range of 0 ÷ 59, thus $G_{T/6} = y(60)$ and $F_{T/6} = 1 - G_{T/6}$. Supposing time constant of the load equal to $T/2$ and

$$F_\Delta = 0.994\ 4598;\ G_\Delta = 0.005\ 5401$$

those values of $F_{T/6}$, $G_{T/6}$ will be

$$F_{T/6} = F_\Delta\, q^{N-1} = F_\Delta^{60} = 0.716\ 52923,$$

because of $q = F_\Delta$.

$$G_{T/6} = G_\Delta\frac{1 - F_\Delta^{60}}{1 - F_\Delta} = 1 - F_\Delta^{60} = 0.283\,4707$$

Now, one can calculate state-variable $x\left(n\frac{T}{6}\right)$ for any n, Fig. 4.

It is also possible to change the step of series (sequences) e.g. for step equal $T/2$, by determining of $F_{T/2}$ and $G_{T/2}$:

$$F_{T/2} = F_{T/6}^3 = 0.367\,8764,$$

and regarding to $G_{T/6}$:

$$x(T/6) = F_{T/6}x(0) + G_{T/6}X_\infty$$

$$x(T/3) = F_{T/6}x(T/6) + G_{T/6}2X_\infty$$

$$x(T/2) = F_{T/6}x(T/3) + G_{T/6}2X_\infty \rightarrow\rightarrow\rightarrow G_{T/2} = 0.835\,2386.$$

So, then one can calculate

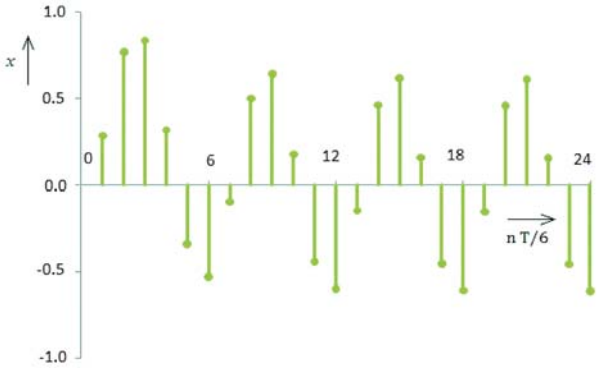

Fig. 4 Discrete response sequence of state-variable $x\left(n\frac{T}{6}\right)$ of three-phase inverter

$$x_{n+1} = F_{1/2}x_n + G_{1/2}\left\{u\left(n\tfrac{T}{2}\right)\right\}$$

where $u\left(n\frac{T}{2}\right) = U(-1)^n$.

Steady state determination

The steady state value of 'periodical' sequence $x\left(n\frac{T}{6}\right)$ can be determined, based on condition

$$x(0) = -x\left(\frac{T}{2}\right) \text{ or vice versa,i.e. } x\left(\frac{T}{2}\right) = -x(0).$$

Then

$$x\left(\frac{T}{2}\right) = F_{1/2}\left[-x\left(\frac{T}{2}\right)\right] + G_{1/2}X_\infty \rightarrow$$

$$\rightarrow x\left(\frac{T}{2}\right) = \frac{G_{1/2}}{1+F_{1/2}}X_\infty = 0.610\,6053X_\infty,$$

so $x(0) = X_0 = -0.610\,6053\,X_\infty$.

Setting this value into $\{x_n\}$ or $x(n+1)$ we get:

$$X_0 = -0.610\,6053(n=0);$$

$$X_{T/6} = -0.154\,0492(n=1);$$

$$X_{T/3} = +0.456\,5561(n=2);$$

$$X_{T/2} = +0.610\,6053(n=3).$$

Based on zero order hold function [6] and total mathematical induction one finally yields:

For three-phase Clarke transformed system

$$u_\alpha(k\Delta) = U_{DC}\frac{2}{3}\sin\left[\text{integer}\left(\frac{6}{T}k\Delta\right)\frac{\pi}{3} + \frac{\pi}{6}\right] \quad (17a)$$

$$u_\beta(k\Delta) = -U_{DC}\frac{2}{3}\sin\left[\text{integer}\left(\frac{6}{T}k\Delta\right)\frac{\pi}{3} + \frac{\pi}{6}\right]. \quad (17b)$$

where 'integer' means integer function, T is time period and $k\Delta$ is discretizing time.

Derived relations for voltages can be used for state variable calculations in electrical engineering systems.

$$x(k+1) = F_\Delta x_k + G_\Delta u_{\alpha,\beta}(k\Delta), \quad (18)$$

where F_Δ a G_Δ are discrete impulse responses of state-variables (see above).

The steady state waveform of $\{x(k.\Delta)\}$ is shown in Fig. 5.

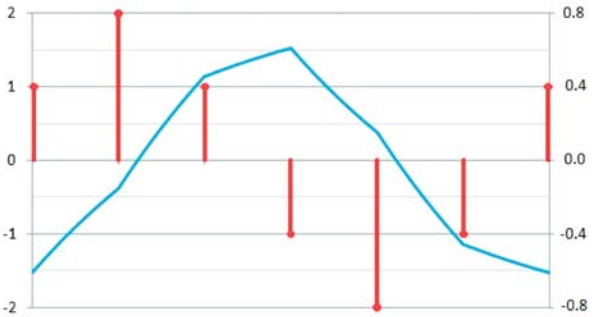

Fig. 5 Steady state waveform of state variable x(k.Δ)

By application of above given approach it is possible to analyze model, and simulate any sample of output voltage of power voltage sourced inverter, like 12-pulse samples, Fig. 6.

As the last example, transient- and steady-state waveforms of state variable under sine PWM supply with minimum number of switching states (12-pulse switching voltage function) are shown in Fig. 7.

6. Conclusions

Using direct and inverse Z-transform and numerical series (sequences) it is possible to derive functions as discrete voltage sequences from output voltage of power converters. These impulse switching functions can then be used to express the state variables of electrical circuits which are connected to output of the converters. Presented techniques are suitable for both transient- and steady-state behavior investigations of power converters. Unlikely to pure numerical computing, ISFs make it possible to calculate variable values at any time instants.

Acknowledgement

The authors wish to thank for the financial support to Slovak Research and Development Agency project No. APVV-0138-10 and R&D operational program Centre of excellence of power electronics systems and materials for their components No. OPVaV-2008/2.1/01-SORO, ITMS 26220120046 funded by European regional development fund (ERDF).

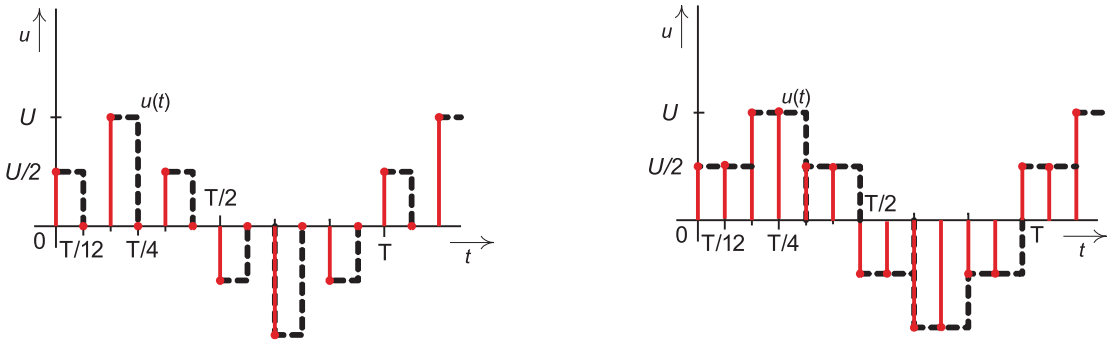

Fig. 6 Impulse switching function of 12-pulse output voltage of 3-phase converter: a) – with half-width of impulses; b) – with half-step of the impulse sequence

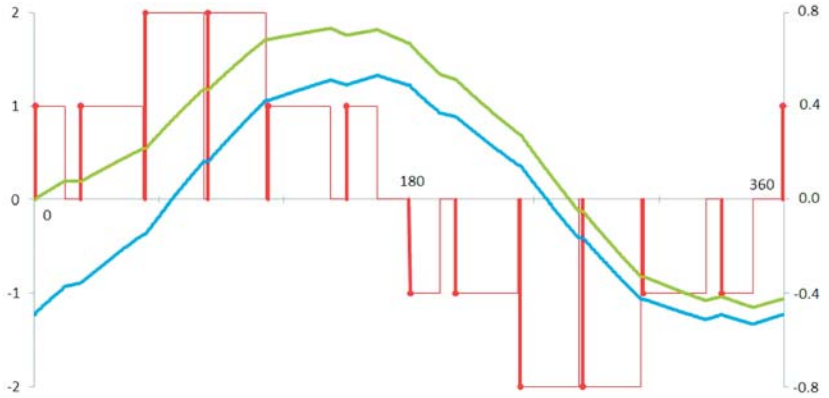

Fig. 7 State variable response under sine PWM supply
Legende: red – impulse switching function, blue – transient response, green – steady state waveform

References

[1] ZASKALICKA, M., ZASKALICKY, P., BENOVA, M., ABDALMULA, M. A. R., DOBRUCKY, B.: Analysis of Complex Time Function of Converter Output Quantities Using Complex Fourier Transform/Series. *Communications – Scientific Letters of the University of Zilina*, No. 1(12), pp. 23–30, 2010.

[2] DOBRUCKY, B., MARCOKOVA, M., POKORNY, M., SUL, R.: Using orthogonal and discrete transform for single-phase PES transients - a new approach. In: *Modelling, identification, and control: Proceedings of the 27th IASTED Int'l Conference,* Feb. 11–13, 2008, Innsbruck, Austria : Acta Press, 2008, ISBN 978-0-88986-633-1, pp. 60–65.

[3] JARDAN, R. K., DEWAN, B. S.: General Analysis of Three- Phase Inverters, IEEE Transactions on IGA, No. 6, pp. 672–679, 1969.

[4] DOBRUCKY, B., BENOVA, M., POKORNY, M: Using Theory of Series for Distortion Determination of Non-Harmonic Quantities of Two-Phase Systems. In: *Int;l School on Non-Sinusoidal Currents and Compensation: Proceedings of the 10th conference-seminar,* June 15–18, 2010, Łagów, Poland, IEEE, 2010, ISBN 978-1-4244-7894-1, pp. 37–42.

[5] GULDAN, V., MARCOKOVA, M.: Orthogonal Polynomials and Related Special Functions Applied in Geosciences and Engineering Computations. *Communications – Scientific Letters, of the University of Zilina,* vol. 12, No. 1, pp. 12–15, 2010.

[6] VICH, R.: *Z-transformation and some of its Utilization (in Czech),* SNTL Mathematical Seminar, Prague, 1983.

[7] ARAMOVIC, J. G., LUNC, G. L., ELSGOLC, L. C.: *Functions of Complex Variable, Operator Calculus, Stability Theory (in Russian – translated into Slovak)*, Alfa, Bratislava, 1973.

[8] MORAVCIK, J.: *Mathematical Analysis 3 (in Slovak),* Textbook, Alfa Publishing House, Bratislava, 1992, ISBN 80-05-01044-3.

Vasileios Drakopoulos *

FRACTAL-BASED IMAGE ENCODING AND COMPRESSION TECHNIQUES

In computer science and information theory, data compression*,* source coding*, or* bit-rate reduction *is the process of encoding digital information using fewer bits than the original representation. Specifically,* digital-image compression *is important due to the high storage and transmission requirements. Various compression methods have been proposed using different techniques to achieve high compression ratios.* Fractal image encoding *is a technique based on the representation of an image by contractive transformations.* Fractal-based image compression *methods belong to different categories according to the different theories they are based on. In this article, first we try to clarify the terminology used and then to comprehensively unveil the mathematical principle behind* fractal image compression *as well as to briefly overview a variety of schemes that have been investigated.*

Keywords: *Approximation, coding, dimension, fractal, image compression, image encoding, interpolation, iterated function system, local, partitioned, recurrent, transformation.*

1. Introduction

The *fractal transform* was discovered in 1988 by Michael F. Barnsley. It is the basis for an image compression scheme which was initially developed by Alan D. Sloan and M. F. Barnsley at Iterated Systems, Inc. They used the similarities on different scales throughout images to assist in compression. Since then, the research literature on *attractor image coding, fractal-based image coding, fractal image coding, fractal-based image compression, fractal image compression, fractal-based image encoding, fractal image encoding* and *fractal image approximation* has experienced a rapid growth. First of all, let's understand the interconnections between these topics by clarifying the terms coding and encoding.

1.1 Etymology and Meaning

The origin of the word *code* is traced to the Latin word *codex*, a manuscript (hand-written) volume, which in turn comes from the Latin *caudex*, trunk of a tree or block of wood. It can be used as either a noun or a verb. When used as a noun, it means a collection of laws or a system of principles and rules (canons). In our context, it means a system of symbols and rules used as instructions (statements) to a computer or the symbolic arrangement of them – a computer program; for instance, instructions written by a programmer in a programming language are often called *source code*.

When *code* is used as a verb, it is commonly confused with *encode*. There is a strong difference between the two words:

- to *code* means to express information through a proper standard representation. In the context of computer science it refers to write or revise a computer program.
- to *encode* means to perform an operation that transforms some information from one representation form to another. Something that is performing the act of encoding is, for example, an encrypter or a compressor.

Saying 'image-coding schemes' or 'image-coding methods' literally means that the scheme or the method expresses information relative to an image. Saying instead 'image-encoding schemes' or 'image-encoding methods' literally means that the scheme or the method is an entity performing encoding on the images, that is, transforming an image from one representation form to another, which is the correct for our purpose. It looks like many computer scientists use this wrong wording as standard nomenclature.

1.2 Key Terms

Compression is commonly confused with the notion of encoding. Compression is done solely to lessen the number of symbols to represent given piece of information. It is achieved with the help of specific encoding of information. The process of reducing the size of a data file is popularly referred to as *data compression*,

* **Vasileios Drakopoulos**
School of Science & Technology, Hellenic Open University, Greece, E-mail: vasilios@tutors.eap.gr

although its formal name is *source coding* (coding done at the source of the data before it is stored or transmitted). *Image compression* is the application of data compression on digital images. The objective of image compression is to reduce irrelevance and redundancy of the image data in order to be able to store or transmit data in an efficient form. Compression can be either lossless or lossy.

The term *fractal* is coined by Benoît B. Mandelbrot in 1975, about a decade after the publication of his paper on statistical self-similarity in the coastline of Britain. One often cited description that he published to describe geometric fractals is 'a rough or fragmented geometric shape that can be split into parts, each of which is (at least approximately) a reduced-size copy of the whole'; this is generally helpful but limited. A fractal is by definition a set for which the *Hausdorff-Besicovitch* dimension strictly exceeds its *topological dimension.* However, since Hausdorff-Besicovitch dimension is often difficult to calculate, the *fractal dimension* is used instead.

An *iterated function system* is a method for constructing fractals and makes the basis of most fractal-based image compression methods. A *fractal interpolation function* can be considered as a continuous function whose graph is the *attractor* of an appropriately chosen iterated function system. If this graph, usually of nonintegral dimension, belongs to the three dimensional space and has Hausdorff–Besicovitch dimension between 2 and 3, then the resulting attractor is called *fractal interpolation surface*.

Fractal compression refers to a number of lossy compression methods, based on *fractals*. When applied to digital images, it is called *fractal image compression*. It differs from pixel-based compression schemes such as Joint Photographic Experts Group (JPEG), Graphics Interchange Format (GIF) or Moving Picture Experts Group (MPEG) since no pixels are saved; for comparison's sake see [1]. It is best suited for textures and natural images, relying on the fact that parts of an image often resemble other parts of the same image. Special algorithms convert these parts into mathematical data called *fractal codes* which are used to recreate the encoded and compressed image. These codes can be decoded to fill any screen size without the loss of sharpness that occurs in conventional compression schemes.

The purpose of this article is to overview some basic approaches to fractal-based image encoding and compression in very simple terms, with as little mathematics as possible. Before delving into the main study, we first present the development of an iterated function system. Next, we examine the theoretical formulation of affine fractal interpolation functions as attractors of an appropriately defined iterated function system in two and three dimensions. Moreover, we examine an extension of the affine fractal interpolation functions, namely the piecewise affine fractal interpolation functions. Furthermore, some fundamental fractal compression schemes which use iterated function systems will be presented. Main differences with other fractal-based image compression schemes will be briefly explained. Finally, some conclusions will be drawn. A fairly full picture of the relevant literature is presented in [2] and [3] until the day of their publication. The concepts of fractals, iterated function systems and local iterated function systems are discussed and different implementations of compression of both still images and image sequences are reviewed in [4], [5], [6], [7], [8] and [9]. The bibliography presented here contains the recent bare essentials which are not included in the aforementioned articles.

2. Fractal Image Generation

In mathematics, an *iterated function* is a function which is composed with itself, possibly *ad infinitum*, in a process called iteration. *Iteration* means the act of repeating a process with the aim of approaching a desired goal, target or result. The formal definition of an iterated function on a set X follows. Let X be a set and f a function from X to itself i.e. a *transformation*. Define f^k as the k-th iterate of f, where k is a non-negative integer, by $f^0 = \mathrm{id}_X$ and $f^{k+1} = f \circ f^k$, where id_X is the identity function on X and $f \circ g$ denotes function composition.

A *contraction mapping,* or *contraction,* on a metric space (X, ρ) is a transformation f, with the property that there is a nonnegative real number $s < 1$ such that for all x and y in X, $\rho(f(x), f(y)) \leq s \cdot \rho(x, y)$, where ρ is a *distance function* between elements of X. The smallest such value of s is called the *Lipschitz constant* or *contractivity factor* of f. If the above condition is satisfied for $s \leq 1$, then the mapping is said to be *non-expansive*. A contraction mapping has at most one *fixed point*, i.e. a point x^* in X such that $f(x^*) = x^*$. Moreover, the *Banach fixed point theorem*, also known as the *contraction mapping theorem* or *contraction mapping principle*, states that every contraction mapping on a nonempty, complete metric space has a unique fixed point, and that for any x in X the iterated function sequence $x, f(x), f(f(x)), f(f(f(x))), \ldots$ converges to the fixed point. Furthermore, this fixed point can be found as follows: Start with an arbitrary element x_0 in X and define an iterative sequence by $x_n = f(x_{n-1})$ for $n = 1, 2, 3, \ldots$. This sequence converges and its limit is x^*.

An *iterated function system*, or *IFS* for short, is defined as a collection of a complete metric space (X, ρ), e.g. $(\overline{\mathbb{R}}^n, \|\cdot\|)$ or a subset, together with a finite set of continuous transformations $\{w_i : X \to X, i = 1, 2, \ldots, M\}$. It is often convenient to write an IFS formally as $\{X; w_1, w_2, \ldots, w_M\}$ or, somewhat more briefly, as $\{X; w_{1-M}\}$. If w_i are *contractions* with respective contractivity factors s_i, $i = 1, 2, \ldots, M$, the IFS is termed *hyperbolic*.

John E. Hutchinson showed in [10] that, for the metric space $\overline{\mathbb{R}}^n$, such a (hyperbolic) system of functions has a unique compact (closed and bounded) *fixed set S*. One way for constructing a fixed set is to start with an initial point or set S_0 and iterate the actions of the w_i, taking S_{n+1} to be the union of the image of S_n under the w_i; then taking S to be the closure of the union of the S_n. Symbolically, the unique fixed (nonempty compact) set $S \subset \mathbb{R}$ has the property

$$S = \bigcup_{i=1}^{M} w_i(S).$$

The set S is thus the fixed set of the *Hutchinson operator*

$$H(A) = \bigcup_{i=1}^{M} w_i(A),$$

where A is any subset of $\mathbb{R}^n$. The operator H itself is a contraction with contractivity factor $s = \max\{s_1, s_2, ..., s_M\}$ ([11], Theorem 7.1, p. 81 or [12]). The existence and uniqueness of S, which is called the *attractor* of the IFS, is a consequence of the contraction mapping principle as is the fact that $\lim_{k\to\infty} H^k(A) = S \equiv \mathcal{A}_\infty$ for all A in $\mathcal{H}(\mathbb{R}^n)$, where $\mathcal{H}(X)$ is the metric space of all nonempty, compact subsets of X with respect to some metric, e.g. the *Hausdorff metric*. The operator H is also called the *collage map* to alert us to the fact that $H(A)$ is formed as a union or 'collage' of sets.

Fractals derived by IFSs can be of any number of dimensions, but are commonly computed and drawn in 2D. A fractal is made up of the union of several copies of itself, each copy being transformed by a function (hence 'function system'). The canonical example is the *Sierpinski gasket*; see Fig. 1. The functions are normally contractions which means they bring points closer together and make shapes smaller. Hence, such a shape is made up of several possibly-overlapping smaller copies of itself, each of which is also made up of copies of itself, ad infinitum. This is the source of its self-similar nature.

Note that this infinite process is not dependent upon the starting shape being a triangle – it is just clearer that way. The first few steps starting, for example, from a square also tend towards a Sierpinski gasket; see Fig. 2.

Sometimes each function w_i is required to be a linear, or more generally an affine transformation, and hence represented by a matrix. A transformation w is affine, if it may be represented by a matrix $\mathbf{A}$ and translation $\mathbf{t}$ as $w(\mathbf{x}) = \mathbf{A}\mathbf{x} + \mathbf{t}$, or, if $X = \mathbb{R}^2$,

$$w\begin{pmatrix} x \\ y \end{pmatrix} = \begin{pmatrix} a & b \\ c & s \end{pmatrix}\begin{pmatrix} x \\ y \end{pmatrix} + \begin{pmatrix} d \\ e \end{pmatrix}. \qquad (1)$$

The *code* of w is the 6-tuple (a, b, c, s, d, e) and the *code of an* IFS is a table whose rows are the codes of $w_1, w_2, ..., w_M$. For the three-dimensional case (grey-scale images) this becomes

$$w\begin{pmatrix} x \\ y \\ I(x,y) \end{pmatrix} = \begin{pmatrix} a_{1,1} & a_{1,2} & a_{1,3} \\ a_{2,1} & a_{2,2} & a_{2,3} \\ a_{3,1} & a_{3,2} & a_{3,3} \end{pmatrix}\begin{pmatrix} x \\ y \\ I(x,y) \end{pmatrix} + \begin{pmatrix} b_1 \\ b_2 \\ b_3 \end{pmatrix}, \qquad (2)$$

where $I(x, y)$ denotes the grey-scale value at location (x, y). So, the similarity that exists in different parts of an image could be described in a finite set of instructions and data. Using some image-areas of the image, by rotating, resizing and stretching them, it is possible to generate other parts of the image. However, IFSs may also be built from non-linear functions, including *projective* and *Möbius* transformations.

The most common algorithm to compute fractals derived by IFSs is called the chaos game or *random iteration algorithm*. It consists of picking a random point in the plane, then iteratively applying one of the functions chosen at random from the function system and drawing the point. An alternative algorithm, the *deterministic iteration algorithm*, or *DIA* for short, is to generate each possible sequence of functions up to a given maximum length and then to plot the results of applying each of these sequences of functions to an initial point or shape.

3. Fractal Interpolation

Based on a theorem of J. E. Hutchinson ([10], p. 731) and using IFS theory [12], M. F. Barnsley introduced a class of functions (see [11]) which he called *fractal interpolation functions*. He worked basically with affine fractal interpolation functions, in the sense that they are obtained using affine transformations. Their main difference from elementary functions is their fractal character. Since their graphs usually have non-integral dimension, they can

Fig. 1 The evolution of the Sierpinski gasket

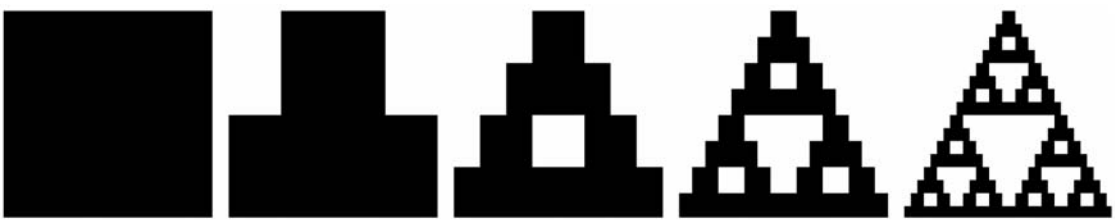

Fig. 2 Iterating from a square

be used to approximate image components such as the profiles of mountain ranges, the tops of clouds and horizons over forests, to name but a few. Applications of this theory include modelling of discrete sequences as in [13], modelling of speech signals as in [14] and compression of static images as in Ref. [AlCl94] of [2].

3.1 Interpolation Functions in $\mathbb{R}$

Let the continuous function f be defined on a real closed interval $I = [x_0, x_M]$ and with range the metric space $(\mathbb{R}, |\cdot|)$, where $x_0 < x_1 < \cdots < x_M$. It is not assumed that these points are equidistant. The function f is called an interpolation function corresponding to the *generalized set of data* $\{(x_m, y_m) \in K = I \times \mathbb{R} : m = 0, 1, ..., M\}$, if $f(x_m) = y_m$ for all $m = 0, 1, ..., M$ and $K = I \times \mathbb{R}$. The points $(x_m, y_m) \in \mathbb{R}$ are called the *interpolation points*. We say that the function f *interpolates* the data and that (the graph of) f passes through the interpolation points.

Let us represent our, real valued, set of *data points* as $\{(u_n, v_n): n = 0, 1, ..., N; u_n < u_{n+1}\}$ and the interpolation points as $\{(x_m, y_m) : m = 0, 1, ..., M; M \leq N\}$, where u_n is the sampled index and v_n the value of the given point in u_n. Let $\{\mathbb{R}^2; w_{1-M}\}$ be an IFS with affine transformations of the special form (see (1))

$$w_i\begin{pmatrix}x\\y\end{pmatrix} = \begin{pmatrix}a_i & 0\\ c_i & s_i\end{pmatrix}\begin{pmatrix}x\\y\end{pmatrix} + \begin{pmatrix}d_i\\e_i\end{pmatrix}$$

constrained to satisfy

$$w_i\begin{pmatrix}x_0\\y_0\end{pmatrix} = \begin{pmatrix}x_{i-1}\\y_{i-1}\end{pmatrix} \text{ and } w_i\begin{pmatrix}x_M\\y_M\end{pmatrix} = \begin{pmatrix}x_i\\y_i\end{pmatrix} \quad (3)$$

for every $i = 1, 2, ..., M$. Solving the above equations results in

$$a_i = \frac{x_i - x_{i-1}}{x_M - x_0},\ d_i = \frac{x_M x_{i-1} - x_0 x_i}{x_M - x_0},$$

$$c_i = \frac{y_i - y_{i-1}}{x_M - x_0} - s_i\frac{y_M - y_0}{x_M - x_0},$$

$$e_i = \frac{x_M y_{i-1} - x_0 y_i}{x_M - x_0} - s_i\frac{x_M y_0 - x_0 y_M}{x_M - x_0}$$

i.e. the coefficients a_i, c_i, d_i, e_i are completely determined by the interpolation points, while the s_i are free parameters satisfying $|s_i| < 1$ in order to guarantee that the IFS is hyperbolic with respect to an appropriate metric for every $i = 1, 2, ..., M$. The transformations w_i are *shear transformations*: line segments parallel to the y-axis are mapped to line segments parallel to the y-axis contracted by the factor $|s_i|$. For this reason, the s_i are called *vertical scaling* (or contractivity) *factors*.

The IFS $\{\mathbb{R}^2; w_{1-M}\}$ has a unique attractor that is the graph of some continuous function which interpolates the data points. This function is called a *fractal interpolation function*, or *FIF* for short, because its graph usually has non-integral dimension. A *section* is defined as the function values between interpolation points. It is a *self-affine* function since each affine transformation w_i maps the entire (graph of the) function to its section. The above function is known as *affine FIF*, or *AFIF* for short. For example, let {(0, 0), (0.4, 0.5), (0.7, 0.2), (1, 0)} be a given set of data points. Fig. 3 shows the graph of an AFIF with $s_1 = 0.5$, $s_2 = -0.2$ and $s_3 = 0.4$. The closeness of fit of a FIF is mainly influenced by the determination of its vertical scaling factors. No direct way to find the optimum values of these factors exists and various approaches have been proposed in the literature.

3.2 Piecewise Affine Fractal Interpolation

The *piecewise self-affine* fractal model is a generalization of the affine fractal interpolation model and has its mathematical roots

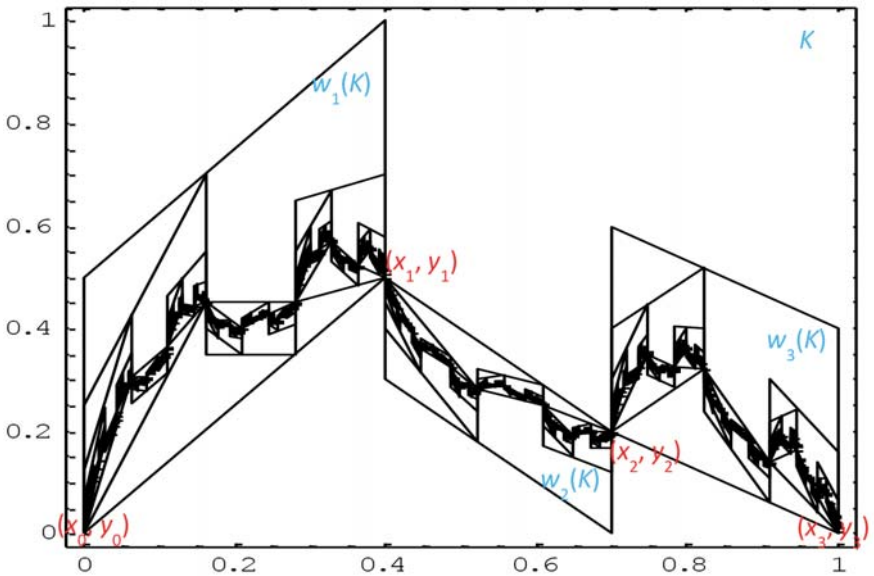

Fig. 3 The construction of an affine FIF starting from the unit square and using the DIA

embedded in *recurrent IFS*, or *RIFS* for short, theory. A pair of data points $\{(\tilde{x}_{i,j}, \tilde{y}_{i,j}): i = 1, 2, ..., M; j = 1, 2\}$, which are called *addresses* or *address points*, is now associated with each *interpolation interval*. Each pair of addresses defines the *domain* or *address interval*. The constraints (3) become

$$w_i\begin{pmatrix}\tilde{x}_{i,1}\\ \tilde{y}_{i,1}\end{pmatrix} = \begin{pmatrix}x_{i-1}\\ y_{i-1}\end{pmatrix} \text{ and } w_i\begin{pmatrix}\tilde{x}_{i,2}\\ \tilde{y}_{i,2}\end{pmatrix} = \begin{pmatrix}x_i\\ y_i\end{pmatrix}$$

subjected to $\tilde{x}_{i,1} - \tilde{x}_{i,2} > x_i - x_{i-1}$ for every $i = 1, 2, ..., M$. Solving the above equations results in

$$a_i = \frac{x_i - x_{i-1}}{\tilde{x}_{i,2} - \tilde{x}_{i,1}},\ d_i = \frac{\tilde{x}_{i,2}x_{i-1} - \tilde{x}_{i,1}x_i}{\tilde{x}_{i,2} - \tilde{x}_{i,1}},$$

$$c_i = \frac{y_i - y_{i-1}}{\tilde{x}_{i,2} - \tilde{x}_{i,1}} - s_i\frac{\tilde{y}_{i,2} - \tilde{y}_{i,1}}{\tilde{x}_{i,2} - \tilde{x}_{i,1}},$$

$$e_i = \frac{\tilde{x}_{i,2}y_{i-1} - \tilde{x}_{i,1}y_i}{\tilde{x}_{i,2} - \tilde{x}_{i,1}} - s_i\frac{\tilde{x}_{i,2}\tilde{y}_{i,1} - \tilde{x}_{i,1}\tilde{y}_{i,2}}{\tilde{x}_{i,2} - \tilde{x}_{i,1}}$$

for every $i = 1, 2, ..., M$. The function constructed as the attractor of the above-mentioned IFS is called *recurrent fractal interpolation function*, or *RFIF* for short, corresponding to the interpolation points. A RFIF is a piecewise self-affine function since each affine transformation w_i maps the part of the (graph of the) function defined by the corresponding address interval to each section.

3.3 Interpolation Functions in $\mathbb{R}^2$

Suppose we refer to an image as a function $z = z(x, y)$ that gives the grey level at each point (x, y). Let the discrete data $\{(x_i, y_j, z_{i,j} = z(x_i, y_j)) \in \mathbb{R}^3 : i = 0, 1, ..., N; j = 0, 1, ..., M\}$ be known. Each affine mapping that comprises the hyperbolic IFS $\{\mathbb{R}^3; w_{1-N,\,1-M}\}$ is given by the following special form of (2)

$$w_{n,m}\begin{pmatrix}x\\ y\\ z\end{pmatrix} = \begin{pmatrix}a_{n.m} & b_{n.m} & 0\\ c_{n.m} & d_{n.m} & 0\\ e_{n.m} & g_{n.m} & s_{n.m}\end{pmatrix}\begin{pmatrix}x\\ y\\ z\end{pmatrix} + \begin{pmatrix}h_{n.m}\\ k_{n.m}\\ l_{n.m}\end{pmatrix},$$

with $|s_{n,m}| < 1$ for every $n = 1, 2, ..., N$ and $m = 1, 2, ..., M$. The condition

$$\left\|\begin{matrix}a_{n,m} & b_{n,m}\\ c_{n,m} & d_{n,m}\end{matrix}\right\| < 1$$

ensures that

$$u_{n,m}\begin{pmatrix}x\\ y\end{pmatrix} = \begin{pmatrix}a_{n,m} & b_{n,m}\\ c_{n,m} & d_{n,m}\end{pmatrix}\begin{pmatrix}x\\ y\end{pmatrix} + \begin{pmatrix}h_{n,m}\\ k_{n,m}\end{pmatrix}$$

is a similitude and the transformed surface does not vanish or flip over.

FIFs are suitable for data sets with points linearly ordered with respect to their abscissa. This is often sufficient, e.g. when interpolating time series data. In practice, however, there are many cases where the data are suitable for fractal interpolation but define a curve rather than a function, e.g. when modelling coastlines or plants. There exist methods for constructing *fractal interpolation curves* based on the theory of FIFs. These methods use various approaches, such as generalizations to higher dimensions, use of index coordinates or application of reversible transformations.

4. Fractal Image Encoding and Compression

Fractal encoding relies on the fact that all natural, and most artificial, objects contain redundant information in the form of similar, repeating patterns or fractals. The encoding process is computationally intensive. Depending upon the resolution and contents of the input bitmap data, and output quality, compression time, and file size parameters selected, compressing a single image could take anywhere from a few seconds to a few hours on even a fast computer; see also [15]. Decoding a fractal image is a much simpler process. All the decoding process needs to do is to interpret the fractal codes and translate them into a bitmap image.

The fundamental principle of fractal-based image compression consists of the representation of an image by an IFS of which the fixed point is 'close' to that image. In other words, the encoding process is first to find an IFS and then a suitable operator H whose fixed point is 'close' to the given image.

4.1 Based Directly on the Collage Theorem

The *collage theorem* characterizes an IFS whose attractor is close, relative to some metric, to a given set. The IFS described is composed of contractions whose images, as a collage or union when mapping the given set, are arbitrarily close to the given set.

If $B \in (\mathcal{H}(\mathbb{R}^n), h)$, where h is a metric, obeys $h(B, H(B)) \leq \varepsilon$, then

$$h(B, \mathcal{A}_\infty) \leq \frac{\varepsilon}{1 - s},$$

where $s = \max[s_i : i = 1, 2, ..., N]$. Therefore, the closer the union is to the given set, the closer the attractor of the IFS will be to the given set. The theorem, however, is not constructive, it does not indicate how to find a set of proper mappings, but rather, it provides a way to test an IFS without need for computation of the attractor.

To find an IFS for an image, based on the collage theorem and the property of IFS attractors, we split the whole image into non-overlapping segments whose union covers the entire image. If each segment is a transformed copy of the entire image or is very close to it, the combination of these transformations is the IFS of the original image. In other words, to encode an image into IFS is to find a set of contractive affine transformations, $w_1, w_2, ..., w_N$, so that the original image B is the union of the N subimages: $B = w_1(B) \cup w_2(B) \cup \cdots \cup w_N(B)$.

4.2 Based on the Fractal Transform

The fractal transform [16] was considered to solve effectively the problem of finding a fractal which approximates a digital 'real world image.' This first practical fractal compression system for digital images resembles a vector quantization system using the image itself as the codebook.

Fractal Transform compression

Start with a digital image A_1. Downsample (subsample) it by a factor of 2 to produce image A_2. Now, for each block B_1 of 4×4 pixels in A_1, find the corresponding block B_2 in A_2 most similar to B_1 and then find the grey-scale or RGB offset and gain from A_2 to B_2. For each destination block, output the positions of the source blocks and the color offsets and gains.

An image compressed in this way contains a minimal area plus a transformation matrix that contains all required information to reconstruct something similar to the original image by rotating, resizing and stretching this area. Therefore the task of fractal encoding algorithms is to find redundant areas of an image and to reduce these areas to the necessary information about attractor and transformation matrix. To perform this task, the image is divided into *domains* in coarse or fine resolution depending on the redundancy of the image. Then the routine searches the image for *ranges* that have a similarity to the domain that can be described by an affine transformation matrix. The names of these blocks are reversed in Ref. [7, p. 181] of [3].

Fractal Transform decompression

Starting with an empty destination image A_1, repeat the following algorithm several times: Downsample A_1 down by a factor of 2 to produce image A_2. Then copy blocks from A_2 to A_1 as directed by the compressed data, multiplying by the respective gains and adding the respective color offsets.

This algorithm is guaranteed to converge to an image, and it should appear similar to the original image. In fact, a slight modification of the decompressor to run at block sizes larger than 4×4 pixels produces a method of stretching images without causing the blockiness or blurriness of traditional *linear resampling algorithms.*

4.3 Based on Local (Partitioned) IFS

IFS approximates each part of the image by a transformed version of the *whole* image, but our intuition suggests that real-world images, generally, do not contain parts that are affine transforms of the whole image (Fig. 4). Nevertheless, different parts of the image may become similar under certain affine transformation. Therefore, an extension of the IFS, the *Local* or *Partitioned* IFS, has been developed to approximate each part of the image by a transformed version of *another part* of the image. The first automated compression scheme for real world images using PIFS was developed by Arnaud E. Jacquin (Ref. [26] of [3]) in 1992.

Suppose we are given an image f we wish to encode. We divide the image into *range blocks* R_1, R_2, ..., R_i, ..., R_N, such that $f = R_1 \cup R_2 \cup \cdots \cup R_N$ and $R_i \cap R_j = \varnothing$ when $i \neq j$. Therefore, the range blocks cover the whole image and do not overlap. The image is also divided into overlapping *domain blocks* D_1, D_2, ..., D_j, ..., D_M. For each range block R_i, we find a contractive transformation wi and a domain block D_j, so that $R_i \approx w_i(D_j)$. The combination of w_1, w_2, ..., w_i, ..., w_N is called PIFS H. If H is simpler than the original image, we can encode f into H and achieve certain compression. When decoding, according to the contractive mapping fixed point theorem, as long as H is contractive, repeated application of H to an arbitrary image will result in a fixed image. When $H(f)$ is close to f, the fixed image will be close to the original image f.

The three main issues involved in the design and implementation of a fractal block-coding system based on the above idea are (i) how the image is partitioned, (ii) the choice of a distortion measure between two images and (iii) types of contractive affine transformations to be used. We do not intend to discuss these

Fig. 4 The original 256 × 256 × 8 bpp image of Lenna (left) and self-similar portions of Lenna's image (right)

issues; see [17] for highlighting the solution to the key and open issues in the fractal coding. It is noteworthy to mention, though, how important is to find a similar block so that the IFS accurately represents the input image, so a sufficient number of candidate blocks for D_i need to be considered. On the other hand, a large search considering many blocks is computationally costly. This bottleneck of searching for similar blocks is why fractal encoding is slower than for example DCT, the underlying compression technique in JPEG, and wavelet based image representations.

4.4 Based on RIFS or on FIF

A RIFS is an improvement of LIFS using elements of the theory of *Marcovian stochastic processes* which can produce more natural looking images; see [18]. An image compression scheme using fractal interpolation surfaces which are attractors of some RIFSs is introduced in [19]. Alternative image compression methods which use the method presented in Subsection 3.3 can be found in [20]. Many enhancements and variations exist, as for example [21], but they fall beyond the scope of this discussion.

The resolution independence of a fractal-encoded image can be used to increase the display resolution of an image. During this process, also known as fractal interpolation, an image is encoded into fractal codes via fractal compression and subsequently decompressed at a higher resolution. The result is an up-sampled image in which an appropriately chosen iterated function system has been used as the interpolant. Because fractal interpolation operates on geometric information in the image, rather than pixel information, it maintains geometric detail very well compared to other interpolation methods.

5. Conclusions

Our clarification of terminology used in the existing literature led to the conclusion that fractal image compression is also called as fractal image encoding because a compressed image is represented by contractive transformations and mathematical functions required for reconstructing the original image.

Lossless compression methods are sometimes preferred for artificial images such as technical drawings, icons or comics. This is because lossy compression, especially when used at low bit rates, introduce compression artifacts. Lossless compression may also be preferred for high value content, such as medical imagery or image scans made for archival purposes. Lossy methods are especially suitable for natural images such as photos in applications where minor loss of fidelity is acceptable to achieve a substantial reduction in bit rate. For further details see [22] and [23].

Fractal image compression enables an incredible amount of data to be stored in highly compressed data files. An inherent feature of fractal compression is that images become resolution independent after being converted to fractal code. This is because the iterated function systems in the compressed file scale indefinitely. This indefinite property, known as *fractal scaling* or *fractal zooming*, leaves no trace of the original pixel structure.

Acknowledgement

The author would like to thank Prof. Mariana Marčoková and Prof. Ing. Branislav Dobrucky for the invitation to write this article based on the lectures he gave two years ago at the University of Zilina. He also wishes to thank both reviewers for their comments.

References

[1] RUSS , J. C., *The Image Processing Handbook*, 6th ed., CRC Press LLC, 2011.
[2] SAUPE, D., HAMZAOUI, R.: A Review of the Fractal Image Compression Literature, *ACM SIGGRAPH Computer Graphics,* vol. 28, No. 4, 1994, pp. 268–276.
[3] WOHLBERG, B., DE JAGER, G.: A Review of the Fractal Image Coding Literature, *IEEE Trans. Image Process.,* vol. 8, No. 12, 1999, pp. 1716–1729.
[4] CHAURASIA, V., SOMKUWAR, A.: Review of a Novel Technique: Fractal Image Compression, *Int. J. Emerging Technol.*, vol. 1, No. 1, 2010, pp. 53–56.
[5] CHAUDHARI, R. E., DHOK, S. B.: Review of Fractal Transform Based Image and Video Compression, *Int. J. Comput. Appl.,* vol. 57, No. 19, 2012, pp. 23–31.
[6] DHAWAN, S.:A Review of Image Compression and Comparison of its Algorithms, *Int. J. of Electronics & Commun. Technol.,* vol. 2, No. 1, 2011, pp. 22–26.
[7] GHARAVI-ALKHANSARI, M., HUANG, T. S.:, Fractal-based Image and Video Coding, in L. Torres and M. Kunt (eds.), *Video coding:* The second generation approach, pp. 265-303. Kluwer Academic Publishers : Boston, 1996.
[8] LU, G.: Fractal-based Image and Video Compression, in K. R. Rao and P. C. Yip (eds.), *Chapter 7: The transform and data compression handbook,* CRC Press LLC, Boca Raton, 2001.
[9] ZHAO, E., LIU, D.: Fractal Image Compression Methods: A Review, *Proc. IEEE Int. Conf. Inf. Technol. and Appl.*, vol. 1, 2005, pp. 756–759.
[10] HUTCHINSON, J. E.: Fractals and Self Similarity, *Indiana Univ. Math. J.*, vol. 30, No. 5, 1981, pp. 713–747.
[11] BARNSLEY, M. F.: *Fractals Everywhere,* 2nd ed., Academic Press Professional, 1993.

[12] BARNSLEY, M. F., DEMKO, S.: Iterated function systems and the global construction of fractals, *Proc. R. Soc. Lond. Ser. A Math. Phys. Eng. Sci.*, vol. 399, No. 1817, 1985, pp. 243–275.
[13] MAZEL, D. S., HAYES, M. H.: Using Iterated Function Systems to Model Discrete Sequences, *IEEE Trans. Signal Process.,* vol. 40, No. 7, 1992, pp. 1724–1734.
[14] VEHEL, J. L., DAOUDI, K., LUTTON, E.: Fractal Modeling of Speech Signals, *Fractals,* vol. 2, No. 3, 1994, pp. 379–382.
[15] FURAO, S., HASEGAWA, O.: A Fast no Search Fractal Image Coding Method, *Signal Process.: Image Commun.*, vol. 19, No. 5, 2004, pp. 393–404.
[16] BARNSLEY. M. F., Anson, L. F.: *The Fractal Transform,* Jones and Bartlett Publishers, Inc, 1993.
[17] Koli, N. A., Ali, M. S.: A Survey on Fractal Image Compression Key Issues. *Inf. Technol. J.*, vol. 7, No. 8, 2008, pp. 1085–1095.
[18] HURT, J. C. : Fractal Image Compression and Recurrent Iterated Function Systems, *IEEE Comput. Graphics & Appl.*, vol. 16, No. 4, 1996, pp. 25–33.
[19] BOUBOULIS, P., DALLA, L., DRAKOPOULOS, V.: Image Compression Using Recurrent Bivariate Fractal Interpolation Surfaces, *Int. J. Bifurc. Chaos,* vol. 16, No. 7, 2006, pp. 2063–2071.
[20] DRAKOPOULOS, V., BOUBOULIS, P., THEODORIDIS, S.: Image Compression Using Affine Fractal Interpolation on Rectangular Lattices, *Fractals,* vol. 14, No. 4 2006, pp. 259–269.
[21] CHERNOYAROV, O. V. BREZNAN, M.: Optimal and Quasioptimal Algorithms of Distinction of the Compressed Images in Base of Orthogonal Polynomials, *Communications – Scientific Letters of the University of Zilina,* vol. 14, No. 2, 2012, pp. 22–26.
[22] BARNSLEY, M. F., SAUPE, D., VRSCAY, E. R. (eds.): *Fractals in Multimedia,* Springer-Verlag : New York, 2002.
[23] NIKIEL, S.: *Iterated Function Systems for Real-Time Image Synthesis,* Springer-Verlag : London, 2007.

Matus Ocilka – Dobroslav Kovac – Irena Kovacova – Jan Perdulak
– Andrii Gladyr – Dmytro Mamchur – Iurii Zachepa – Tibor Vince – Jan Molnar *

SERIAL RESONANT CONVERTER AND LOAD COIL FOR HIGH FREQUENCY HEATING

The paper deals with the design of the voltage source half-bridge resonant inverter with the specific load coil, which is suitable for induction heating applications. To ensure the correct functionality and right frequency range of the self-resonant converter, the parameters as inductance, self-capacitance and resistance of the coil have to be obtained. Parameters of the coil are estimated by utilizing software that uses finite elements method of solution. In order to estimate the accuracy of model, the experimental verifications were taken. For this purpose, the spiral coil made on printed circuit board was created and its parameters were calculated, simulated and compared with measurement results.

Keywords: *Induction heating, induction coil, resonant converter, finite elements method.*

1. Introduction

Induction heating (IH) is widely used in many industrial applications including melting, heating prior to metalworking hardening, during manufacturing of semiconductors (doping, refining) and in domestic applications such as induction cookers. Electromagnetic induction is a method of heating electrically conductive materials such as metals. Such phenomenon relies on two mechanisms of energy dissipation. These are losses due to Joule heating and losses associated with magnetic hysteresis. First of these, is primary mechanism of heat generation in electrically conductive nonmagnetic materials (aluminum, copper, steels above Curie temperature). Electrical currents or eddy currents which are internally induced in material dissipate the energy and bring about the heat. Second mechanism is present in magnetic materials. The explanation of hysteresis losses states that heat generation is caused by friction between molecules, or so called magnetic dipoles, when ferromagnetic metals are first magnetized in one direction and then in the other. The energy needed to turn the dipoles is dissipated as heat.

The induction heating system (Fig. 1) consists of a source of alternating current, an induction coil and load which is eddy current based heating material.

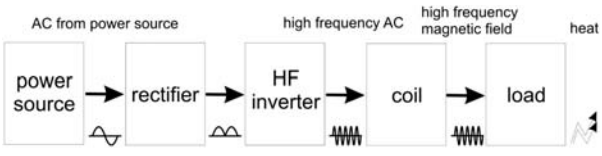

Fig. 1 Induction heating system

The coil is connected to the power supply. The flow of AC current through the coil generates the alternating magnetic field which cuts through the workpiece and thus generates the heat. Generation of heat increases with frequency and amplitude of AC current. The more frequency increases, the more are eddy currents located near the surface of workpiece. The common characteristic of the induction heating applications are high efficiency, quick heating, energy savings, ease of automation, quiet, clean and safe working conditions [1], [2].

High frequency converters

IH system as stated before consists of source of AC current coil and the workpiece to be heated. There are various high frequency inverter circuit topologies, such as: full bridge, half bridge, single-ended push-pull, center tap push-pull and boost half bridge. Most of the IH systems are constructed as resonant inverters operating at high frequencies. Of these, the voltage source type ZCS (zero current switching), ZVS (zero voltage switching), ZVZCS (zero voltage – zero current switching), SEPP (Single-Ended Push Pull) resonant and quasi-resonant hybrid high frequency inverter has unique features; such as simple configuration, high efficiency and wide soft commutation range [3].

Increasing the switching frequencies improves the performance and power density of the inverter. However, with increasing the switching frequencies some disadvantages appear due to the high commutation losses in the switching and appearance of electromagnetic interference. These factors occur mainly in inverter topologies that use the full-bridge inverter configuration. The use of resonant converter which offers the interesting option for an application requires previous specification [4], [5], [6].

* **Matus Ocilka[1], Dobroslav Kovac[1], Irena Kovacova[1], Jan Perdulak[1], Andrii Gladyr[2], Dmytro Mamchur[2], Iurii Zachepa[2], Tibor Vince[1], Jan Molnar[1]**
[1] Address: Department of Theoretical Electrical Engineering and Electrical Measurement, Technical University of Kosice, Slovakia,
E-mail: matus.ocilka@tuke.sk
[2] Address: Department of Automatic Management and Electrical Drive, Kremenchuk Mykhailo Ostrohradskyi National University, Ukraine

Voltage source half-bridge resonant inverter

The use of full-bridge resonant converter brings some disadvantages due to high switching losses and electromagnetic interference. Moreover, the configuration and control algorithm of such a converter is more complicated than, for example, in half-bridge topology. For our purpose the voltage source half-bridge resonant converter topology is used. The converter topology is depicted in Fig. 2 and consists of two switches (S_1, S_2), two antiparallel diodes and load which is a working coil that serves as a resonant circuit.

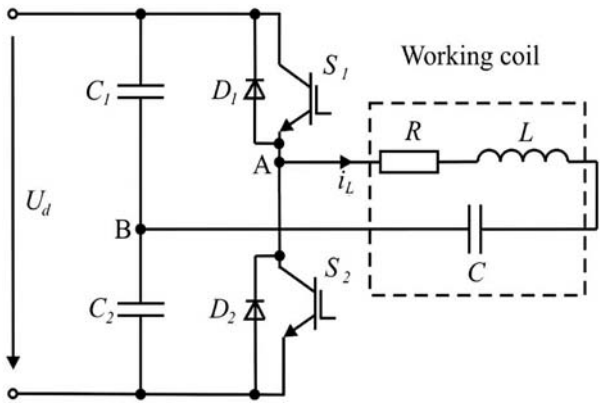

Fig. 2 Half-bridge series resonant inverter

The parameters of working coil such as inductance, self-capacitance and resistance have to be known because the switching frequency of converter has to be set as close as possible to resonant frequency of the coil/circuit. Since the self-capacitance of coils is in general very small, the resonant frequencies lie in a range of MHz. The desired resonant frequency is commonly set by adding tuning capacitor into the circuit. In our case, no tuning capacitance is added to the resonant circuit, thus the careful attention in designing the coil has to be taken to bring the resonant frequency of the coil in a range of hundreds of kHz. For obtaining these parameters for given coil designs the finite elements method of solution is used.

2. Finite elements method of solution

For calculation of inductance and self-capacitance of coils there are several analytic approaches and models. Due to the complex nature of the approximations, where the coil's geometry, mutual inductance or self inductance has to be considered, the analytic approach can be overly difficult. High accuracy and precision during design stage is essential, because when printed on circuit board, the inductor can't be changed anymore. Thus the using of finite element method can be a good alternative of solving such problems and can give us information about parameters of the coil in some range and can provide us with some initial conditions in designing such devices [7], [8].

For our purpose the software package called COMSOL Multiphysics was used. It is a software that solves systems of coupled three-dimensional partial differential equations. The COMSOL Multiphysics engineering simulation software environment facilitates all steps in the modeling process – defining geometry, meshing, specifying physics, solving, and then visualizing results. Model set-up is quick thanks to a number of predefined physics interfaces for applications ranging from fluid flow and heat transfer to structural mechanics and electromagnetic analyses. Material properties, source terms and boundary conditions can all be arbitrary functions of the dependent variables. It can model the complex problems, geometries or material properties in 2D or 3D representation for better understanding of some phenomena. In this case, COMSOL Multiphysics solves the magnetic and electric fields created by the coil that is placed in electrical circuit and calculates the inductance, resistance and capacitance of the coil.

3. Simulation models and experimental verification

The spiral coil is a spiral – shaped formation made of copper. This copper spiral is electrically conductive showing electrical resistance for the direct current. For the alternating current the inductor shows, apart from electrical resistance, also a property called inductance, which describes the capability of producing a magnetic field around the inductor. From the electrical point of view the inductance acts as complex impedance being proportional to the frequency of alternating current. The ideal inductor shows only the inductance while its electrical resistance is negligible.

The coil geometry

The proposed double-layer coil is shown in Fig. 3.

The above mentioned coil is physically described by the following parameters: d_{in} as the inner diameter [mm], d_{out} is outer diameter [mm], s expresses the spacing between turns [mm], w is the width of conductor [mm], h is height of conductor [mm] and d [mm] represents the distance of both spirals.

Inductance of the coil - analytic solution

Calculation of inductance value of one layer of such coil can be done using the following equation [9]:

$$L = \frac{\mu_0 N^2 d_{avg} C_1}{2}\left(\left(\ln\frac{C_2}{\rho}\right) + C_3\rho + C_4\rho^2\right). \quad (1)$$

Where ρ is the fill ratio:

$$\rho = \frac{d_{out} - d_{in}}{d_{out} + d_{in}}. \quad (2)$$

And d_{avg} is average diameter:

$$d_{avg} = \frac{d_{out} - d_{in}}{2}. \quad (3)$$

Constants C_1 - C_4 are shape dependent constants and their values according to [9], are $C_1 = 1.00$, $C_2 = 2.46$, $C_3 = 0.00$, $C_4 = 0.20$, and $\mu_0 = 4\pi \times 10^{-7}$ H.m^{-1}. The inductance of double-layer coil is given by the following equation

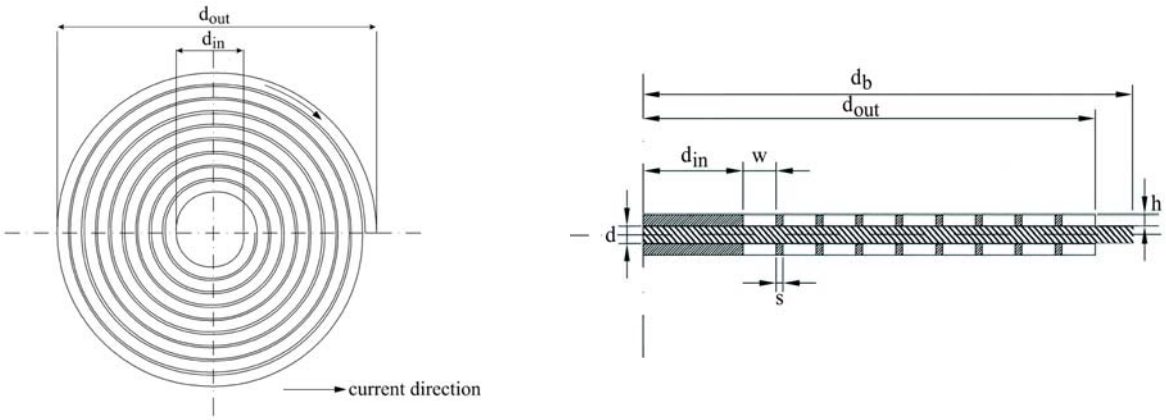

a) *b)*

Fig. 3 Designed double-layer spiral coil a) top view b) side view

$$L_{tot} = L_1 + L_2 \pm 2M \,. \tag{4}$$

Where L_1 and L_2 are the self-inductances of both coils and M is the mutual inductance between coils. Mutual inductance is difficult to calculate because it depends on many factors as follows: distance between coils, geometry, and mutual geometry of particular conductors. The inductance increases or decreases total inductance of the coil depending on currents directions passing through the coils. In our case the currents of both coils pass through coils in the same direction. The mutual inductance can be determined as:

$$M = K_c \sqrt{L_1 L_2} \,. \tag{5}$$

Where K_c is the coupling factor and its value must lie in interval $\langle 0;1 \rangle$. The coupling factor can be determined using the following formula [9]:

Where $x = d$ is the mutual distance of both coils, constants *A, B, C, D* according to [9], are:

$$A = 0.184,\ B = -0.525,\ C = 1.038,\ D = 1.001.$$

Inductance of the coil - simulation model

The model of coil is shown in Fig. 4a) and it is modeled in COMSOL Multiphysics in AC/DC module. The model is created in 2D axisymmetric space dimension and the coil is surrounded with an air domain and its boundary serves as magnetic insulation [10].

This model is not exact spiral geometry and it was adapted for solving in 2D axisymmetric space dimension because spiral-shaped formation of the coil is not axisymmetric. One layer of the coil is created from 9 rings as depicted in Fig. 4b).

$$K_c = \frac{N^2}{0.64 \cdot \left(Ax^3 + Bx^2 + Cx + D\right) \cdot \left(1.67N^2 - 5{,}84N + 65\right)} \,. \tag{6}$$

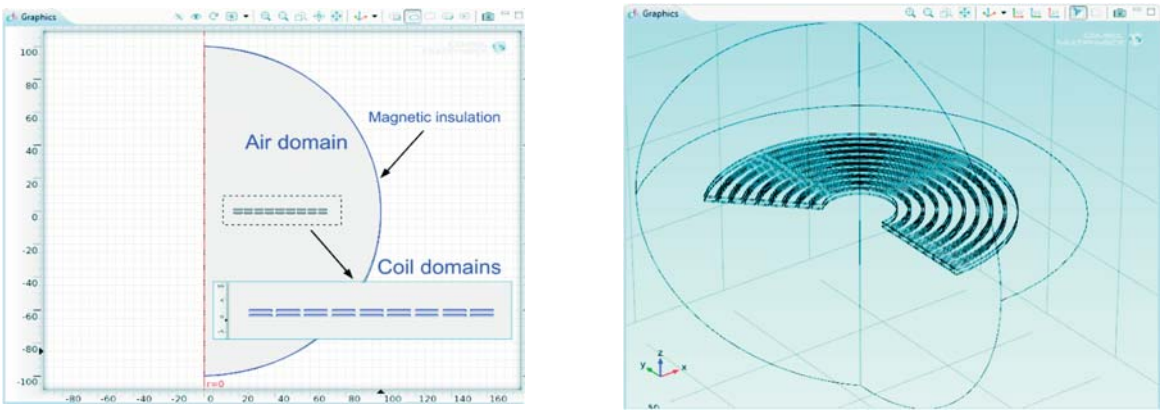

a) *b)*

Fig. 4 Double-layer coil in COMSOL a) model of the coil b) model of the coil in 3D

The parameters used in calculation and simulations are in Table. 1.

Parameters used in simulation for double-layer coil Tab. 1

Number of turns:	N = 9
Outer diameter:	dout = 142 mm
Inner diameter:	din = 30 mm
Width of conductor:	W = 5 mm
Spacing between turns:	s = 1 mm
Height of conductor:	h = 0.8 mm
Distance of coils:	d = 1.5 mm

Analytic results

The inductance of one coil using (1) is $L_1 = 6.19$ µH. Both coils have the same geometry, so the inductance of second coil must be the same $L_2 = 6.19$ µH. Using (4) we can calculate the total inductance of double-layer coil. The coupling factor according to (6) is $K_c = 0.855$ and mutual inductance (5) is $M = 5.29$ µH. Then the total inductance using analytic approach is $L_{tot} = 22.90$ µH.

Simulation results

For simulation the model shown in Fig. 4a) was used. Copper with conductivity $\sigma = 5.997 \times 10^7$ S.m^{-1} was selected as the material for coil. The coil was driven by current $I_0 = 20$ A, the model was calculated in a frequency domain with $f = 60$ Hz. Mesh is a very important parameter of simulation. Proper size and shape of mesh elements influence the accuracy of solution; the finer the mesh elements, the better the solution accuracy. It is very important to find optimal number of elements. In our case the triangular mesh of 288500 elements with maximum size of 2 mm was created.

Inductance of coil solved by the software is $L = 24.04$ µH. Fig. 5 shows magnetic flux density. The magnetic field is strongest in the middle of the coil and decreases with increasing radius of the coil.

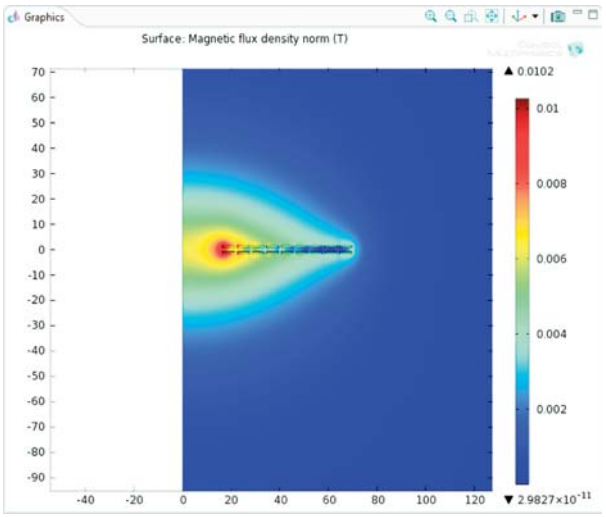

Fig. 5 Magnetic flux density

Experimental measurements

The experimental measurements were taken with a coil made on a printed circuit board. The values of inductance are listed in Table 2.

Experimental measurements of double-layer coil Tab. 2

Frequency	60	5 k	100 k	200 k	[Hz]
L	25.0	25.0	24.5	24.0	[µH]

It can be seen that the difference between the simulation model and experimental measurements at frequency $f = 60$ Hz is 3.84 %

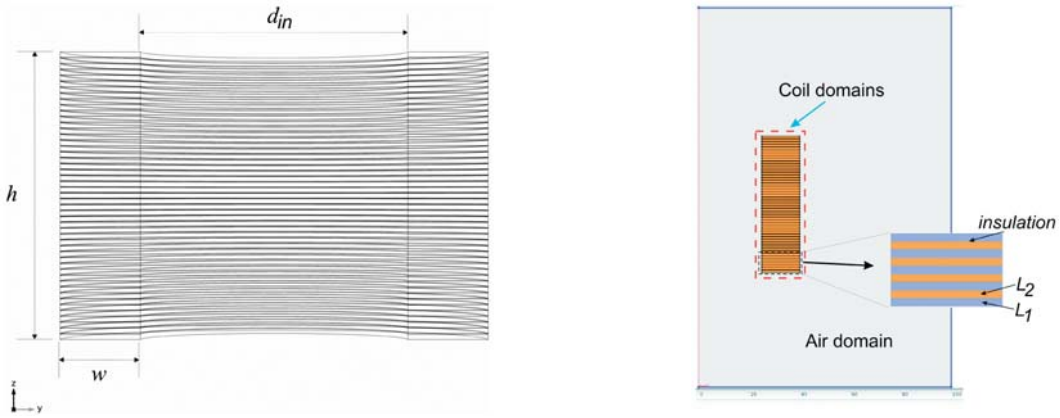

a) *b)*

Fig. 6 Working coil for IH application a) designed coil b) model of the coil in COMSOL

and difference between analytic and experimental measurements is 8.4 %.

4. Load coil for converter

The proposed coil for IH heating application is illustrated in Fig. 6a). The coil is made of two coils connected in series. The outer coil has 25 turns and between these turns the turns of the second coil are inserted. This coil has 24 turns. The thickness of insulation between each turn is $d_i = 0.1$ mm. This insulation serves as dielectric material.

Since the coil serves as a resonant circuit and no additional tuning capacitor is used the self-resonant frequency of the coil can be controlled by setting the number of turns of the coil, or by changing the cross section area of conductor, or distance between particular turns. Such circuit is shown in Fig. 7.

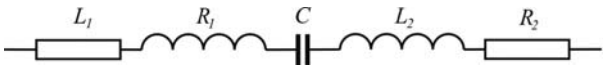

Fig. 7 Circuit of proposed coil

To achieve the desired resonant frequency the parameters such as inductance and resistance of both coils and the capacitance of the whole system have to be calculated. For this purpose the above mentioned approach for a double-layer coil can be used because the difference between the simulation and experimental measurement is 3.84 %.

The simulation model of this coil is depicted in Fig. 6b). In order to solve inductance in COMSOL, the magnetic fields toolbox (MF) was selected. Calculation was made in a frequency domain with frequency set at $f = 50$ kHz and the coils were driven by current $I = 10$ A. The simulation results for magnetic field are shown in Fig. 8.

Figures 8 shows the magnetic field created by current passing through both coil. Again, it can be seen that the magnetic field is strongest in the middle of the coil. The calculated parameters (at $f = 50$ kHz) of this coil are listed in Table 3.

Calculated parameters of designed coil — Tab. 3

Inductance of first coil	$L_1 = 35.5627$ µH
Resistance of first coil	$R_1 = 393.74$ mΩ
Inductance of second coil	$L_2 = 34.4492$ µH
Resistance of second coil	$R_2 = 416.55$ mΩ
Capacitance of coil	$C = 30.1397$ nF

The resonant frequency of this circuit is $f_0 = 109\,827$ Hz. The switching frequency of converter has to be set equal to resonant frequency of the circuit.

Simulation of converter

The theoretical waveforms of this topology that are obtained in PSPICE are shown in Fig. 9.

The switching frequency of converter was approximately $f_s = 110$ kHz. The control algorithm adjusts the switching of transistors when load current crosses zero value. It can be seen that the switching losses occur on the switches because the control of converter delays the turn on/off of transistors by approximately 2–3 µs. This problem can be removed by switching the transistors before the load current reaches zero.

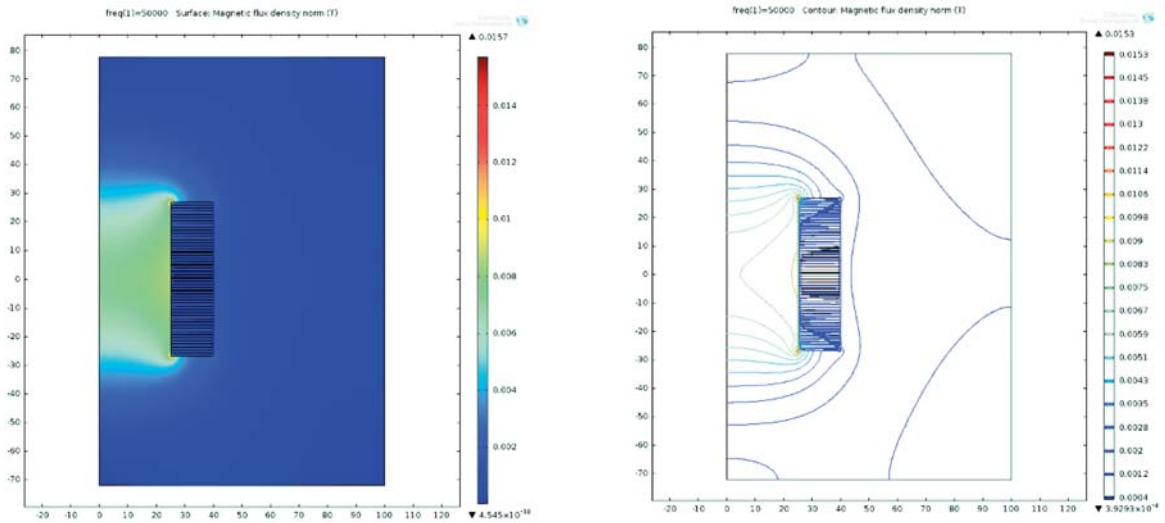

a) *b)*

Fig. 8 Magnetic flux density [T] a) surface b) contour

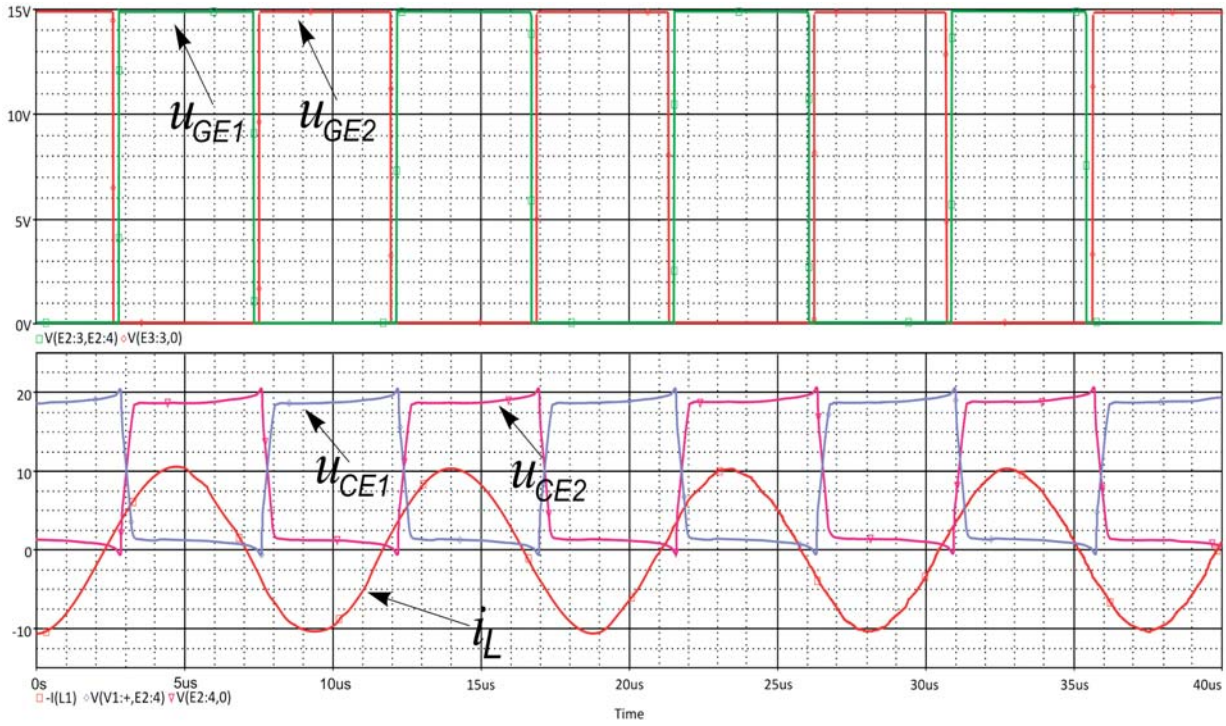

Fig. 9 Waveforms of converter in PSPICE

5. Conclusion

In the paper the half bridge series resonant converter and load coil for this converter were presented. The converter topology is simple configuration, ensures suitable control and offers the best overall performance with respect to converter utilization. In the paper the simulation waveforms of proposed converter were presented. With a suitable algorithm of control, the switching losses on transistor can be reduced and thus the efficiency of inverter can be increased. In the next part the load coil for the inverter was presented. The coil serves as a resonant circuit for converter. First, the verification model of spiral coil was created to verify the model accuracy with experimental measurement on a real double-layer coil built on a printed circuit board. Using this simulation the model of load coil for induction heating was created. The simulation provided us with parameters such as inductance, resistance and self-capacitance. The parameters were then used in simulation of the converter as load. It can be seen that the self-resonant frequency of coil was brought to approximately 100 kHz. The future work will be focused on building the system utilizing such designed coil and converter.

Acknowledgment

The paper has been prepared under the support of Slovak grant projects KEGA No. 005TUKE-4/2012.

References

[1] ZIN, S., SEMIATIN, S. L.: *Elements of Induction Heating: Design, Control, and Applications,* ASM International, 1988

[2] DOLEZEL, I., ULRYCH, B.: Induction Heating of Very Thin Metal Plates Modelled by Electric Vector Potential. *Communications - Scientific Letters of the University of Zilina,* No. 2A, 2011, pp. 19–24.

[3] MIURA, Y., HASHEM, M. H., HIRAKI, E., YASURI, K., IWAI, T., AHMED, N. A., LEE, H. W., NAKAOKA, M.: *A New Zero Current Switching Duty Cycle Controlled High Frequency Multi Resonant Inverter for Consumer Power Applications,* Electrical Machines and Systems, ICEMS 2005, Sept. 2005, pp. 1112–1117.

[4] KOVACOVA, I., KOVAC, D., VINCE, T.: *Electromagnetic Compatibility,* Published by TU FEI, Kosice, p. 138, 2009, ISBN 978-80-553-0150-1.

[5] KOVAC, D., KOVACOVA, I., MOLNAR, J.: *Electromagnetic Compatibility - Measurement,* Published by TU, FEI, pp. 72, 2009, ISBN 978-80-553-0151-8.

[6] SPANIK, P., KANDRAC, J., FRIVALDSKY, M., DRGONA, P.: Verification of Operation Modes of Designed LLC Resonant Converter, *Communications - Scientific Letters of the University of Zilina,* No. 2A, 2011, pp. 67–73
[7] Paese, E., Geier, M., Pacheco, J. L., Homrich, R. P., Ortiz, J. C. S.: *Mathematical Modeling of an Electromagnetic Forming System with Flat Spiral Coils as Actuator,* 4th Intern. Conference of High Speed forming, 2010, pp. 219–228.
[8] TANG, W., ZHU, Y., CHOW, Y. L.: *Inductance Calculation of Spiral Inductors in Different Shapes,* Proc. of Microwave Conference, 2005. APMC 2005. Asia-Pacific, vol. 5, pp. 3, 4–7, Dec. 2005.
[9] ZHAO, J.: *A New Calculation for Designing Multilayer Planar Spiral Inductors,* Electronics Design, Strategy, News, July 2010.
[10] KOVAC, D., OCILKA, M., VANSAC, M.: *Calculating of Inductance of Spiral Coil Using COMSOL Multiphysics:* ESMO 2012, Kremenchuk Mykhailo Ostrohradskyi National University, Ukraine, pp. 89–90, ISSN 2079-5106.

Michal Prazenica – Michal Kabasta – Slavomir Kascak – Juraj Koscelnik – Jozef Buday *

TWO-PHASE TWO-STAGE HF MATRIX CONVERTER FOR SUPPLYING TWO-PHASE MOTOR LOAD

This paper deals with the two-stage two-phase electronic systems with orthogonal output voltages and currents - DC/HF_AC/2AC. It also introduces the design and prototype of two-stage DC/HF_AC/2AC high frequency converter with two-phase orthogonal output using two single-phase matrix converters in full-bridge connection operated with the unipolar PWM. Simulation and experimental results of matrix converter for both steady and transient states for IM motors are given in the paper together with experimental verification under R-L load. The results confirm a very good time-waveform of the phase current and the system seems to be suitable for low-cost application in automotive/aerospace industries and application with high frequency voltage sources.

Keywords: *Matrix Converter, Two-Phase Induction Machine TPIM, Orthogonal System.*

1. Introduction – Single-phase HF Matrix converter

The matrix converters are among to direct converters – there is a direct conversion of the input voltage to the output voltage with another frequency. The use of high switching frequency reduces the effect of harmonic current back to the power grid. The bidirectional switches are necessary because they allow flow current in both directions. The basic connection of direct converter – matrix converter (3×3) is shown in Fig. 1a. From this scheme is derived the connection of single-phase matrix converter, Fig. 1b, [1] and [2].

The relations between output and input voltages, and between output currents and vo are:

$$\left[v_O(t)\right] = \left[M(t)\right]\cdot\left[v_I(t)\right] \quad \text{and}$$

$$\left[v_O(t)\right]' = \left[A\right]\cdot\left[i_O(t)\right] + \left[B\right]\cdot\left[v_O(t)\right] \qquad (1, 2)$$

where [*M*(*t*)] is modulation matrix, $m_{\alpha A}(t) = \frac{t_{\alpha A}}{T_{seq}}$ is modulation index, $t_{\alpha A}$ is time of switched state, with restrictions:

$$\sum_{K=a,b,c} m_{KA}(T) = \sum_{K=a,b,c} m_{KB}(T) = \sum_{K=a,b,c} m_{KC}(T) = 1 \qquad (3)$$

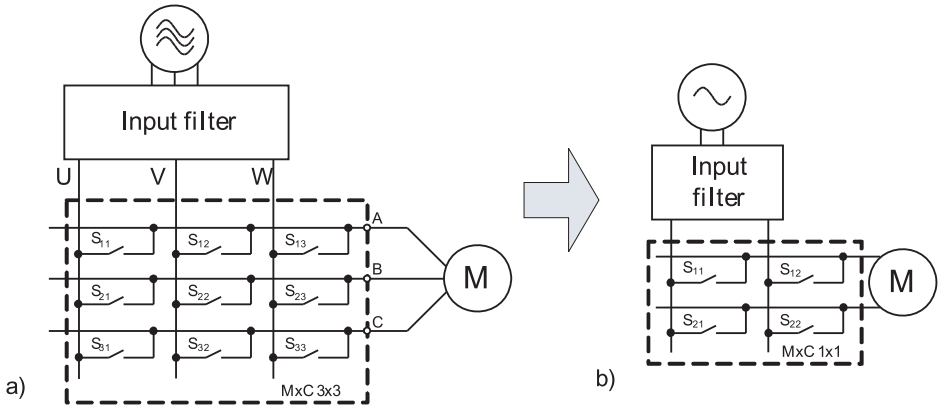

Fig. 1 Scheme of matrix converter (a) and single-phase derivation (b)

* **Michal Prazenica[1], Michal Kabasta[2], Slavomir Kascak[1], Juraj Koscelnik[1], Jozef Buday[3]**
[1] Department of Mechatronics and Electronics, Faculty Electrical Engineering, University of Zilina, Slovakia, E-mail: michal.prazenica@fel.uniza.sk
[2] ABB s.r.o., Ostrava, Czech Republic
[3] EVPU a.s., Nova Dubnica, Slovakia

2. Two-stage two-phase systems with HF AC interlink and matrix converters (DC/HF_AC/2AC)

Two-stage two-phase systems with HF AC interlink and matrix converters (DC/HF_AC/2AC) usually consist of a single-phase voltage inverter, AC interlink, HF transformer, 2-phase AC/AC converter and 2-phase AC motor. This is the best choice due to an AC interlink direct converter (cyclo or matrix converter). The system with matrix converter and high frequency AC interlink can generate two-phase orthogonal output with both the variable voltage and the frequency [3], [4] and [5]. The proposed scheme of two-stage two-phase converter system is shown in Fig. 2. The switching frequency of the converter is rather high (~ tens of kHz) and the second stage operates with twice switching frequency. Since the voltages of the matrix converter system should be orthogonal ones, the second phase converter is the same as the first one and its voltage is shifted by 90 degree. The switches of the inverter operate with hard commutation, the switches of matrix converters are partially soft-commutated in the zero-voltage instants of the AC voltage interlink using unipolar PWM [6]. Therefore, the expected efficiency of the system can be higher than usually by using the classical three-phase inverter .

3. Control of matrix converter with high-frequency input

The theoretical analysis of single-phase matrix converter has been done, e.g. [4] and [6]. The full-bridge converter provides unipolar and bipolar PWM control. Switching-pulse-width can be determined on the basis of the equivalence of average values of reference waveform and the result is the average value of positive or negative switching pulse area during switching period [7].

The switching instant is equal to:

$$t_s(k) = \frac{1}{U_{DC}} \cdot S_\Delta(k) \tag{4}$$

and the area under sine wave during k-switched interval $S_\Delta(k)$ is:

$$S_\Delta(k) = U_m \cdot \frac{m_f}{2\pi} \cdot \left[\cos\left(\frac{2\pi}{m_f} \cdot k\right) - \cos\left(\frac{2\pi}{m_f} \cdot (k+1)\right)\right] \tag{5}$$

The total harmonic distortion of the current is:

$$\frac{\sqrt{\sum I_v^2}}{I_1} = \sqrt{\frac{I^2 - I_1^2}{I_1^2}} = \sqrt{\left(\frac{I}{I_1}\right)^2 - 1} = \\ = \sqrt{\left[(8.34822/8.34386)2 - 1\right]} = \sim 2\% \tag{6}$$

Fourier analysis is useful and needed for the determination of total harmonic distortion of the phase current of the matrix converter. Unipolar switching strategy of one full-bridge matrix converter can be explained using Fig. 3 in greater details [4] and [8], [9], [10], [11].

4. Simulation Experiment

The simulation model of a two-stage converter was modeled in OrCAD programming environment, Fig. 4 and the simulation model of motor load was modeled in MatLab programming environment and they together were connected using Matlab SPLS. The simulation results of two-stage single-phase full-bridge matrix converter with R-L load are shown in Fig. 5. Both stages of converter are realized in full-bridge connection – (unipolar or bipolar PWM can be used). To protect the inverters against overvoltage surges in both stages the floating protection is used, which returns stored energy back to the DC-link and, thereby, improves the efficiency of the converter.

The simulation results show the response of the two-phase AS motor (230 V/150 W, 50 Hz, 2730 rpm) to step change of motor load (in open loop). At time $t = 0.2$ s the motor was loaded with torque ($M = 1$ Nm). The simulated waveforms during start-up of the two-phase induction machine (TPIM) supplied by two-phase switched voltage (*PWM*, $U_{DC} = 350$V, $f_{sw1} = 10$kHz, $f_{sw2} = 20$kHz, $U_{outAC} = 230$V, $f_{out} = 50$Hz) voltage shifted by 90 degree are depicted in Fig. 6.

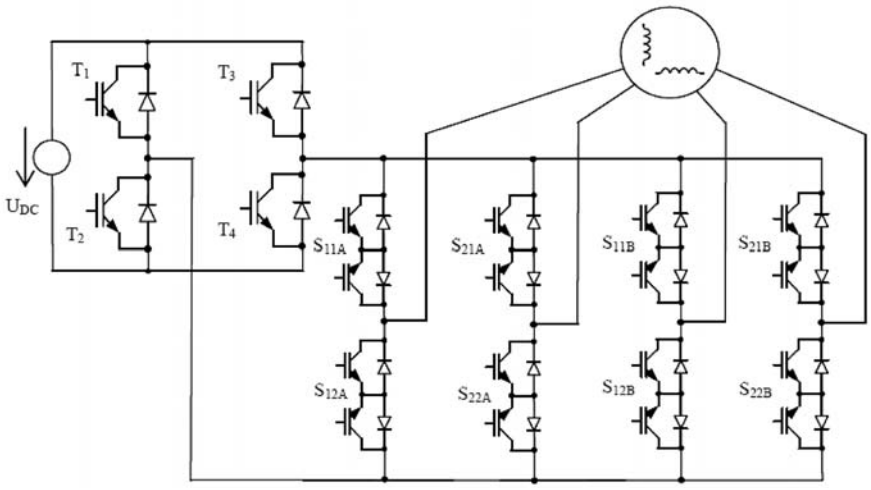

Fig. 2 Two-stage two-phase systems with HF AC interlink, matrix converters and motor load

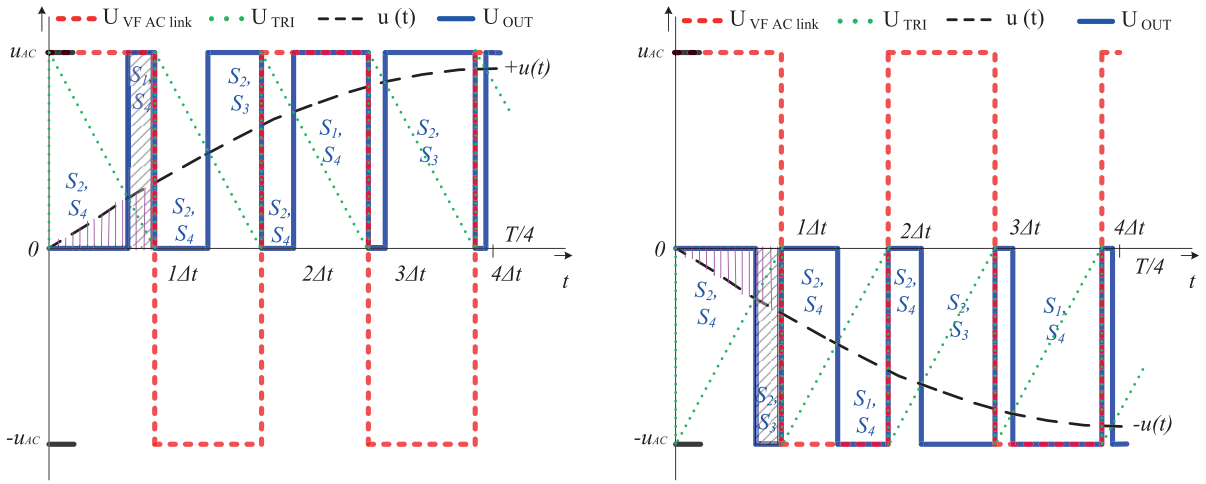

Fig. 3 Switching strategy for positive (a) and negative (b) half period of operation

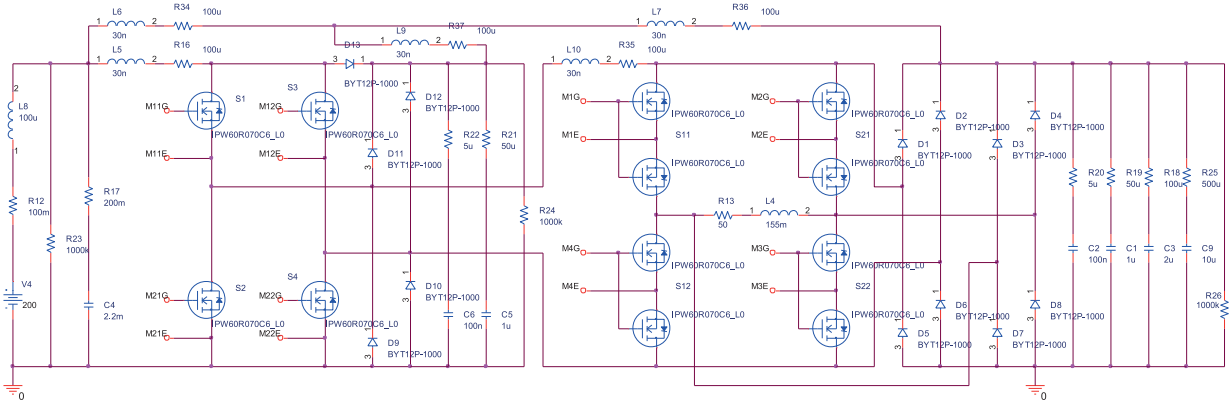

Fig. 4 Simulation model of two-stage single-phase converter

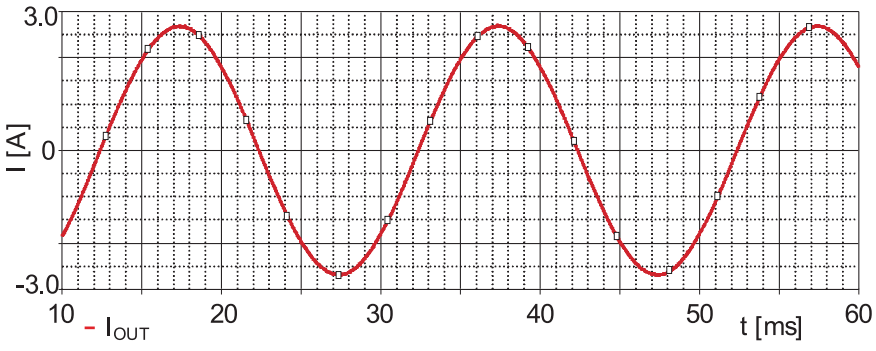

Fig. 5 Simulated waveform of output current of the single-phase converter under R-L load (U_{DC} = 350V, R = 10 Ω, L = 30 mH, f_{SW1} = 10 kHz, f_{SW2} = 20 kHz, f_{OUT} = 50 Hz)

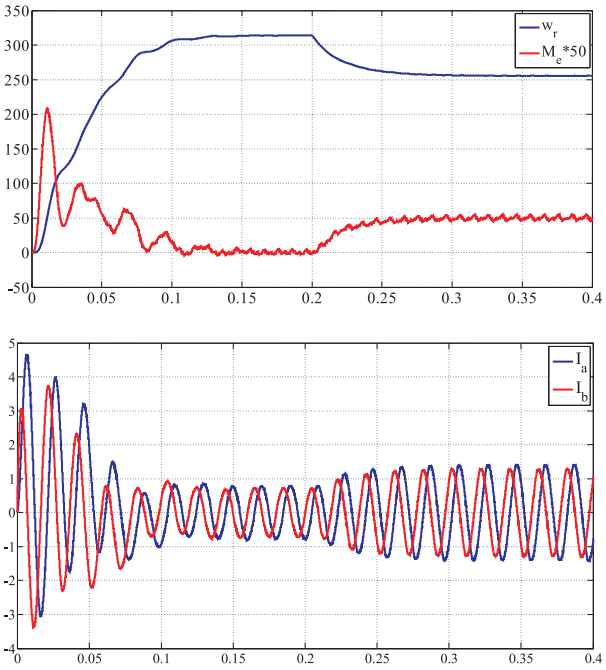

Fig. 6 Time-waveforms speed, torque and currents of TPIM during start-up

5. Experimental verification

The switching strategy described in previous chapter is used on the two-phase two-stage converter. The first stage was the voltage source inverter (VSI) and the second stage two matrix converters (MxC) were realized in a bridge connection without transformer in HF interlink. In this case the matrix converter works as a cyclo-converter. The block scheme and photo of converter are shown in Figs. 7 and 8.

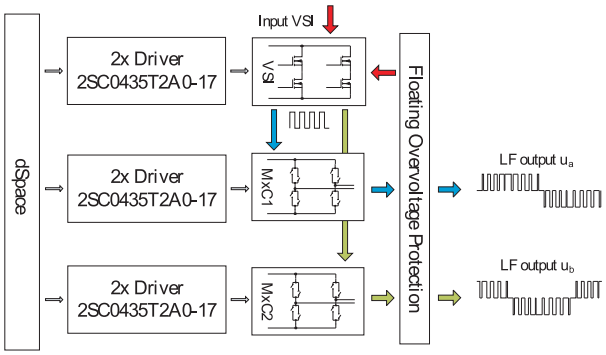

Fig. 7 Block scheme of two-stage two-phase converter with HF_AC interlink and matrix converters

Figure 9 depicts output voltages and currents from the matrix converter. Yellow and blue waveforms are output voltages. Purple and green wave forms are output currents. The output phase is shifted by 90 degrees. The waveforms of current in HF interlink and output currents are shown in Fig. 10.

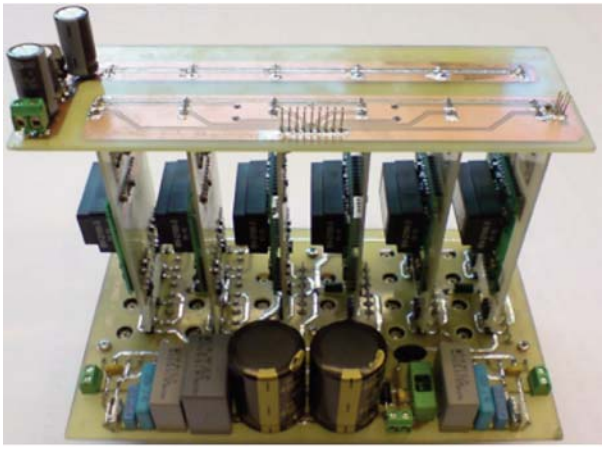

Fig. 8 Photography of complet two phase two stage converter with high-frequency AC link and ortogonal output

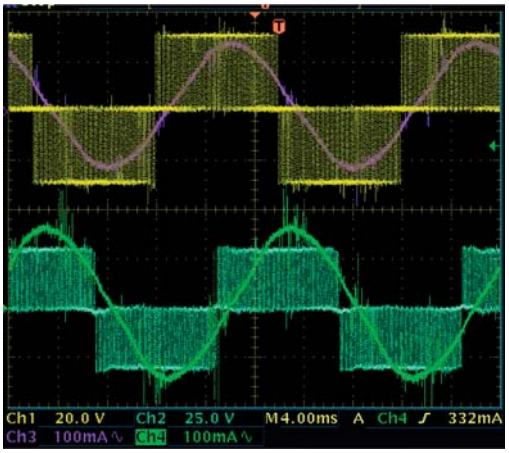

Fig. 9 Waveforms of output voltages and currents for unipolar control

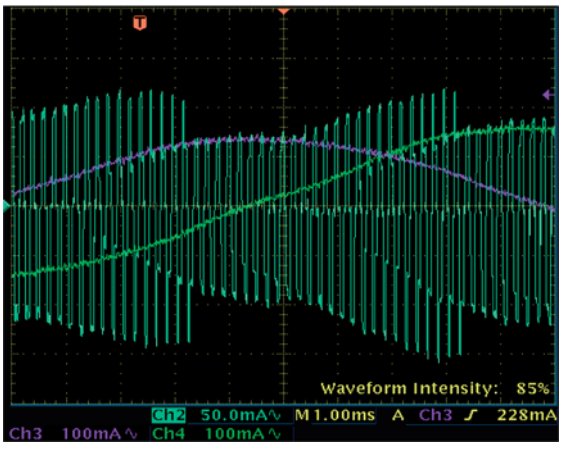

Fig. 10 Waveforms of output and HF interlink currents

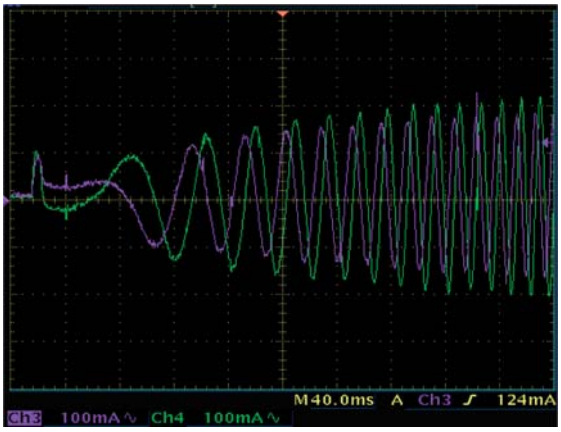

Fig. 11 Real stator currents of two-phase induction motor during start-up

From Fig. 11 we can see that the amplitudes of the stator current are not the same because the two-phase induction machine was unsymmetrical. Maximum efficiency of the proposed two-phase two-stage converter is nearly 94% at switching frequency 5kHz (in first-stage) and 10kHz (in second-stage).

6. Conclusion

The article shows a new concept of an electric drive system for electric vehicle and industrial application. It consists of the two-stage converter created by the single-phase converter and two single-phase matrix converters commutated by HF-AC input voltage, and two-phase induction TPIM or synchronous motors with PM. Simulation and experimental results showed good agreement between simulated and real output time waveforms. If this type of inverter is used to supply two-phase drive, high efficiency and very good mechanical parameters can be achieved (by two-phase – orthogonal supply of two-phase motor – TPIM, drive develops maximum torque).The maximum efficiency of the proposed two-phase two-stage converter is nearly 95% at switching frequency 1kHz (in first-stage) and 2kHz (in second-stage).

Acknowledgement(s)

The authors wish to thank for the financial support to R&D operational program Centre of excellence of power electronics systems and materials for their components No. OPVaV- 2008/2.1/01-SORO, ITMS 26220120046 funded by European regional development fund (ERDF) and APVV Agency for the project No. 0138/10.

References

[1] HAVRILA, R.: *Analysis and Design of Single Phase Fed Matrix Converter with DSP Implementation (in Slovak),* Medzinarodna studentska vedecka a odborna konferencia, Elektroenergetika a silnoprudova elektrotechnika'97, FEI STU : Bratislava, 1997, pp. 20–26

[2] DOBRUCKY, B., MARCOKOVA, M., KABASTA, M.: *Using Orthogonal Transform for Solution of Matrix Converter Power Circumstances in Mathematica® Environment,* Intern. Conference APLIMAT 2008, Bratislava, pp. 735–739, ISSN 1337-6365

[3] DOBRUCKY, B., BENOVA, M., FRIVALDSKY, M., PRAZENICA, M.: Choosing Modulation Strategies for 2-stage Combine LLC- and Direct Converter – Modelling, Simulation, Application, *Communications - Scientific Letters of the University of Zilina,* vol. 13, No. 2A, 2011, pp. 25–31, ISSN 1335-4205

[4] BENOVA, M., DOBRUCKY, B., SZYCHTA E., PRAZENICA, M.: Modelling and Simulation of HF Half-Bridge Matrix Converter System in Frequency Domain, *Logistyka,* 2009, No. 6, p. 87. ISSN 1231–5478

[5] DOBRUCKY, B., BENOVA, M., SPANIK, P.: Using Complex Conjugated Magnitudes – and Orthogonal Park/Clarke Transformation Methods of DC/AC/AC Frequency Converter, *Electronics and Electrical Engineering,* No. 5 (93), pp. 29–34, Kaunas, 2009, ISSN 1392–1215.

[6] DOBRUCKY, B., BENOVA, M., MARCOKOVA, M., SUL, R.: Analysis of Bipolar PWM Functions Using Discrete Complex Fourier Transform in Matlab, Proc. of the 17th Technical Computing Prague Conf., Prague, Nov. 2009, p. 22, ISBN 978-80-7080-733-0

[7] DOBRUCKY, B., MARCOKOVA, M., POKORNY, M., SUL, R: *Using Orthogonal- and Discrete Transform for Single-Phase PES Transients - a New Approach,* Proc. of the 27th IASTED Intern. Conference Innsbruck, February 2008, pp. 60–65, ISBN 978-0-88986-711

[8] ZASKALICKY, P., DOBRUCKY, B.: Complex Fourier–series mathematical model of a three-phase inverter with Improved PWM output voltage control; *Elektronika ir Elektrotechnika*, No. 7(123), 2012, pp.65–68, ISSN 1392–1215.

[9] ZASKALICKA, M., ZASKALICKY, P., BENOVA, M., ABDALMULA, M. A. R., DOBRUCKY, B.: Analysis of Complex Time Function of Converter Output Quantities Using Complex Fourier Transform/Series. *Communications - Scientific Letters of the University of Zilina,* No. 1(12), pp. 23–30, 2010, ISSN 1335-4205.

[10] DRGONA, P., PRIKOPOVA, A., FRIVALDSKY, M., PRIECINSKY, M.: Simulation Based Method for Design and Application of Digital Control System, *Communications - Scientific Letters of the University of Zilina,* vol. 13, No. 2A, 2011, ISSN 1335-4205.

[11] GANG LI, KAIN SUN, LIPEI HUANG,: A Novel Algorithm of Space Vector Modulated Two-Stage Matrix Converter, International Cobference on Electrical Machines and Systems – ICEMS 2008, pp 1316–1320, ISBN 978-1-4244-3826-6.

Peter Girovsky – Jaroslava Zilkova – Jaroslav Timko – Jan Girovsky *

AN ADAPTIVE NEUROCONTROLLER FOR INDUCTION MOTORS

The paper is focused on presenting possibilities of applying artificial neural networks (ANN) at creating a speed controller of an induction motor drive. The presented method of control takes advantage of approximating properties of multi-layer feedforward networks. The availability of the proposed neurocontroller is verified through the Matlab simulation. The effectiveness of the controller is demonstrated for different operating conditions and motor parameter changes of the drive system.

Keywords: *Neural network, control, induction motor.*

I. Introduction

Most of the technical systems in practice are non-linear. However, many systems can be represented without any significant loss of accuracy by an equivalent linear representation. Control designs based on system linearization are a widely applied technique in the industry. Other systems are increasingly characterized by complex non-linear dynamics (e.g. high non-linearity, abrupt parameter variations, external disturbances etc.). The important non-linear diversity is the main reason why no systematic and generally applicable theory for non-linear control design has been developed yet. It is the ability of the artificial neural networks to model non-linear systems that can be the most readily exploited in the synthesis of non-linear controllers. Neural networks have been used to formulate a variety of control strategies [1] [5].

Two basic design approaches are [2]:

- direct inverse control – it uses a neural inverse model of the system as a controller,
- indirect design – the controller uses a neural network to predict the system output.

Different structures of neurocontrollers for control of non/linear systems, especially induction motor drive have been presented [6] – [13].

We are interested in different already existing methods used to develop a neural controller based on an inverse model of a system. The main idea of the design was to design an adaptive neuro controller of induction motor only on based input-output motor parameters. These parameters were defined as the stator voltages and currents and rotor speed.

Following part of the paper is focused on explaining the method and demonstration the use of ANN for purposes of controlling in simulation studies for a squirrel-cage induction motor drive. Last part of the paper demonstrates sensitivity of the speed controller to motor parameters changes.

2. Design of the controller

In real life, the most frequently used are two concepts of inverse neural model architecture: the general training and specialized training architecture [2]. The latter architecture brings some advantages when compared with the former one: The method is intended directly for controlling and in the case of multidimensional systems, as a drive with an induction motor, the model can closely simulate a real system.

Multi-layer neural networks (MLP) can be utilized when creating a system inverse neural model. The use of the MLP type static neural networks presents the simplest solution, however the representation of the system dynamic remains problematic with this neural model. The application of a MLP type neural network with time delaying of the input layer signals can present the solution for introducing the process dynamics into MLP type static neural network. The solution falls among the simplest ones, and the advantage of utilizing this network type rests with the opportunity of its training by traditional backpropagation algorithm for multi-layer networks.

The main requirement we have specified is maintaining the desired speed of the induction motor. Considered for the neurocontroller output were the voltage components that would present

* **Peter Girovsky[1], Jaroslava Zilkova[1], Jaroslav Timko[1], Jan Girovsky[2]**
[1] Department of Electrical Drives and Mechatronics, Technical University of Kosice, Slovakia, E-mail: peter.girovsky@tuke.sk
[2] Laboratory for Micro and Nanotechnology, Paul Scherrer Institut, Villigen, Switzerland

an action intervention for PWM modulation, which would eventually produce the stator voltage desired values from the mains voltage (rectified via using an uncontrolled rectifier). Since the neurocontroller output in such a structure is not directly equal to voltage fed into the motor we have abandoned the idea to establish an accurate inverse model; considered for input quantity of the quasi-inverse neural model were rather the desired and at a time also real (measured) motor speeds (Fig. 1).

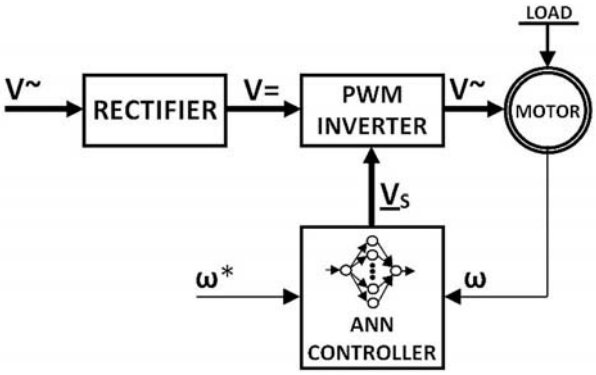

Fig. 1 ANN induction motor control scheme

The design of the neurocontroller is based rightly on known values of these speeds. A typical technique for control synthesis purposes is based on using a description of the induction motor in rotating reference frames (*x, y*). The use of such rotating reference frames has the benefit of simplifying the model of the motor from the point of view of controller design. In this section design of the neural controller will be presented.

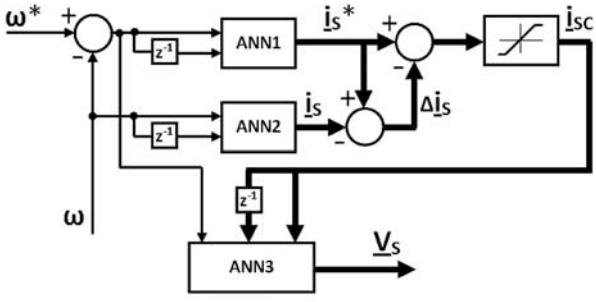

Fig. 2 Block scheme of the ANN controller

The neurocontroller (Fig. 2) consists of three multilayer perceptron (MLP) networks with backpropagation learning algorithm.

The first subsystem ANN1 of the neurocontroller serves for desired current components reconstruction and the second subsystem, ANN2 serves for real current components identification. To reduce the value of the control current in control structure was used saturation block.

The third of them, ANN3 serves for corresponding voltage components reconstruction for PWM converter. These voltage components present action intervention for PWM modulation that would make up the desired stator voltage values from the mains voltage (rectified using an uncontrolled rectifier). The overall control structure is shown in Fig. 1.

The first and second neural networks are identical. Their inputs are values of angular speed, expected and actual, in *k*-th and $(k-1)$th step. The structure of the ANNs is shown in Fig. 3.

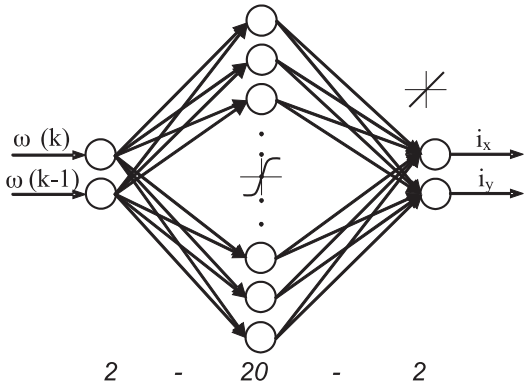

Fig. 3 The structure of the ANN1 and ANN2

The neural networks are trained to approximate the time-varying function of f and to give the ANN estimated one-step-ahead predicted stator current components:

$$\begin{aligned} i_{sx}^{*}(k+1) &= f\left[\omega^{*}(k), \omega^{*}(k-1), w\right], \\ i_{sy}^{*}(k+1) &= f\left[\omega^{*}(k), \omega^{*}(k-1), w\right], \end{aligned} \tag{1}$$

and

$$\begin{aligned} i_{sx}(k+1) &= f\left[\omega(k), \omega(k-1), w\right], \\ i_{sy}(k+1) &= f\left[\omega(k), \omega(k-1), w\right]. \end{aligned} \tag{2}$$

Reconstructed actual stator current (1) corrects desired value of current from the first ANN (2):

$$\Delta i_s(k+1) = i_s^{*}(k+1) - i_s(k+1) \tag{3}$$

Resulting signal of the correction:

$$i_{sc}(k+1) = i_s^{*}(k+1) + \Delta i_s(k+1) \tag{4}$$

in *k*-th and $(k-1)$th steps and the desired speed value present inputs to the third ANN, which generates appropriate voltage values for PWM converter:

$$u_s(k+1) = g\left[i_{sc}(k+1), i_{sc}(k), \omega^{*}, w\right] \tag{5}$$

The structure of the ANN3 is shown in Fig. 4.

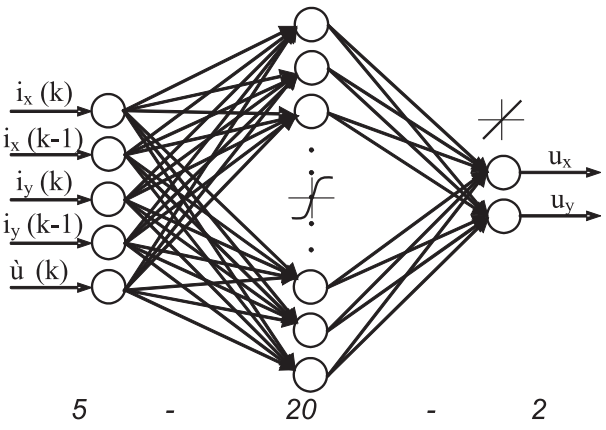

Fig. 4 The structure of the ANN3

MLP networks are used for all *f* and *g* approximations. The number of inputs to each of them is determined by the relation (1), (2) or (5). Twenty hidden neurons in one hidden layer of every neural subsystem employ the hyperbolic tangent functions.

All the networks are trained off-line in order to minimise the control performance. Training patterns for an ANN controller were prepared by numerical simulations of the induction motor model with help of Matlab/Simulink and Neural Network Toolbox. In simulations the nominal data of a 3 kW induction motor were used. The backpropagation training algorithm with Levenberg-Marquardt's modification was used for the training procedures.

3. Simulation results

Presented in this section will be the results simulated in MATLAB environment for given connection of the control diagram shown in Fig. 1, where the designed neural controller was implemented. The testing of the neural controller was performed on the induction motor with the following motor parameters:

$U = 220$ V/50 Hz, $I_N = 6.9$ A, $P = 3$ kW, $n_N = 1420$ rpm,

$R_1 = 1.81\ \Omega$, $R_2 = 1.91\ \Omega$, $L_{1\sigma} = L_{2\sigma} = 0.00885$H,

$L_h = 0.184$H, $p_p = 2$, $T_N = 20.17$ Nm, $J_N = 0.1$ kgm^2,

where:
U – voltage
I_N – nominal current
P_N – nominal power
nN – nominal speed
R_1, R_2 – stator and rotor resistance
$L_{1\sigma}$, $L_{2\sigma}$, L_h – stator stray, rotor stray and main inductance
p_p – number of pole pairs
T_N – nominal torque
J_N – nominal moment of inertia

In the following figures the speed control quality is presented. The neural speed controller was trained in the wide range of speed and load torque changes based on the simultation results obtained for induction motor model. Then the trained controller was tested for speed reference signal different than the one used in the training procedures. These test signals together with results of simulations are presented in Figs. 5 and 6. The characteristics were obtained for nominal parameters of the induction motor.

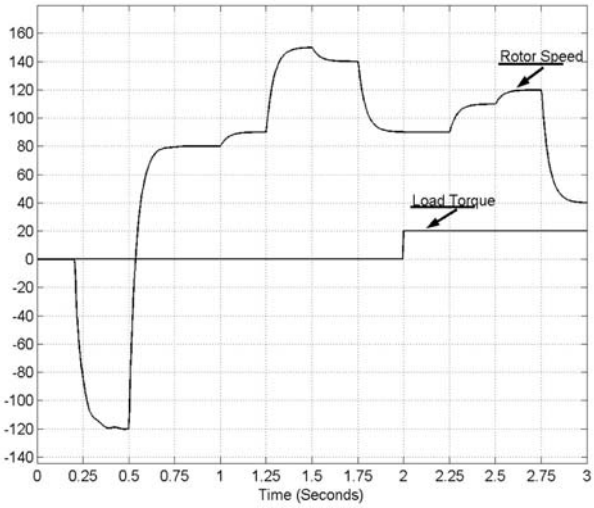

Fig. 5 The course of angular speed at changes speed reference value and at change of load torque

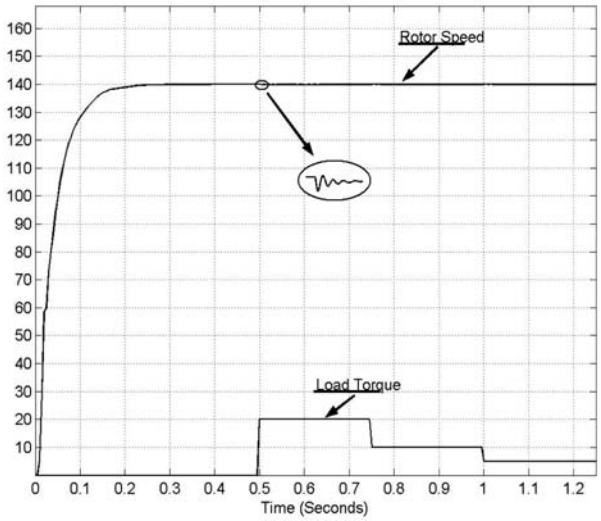

Fig. 6 The course of motor speed at load test

A. Sensitivity of the speed controller to motor parameter changes

The trained controller was tested also for changed motor parameters different than the one used in the training procedures. These test signals together with results of simulations are presented in Figs. 7, 8 and 9.

Figure 7 illustrates the courses of the motor speed if the moment of inertia J is equal to: $J1$ for the nominal value, $J2$ for 200% and $J3$ for 300% of the nominal value of moment of inertia.

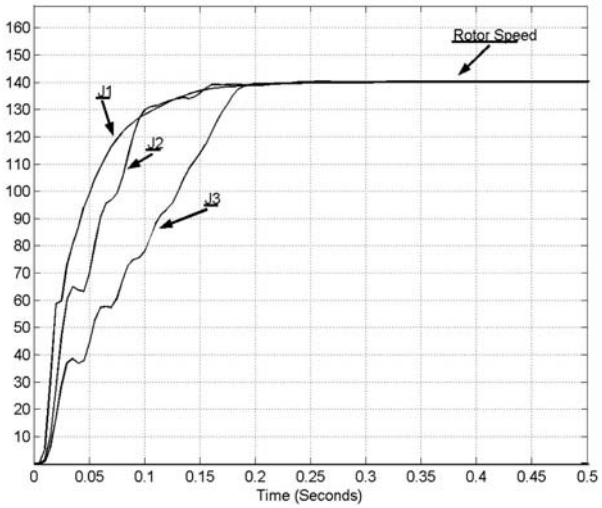

Fig. 7 The courses of the angular motor speed for moment of inertia changes

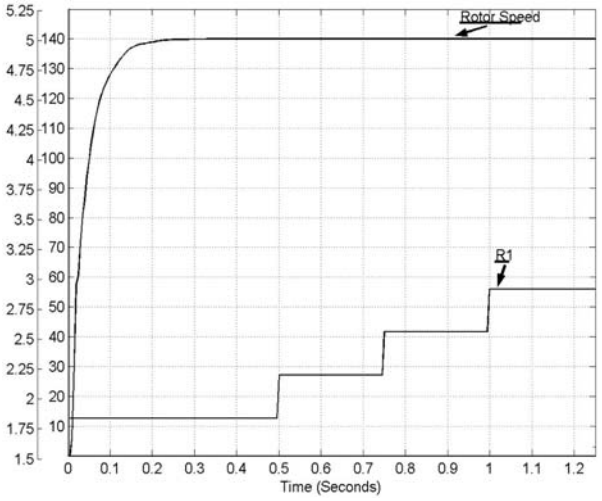

Fig. 8 The course of the motor speed for stator resistance changes

Figure 8 illustrates the courses of the motor speed if the stator resistance R_1 is gradually changed from nominal value in $t = 0{,}5$ s to the 160% of nominal value R_1.

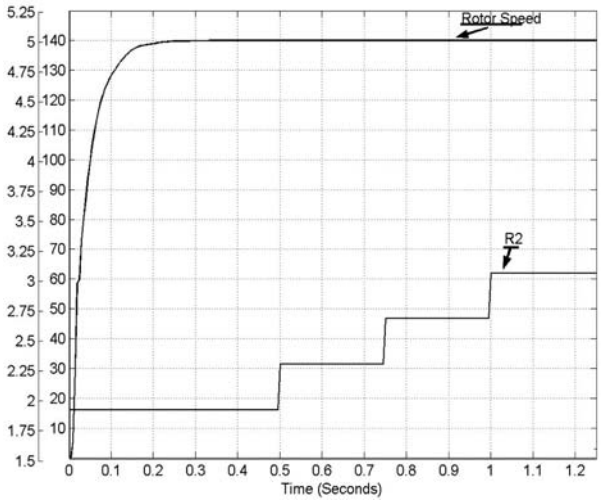

Fig. 9 The course of the motor speed for rotor resistance changes

Figure 9 illustrates the courses of the motor speed if the rotor resistance R_2 is gradually changed from nominal value in $t = 0.5$ s to the 160% of nominal value R_2

4. Conclusion

The paper deals with the design of a neural controller for induction motor drive control based on a quasi-inverse model of the system. The design of the controller is based on sensor information relating to angular speed of an induction motor. The control task is to reach the motor desired angular speed. The neurocontroller consists of three feedforward neural networks with Levenberg-Marquardt modification of backpropagation learning algorithm. Hidden neurons in each hidden layer of neural subsystems employ the hyperbolic tangent functions. All the networks are trained off-line mode in order to minimise the control performance. Training samples for training of the ANN subsystems were obtained via simulation of an induction motor model in MATLAB environment. First subsystem of the neurocontroller serves for reconstruction of desired current components and the second subsystem serves for reconstruction of real current components. The third of them serves for corresponding voltage components reconstruction for PWM converter. The controller was tested on motor parameters changes, like moment of inertia, stator and rotor resistances.

Obtained simulation results demonstrated good performance of this method.

Acknowledgement

The authors wish to thank for the support to the R&D operational program Centre of excellence of power electronics systems and materials for their components No. OPVaV-2008/2.1/01-SORO, ITMS 26220120003 funded by European regional development fund (ERDF).

Thanks for the support to project APVV-0185-10.

References

[1] LEVIN, A. U., NARENDA, K. S.: Control of Nonlinear Dynamical Systems Using Neural Networks: Controllability and Stabilization. *IEEE Transactions on Neural Networks,* vol. 4, 1993, pp.192–206.

[2] LEVIN, A. U., NARENDA, K. S.: Control of Nonlinear Dynamical Systems Using Neural Networks – Part II: Observability, Identification and Control. *IEEE Transactions on Neural Networks,* vol. 7, 1996, pp. 30–42.

[3] VAS, P.: *Artificial Intelligence Based Electrical Machines and Drives.* Oxford : Oxford University Press, 1999.

[4] ZILKOVA, J.: *Artificial Neural Networks in Process Control,* Kosice : Mercury-Smekal, 2001, 49 p., ISBN 80-89061-15-X.

[5] BORBEL, M., ZILKOVA, J., TIMKO, J.: *Inverse Control of the DC Motor Using Neural Network (in Slovak),* Proc. SYMEP, Praha, 2004, p. 5.

[6] BRDYS, M. A., KULAWSKI, G. J.: Dynamic Neural Controllers for Induction Motor, *IEEE Transactions on Neural Networks,* vol. 10, 1999, No. 2, pp. 340–355.

[7] BURTON, B., HARLEY, R. G., DIANA, G., RODGERSON, J. L.: Implementation of a Neural Network to Adaptively Identify and Control VSI-Fed Induction Motor Stator Currents, *IEEE Transaction on Industry Applications,* vol. 34, No. 3, 1998.

[8] GIROVSKY, P., TIMKO, J., ZILKOVA, J.: Modeling of Neural Network Speed Estimator for Field Oriented Control of Induction Motor, Metalurgija, vol. 49, No. 2, 2010, pp. 231-235.

[9] KUCHAR, M., BRANDSTETTER, P., KADUCH, M.: *Sensorless Induction Motor Drive with Neural Network,* IEEE Annu. PowerElec. Specialists Conf., 2004, pp. 3301–3305.

[10] TIMKO, J., ZILKOVA, J., GIROVSKY, P.: *Modeling and Control of Electric Drives Using Neural Networks (in Slovak),* Kosice : C-press, 2009. 202 p., ISBN 978-80-8086-124-7.

[11] VITTEK, J., BRIS, P., STULRAJTER, M., PACHA, M.: *Chattering Free Sliding Mode Control Law for Position Control of the Drive Employing Induction Motor,* Power Engineering Conference 2008, AUPEC '08, Australasian Universities, 2008, pp. 1–6, 14-17.

[12] WISHART, M., HARLEY, T. R. G.: Identification and Control of Induction Machines Using Artificial Neural Networks, *IEEE Transaction on Industry Applications,* vol. 31, No. 3, 1995.

[13] VITTEK, J., ALTUS, J., BEDNARIK, B., TABACEK, R., DODDS, S. J., PERRYMAN, R.: Research of New Sensorless Speed Controlled Drives with Induction Motors for Traction Applications, *Communications - Scientific Letters of the University of Zilina,* No. 2–3, 2001, ISSN 1335-4205.

Pavel Zaskalicky – Ludek Schreier *

USING FOURIER ANALYSIS FOR TORQUE ESTIMATION OF TWO-PHASE INDUCTION MOTOR SUPPLIED BY HALF-BRIDGE INVERTER WITH PWM CONTROL

The paper deals with the steady state analysis of electromagnetic torque ripples of a two-phase induction machine, which is supplied by a half-bridge connected inverter with IGBT transistors. The inverter output voltage is controlled by a PWM of the input DC voltage. The complex Fourier series analysis of the inverter output voltage was made to obtain the spectrum of voltage-supply harmonics. Particular voltage harmonics were applied to the two-phase induction machine numerical model so that the electromagnetic torque waveforms for various operation conditions were obtained.

Keywords: *Two-phase inverter, Induction machine, Torque ripple, Fourier series, Mathematical model.*

1. Introduction

Electrical low-power drives (around 100W) with a single-phase induction motors, used in different appliances and industrial devices are at present increasingly replaced by two-phase motors.

The characteristics of two-phase motors do not substantially differ from those of three-phase motors. Their advantage is simpler winding, which is of great importance for automated production. The two-phase motors are manufactured as either cage induction motors or permanent magnet synchronous motors. They are used e.g. as drives of pumps in washing machines and dishwashers and as drives of circulating pumps for central heating. A permanent magnet is water and lye resistant, which makes it possible to produce an absolutely waterproof pump. The two-phase voltage is generated by converters supplied from a single-phase network.

The use of a two-phase motor has several advantages. The stator winding has the simplest form. Three shifted coil windings constitute one phase winding. The stator windings can be configured in either a serial or parallel two-phase system.

Both windings are usually identical. The windings which form one phase are connected in such a way as to induce opposite magnetic polarity.

Figure 1 illustrates a prototype of a two-phase induction motor.

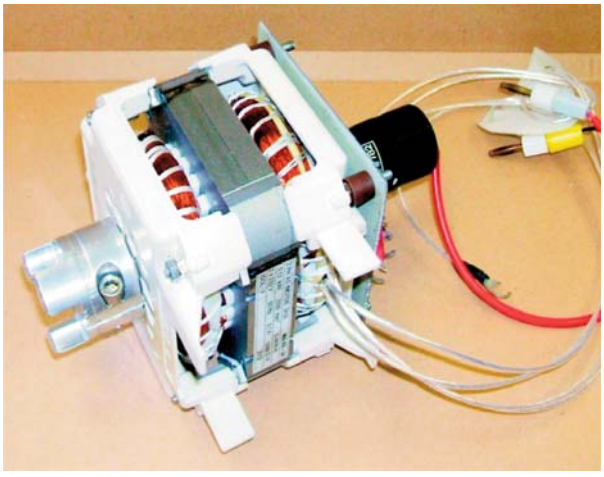

Fig. 1 Prototype of a two-phase induction motor

2. Mathematical model of the supply converter

The analysis of the inverter operation at steady state was made under the following simplifying conditions:

- The power switch can handle unlimited currents and can block unlimited voltages.
- The voltage drop across the switch and leakage current through switch are zero.

* **Pavel Zaskalicky[1], Ludek Schreier[2]**
[1] Department of Electrical Engineering and Mechatronic, Faculty of Electrical Engineering and Informatics, Technical University of Kosice, Slovakia, E-mail: pavel.zaskalicky@tuke.sk
[2] Department of Electrical Engineering and Electrophysics, Institute of Thermomechanics AS CR, v.v.i, Praha, Czech Republic

- The switch is turned on and off with no rise and fall times.
- The sufficient value of capacitance of the input voltage capacitor divider makes it possible to consider a constant DC voltage of the converter input.

These assumptions help us simply analyse a power circuit and set up a mathematical model of the inverter at steady state. Figure 2 shows a two-phase converter circuit configuration.

The output voltage level of the inverter can be controlled by reducing the DC source voltage. Another way of the voltage control is notching, when the transistors in the inverter circuit are turned on and off, which results in producing zero periods of equal lengths.

The improvement to the notched waveform means that the interval when the transistors are switched on is the longest at the peak of the wave. This way of control is known as the pulse width modulation (PWM).

It can be observed that the length of each pulse corresponds approximately to the area under the sine-wave between the adjacent mid-points when the transistors are switched off. The pulse width modulated wave has much lower harmonic content than waveform modulated in a different way

If the desired reference voltage is sine wave, two parameters define the control [1]:

- *Coefficient of the modulation m* – equal to the ratio of the modulation and reference frequency.
- *Voltage control coefficient r* – equal to the ratio of the desired voltage amplitude and the DC supply voltage.

Mostly, the synchronous modulation is used. In synchronous modulation, the modulation frequency is an integer multiple of the frequency of the reference sine wave.

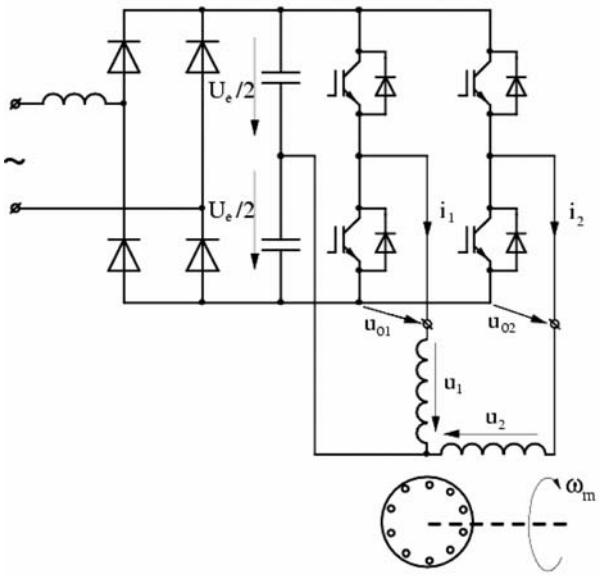

Fig. 2 Supply converter circuit layout

Generally, to control the inverter, a numerical control device is used. The turn on (α) and turn off (β) angles are calculated on the basis of the reference sine wave. That means the reference sine wave is replaced by discrete voltage impulses. If the coefficient of modulation *m* is sufficiently great, the difference between real values and discrete values is negligible.

The inverter output voltage of the first branch can be mathematically expressed as a complex Fourier series in the form [2], [3] and [4]:

$$u_{01} = U_e \sum_{k=-\infty}^{\infty} \sum_{n=1}^{m} c_{01n} e^{jk\theta} \tag{1}$$

with Fourier coefficients:

$$\begin{cases} c_{01n} = \dfrac{1}{j2k\pi}\left(e^{-jk\alpha_{01n}} - e^{-jk\beta_{01n}}\right) & for\ k \neq 0 \\ c_{01n} = \dfrac{\beta_{01n} - \alpha_{01n}}{2\pi} & for\ k = 0 \end{cases}$$

Similarly for the second branch:

$$u_{02} = U_e \sum_{k=-\infty}^{\infty} \sum_{n=1}^{m} c_{02n} e^{jk\theta} \tag{2}$$

with Fourier coefficients:

$$\begin{cases} c_{02n} = \dfrac{1}{j2k\pi}\left(e^{-jk\alpha_{02n}} - e^{-jk\beta_{02n}}\right) & for\ k \neq 0 \\ c_{02n} = \dfrac{\beta_{02n} - \alpha_{02n}}{2\pi} & for\ k = 0 \end{cases}$$

Calculated waveforms of the branch voltages are unipolar. Based on the voltage equation, the phase voltages are given as a difference between the branch voltages and the voltage of the capacitor divider:

$$\begin{aligned} u_1 &= u_{01} - \frac{U_e}{2} = U_e \sum_{k=-\infty}^{\infty} \sum_{n=1}^{m} c_{01n} e^{jk\theta} - \frac{U_e}{2}; \\ u_2 &= u_{02} - \frac{U_e}{2} = U_e \sum_{k=-\infty}^{\infty} \sum_{n=1}^{m} c_{02n} e^{jk\theta} - \frac{U_e}{2} \end{aligned} \tag{3}$$

In Fig. 3, the phase voltage waveforms are shown. The voltages are bi-polar with amplitude equal to half of DC input voltage [5].

3. Harmonic analysis of the supply voltages

On the basis of Fourier series formulas of the supply voltages, a harmonic analysis of the supply waveforms can be made.

The amplitude of each harmonic is calculated on the basis of equations (3). The amplitude of kth harmonic is given:

$$A_k = \sum_{n=1}^{m} \left(c_{01n}^{k} + c_{01n}^{-k}\right) \tag{4}$$

Figure 4 depicts a harmonic analysis of the PWM output voltage for frequency of and modulation frequency of .

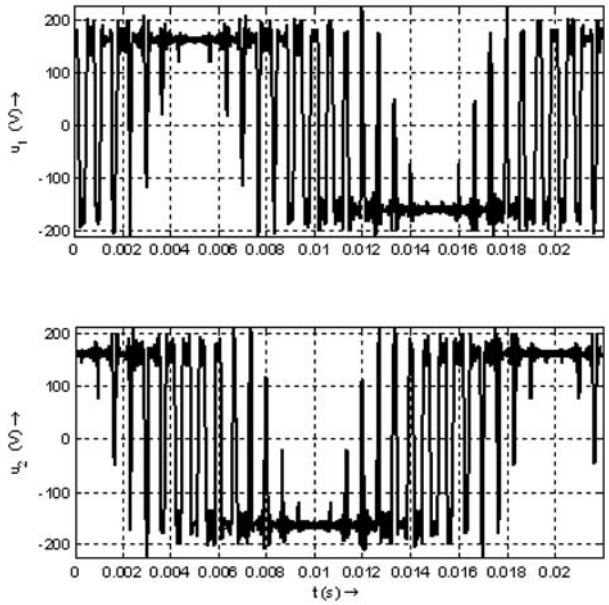

Fig. 3 Waveforms of the phase voltages

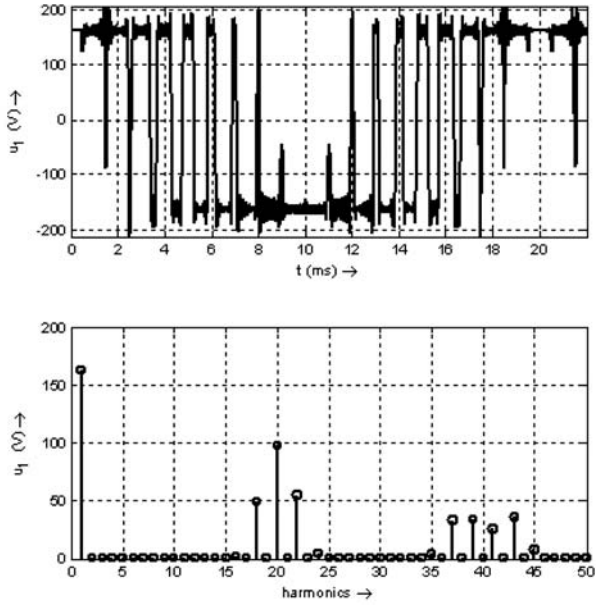

Fig. 4 Harmonic analysis

In Table 1, the parameters of the main harmonics are given.

The main harmonics Table 1

Harmonic	Amplitude	1st phase	2nd phase
1	162.3 V	cos	sin
18	48.4 V	-cos	cos
20	97.8 V	cos	cos
22	54.2 V	-cos	cos
37	32.6 V	cos	sin
39	33.3 V	-cos	sin
41	25.7 V	-cos	-sin
43	25.4 V	-cos	-sin

4. Mathematical model of a two-phase induction motor

A mathematical model of a two-phase induction machine can be easily derived from the equations of a single-phase motor with an auxiliary winding [6].

In the case of a two-phase machine, both the stator windings are mutually rotated by 90 electric degrees and have the same number of turns. On condition that the real axis of the system of coordinates coincides with the axis of the winding 1, it can be written as

$$u_1 = R_S i_1 + L_S \frac{di_1}{dt} + L_h \frac{di_{R\lambda\alpha}}{dt} \tag{5}$$

The axis of the winding 2 coincides with the imaginary axis and is described by the equation

$$u_2 = R_S i_2 + L_S \frac{di_2}{dt} + L_h \frac{di_{R\lambda\alpha}}{dt} \tag{6}$$

A cage rotor can be described by equations

$$0 = R_{RS} i_{R\lambda\alpha} + L_{RS} \frac{di_{R\lambda\alpha}}{dt} + p\omega_m \left(L_{RS} i_{R\lambda\beta} + L_h i_2\right) \tag{7}$$

$$0 = R_{RS} i_{R\lambda\alpha} + L_{RS} \frac{di_{R\lambda\alpha}}{dt} - p\omega_m \left(L_{RS} i_{R\lambda\alpha} + L_h i_1\right) \tag{8}$$

Torque T in the air gap is given by the equation

$$T = pL_h \left(i_{R\lambda\beta} i_1 - i_{R\lambda\alpha} i_2\right) \tag{9}$$

Equations (5) to (9) are valid under assumptions currently considered in the theory of electrical machines.

Particular symbols represent:
R_S stator resistance,
R_{RS} rotor resistance,
L_S stator inductance,
L_{RS} rotor inductance,
L_h main inductance,
p number of pole pairs,
u_1 and u_2 stator voltages
$i_{R\lambda\alpha}$ and $i_{R\lambda\alpha}$ real imaginary parts of the spatial vector of rotor currents and
ω_m mechanical speed.

Subscript S at rotor parameters means that rotor resistance and inductance were referred to the effective number of stator turns. Subscript λ at the real α and imaginary β components of rotor

currents means that these quantities were referred to the effective number of stator turns and transformed to the stator coordinate system.

The equations of a two-phase induction motor were supplemented with the equation of motion

$$\frac{d\omega_m}{dt} = \frac{1}{J}(T - T_l) \tag{10}$$

where J is the moment of inertia and T_1 is the load torque. Based on equations (5) and (9), a numerical model of a two-phase induction machine was set up. This model makes it possible to simulate the behaviour of a considered machine in steady and transient states.

5. Examples of simulations

The following five figures show waveforms of the stator currents, rotor currents, magnetizing current, torque and speed in steady state. The parameters of the prototype of the two-pole induction motor from Fig. 1 were used in the model. The nominal values of the motor are: power 40 W; supply voltages 2 × 115 V, 50 Hz; current 0.26 A; rotating speed 2640 rpm; torque 0.145 Nm.

The motor has the parameters:
$R_S = 31\ \Omega$;
$R_{RS} = 51\ \Omega$;
$L_{1h} = 1.181$ H;
$L_S = L_{RS} = 1.331$ H;
$J = 0.000141$ kgm/s^2;

The value of the load torque was $T_1 = 0$ and the moment of inertia were chosen in such a way so that the course of speed was not substantially influenced by torque ripples. The simulated voltages u_1 and u_2 were approximated by all harmonics stated in Table 1. The waveforms u_1 and u_2 are shown in Fig. 5. The simulated waveforms of currents i_1 and i_2 and the components of rotor currents $i_{R\lambda\alpha}$ and $i_{R\lambda\beta}$ are in Figs. 6 and 7.

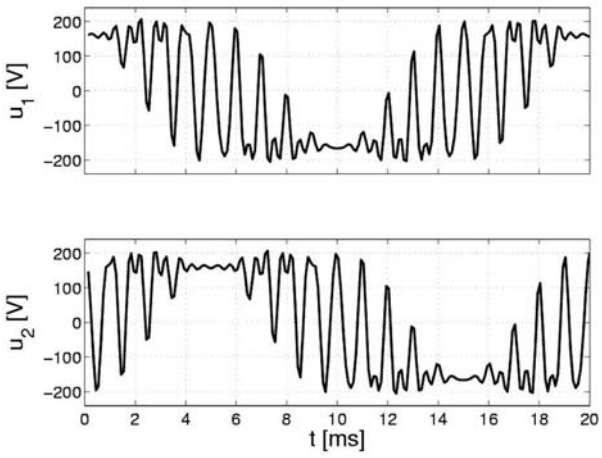

Fig. 5 Waveforms of supply voltages

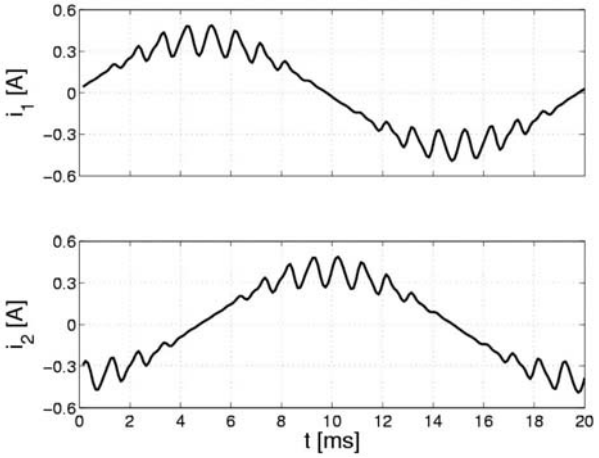

Fig. 6 Stator currents

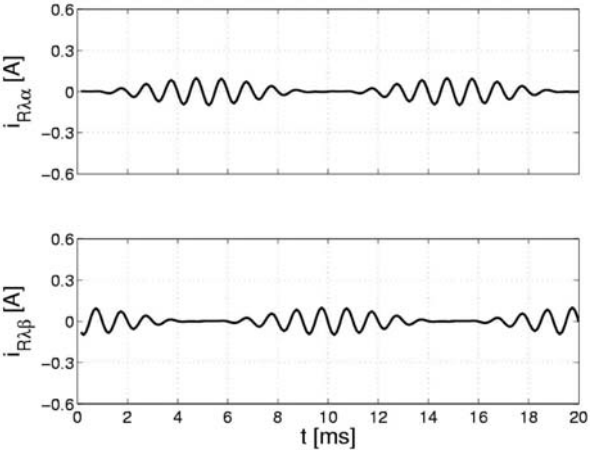

Fig. 7 Rotor current components

It is clear from Fig. 6 that phase-shift between currents i_1 and i_2 is ninety degrees and they have the same value of magnitudes. Thus, no negative-sequence component arises. Also, no pulsations of two-multiply of basic frequency (50 Hz) are presented.

The distortion of the currents due to the time harmonics of the voltage is apparent. The flux in the yoke and in the air gap is proportional to the magnetizing current. The real and imaginary components of the magnetizing current are defined as:

$$i_{\mu\alpha} = i_1 + i_{R\lambda\alpha} \tag{11}$$

$$i_{\mu\beta} = i_2 + i_{R\lambda\beta} \tag{12}$$

The waveforms of the components of the magnetizing current are in Fig. 8. The distortion of the flux in the yoke due to the time harmonics in stator voltages is small in comparison with the distortions of the currents.

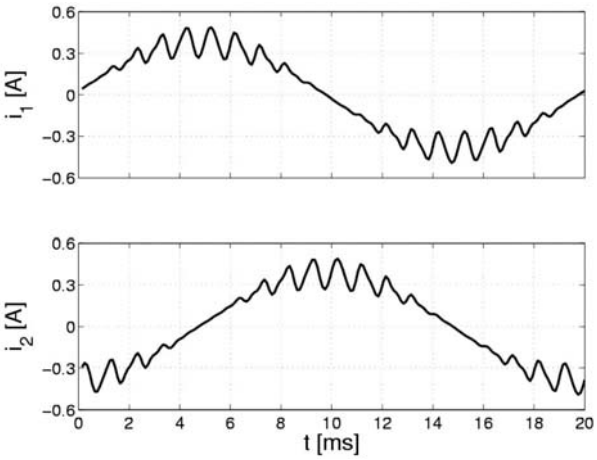

Fig. 6 Stator currents

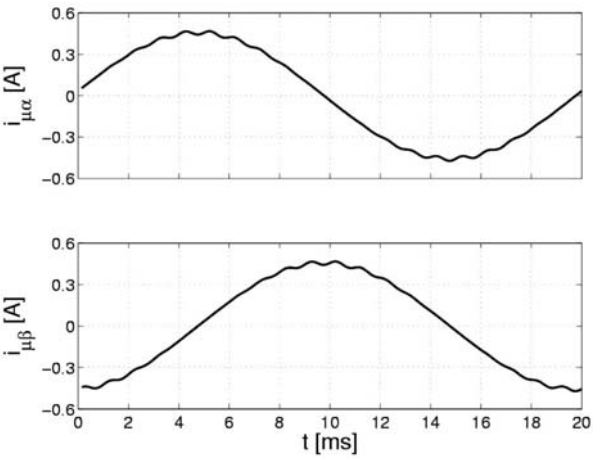

Fig. 8 Components of magnetising current

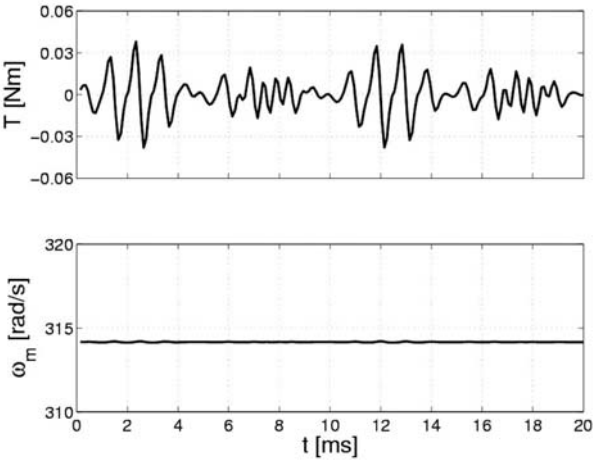

Fig. 9 Torque and speed

It is apparent that the magnitude of space vector of fundamental harmonic of the flux along the air gap is constant in steady state. The torque in no-load operation is shown in Fig. 9.

To estimate the influence of higher harmonics of currents the equal quantities as in Figs. 5 to 9 were simulated in case that only the fundamental wave and three higher harmonics of the lowest order in Table 1 were considered. The voltages u_1 and u_2 are in Fig. 10. The approximation of stator voltages is worse than in the case shown in Fig. 5. The simulated stator currents are shown in Fig. 11. Figure 12 shows the torque and speed. The differences between the quantities in Figs. 6 and 11 and between the quantities in Figs. 9 and 12 are practically negligible. The same can be stated about the waveforms of the components of the rotor and magnetizing current, therefore, they are not presented.

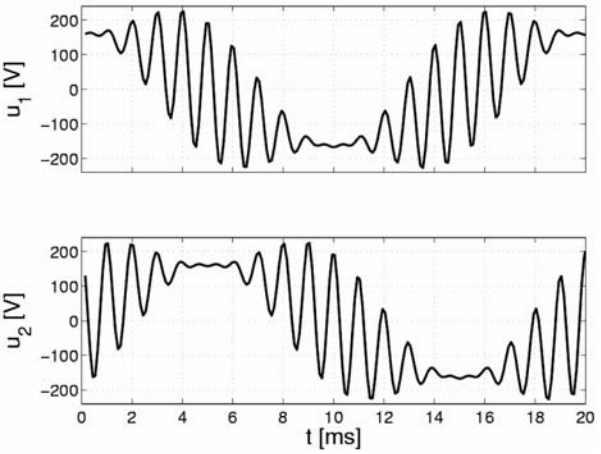

Fig. 10 Waveforms of supply voltages, the 18-th, 20-th and 22-nd harmonics considered

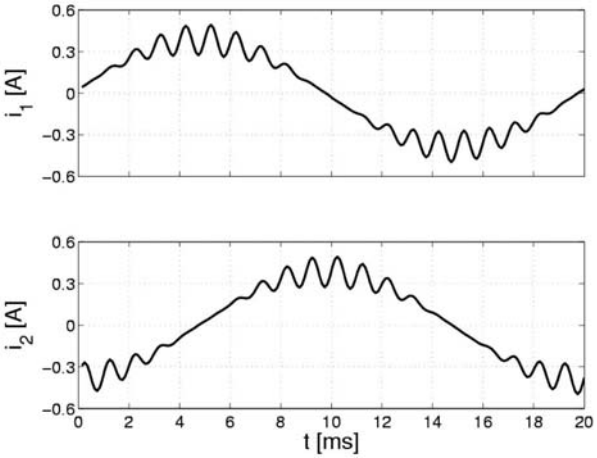

Fig. 11 Components of magnetising current the 18-th, 20-th and 22-nd harmonics considered

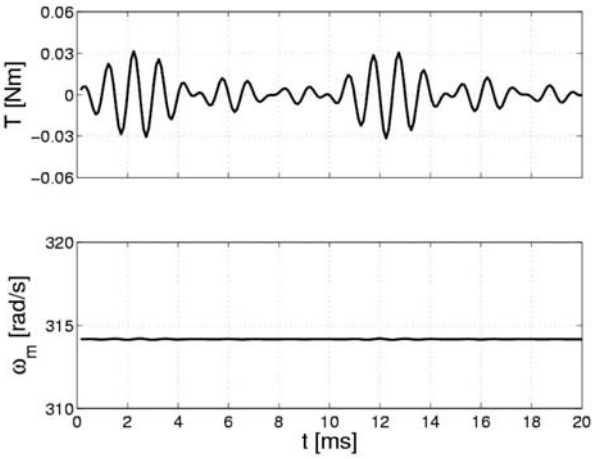

Fig. 12 Torque and speed the 18-th, 20-th and 22-nd harmonics considered

6. Conclusions

At it is apparent from the waveforms of stator currents and torque, the advantage of a two-phase motor compared with a single-phase motor is that the currents and flux of the fundamental spatial wave give rise only to the positive-sequence component while in a single-phase machine also the negative-sequence component arises.

In case of the considered modulation frequency, it is quite sufficient to consider, besides the fundamental harmonic of the stator voltages, only three waves of the lowest order. The influence of other harmonics on the waveforms of the currents of the flux and torque is very low and can be, therefore, neglected.

Acknowledgment

The financial support of the Slovak Research and Development Agency under the contract No: APVV -0138-10 and the Institutional support RVO: 61388998 are acknowledged.

References

[1] TAKEUCHI, T. J.: *Theory of SCR Circuit and Application to Motor Control;* Electrical Engineering College Press, Tokyo, 1968.

[2] ZASKALICKY, P., DOBRUCKY, B.: *Complex Fourier-series Mathematical Model of a Three-phase Inverter with Improved PWM Output Voltage Control;* Elektronika ir Elektrotechnika, No. 7 (123), pp. 65–68, 2012, KTU, Kaunas.

[3] ZASKALICKA, M., ZASKALICKY, P., BENOVA, M., MAHMUD A. R., DOBRUCKY, B.: Analysis of Complex Time Function of Converter Output Quantities Using Complex Fourier Transform/series; *Communications - Scientific letters of the University of Zilina,* vol. 12, No. 1, pp. 23–30, 2010, Zilina.

[4] ZASKALICKY, P., KANUCH, J.: *Complex Fourier Series Mathematical Model of a Single Phase Inverter with PWM of a Output Voltage;* SMC'2009, XIII Intern. Conference System Modelling and Control, October 12–14, 2009, Zakopane.

[5] DOBRUCKY, B., BENOVA, M., SPANIK, P.: Using Complex Conjugated Magnitudes- and Orthogonal Park-Clarke Transformation Methods of DC/AC/AC Frequency Converter, *Elektronika ir Elektrotechnika T 170,* No. 5(93), 2009, pp. 29–33, 2009.

[6] SCHREIER, L., BENDL, J., CHOMAT, M.: *Contribution to Analysis of Steady-State Operation of Single Phase Induction Motors,* Intern. Conference on Low Voltage Electric Machines LVEM 2007, pp. 88–91, November 2007, Brno.

Slawomir Olszowski – Jozef Buday – Jozef Kuchta – Jan Michalik *

ANALYSES OF THE CAUSES OF COMMON RAIL PIEZOELECTRIC AND ELECTROMAGNETIC INJECTORS' PREMATURE DESTRUCTION IN SELF-IGNITION ENGINES

In self-ignition engines with Common Rail direct fuel injection, premature destruction of injectors has been observed. New elements are also touched by the problem. In order to solve it, a group of international experts in the area have gathered. Destroyed piezoelectric and electromagnetic injectors' elements of BOSCH, DELPHI, DENSO, have been examined. Mechanical damages influencing electronic diagnostic signal have been presented. Some system solutions possible to perform as far as diagnostic prevention is concerned have been described. Some useful electronic diagnostic methods of fuel system, signal analysers: RMOG and ERDIA PRO, have been presented.

Keywords: *Diagnostics of piezoelectric and electromagnetic injectors CR, acoustic emission signature, electronic analysers: RMOG, EDIA PRO.*

1. Introduction

Direct fuel-injection systems with Common Rail (CR) possess electromagnetic or piezoelectric injectors started with the use of electric signal from the engine controller (EDC_C_).The controller controls the fuel flow through leakage channel and steering dose while direct fuel injection is the result of the fuel pressure difference between high pressure chamber and steering one. In some leakage-free cases of piezoelectric injectors the steering closes the injector with the use of electric signal. Disappearance of the signal opens injector's valve. Mobile elements of injectors are greased with the fuel, the one that is injected to the combustion chamber, not the engine oil. As a result, durability of the injector depends on the quality and clarity of the fuel.

2. Examination of chosen elements of the fuel system

Service procedures clearly describe methods used to control Common Rail injectors of both kinds: the piezoelectric as well as electromagnetic ones. The most basic one is the control of the leakage channel and steering dose [1, 2, 3, 4] with the use of specific measurement vessels. This method is possible to perform in some technical cases, e.g. leakage free injectors. This method cannot be used in many cases although it is the most common method used in car services. What is more, it needs the interference of the back flow of the fuel system into the low pressure side. Such a control, in many cases does not give the expected results because it is not possible to control the single fuel injection doses. It happens that in spite of getting the positive test results, the injector will not work properly in the engine. When such a situation occurs, there is a need to set the injector in a special control place, e.g. EPS200A or special assay table. It is possible to run tests there such as measurement of the quality of the injection dose as well as leakages for 1000 fuel injections in correct control pressures of rail and correct injection times e.g. DS2 (Fig. 1), CRU.2, EPS200A (Fig. 2), STPiW – 3 (Fig. 3), EPS708 and EPS815.

Fig. 1. Examination of the injector with the use of Common Rail injectors diagnostic test stand DS2 by Magneti Marelli

To conclude, in order to correctly check the starting condition of each injector it is needed to control correctness of injec-

* **Slawomir Olszowski[1], Jozef Buday[1], Jozef Kuchta[2], Jan Michalik[2]**
[1] Faculty of Transport and Electrical Engineering, Kazimierz Pulaski University of Technology and Humanities in Radom, Poland, E-mail: s.olszowski@ekspertyzy-szkolenia.pl
[2] EVPU, Elektrotechnicky vyskumny a projektovy ustav, Nova Dubnica, Slovakia

Fig. 2. Examination of the injector with the use of Common Rail injectors diagnostic test stand EPS 200A by BOSCH

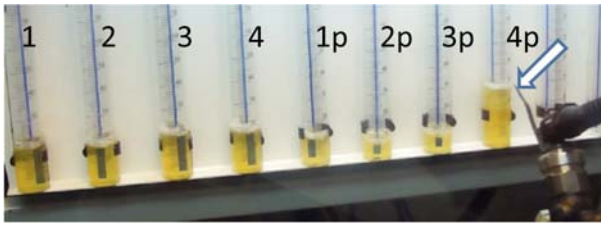

Fig. 3. Measurement of injection dose and volume of the fuel coming through the leakage channel as well as steering dose on the assay table; on the left 1, 2, 3, 4-measurement graduation cylinder of injection dose, 1p, 2p, 3p, 4p – measurement graduation cylinder of leakage channel and steering dose

tion dose (quantitative comparison) for separate cylinders [5, 6] or run the tests of injectors with the use of functions available in the service.

2.1 Laboratory examination of damaged injectors

When the examination described in point 2 was finished, it was needed to check which elements of injectors are commonly damaged. To achieve this, chosen injectors, their separate parts, have been evaluated again.

2.1.1. Slide examination of injectors' elements

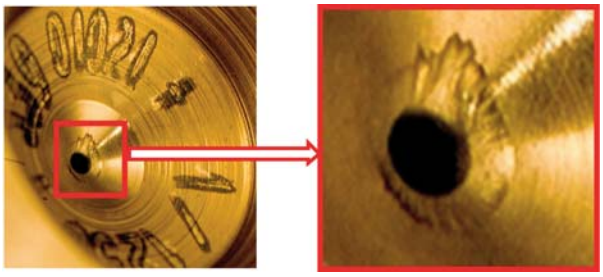

Fig. 4. Damaged steering valve socket in a new injector after the work with the constant contaminants in the fuel

Figs. 4 and 5 present some types of exploitation steering valve socket damages. It is possible to observe damages caused by erosion. They are the results of soft pollution and hard closure of steering valve. The small leakage caused fuel flow under the high pressure from the steering chamber which leads to the permanent damage of the injector.

As it has been proved, injectors of engines with the Common Rail injector system are prematurely damaged even in totally new drive units. Every type of presented damage (Figs. 6, 7, 8) needs

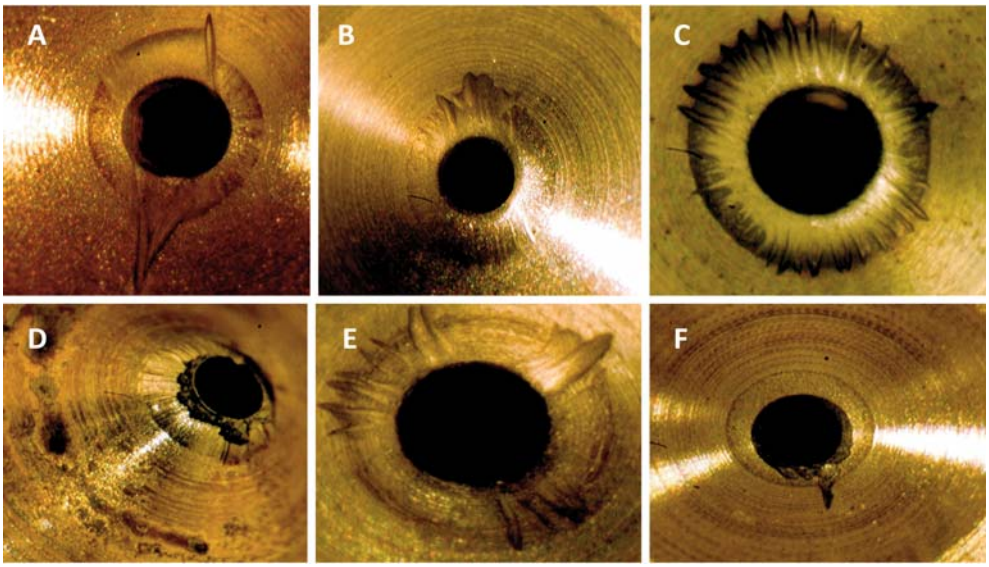

Fig. 5. Examples of damages of steering valve socket while exploitation

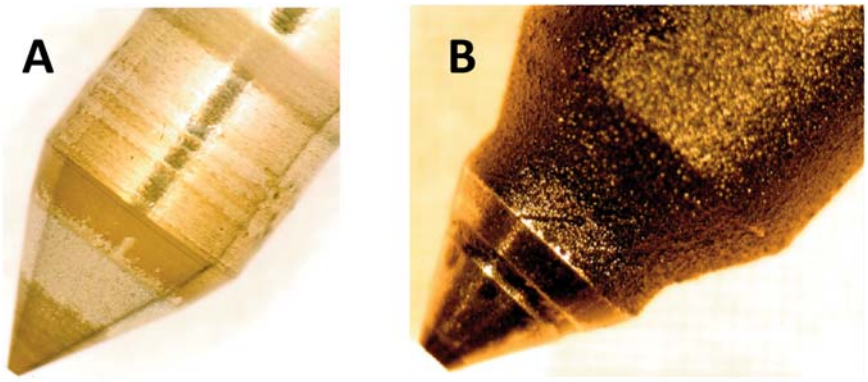

Fig. 6. Examples of damages of atomizer needle. A- lack of lubrication in atomizer frame(oil thinned with petrol), B-engine exploitation with the use of vegetable oil bought in a shop

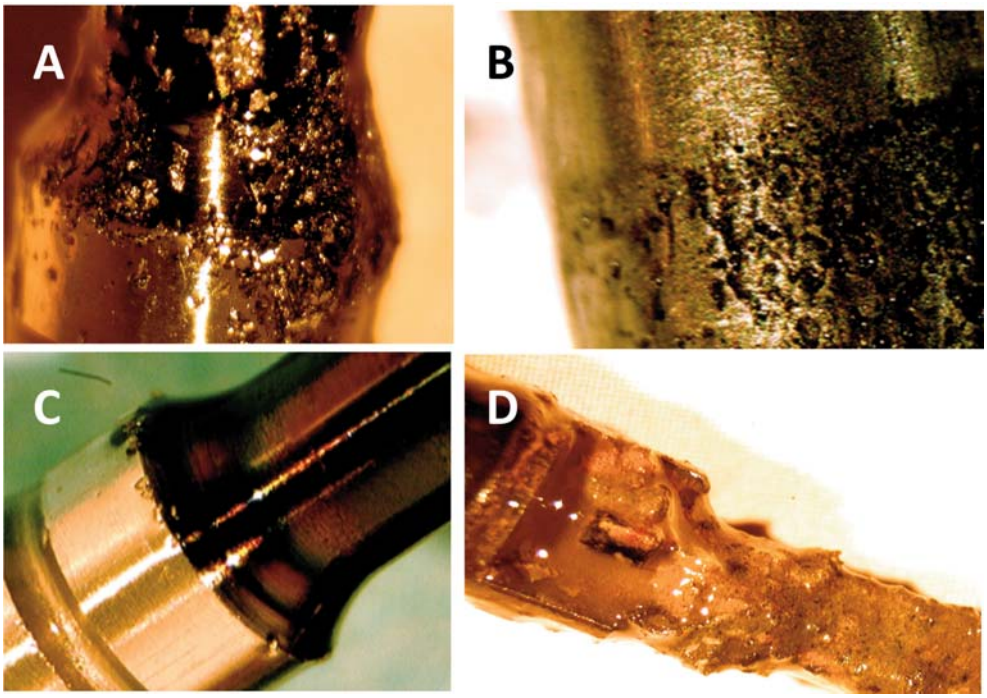

Fig. 7. Other damages of the injectors elements, A-filings in the fuel, B-corrosion of elements, C-beginning of the perspective costs, D-silt in the fuel

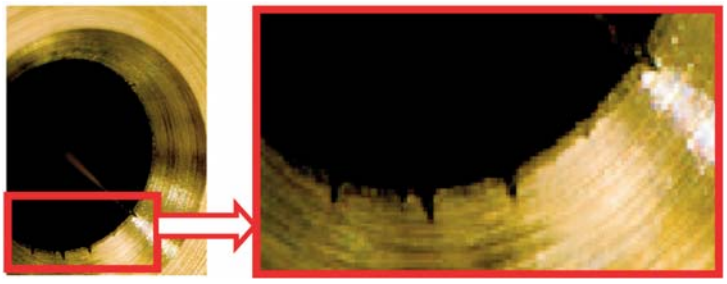

Fig. 8. The example of the injectors leakiness in steering valve socket

to be treated separately and individually. However, on the basis of the researches, it is possible to point out some general hypotheses of damages' causes. Thanks to it, it seems possible to avoid such problems in the future and solve them fast.

Not only used but also new injectors get damaged.

1. With the use of statistic results of damages presented in the article [1] as well as the results of present injector components it seems possible to state that the most common reason of damages are:
   A. Incorrect kind of fuel
   B. Polluted fuel
      - bad quality fuel filters
      - filings from fuel system elements, especially from the high pressure pumps
      - water in the fuel
      - bad quality fuel.
2. Qualifications of staff in service section.

As it is observed, it is not enough to exchange the damaged element. With the technical development, it is needed to examine the cause of damage. As it has been presented in the research, it is not possible to do the correct diagnoses of the piezoelectric and electromagnetic CR injectors damages' causes without microscopic research.

3. Final conclusion

Technology development as far as vehicles are concerned, becomes a real problem for their users because of innovative, advanced systems as well as the level of qualification of the staff of service sector [7]. Innovative technologies used for production of Common Rail injectors, are step forward in range of the accuracy of manufacturing in comparison to the quality of the fuel commonly used on the market.

Bearing in mind the fact that before, it was needed to exchange the fuel filter in self-ignition engine after 30 thousand km. Nowadays it is 60 thousand km, so it seems to be clear that gathering greater amount of money from the sale of more expensive components of injection system was a priority for the producers rather than solving or preventing the problem.

The research team after detailed analyses of the results concluded that the every year examination of the vehicle in the Car Control Station with usage of EDIA Pro and RMOG can be a good solution to prevent the environmental pollution due to the faulty working CR injectors.

It is not possible for a driver to observe the faulty work of the engine in the first phase as HP pump is enough to cover a greater need for fuel, which is a result of the GZS leakiness.

A correct diagnosis can be done by checking the pressure fall in the fuel container with the use of EDIA PRO [8] and with the use of the innovative method RMOG. These methods are additional. The first one, makes it possible to precisely analyze the parameters of fuel system parameters, the second one analyzes spectrum results. This spectrum is a combination of time and frequency of the acoustic emission signal of working injector [6, 9, 10]. However, it is a new innovative method unknown in the world yet.

References

[1] OLSZOWSKI, S., MARCZAK, M.: Diagnostics of New Generation Diesel Engines. *Diagnostyka* No. 4(48), 2008, Polskie Towarzystwo Diagnostyki Technicznej, pp. 83-88.
[2] OLSZOWSKI, S.: Innovative Method of Diagnostics of Common Rail Injectors. *Czasopismo Logistyka,* No. 2, Poznan, 2008.
[3] DOBRUCKY, B., SPANIK, P., SUL, R.: Improvement of Power Electronic Structure Characteristics Using Sic Technology – Overview. *Communications – Scientific Letters of the University of Zilina,* No. 1, 2006
[4] JURISICA, L.: Mechatronics Systems. *Communications – Scientific Letters of the University of Zilina,* No. 1, 2007
[5] OLSZOWSKI, S.: *The Methods of Diagnosis of the Innovatory Management Systems in Cars.* IX Inter. conference Transport Systems Telematics. Politechnika Slaska. Katowice-Ustron, November, 2009.
[6] OLSZOWSKI, S.: Common Rail System in Transport Facilities – Current and Future Problems. *Czasopismo Drogi,* No. 4, pp. 97–103, 2009.
[7] KALLAY. F., PENIAK, P.: The Communication in Mechatronic Systems. *Communications – Scientific Letters of the University of Zilina,* No. 1, 2007.
[8] OLSZOWSKI, S., OLSZOWSKI, T: *Non-invasive Method of Diagnostics Common Rail System Condition.* Transcomp – Intern. Conference Computer Systems Aided Science, Industry and Transport, 2012
[9] OLSZOWSKI, S., CHOJNACKI, T.: *Diagnostics of Unconventional Defects in the Systems of Cleaning Exhaust Fumes.* Transcomp – Intern. Conference Computer Systems Aided Science, Industry and Transport, 2009
[10] OLSZOWSKI, S.: *Ecological and Functional Aspect of Technical Exploitation of New Generation Common Rail Systems.* Computer systems aided science and engineering work in transport, mechanics and electrical engineering. Monograph. Kazimierz Pulaski Technical University of Radom: Faculty of Transport, pp. 459–465, 2008.

Zdenek Dvorak – Maria Luskova – Petr Hruza – Radovan Sousek *

COMPLEX AUTOMATED INFORMATION SYSTEM FOR REMOTE MANAGEMENT OF CRISIS SITUATIONS IN RAIL TRANSPORT

The paper deals with topical information from the area of crisis information support. The contributing authors work at three co-operating universities where the subject of transport support in crises is tackled. At present the electronic support of crisis management in transport is necessary prerequisite for the functioning of transport system under both common and emergency situations. The outcomes of scientific research projects are new even from a broader European perspective. The preparation of complex automated information system for remote management of crisis situations in rail transport is new and has not been published yet. The outcomes of extensive analysis, gradually developed methodologies and data sets are presented in the paper together with the current outcomes regarding the electronic support of crisis management in transport.

Keywords: *Crisis situation, transport security, information support, information system, rail transport.*

1. Introduction

During the last decade the global security research was markedly focused on solving the problems of critical infrastructure. The USA in co-operation with Canada has developed their own electronic expert information system [1] the aim of which is to reduce risks in all sectors of critical infrastructure. A significant progress in the area of electronic information support has been made mainly in Australia [2] and [3].

The European security research in the area of critical infrastructure is carried out in two lines. Firstly it is the EU's Seventh Framework Programme and its "Security" calls. Several extensive projects focused on the protection of critical infrastructure are solved every year within this call. The significant projects in this area are Comicin, Micie, and WSAN4CIP [4] and [5].

The European Union and its member states have started preparing their own European Critical Infrastructure Warning Information Network (CIWIN). Building other information portals is an important part contributing to the protection of critical infrastructure. One of them has been prepared within the European educational project called Competency Based e Portal of Security and Safety Engineering. Work on the project was in progress from 2009 2012 at Zilina University and the "eSEC" portal was the outcome of it [6]. The authors participated in the preparation of the following projects within the national projects on the protection of critical infrastructure:

- Project APVV-0202-12 on Communication Technologies Aided Protection of Critical Infrastructure in the Slovak Republic (the project is in the assessment phase)
- Complex Automated Information System for Remote Management of Crisis Situations in Rail Transport with Focus on Critical Infrastructure is the project prepared in the Czech Republic. The work on the project is planned for years 2012-2015.

Real crisis and emergency events, which often occur in transport and energetic infrastructure, threaten population and surrounding facilities. At present there are not any complex information systems enabling the transfer of information from the administrator of infrastructure to regional structures and vice versa [4] and [5]. The aim of the paper is to present the project of applied research, which would contribute through communication technologies to the improved exchange of information during crises and emergencies.

The project VG20122015070/Ministry of Interior of the Czech Republic on the "Complex Automated Information System for Remote Management of Crisis Situations in Rail Transport with Focus on Critical Infrastructure", called KISDIS, started in 2012. The first stage included the information analysis of available materials abroad with the aim to find similar projects carried out in particular European countries. The outcomes of the analysis confirmed that the electronic support for the management of crisis situations in rail transport has not been solved in any of the countries included in the survey.

* **Zdenek Dvorak[1], Maria Luskova[1], Petr Hruza[2], Radovan Sousek[3]**
[1] Research Department of Crisis Management, University of Zilina, Slovakia, E-mail: zdenek.dvorak@fsi.uniza.sk
[2] University of Defense, Brno, Czech Republic
[3] Radovan Sousek, Department of Transport Technology and Control, University of Pardubice, Pardubice, Czech Republic

Lessons learned from extensive floods in the Czech and Slovak Republic in the last decade clearly showed the need for rapid and efficient dissemination of information to experts, as well as public. Therefore experts on rail transport co-operate with experts on regional crisis management during their work on the project.

There have been 23 types of hazards defined and accepted by all departments in the Czech Republic [7] and [8]. The first stages of the project in 2012-2013 are aimed at developing the methodology which will exploit earlier defined types of hazards in the area of rail transport of the Czech Republic. With regard to the overall goal of the project it was necessary to define a functioning data set, which will be the basis for the future expert information system. The outcomes of initial stages are very original. The proposed methodology has been tested in the conditions of rail transport and it is assumed that it will be certified on a national level. The outcomes of initial stages have become a real basis for the functioning of future complex information system for remote management of crisis situations in rail transport.

2. Outcomes of the analytical part of the project

The whole analysis of the project has been aimed at updating a large information base. Updated information has been collected on the ways critical infrastructure is protected in the transport sector in Germany, Poland, Austria and the Slovak Republic. Special attention has been paid to the current outcomes of the projects within the 7th EU Framework Programme aimed at improving the long-distance control of rail transport and the information support of crisis management. A significant part of analytical survey has been focused on a comparative analysis of legal environment in particular European countries. Bearing in mind the main aim of the project the further effort has been made to analyse mutual compatibility of the systems transferring the information from the information system through internet to SMART mobiles. The testing of individual mobile phones operational systems and the assessment of possible risks resulting from the transfer of information between an internet server and SMART mobiles were other significant analytical activities. At present the crisis management staff on rail has been gradually equipped with intelligent mobiles. Further procedure has been set within the KISDIS project based on the above mentioned analysis.

The methodology for the selection of hazards has been preconditioned by a number of constraints. The first condition was the fact that rail transport is considered to be a compact system. For the needs of the research the rail transport infrastructure has been divided into individual railway lines and stations. The method of generalization has been applied for acquiring corresponding parameters and the railway lines (or their parts) have been classified into several types. The second condition was to divide railway stations into five classification categories. Such an approach required the documentation for one station and one type of railway line. Different types were distinguished by names in operational documentation then.

The procedure of activities according to the methodology represents the first step in the process of planning the measures for managing the crisis situations on rail and requires a good knowledge of the assessed railway line, terminology of transport, logistic and construction guidelines of the Railway Infrastructure Administration (hereinafter RIA). The methodical instructions enable not only the selection of hazards from the list provided by the railway controller crisis information system. The methodology is logically ordered in compliance with the definition of hazard as one source of risk. Prior the final determination of particular type of hazard it integrates the completed analyses into one table in the order which is introduced in the KISDIS programme software environment

2.1 Multicriterial assessment of possible impacts

Impacts on rail infrastructure (a subsector of critical infrastructure) are assessed by comparing a selected location with assumed consequences. The assessment includes both a particular location of critical infrastructure and the possibilities that a particular event may have an impact on the functionality of the element of critical infrastructure [9] and [10].

In case the location is hazardous, or the consequences have impact on the functionality of the element of critical infrastructure, its identification is changed (e.g. highlighted) and considered to be of higher priority during further processing. The multicriterial assessment is carried out in the following order of importance:

1 The determination of hazardous location;
2 The determination of risk source;
3 The activation of risk source;
4 Reason why the risk source may be activated;
5 Event which may occur upon the activation of risk source;
6 Assumed consequences [11].

Risk sources are always connected with a particular location. The crossings of railway lines with other line infrastructures are very frequent activation mechanisms of risks. Other frequent causes include unintentional mistakes of traffic participants, extreme weather conditions and technical breakdowns. The research team ambition is to develop a fully automated complex system for remote management of emergencies [12] and [13].

2.2 General classification of hazards on railway

The authors firstly defined the general classification of hazards for rail transport on the basis of extensive analyses of real emergencies in rail transport and with the effort to employ the existing classification of hazards. The risk sources were transferred into particular hazard type names due to the preparation of a model and possible programming. It is registered in one sentence consisting of four parts, i.e. EVENT – RISK SOURCE ACTIVATION – LOCATION – CAUSE, in the following format:

1. “name of EVENT” caused by;
2. “name of RISK SOURCE ACTIVATION”;

3. in “name of LOCATION”;
4. caused by “name of CAUSE”.

Note: information written in quotation marks is inserted automatically from the database.

The range of own analytical research activities is evident from the decreasing number of generated types of hazards. All possible types of hazards, i.e. 12,032, were generated in the initial proposal. By removing the duplications their number decreased to 2,800. Extensive expert discussions and the removal of unlikely hazards with negligible impacts resulted in 627 types of hazards, which are significant part of the proposed methodology.

The term change of operational conditions is used in the methodology for naming all the EVENTS on the railway. It may be characterized as a course of action which disturbed the traffic on railway and in order to identify the type of event better it may be subdivided in the following way:

- the stoppage of traffic – hazard may result in inability to operate the rail transport;
- the change of schedule – hazard may result in the reduced range of transport;
- the change of technology – hazard may have an impact on the work scheme;
- the change of service – although the infrastructure is not disturbed, the identified hazards may result in the change of services being offered.

The second important step is naming the RISK SOURCE ACTIVATION, which stems from the identification of risk sources. The risk sources identified in rail transport are facilities in railway infrastructure, railway buildings, constructions, operational personnel, customers and buildings and facilities near the railway line. Expert analyses, which took several months, defined 35 activation mechanisms altogether (e.g. fire, flood, explosion, collision, etc.).

The third step includes analysing the location of the type of hazard by connecting the activation mechanisms with the risk sources. There were 50 possible combinations defined during an extensive expert discussion. These combinations in railway transport are significant and of quite high probability.

The CAUSES were divided into two basic groups (natural and man-made). The further procedure was based on putting them in relation to risk source activation. The risk source activation was related to location in the previous step (e.g. railway line, station, building, train). Probability of such combinations has to be always assessed. Unreal combinations have been excluded from further analysis. More causes have been considered (i.e. synergic effect) when calculating the type of threat. Their assessment and ordering resulted in 14 groups of causes according to their common characteristics, part of which is shown in Table 1. They are written into the type of threat under the term in the column “name of Cause”.

General description of the types of hazards in rail transport has been developed according to the above mentioned procedure and in numerous, documented expert discussions. Note: Similar general description of the types of hazards has been simultaneously developed for road transport, but this is not further pursued within this project. Thus the methodical basis has been developed for the future expert information system for remote management of emergencies in rail transport. It is obvious that its real functioning requires available and realistic data set.

Table of particular causes in relation to the name of cause (sample) Table 1

No	Name of cause	Content
1	Atmospheric and cosmic anomalies	Storm, other electric phenomena in the atmosphere, cosmic radiation, magnetic anomalies, meteor impact
2	Biological emergency	Extremely increased reproduction of insects transmitting the infection, increased numbers of weeds, viruses, bacteria, animal vermin, wild infected animals

3. Outcomes discussion

The standard part of applied research is the analysis of acquired outcomes and discussion about their benefits for the project. The acquired theoretical and practical outcomes may be assessed in the following levels. The first set of outcomes was based on a partial goal, which was aimed at identification and selection of suitable data. This goal has been met by creating the real data sets within the KISDIS project. The second set of outcomes has been aimed at real and practical benefits of the methodology for selecting and processing the types of hazards. The third set of outcomes resulted in the domain analysis and model cases to be employed in practice.

3.1 Identification and selection of suitable data

The most significant data basis for the types of hazards in transport is The Type Plan of the Ministry of Transport called “Large-Scale Disturbance of Transport System Functionality” [7]. At present the Plan has five annexes dealing with individual types of transport. The annexes are focused on rail transport, road transport, road economy, civil aviation, and domestic water transport.

The Type Plan provides users with data for crisis planning in rail transport. It also lists the risks related to the railway traffic, scenarios of development of crisis situations, primary and secondary impacts of crisis situations, conditions and prerequisites for managing the crisis situations, recommended type procedures, and requirements for resources.

Crisis plan is another significant data basis. It includes the summary of planning, methodical and information documents and data required for decision-making, control and co-ordination activities in a crisis situation. It standardizes the procedures of crisis

management authorities in the area of transport, provides basic data and characteristics of possible crisis situations (it includes type plans) and determines possible solutions including their impacts on transport.

3.2 Methodology for selecting and processing the types of hazards

The development of the methodology for selecting and processing the types of hazards was the main aim of the initial phase of the KISDIS project. Determining the types of hazards was the synthesis of general criteria, which includes all possible combinations generated from the event, risk source activation, location and cause. The names have been compiled into a sentence in the following form and order (see Table 2):

Syntax of creating the name for the type of hazard in the KISDIS project — Table 2

Event	Risk source activation	Location	Cause
Change of operational conditions due to	Bombardment of railway vehicle	On the railway line	Atmospheric and cosmic anomalies
Change of operational conditions due to	Immobility of traction vehicle	In train	Mistake caused by human factor.

Defining the types of hazards, their testing and verification in co-operation with experts on rail transport and regional crisis management resulted in the summary Table containing 627 types of relevant and quite probable types of hazards. The type names of hazards have become the basic database for prepared expert information system.

3.3 The model of system employment

The KISDIS information system consists of control and monitoring nodes. It includes at least one control node with the *KISDIS Windows system* and at least one monitoring node with the *KISDIS Internet system.* In case of need a monitoring node of another information system may be added to the KISDIS system.

The main part of the *KISDIS Windows* system consists of three main components (see Fig. 1):
- KISDIS Windows Client,
- KISDIS Windows Mobile,
- KISDIS Windows Server.

The *KISDIS Windows Client* component will serve for inserting and editing the information on the management of crisis situations in the database. The KISDIS Windows Client component will be installed into the crisis manager's work station.

The *KISDIS Windows Mobile* component will serve for receiving, displaying and reverse sending of information on the duties of task forces. This component will be installed into the task forces´ mobile phones.

The *KISDIS Windows Server* component will provide the exchange of information between the KISDIS Windows Client and the KISDIS Windows Mobile components. The information will be stored into the KISDIS database. Each control node will have one KISDIS database.

The mutual independence of all three components has been chosen as the main criterion of functionality of the whole KISDIS Windows system. Thus each component has been operational even in case the other components are not. The following Figure shows the basic employment of individual components of the KISDIS Windows information system and their inter relations.

The surrounding co-operating information systems are standard e-mail servers enabling communication through IMAP and SMTP protocols and database servers or database files. Smart phones and Internet infrastructure are also parts of surrounding co-operating systems.

The *KISDIS Internet system* consists of the network of servers – nodes of the "KISDIS Internet Server" type and remote users – nodes of the "Remote user" type (see Fig. 2). The servers use HTTP server for providing information in the form of web pages. The servers may mutually update their data through the port types of web services. Server also implements the port types for the third parties' information systems – node "Another remote server".

The remote users cannot communicate directly with each other within the KISDIS network; they are in the role of a client.

4. Conclusion

The first outcomes of the KISDIS project have been published in the paper. The universal employment of the proposed expert information system in relation to the administrator of critical infrastructure and public administration is a prerequisite for its future employment in the Czech Republic and possibly in other EU countries. The authors of the project believe that other activities of the project will result in the certification of the developer methodology on a national level. The primary goal of the project is to improve the information support of crisis management in two different areas – in rail transport and municipal crisis management.

The first stage of the project is dealing with risk sources identification, development of basic data structure for the future expert information system and structure of the proposed measures. Within the risk sources identification the first stage was oriented on creating a list of all theoretically possible threats in a railway transport. Their total number was 12 032 but after elimination of the contentual duplicities their number changed to 2800 threats that will be used in the expert system. Working with data structure was

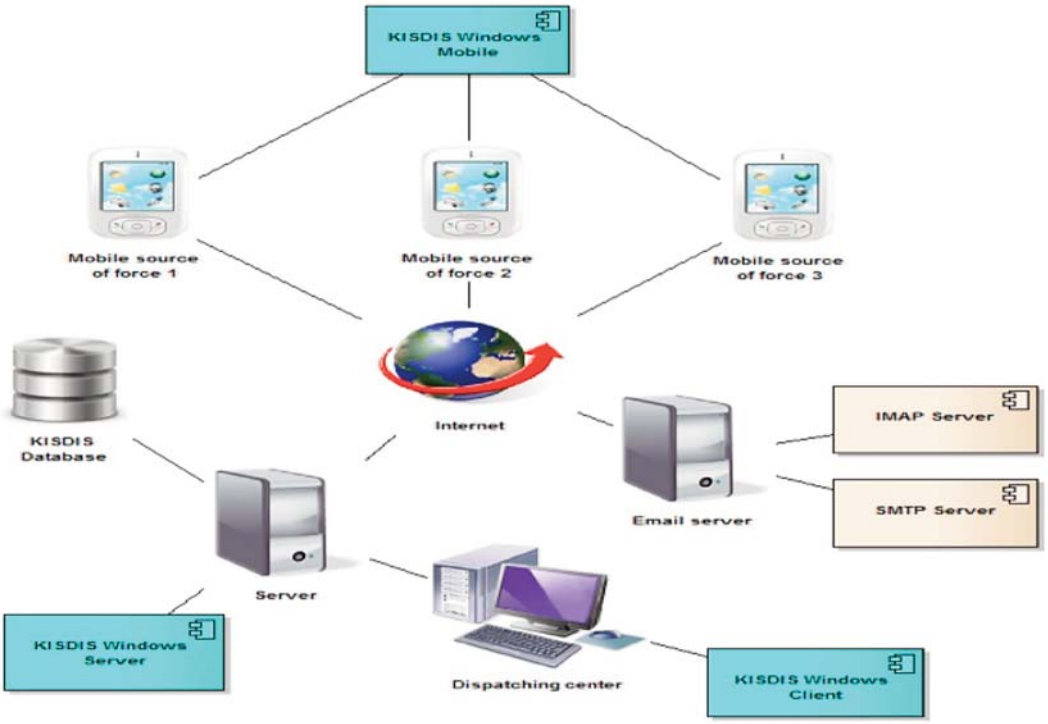

Fig 1. Basic KISDIS Windows model of employment

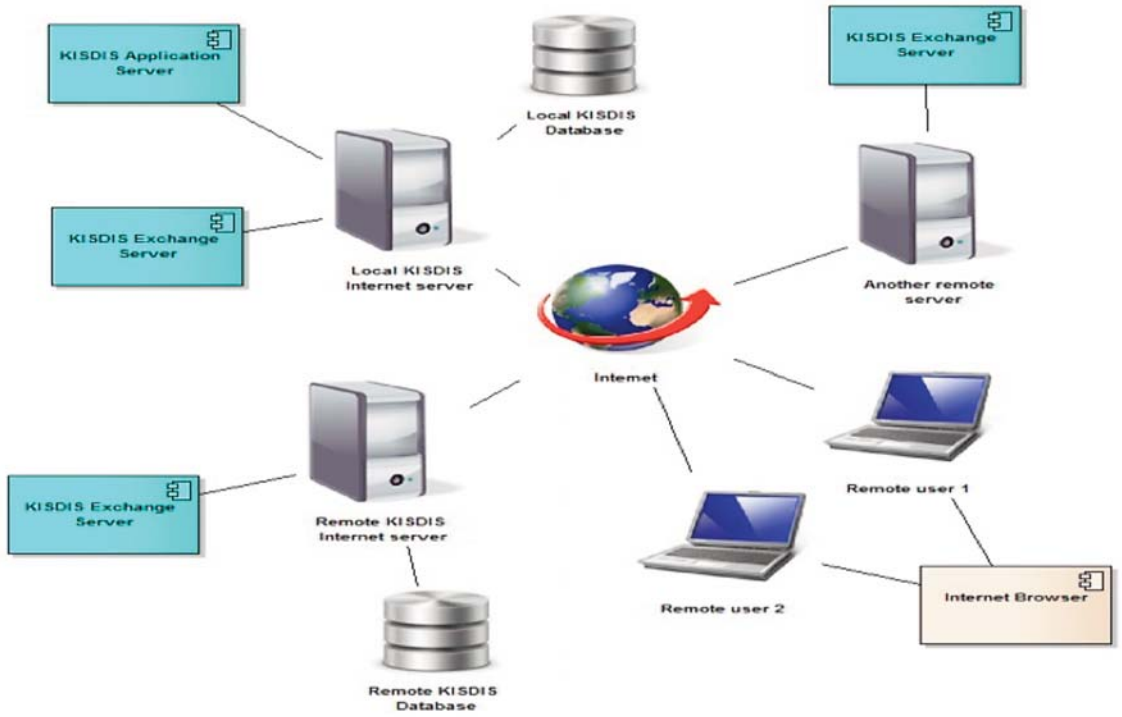

Fig. 2 KISDIS Internet – basic model of employment

oriented on exact description of the event, risk activating mechanism, place and causes. In successive steps 615 type of threats were specified that will be detailed and elaborated in the form of standard recommendations file.

Acknowledgements:

The outcomes presented in this contribution are part of the project on "The Complex Automated Information System for Remote Management of Crisis Situations in Rail Transport with Focus on Critical Infrastructure". The project is granted by the Ministry of Interior of the Czech Republic under No. VG20122015070. The authors would also like to thank the "Centre of Excellence for Systems and Services of Intelligent Transport" (ITMS 26220120028) for building the infrastructure being used.

References

[1] DVORAK, Z., FUCHS, P., NOVAK, J., SOUSEK, R.: Individual and Social Risk During Transportation of Dangerous Substances, *Communications - Scientific letters of the University of Zilina,* ISSN 1335-4205, vol. 13, No. 2, 2011,

[2] Web:http://www.tisn.gov.au/Documents/Australian+Government+s+Critical+Infrastructure+ Resilience+Strategy.pdf

[3] RISTVEJ, J., ZAGORECKI, A.: Information System for Crisis Management – Current Applications and Future Directions, *Communications - Scientific Letters of the University of Zilina,* ISSN 1335-4205. vol. 13, No. 2/2011

[4] Web: http://cordis.europa.eu/fp7/ict/critinfpro/projects_en.html

[5] Web: http://www.future-internet.eu/activities/fp7-projects.html).

[6] Web: http://.eSECportal.eu

[7] Type Plan of the Ministry of Transport. *Large-Scale Disturbance of Transport System Functionality.* Ministry of Transport of the Czech Republic No. 116/2010-030-CRS, 1st November 2010

[8] *Crisis Plan of the Ministry of Transport of the Czech Republic,* No. 32/2005-CNP by 15th March 2005. Prague, Ministry of Transport, 2005

[9] VIDRIKOVA, D., DVORAK, Z., KAPLAN, V.: *The Current State of Protection of Critical Infrastructure Elements of Road Transport in Conditions of the Slovak Republic,* Proc. of 15th intern. conference Transport Means 2011, Kaunas University of Technology, 2011

[10] DVORAK, Z., SOUSEK, R. ENGLICH, J.: Preparation for Solution of Crisis Situations in Railway Transport in the Czech Republic. *Logistyka i Transport,* Poland, 2007

[11] SOUSEK, R. et al: *Methodology of Critical Transport Infrastructure Objects Identification.* Proc. of 5th intern. scientific conference Theoretical and practical issues in transport, Pardubice, University of Pardubice, 2010

[12] DVORAK, Z., LEITNER, B., SVENTEKOVA, E., SOUSEK, R.: *Managing of Risks in Railway Transport,* Monograph Institute J. Pernera, University of Pardubice, 2011

[13] MAJERNIK, M., PANKOVA JURIKOVA, J.: Theoretical Methodological Aspects of Integrated Risk Management Standardization, *Communications - Scientific Letters of the University of Zilina,* vol. 13, No. 2, 2011, ISSN 1335-4205.

Andrzej Rogowski *

COMMENTS ON THE POWER OF KOLMOGOROV TEST

This paper presents the results of estimating the power of Kolmogorov test and its modifications for testing hypothesis about an exponential distribution against the alternative hypothesis (population has a Weibull distribution). The power of test was calculated based on a distribution of empirical cumulative distribution function and limiting distribution, as well as computer-simulation methods. Some important properties and limitations were given that are related to power simulation study of goodness-of-fit tests.

Keywords: Statistical test, Kolmogorov test, power of a test, exponential distribution, simulation.

1. Introduction

The λ Kolmogorov test is one of the best-known goodness-of-fit tests for testing the hypothesis about the type of a probability distribution for a continuous distribution. Despite the vast literature, its use still arouses controversy. Among the most frequently tested hypotheses about the type of a distribution are the hypothesis of normality, also called normality test, and the hypothesis of exponentiality, or exponentiality test. To verify hypotheses about a normal distribution researchers use primarily tests (particularly for small samples) specialized in these types of hypotheses, called normality tests (e.g. Shapiro–Wilk, Epps–Pulley, skewness and kurtosis tests). Nonetheless, Kolmogorov test is still applied, as well as its modifications for testing normality of distribution, such as Kolmogorov–Lilliefors and other general goodness-of-fit tests, like Cramer–von Mises, Watson, Anderson–Darling tests. The importance of testing hypotheses about normal and exponential distributions is undeniable since such distributions play an important role in contemporary science and technology. It might be said that based on normal distribution are among others: statistics, metrology and prediction theory. Also, we cannot overate the importance of exponential distribution, especially in the theory of reliability and safety, diagnostics and maintenance theory, queuing theory and in various transport applications. The exponential distribution fields gives an important advantage of relatively simple calculations, whereas in the case of "competitive" distributions calculations are bound to be more complicated. Often it is not possible to obtain analytical solutions and, therefore, simulation study remains as the last alternative. However, the use of an exponential distribution is always combined with adopting strong assumptions, whose truth is frequently put into question. Thus, "the way" of assessing the admissibility of an exponential distribution is to verify the hypothesis based on empirical study that the probability distribution of the investigated variable is exponential, i.e. it does not differ in terms of statistical significance from exponential distribution. As long as this study is to provide reliable assessment of the applicability of exponential distribution, it is necessary to know what risk carries not rejecting a false hypothesis about an exponential distribution, i.e. what is the power of the used test. The vast majority of tests allow to control the type I error, i.e. the probability of rejecting a true hypothesis (so-called test of significance), however, most of them do not allow to control the error of type II, i.e. not rejecting a false hypothesis in favor of the alternative hypothesis. It has only been postulated to select tests (as well as size of random sample) so that the type II error would not exceed the type I error. Currently, it is rather postulated that an error of type II should not exceed 0.2, thereby the power of a test should not be less than 0.8 (80%). The issue of the test power creates another problem, namely, what decision to make when different tests give contradicting results.

In paper [1] we have analyzed the results compliance of testing the composite hypothesis of normality for 10 basic normality tests, including modified tests for composite hypotheses. The level of significance is equal to 0.05. Simple samples of size up to $n = 44$ were generated, coming from populations with either normal distribution or other distributions, like T-Student, Gamma, chi-square, exponential. It was found that at least eight tests gave the same result, approximately:

85% when a sample was drawn from a normal distribution,
72% when a sample was drawn from a Student-t distribution,
70% when a sample was drawn from a chi-square distribution,
82% when a sample was drawn from a Gamma distribution,
100% when a sample was drawn from an exponential distribution.

However, only from 51 to 72% of choices for individual tests were correct, provided that excluded were the samples with an exponential distribution strongly differing from a normal distribution. The highest percentage of correct choices was observed for the skewness test (72%), then for the Epps-Pulley test (67%). The Shapiro-Wilk and Andreson-Darling test gave about 64% correct

* **Andrzej Rogowski**
Faculty of Transport and Electrical Engineering, University of Technology and Humanities, Radom, Poland,
E-mail: androgow@wp.pl; a.rogowski@uthrad.pl

answers each, the classical Kolmogorov and Kolmogorov-Liliefors about 59%, but the worst results were obtained for the Watson test (51%) and Cramer-von Mises test (54%).

Furthermore, a study was performed on testing hypotheses about an exponential distribution [2], including checking how many times individual tests do not give a reason to reject the hypothesis about an exponential distribution (composite hypothesis), whenever the generated sample did not come from a population with an exponential distribution (but with e.g. Gamma, power, Weibull, Erlang, chi-square). The verification was carried out for 20 000 random samples. It turned out that the classical Kolmogorov test, for samples of size $n = 25, 50, 75, 100$ gave no reason to reject the hypothesis about an exponential distribution (so the false hypothesis) in 63%, 44%, 35%, 29% of cases respectively. The best results were obtained for the modified Andreson-Darling and Kolmogorov-Stephens tests (36%, 26%, 21%, 19%).

2. Calculating the power of test

The power of a statistical test depends significantly on the test construction, size of a random sample, null hypothesis and alternative hypothesis. In case of parametric tests, there is a bulk of literature on power analysis, as well as modules designed for analyzing the power of tests are available in statistical software. The situation is more difficult in the case of non-parametric tests that are goodness-of-fit tests assessing empirical distributions against hypothetical distributions, especially for composite hypotheses. Basically, the task is solvable if the form of cumulative distribution function (referred to as *c.d.f.* henceforth) is unambiguously specified in the alternative hypothesis. One of available methods is a method of computer simulation, i.e. determining a null hypothesis and generating random samples with a given distribution. Subsequently one should analyze the value of test statistics in relation to the critical value, as well as the value of test statistics with the replacement of null by alternative hypotheses. The fundamental theorem used in generating random samples with a given distribution is as follows:

Theorem 1 ([3]).
If F is the *c.d.f.* of a random variable X, the random variable $F(X)$ has a uniform distribution on the interval [0. 1].

By generating a random sample $\{y_i\}$ with a uniform distribution on the interval (0. 1), and then using the inverse function of the fixed *c.d.f.* of F, we obtain a random sample $\{x_i\}\{F^{-1}(y_i)\}$ of the desired probability distribution.

In our case, we are interested in the power of goodness-of-fit tests under the null hypothesis H_0: the sample comes from a population with exponential distribution, against the alternative hypothesis H_1: the sample comes from a population with A distribution, where A is the Gamma, Weibull or power distribution. We will assume that empirical distribution is defined by empirical *c.d.f.*

$$F_n(x) = \frac{1}{2} card\{x_i : x_i < x\} \tag{1}$$

While generating random samples and testing hypotheses, special attention should be given to certain restrictions and properties arising from chosen techniques of generating samples, types of distributions, as well as the form of hypothesis H_0 and used statistical tests.

Gamma distribution

A random variable X has a gamma distribution with *parameters b, p* (which is written Γ (*b, p*)), if the probability density distribution $f(x)$ is defined by the following formula:

$$f(x) = \begin{cases} 0 & , \quad x \le 0 \\ \dfrac{b^p x^{p-1}}{\Gamma(p)} e^{-bx} & , \quad x > 0, b > 0, p > 0 \end{cases} \tag{2}$$

where b is called a rate parameter, p is called a shape parameter[1] $\Gamma(p) = \int_0^{+\infty} x^{p-1} e^{-x} dx, p > 0$ denotes the Euler's Gamma function. The *c.d.f.* of distribution is given by:

$$F(x) = \begin{cases} 0 & , \quad x \le 0 \\ \dfrac{\Gamma(p, bx)}{\Gamma(p)} & , \quad x > 0, b > 0, p > 0 \end{cases} \tag{3}$$

where $\Gamma(p, bx) = \int_0^{bx} t^{p-1} e^{-t} dt$ is called an incomplete Gamma function.

If a sample is generated from a population with a Gamma distribution, and subsequently with the use of the Kolmogorov, Kolmogorov-Stephens, Cramer-von Mises, Watson and Anderson-Darling tests a composite hypothesis is verified that a sample comes from a population with an exponential distribution, then the test result depends only on a shape parameter p and the value of generated numbers from the interval (0. 1). Therefore, special attention should be put on the quality of the random number generator with a uniform distribution on the interval (0. 1). However, the result does not depend on a rate parameter, i.e. on a fixed sequence $\{y_i\}$ of numbers from the interval (0. 1) and the fixed value of shape parameter p. The value of test statistics for each test is the same for all permissible values of a rate parameter b (but, of course, it varies for different statistics). The reason behind this is that with a fixed size of random sample, statistical values depend only on the value of *c.d.f.* $G(x)$ with an exponential distribution for arguments $x_i = F^{-1}(y_i)$. As we show below, for a composite hypothesis the value of $G(x)$ does not depend on the rate parameter b.

Proof:
Let $\{y_i\}$, $i = 1, ..., n$, be a sequence of numbers from the interval (0. 1), $\{z_i\}$ be a sequence of numbers with the property that for every $i = 1, ..., n$ there

[1] If X has a distribution $\Gamma(b,p)$, then the random variable $Y = bX$ has a distribution $\Gamma(1,p)$. Background information on the use of probability distributions, statistical tests, and critical values can also be found in [6].

$$y_i = \frac{1}{\Gamma(p)}\int_0^{z_i} t^{p-1}e^{-t}dt \tag{4}$$

Let $z_i = bx_i$ ($b > 0$). According to (3) we have

$$F(x_i) = \frac{1}{\Gamma(p)}\int_0^{bx_i = z_i} t^{p-1}e^{-t}dt = y_i \tag{5}$$

and values $x_i = \frac{z_i}{b}$ come from a population with distribution $\Gamma(b,p)$.

We have:

$$\bar{x} = \frac{1}{n}\sum_{i=1}^{n} x_i = \frac{1}{n}\sum_{i=1}^{n}\frac{z_i}{b} = \frac{1}{nb}\sum_{i=1}^{n} z_i = \frac{1}{b}\bar{z} \tag{6}$$

and for the composite hypothesis that the sample comes from a population
with an exponential distribution we have:

$$G(x_i) = 1 - e^{-\frac{x_i}{\bar{x}}} = 1 - \exp\left(-\frac{\frac{z_i}{b}}{\frac{1}{nb}\sum_{i=1}^{n} z_i}\right) = 1 - e^{-\frac{z_i}{\bar{z}}} \tag{7}$$

So from (4), with fixed values of p and y_i, the values of z_i are unambiguously determined and the value of the *c.d.f.* $G(x_i)$ does not depend on the value of b.

Power distribution

A similar situation occurs in the case of a power distribution defined by the *c.d.f.*:

$$F(x) = \begin{cases} 0 & , \ x \le 0 \\ \left(\frac{x}{b}\right)^{\delta} & , \ x \in (0,b], b, \delta > 0 \\ 1 & , \ x > b \end{cases} \tag{8}$$

where b is a rate parameter and δ is a shape parameter.

$$\text{If } \ y_i = \left(\frac{x_i}{b}\right)^{\delta}, \text{ then } \ x_i = b(y_i)^{\frac{1}{\delta}}, \ \bar{x} = \frac{b}{n}\sum_{i=1}^{n}(y_i)^{\frac{1}{\delta}}, \tag{9}$$

$$G(x_i) = 1 - e^{-\frac{x_i}{\bar{x}}} = 1 - \exp\left(-\frac{b(y_i)^{\frac{1}{\delta}}}{\frac{b}{n}\sum_{i=1}^{n}(y_i)^{\frac{1}{\delta}}}\right) = 1 - \exp\left(-\frac{n(y_i)^{\frac{1}{\delta}}}{\sum_{i=1}^{n}(y_i)^{\frac{1}{\delta}}}\right) \tag{10}$$

and with a fixed sequence $\{y_i\}$ and the fixed value of shape parameter δ, the value of the *c.d.f.* $G(x_i)$ does not depend on the rate parameter b.

Weibull distribution

If we generate a Weibull distribution defined by the c.d.f:

$$F(x) = \begin{cases} 0 & , \ x \le 0 \\ 1 - e^{-(bx)^{v}} & , \ x, b, v > 0 \end{cases} \tag{11}$$

where v is a shape parameter, b is a rate parameter, then:

$$\text{If } \ y_i = e^{-(bx_i)^{v}}, \text{ then } \ x_i = b^{-1}(-\ln y_i)^{\frac{1}{v}},$$

$$\bar{x} = \frac{1}{nb}\sum_{i=1}^{n}(-\ln y_i)^{\frac{1}{v}}, \tag{12}$$

$$G(x_i) = 1 - e^{-\frac{x_i}{\bar{x}}} = 1 - \exp\left(-\frac{b^{-1}(-\ln y_i)^{\frac{1}{v}}}{\frac{1}{nb}\sum_{i=1}^{n}(-\ln y_i)^{\frac{1}{v}}}\right) = 1 - \exp\left(-\frac{n(-\ln y_i)^{\frac{1}{v}}}{\sum_{i=1}^{n}(-\ln y_i)^{\frac{1}{v}}}\right) \tag{13}$$

and with fixed sequence $\{y_i\}$ and the fixed value of shape parameter v, the value of the *c.d.f.* $G(x_i)$ does not depend on the rate parameter b.

If we generate a Weibull distribution with a fixed shape parameter v and we form hypothesis H_0 that the distribution comes from a population with a Weibull distribution and with the same shape parameter v, then we use the property that if a random variable X has a Weibull distribution with parameters v and b, then a random variable $Z = X^v$ has an exponential distribution with parameter b^v [4]. This means that the verification of the hypothesis that X has a Weibull distribution, when a shape parameter v is fixed, is equivalent to verifying the hypothesis that Z has an exponential distribution. By using the previous calculations (12), (13):

$$z_i = (x_i)^{v} = \left(b^{-1}(-\ln y_i)^{\frac{1}{v}}\right)^{v} = b^{-v}(-\ln y_i),$$

$$\bar{z} = \frac{1}{nb^{v}}\sum_{i=1}^{n}(-\ln y_i) \tag{14}$$

$$G(z_i) = 1 - e^{-\frac{z_i}{\bar{z}}} = 1 - \exp\left(-\frac{b^{-v}(\ln y_i)}{\frac{1}{nb^{v}}\sum_{i=1}^{n}(\ln y_i)}\right) = 1 - \exp\left(-\frac{n\ln y_i}{\sum_{i=1}^{n}\ln y_i}\right) \tag{15}$$

and with a fixed sequence $\{y_i\}$ and the fixed value of shape parameter v, we found that the value of the *c.d.f.* $G(z_i)$ does not depend on the rate parameter b.

Note also that if for the fixed sequence $\{y_i\}$ we generate the exponential distribution (with parameter $\lambda = b$) described by the function:

$$G(x) = \begin{cases} 0 & , \ x \le 0 \\ 1 - e^{-\lambda x} & , \ x > 0, \lambda > 0 \end{cases} \tag{16}$$

we get a simple sample$\{x_i\}$, then by assuming that $v = 1$ (Weibull distribution for $v = 1$ is exponential) and using (12) and (13) we obtain the same result as in (15), i.e. $G(x_i) = G(z_i)$, so the value of test statistics mentioned at the beginning of goodness-of-fit tests are the same.

These results are important for examining the power of tests and the compatibility of test results, while verifying a hypothesis about an exponential distribution by means of a simulation method. With a fixed sample $\{y_i\}$ drawn from a population with a uniform distribution from the interval (0. 1), the result of goodness-of-fit test (for a composite hypothesis) does not depend on the rate parameter b of generated distribution. This means that a rate parameter may be chosen freely, e.g. $b = 1$, without affecting the results of simulation.

Using the above proven properties and results given in Fisz's book [3], we are able to calculate the power of tests based on the Kolmogorov's statistics for hypothesis about an exponential distribution against the alternative hypothesis (a sample comes from a population with Weibull distribution). For calculating can be used the values of *c.d.f.* of exponential and Weibull distributions (for a fixed shape parameter p) with the rate parameter $b = 1$. Using the limiting distribution Fisz gives a lower bound of the M power of λ Kolmogorov test [3, p. 593] as:

$$M \geq 1 - \frac{1}{\sqrt{2\pi}} \int_a^b e^{-\frac{z^2}{2}} dt \tag{17}$$

where

- $\alpha = \dfrac{-\lambda_\alpha - \delta\sqrt{n}}{\sqrt{F(x_0)\left(1 - F(x_0)\right)}}$
- $b = \dfrac{\lambda_\alpha - \delta\sqrt{n}}{\sqrt{F(x_0)\left(1 - F(x_0)\right)}}$
- $\delta = \left|F(x_0) - G(x_0)\right| = \sup_{-\infty \leq v \leq +\infty} \left|F(x) - G(x)\right|,$
- $G(x)$ and $F(x)$ denote the *c.d.f.* of continuous distributions specified for null and alternative hypothesis respectively,
- λ_α - critical value of test,
- n - sample size.

At the same time

$$M \geq 1 - P\left(nG(x_0) - \lambda_\alpha \sqrt{n} < nS_n(x_0) < nG(x_0) + \lambda_\alpha \sqrt{n}\right) \tag{18}$$

where $S_n(x) = 1/n$ card $\{x_i: x_i < x\}$ is the empirical *c.d.f.* Because $nS_n(x)$, when the sample $\{x_i\}$ comes from a population with distribution described by the *c.d.f.* $H(x)$, has a Bernoulli distribution with parameters $H(x)$ and n, so on the condition that the alternative hypothesis is true, the power of Kolmogorov test should not be less than the probability of getting at most $[nG(x_0) - \lambda_\alpha \sqrt{n}]$ or at least $[1 + nG(x_0) + \lambda_\alpha \sqrt{n}]$ successes[2)] in n Bernoulli's trials with probability of success $p = F(x_0)$.

3. Calculating results

Table 2 demonstrates the estimates of the power of classical λ Kolmogorov and Kolmogorov-Stephens tests (Table 1) using the inequality (17) for a sample of size 100. It was assumed that H_0 denotes the hypothesis that distribution in the general population is exponential distribution, and that H_1 denotes the alternative hypothesis that distribution in the general population is the Weibull distribution with a shape parameter v (for selected values of the parameter v). The level of significance is equal to 0.05. The rate parameter was assumed to be equal to 1. Numerically were determined the values of exponential *c.d.f.* and Weibull distributions, the maximum difference between the *c.d.f.*, as well as and the value of the argument, for which the difference reaches a maximum. Table 3 shows the estimates of test power obtained using the inequality (18) for a sample of size $n = 25$; 50; 75; 100; 1000; 10 000. Table 4 gives the estimates of test power collected by simulation study based on 10 000 random samples. All calculations were performed in the Excel spreadsheet.

4. Conclusions

The analysis of Tables 2 and 3 shows that the lower estimates for both methods ($n = 100$) are very similar, so the differences might be considered negligible. At the same time the power of KS test is greater than of K test and the power of K-S1 is greater than KS test. This is particularly evident for the value of rate parameter close to 1. The differences diminish with the increase and decrease in the value of rate parameter, which is natural since then the power of test increases to 1, and 1 is the upper bound of the power of test. Simulation study did not fully confirm estimates in Tables 2 and 3. The power of tests estimated on the basis of simulations is up to 10 times higher than what the formulas (17) and (18) indicate (it should be borne in mind that these are lower estimates). However, the nature of the changes of the test power is preserved, together with the change of the shape, as well as relationships between the individual tests. Tables 2, 3 and 4 show that the attempt to distinguish the exponential distribution from the Weibull distribution for shape parameter close to 1 is pointless for random samplings of a small size. Significant distinction occurs only for samples of a size approximately tens of thousands (according to Tables 2 and 3), but taking a sample of such size is virtually impossible. Simulation results suggest that at least for the KS test, and the K-S1 test that the sample size should be of at least a few thousand. However, samples of such size happen very rarely in practice. The results of Tables 2, 3 and 4 confirm the previously reached conclusion that the classical Kolmogorov test is not very useful at least for small and medium-sized samples and composite hypothesis. Therefore, the results of hypotheses verification with the use of this test must be approached with extreme caution.

[2)] where $nG(x_0) + \lambda_\alpha \sqrt{n}$ is a natural number

Used statistical tests and critical values of tests

Table 1

Name and designation of the test	Test statistics	Critical value of the test for the significance level $\alpha = 0.05$
Kolmogorov **K**	$D = \sqrt{n}\left(\max_{1\le i\le n}\left(\left\|\frac{i}{n} - F(x_i)\right\|, \left\|F\left(x_i - \frac{i-1}{n}\right)\right\|\right)\right)$	$n = 100$ 1.3403
Kolmogorov–Stephens **K-S**	$D_1 = \left(D + \frac{0.2}{n}\right)\left(\sqrt{n} + 0.26 + \frac{0.5}{\sqrt{n}}\right)$	1.094
Kolmogorov–Stephens **K-S1**	$\sqrt{n}\,D$	$n = 100$ 0.9900

Source: test and critical values of K – [4], K-S test, K-S1 and critical values – [5]

Estimates with the use of formula (17) of lower powers (in %) of K, K-S and K-S1 tests for testing hypothesis about an exponential distribution and Weibull distribution as an alternative hypothesis for selected rate parameters ν for $n = 100$

Table 2

v	x_0	$G(x_0)$	$F(x_0)$	$\lvert G(x_0) - F(x_0)\rvert$	M power of test [%]		
					K	K-S	K-S1
0.30	0.101	0.3950960310044430	0.0960669671141359	0.2990290638903070	99.96	99.99	100.00
0.40	0.129	0.3564748778867340	0.1210260344544170	0.2354488434323170	98.29	99.58	99.78
0.50	0.155	0.3254438727669140	0.1435848225163860	0.1818590502505280	84.63	93.90	96.15
0.60	0.179	0.2996777441522180	0.1638941006029640	0.1357836435492530	51.53	71.77	78.90
0.65	0.190	0.2880686305666230	0.1730408660566380	0.1150277645099850	33.74	54.94	63.83
0.70	0.201	0.2776640401393210	0.1820875684461410	0.0955764716931803	19.53	37.88	46.95
0.75	0.212	0.2683327176459230	0.1910353024335000	0.0772974152124229	10.02	23.44	31.22
0.80	0.222	0.2591618860026900	0.1990846356653410	0.0600772503373488	4.57	13.02	18.73
0.85	0.232	0.2508716553216730	0.2070538766933160	0.0438177786283568	1.87	6.54	10.20
0.90	0.241	0.2425919678739540	0.2141583736116540	0.0284335942622996	0.70	3.01	5.13
0.95	0.250	0.2350488976032350	0.2211992169285950	0.0138496806746403	0.25	1.39	2.62
0.98	0.256	0.2313137013105780	0.2258580312077520	0.0054556701028261	0.16	1.01	1.99
1.02	0.263	0.2259104675072760	0.2312581026888400	0.0053476351815641	0.15	0.95	1.89
1.05	0.268	0.2219181960499450	0.2350922188971360	0.0131740228471907	0.20	1.19	2.29
1.10	0.276	0.2154625763106550	0.2411870692387590	0.0257244929281033	0.43	2.14	3.86
1.15	0.284	0.2095353618438110	0.2472333552938040	0.0376979934499930	0.90	3.92	6.64
1.20	0.292	0.2040950919851770	0.2532314640266430	0.0491363720414658	1.76	6.75	10.81
1.30	0.307	0.1937947833844060	0.2643493990927470	0.0705546157083403	5.42	16.29	23.59
1.40	0.322	0.1850623119905970	0.2753018096700970	0.0902394976794999	12.97	31.09	41.08
1.50	0.335	0.1762558279746490	0.2846619136474400	0.1084060856727910	25.06	48.96	59.75
1.70	0.360	0.1614505387433630	0.3023236739289690	0.1408731351856060	57.38	80.38	87.24
2.00	0.394	0.1437869126506990	0.3256459437595560	0.1818590311088570	91.36	98.05	99.09
2.50	0.441	0.1211584098674260	0.3566072934270440	0.2354488835596170	99.91	99.99	100.00
3.00	0.480	0.1046960415637330	0.3812166081938590	0.2765205666301260	100.00	100.00	100.00
4.00	0.541	0.0820957234975253	0.4178342046013590	0.3357384811038330	100.00	100.00	100.00
5.00	0.588	0.0678754922000777	0.4445629513019820	0.3766874591019040	100.00	100.00	100.00
10.00	0.718	0.0357570490498701	0.5122732653742690	0.4765162163243990	100.00	100.00	100.00

Symbols as in formula (17) and in Table 1
Source: own elaboration

Estimates using the formula (18) of the power (in %) of K, K-S and K-S1 tests for testing hypotheses of an exponential distribution and Weibull distribution as an alternative hypothesis for selected shape parameters v and sample size *n* Table 3

v	*n* = 25			*n* = 50			*n* = 75			*n* = 100			*n* = 1000			*n* = 10 000			*n* = 100 000		
	K	K-S	K-S1	K	K-S	K-S1	K	K-S	K-S1	K	K-S	K-S1	K	K-S	K-S1	K	K-S	K-S1	K	K-S	K-S1
0.30	78.51	91.43	91.43	99.30	99.93	99.93	99.99	100	100	100	100	100	100	100	100	100	100	100	100	100	100
0.40	40.27	64.14	82.22	85.55	96.57	96.57	98.36	99.68	99.87	99.83	99.97	99.99	100	100	100	100	100	100	100	100	100
0.50	10.77	28.28	50.77	41.00	71.45	82.75	72.45	88.76	93.50	92.43	97.45	98.63	100	100	100	100	100	100	100	100	100
0.60	1.14	19.85	19.85	15.03	41.14	56.32	29.67	65.78	65.78	52.40	80.23	86.55	100	100	100	100	100	100	100	100	100
0.65	0.87	5.39	16.76	5.14	21.48	34.62	22.91	45.51	57.60	32.50	53.21	63.38	100	100	100	100	100	100	100	100	100
0.70	0.66	4.32	14.10	3.69	17.05	17.05	10.28	26.57	37.56	16.86	33.73	43.78	100	100	100	100	100	100	100	100	100
0.75	0.50	3.45	3.47	0.85	6.51	13.38	3.69	12.82	20.58	7.24	18.07	25.88	99.68	99.96	99.99	100	100	100	100	100	100
0.80	0.001	2.84	2.84	0.59	4.97	4.99	1.09	5.22	9.60	2.66	8.38	19.86	91.50	97.67	98.68	100	100	100	100	100	100
0.85	0.01	0.36	2.33	0.41	1.41	3.80	0.71	3.70	7.11	0.81	5.81	9.65	54.79	77.06	83.44	100	100	100	100	100	100
0.90	0.02	0.32	2.17	0.07	1.12	2.98	0.17	1.25	2.79	0.22	2.25	4.17	12.88	30.58	42.16	99.98	100	100	100	100	100
0.95	0.02	0.30	0.57	0.06	0.90	1.10	0.12	0.92	2.12	0.15	0.83	1.72	1.34	5.62	8.80	53.46	76.18	82.95	100	100	100
0.98	0.03	0.29	0.62	0.10	0.34	1.06	0.08	0.52	1.23	0.07	0.70	1.46	0.21	1.35	2.89	2.59	9.36	14.60	81.33	93.44	96.07
1.02	0.04	0.30	0.70	0.09	0.36	1.07	0.10	0.57	1.29	0.15	0.64	1.26	0.25	1.37	2.40	2.50	8.88	13.31	78.51	92.12	95.09
1.05	0.05	0.31	0.76	0.11	0.80	1.11	0.12	0.64	1.40	0.17	0.75	1.42	1.25	4.86	7.52	45.62	69.27	77.04	100	100	100
1.10	0.24	0.80	0.90	0.16	1.01	2.09	0.36	1.44	2.69	0.52	1.69	2.87	8.87	22.21	31.86	99.77	99.97	99.99	100	100	100
1.15	0.30	0.98	1.06	0.55	1.24	2.63	0.52	1.96	3.53	0.79	3.89	6.15	32.13	54.81	66.10	100	100	100	100	100	100
1.20	0.38	1.19	1.26	0.73	3.26	3.30	1.43	4.53	7.48	1.99	5.23	8.03	65.98	84.10	88.87	100	100	100	100	100	100
1.30	0.57	1.69	4.36	1.22	4.88	8.76	2.51	7.15	11.21	5.72	12.63	17.76	97.39	99.43	99.70	100	100	100	100	100	100
1.40	0.82	2.32	5.70	3.81	11.99	12.00	6.78	15.95	22.78	13.36	25.01	32.48	99.96	100	100	100	100	100	100	100	100
1.50	1.11	7.07	7.07	5.26	15.30	23.54	14.45	28.68	37.79	18.48	40.36	49.06	100	100	100	100	100	100	100	100	100
1.70	4.68	10.24	19.66	14.89	32.92	32.92	31.86	51.08	61.01	47.11	64.23	72.08	100	100	100	100	100	100	100	100	100
2.00	7.86	15.69	27.58	35.12	58.66	58.66	58.46	76.21	83.30	80.63	90.39	93.65	100	100	100	100	100	100	100	100	100
2.50	25.08	39.65	56.08	64.81	83.72	83.72	89.85	96.22	97.89	97.41	99.15	99.55	100	100	100	100	100	100	100	100	100
3.00	34.02	49.84	65.88	85.04	94.99	94.99	97.48	99.31	99.67	99.80	99.96	99.98	100	100	100	100	100	100	100	100	100
4.00	64.53	78.34	88.52	96.86	99.32	99.32	99.90	99.98	99.99	100	100	100	100	100	100	100	100	100	100	100	100
5.00	74.02	85.39	92.91	99.44	99.78	99.92	99.99	100	100	100	100	100	100	100	100	100	100	100	100	100	100
10.0	95.83	98.40	99.48	99.99	100	100	100	100	100	100	100	100	100	100	100	100	100	100	100	100	100

Symbols as in Table 2
Source: own elaboration

Estimates of power (in %) of K, KS and K-S1 tests for testing hypotheses of an exponential and Weibull distributions for selected shape parameters, when samples came from Weibull distribution. Simulation study of 10 000 random samples Table 4

v	K	K-S	K-S1
0.85	14.05	42.26	48.63
0.90	4.11	20.07	24.94
0.95	1.35	9.51	13.04
0.98	0.65	6.87	10.02
1.02	0.58	7.71	10.45
1.05	1.09	10.20	13.51
1.10	3.68	19.91	25.15
1.15	7.49	32.54	39.06
1.20	14.46	48.21	55.59

Symbols as in formula (17) and in Table 2
Source: own elaboration

Note that the statistical tests do not distinguish between an exponential distribution and other distributions, such as Weibull or gamma, as so for a particular group of parameters this can be an important argument for the application of an exponential distribution in various models, despite theoretical objections to its use. If the differences are "invisible" to the statistical apparatus, they might be considered negligible.

References

[1] ROGOWSKA, R., ROGOWSKI, A.: Compliance of the Results of Hypothesis Testing with Normal Distribution for Selected Statistical Tests (in Polish), Logistyka, No. 3, 2011 (Logistyka – nauka, materialy VIII Konferencji Naukowo-Technicznej „Logitrans" – Logistyka, Systemy Transportowe, Bezpieczenstwo w Transporcie).

[2] ROGOWSKI, A.: Compliance of the Results of Hypothesis Testing with Exponential Distribution for Selected Statistical Tests, *The Archives of Transport,* vol. 24, No. 4, 2012.

[3] FISZ, M.: *Probability Theory and Mathematical Statistics (in Polish),* PWN, Warszawa 1967.

[4] FIRKOWICZ, S.: *Statistical Testing of Products,* WNT, Warszawa 1970.

[5] DOMANSKI, CZ.: *Nonparametric Statistical Tests (in Polish),* PWE, Warszawa 1979.

[6] ROGOWSKI, A.: *The Basics of Probabilistic Methods in Transport (in Polish),* seria Monografie, No. 175, Wydawnictwo Uniwersytetu Technologiczno-Humanistycznego, Radom 2012.

Dusan Jandacka *

CONTRIBUTORY ASSESSMENT OF CREATION OF PM_{10} AS IMPACTED BY VEHICULAR TRAFFIC BASED ON THE PRESENCE OF HEAVY METALS

Emissions from different sources create a very complex mixture in the air both in qualitative and quantitative terms. Their composition is the result of distribution of all the sources in space and time, their size and characteristics of the pollutants on one side, and meteorological and climatic conditions on the other. Department of Highway Engineering of the Faculty of Civil Engineering at the University of Zilina has taken part in the project that focuses on the monitoring of dust particles formation initiated by road transport depending on both the road surface and traffic intensity, load. During the project the monitoring was focused on the measurement of various fractions of particulate matter and 17 heavy metals in the PM 10 fraction. The aim was to identify sources of particulate matter by means of statistical methods. The problem solving assumes the knowledge of multivariate statistical data analysis methods as, for instance, principal components analysis (PCA), factor analysis (FA) and multivariate regression and vector algebra. For the application of methodology suitable software may prove appropriate. The STATISTICA software, a computer program and the method of PCA and FA were used to quantify the contributions of individual sources of air pollution to solid particles. Data matrix with rows corresponding to individual measurements (samples) and columns corresponding to variables (measured pollutants) served as an input for calculations. Pollutants characterizing and defining the sources of pollution were selected as variables.

Keywords: *Particulate matter, road traffic, air pollution, PM_{10}, heavy metals, statistical methods.*

1. Introduction

The Faculty of Civil Engineering at the University of Zilina has been involved with the project, the goal of which is the monitoring of particulate matter creation resulting from the road traffic as well as its contamination in a direct relation to the surface of roads and the traffic load [1, 2, 3].

Heavy metals belong among the most basic groups of contaminants which are monitored in the various parts of the environment. The concerned group of contaminants is quite a large one, including the contaminants having a variable source of their origination and in many cases, the contaminants concerned share a different platform of professional approach from the scientific circles related to their impact and influence as related to the health of population. The subject of monitoring, pursuant to the general law [4] are the following elements: As, Cd, Hg, Pb and Ni. These are generally considered as the most harmful to people and animals. Their limits are governed by the Public Notice [5]. Even some of the other elements may be of dangerous nature, which is to be found in soils where they are necessary in small amounts; however, when accumulated in large quantities, they may have an even more toxic impact than the aforementioned elements. In this way, the following elements are to be considered: Cr, Co, Sn, Sb, Cu, Ni, Ag, Au, Zn, Mo, V, Mn, Fe and other [6]. These elements are bound with fine particles of aerosols. Heavy metals do enter the environment by virtue of natural and anthropogenic processes. Natural sources include in situ weathering processes and atmospheric deposition of metals, oceanic processes and volcanic eruptions. Anthropogenic sources include burning fossil fuels in order to generate electricity, raw materials excavation and ore processing, industrial processes, agricultural activities and a continuously increased usage of motor vehicles.

2. Particulate matter amount determination and chemical analysis of metals

Readings of particulate matter were performed in the close vicinity of the urban connecting route, road in regular intervals, namely 4 times per year. The goal was a long-term monitoring of a proportional representation of particulate matter (PM) in the atmosphere and its behaviour when related to the outer conditions. In the second phase of project a chemical analysis of particulate matter was performed as well as the determination of its possible source.

In order to establish the amount of particulate matter present in the outer atmosphere, a reference method pursuant to the stan-

* **Dusan Jandacka**
Department of Highway Engineering, Faculty of Civil Engineering, University of Zilina, Slovakia, E-mail: dusan.jandacka@fstav.uniza.sk,

dards of STN EN 12341 [7] and STN EN 14907 [8] was used. The measurement readings were performed by means of low volume flow samplers of LECKEL LVS3 (Single Filter Gravimetric Sampler) amounting to the total number of 3 pieces. Concurrently, the three fractions of particulate matter were monitored, which include the following: PM_{10}, $PM_{2.5}$ and $PM_{1.0}$. They were trapped in nitrocellulose filters of the 47 mm diameter and assessed in a gravimetric manner. The monitoring of atmosphere along the concerned road, route was performed in weekly cycles. The particulate matter is bound with various elements and compounds. To test all the chemical components of the particulate matter concerned would be ineffective, quite demanding and financially unsustainable. In the first phase did we concentrate on the monitoring of the selected heavy metals found in the fraction of PM_{10} [9]. Each of these metals may come from a specific source (Table 1). Based on a sufficiently comprehensive database of data it deems possible by the utilization of multidimensional statistical methods (for instance factor analysis), to more closely specify the possible source of these particles.

In order to identify or to determine the present chemical form of an observed element in the sample of particulate matter the spectroscopic methods are utilized. The analyses of filters and the determination of metals present in the fraction of PM_{10} were performed pursuant to the standard of STN EN 14902 [16].

Prior to specifying inorganic pollutants, the filters were reacted by the mixture of acids (HNO_3 and HF) and oxidizing agents with a resultant specification by means of the mass spectrometry method with inductively coupled plasma mass spectrometer ICP MS (Perkin – Elmer ELAN 6000 – USA) in cooperation with the Institute of Geology at the Faculty of Natural Sciences of Comenius University in Bratislava [17].

3. Used statistical methods

Multivariate statistical analyses of PCA – Principal component analysis and FA – Factor analysis were used for statistical assessment.

The primary goal of PCA is the transformation of the original characters of x_j, $j = 1, ..., m$, into a smaller amount of latent variables y_j. These latent variables possess more appropriate and comprehensive properties: their presence is less significant, they capture and represent almost the entire variability of the original characteristics, properties and they are mutually uncorrelated. Latent variables are known as the main components and they represent linear combinations of former variables: the first principal component (PC) y_1 describes the greatest part of variability, hence the dissipation, spread of the original data, the second principal component y_2 on the other hand the greatest part of variability, spread not-contained within y_1 etc.. Mathematically speaking, the first PC is viewed as a linear combination of input characters which covers the greatest variability, spread among the other linear combinations. The disparity between the coordinates of object in the former characters and the principal components, thence the loss of information by the projection into the smaller number of dimensions is known as the fitness rate of PCA model interpretation or it is also called the PCA model error. For the first PC the following relation prevails:

$$y_1 = \sum_{j=1}^{m} v_{1j} x_j \qquad (1)$$

where:
x_j former character, input variable, $j = 1, ..., m$,
v_{1j} coefficients of eigenvectors.

Within the process of factor analysis (FA) so called factor loadings are estimated for particular variables (pollutants) for a generated factor. Factor loadings are the expression of correlations between the particular variables and acquired factors. Based on the values of factor loadings it is possible to specify a group of variables for each factor, those ones which correlate with it in the closest-possible manner. And vice versa, by means of factor loadings, the identified factor is appended with an extent of impact on each of particular variables. The variables with the highest factor loadings for a generated factor are considered as decisive even when interpreting such a factor. A data matrix serves the purpose of input for calculations, whose lines correlate with particular measurements (objects) and bars of variables, i. e. measured pollutant (character).

Sources of metals contained in the particulate matter – in general [10, 11, 12, 13, 14,15] Table 1

Source		Selection of produced metals
Transportation	road surface abrasion	Al, Si, Ca, Mg, C, Na, K
	car-body components abrasion	Cu, Sn, Cr, Pb, Cd, As, Sb, Fe, Al
	brake callipers, pads and rotors abrasion	Cu, Sb, Ba
	tyre wear	Zn, Cd, Pb, Cu
	fuel combustion	Mo, V
	catalytic converter	Pt, Pa, Rh (Platinum metals)
Burning coal and wastes		Zn, Sb, Cu, Cd, Hg, Se, As, Cr, Co, Al
Industry		Sb, Ag, V, Ni, As, In, Cu, Mn, Ce, Co, Cr, Pb
Biomass burning		K
Soil and city-generated dust		Ti, Al, Fe, Mn, Cr, Cu, Th

The variables to be used are those pollutants which are able to specify anticipated sources of pollution.

The basic principle of factor analysis lies in the fact that each of monitored values X_j ($j = 1, ..., p$) may be expressed as a sum of a linear combination of a lesser amount m non-observed (hypothetical) random values $F_1, ..., F_m$ – so called common factors and the further source of variability E_j ($j = 1, ..., p$) – so called specific (residual) elements. Let us suppose that the following model prevails:

$$X_j = \sum_{k=1}^{m} \lambda_{jk} F_k + E_j, j = 1, ..., p, \quad (2)$$

where:

λ_{jk} factor loadings of the k common factor relevant to the j variable and of k factor, $k = 1, ..., m$,

F_k the k-th common factor,

E_j is a random deviation of the exact model, relevant to the k-th value, $j = 1, ..., p$.

Values $X_1, ..., X_p$ are standardized, i. e. they have a zero main value and unit variance. In the matrix form we get the FA model of the following string:

$$X = \Lambda \times \boldsymbol{F} + \boldsymbol{E} \quad (3)$$

The F matrix is called factor matrix. Furthermore, let us suppose that the random vectors F and E are non-correlated. In the FA method it is recommended to have at least 5 samples, while the optimum number of samples could reach 20 per each variable. The appropriateness of factor analysis used is proven by the test of KMO (Kaiser-Meyer-Olkin) and MSA – the extent of internal correlation [18], [19].

a) KMO (Kaiser-Meyer-Olkin) criterion is to be considered as an index for the comparison of magnitudes in experimental correlation coefficients when compared with magnitudes of partial correlation coefficients. Should the sum of squares in partial coefficients among all the pairs of characters remain low in comparison with the sum of squares of pair-forming correlation coefficients, the KMO measure of sampling adequacy shall be close to 1. Low values in KMO on the other hand signify that FA of former characters shall not be interpreted as a good approach taken, as the correlation among all the character pairs may not be substantiated by mediation of other characters. Kaiser defined the measure of KMO, in case the correlation measure is to be assessed, in the following way:
KMO $\approx$ 0.9 signifies excellent degree of correlation, KMO $\approx$ $\approx$ 0.8 still an acceptable degree of correlation, KMO $\approx$ 0.7 average extent of correlation, KMO $\approx$ 0.6 mean, medium extent of correlation, KMO $\approx$ 0.5 weak correlation, KMO lower than 0.5, the correlation to be considered as unacceptably low.

$$KMO = \frac{\sum_{i \neq j}^{m} \sum_{j \neq i}^{m} r_{ij}^2}{\sum_{i \neq j}^{m} \sum_{j \neq i}^{m} r_{ij}^2 + \sum_{i \neq j}^{m} \sum_{j \neq i}^{m} a_{ij}^2} \quad (4)$$

Where r_{ij} is a pair correlation coefficient between the i-th sign and j-th sign and a_{ij} is to be considered a partial correlation coefficient between i-sign and j-sign.

a) MSA represents the measure of internal correlation degree among the former signs and by the very same means the extent of appropriateness for adopting the factor analysis. This index gains values within the interval between 0 up to 1:
$MSA_i \approx 1$, je i-th sign predicated in the most perfect way by means of other signs, $MSA_i \approx 0.8$, predicated still well within range, $MSA_i \approx 0.7$, predicated on an average base, basis, $MSA_i \approx 0.6$, predicated to a medium extent, $MSA_i \approx 0.5$, predicated to a weak extent and if the MSA_i shall remain lower than 0.5 the predication is unacceptable as well as inappropriate.
In order to carry out the FA successfully, a high value in the MSA measure is required. By means of MSA it is also equally possible to monitor the addition and subtraction of former signs, operators and characteristics, as by means of the MSA method, every character, sign or operator may be enumerated and expressed numerically.

$$MSA_i = \frac{\sum_{i \neq j}^{m} r_{ij}^2}{\sum_{i \neq j}^{m} r_{ij}^2 + \sum_{i \neq j}^{m} a_{ij}^2} \quad (5)$$

In order to approximate the contribution of specific sources of PM the method of Absolute Principal Component Scores is adopted, abbreviated as – APCS in conjunction with Multiple Regression Analysis – MRA. First of all the values of factor scores F are estimated. In order to acquire to factor scores with the physics-oriented meaning, the APCS matrix is calculated, in the way that the reference value of factor scores F_0 is calculated, which is subtracted from the calculated F matrix following the relation

$$APCS = F - F_0. \quad (6)$$

By means of utilization of Multiple Regression Analysis, where PM is a dependent variable and APCS are independent variables, one can ascertain the contributions of separately-identified sources. These are added up, while being summarized, as of the determined regression coefficients by means of their multiplication using the mean value of APCS for each common factor as an absolute contribution, which is out of the total concentration of PM re-calculated and transferred into the percentile contribution of given sources [20].

4. Statistical analysis of measured results

Multilayer statistical analyses were applied on the data file consisting of measurements of concentrations in analysed metals (Na, Mg, Al, Ca, Cu, Sb, Ba, Pb, Cd, Cr, As, Mo, V, Mn, Fe, Ni, Zn) as well as PM_{10} concentrations. The overall matrix contained 18 columns (variables) and 108 rows (objects, operators - measurements). This very matrix contains the concentration of metals and PM_{10} for daily and nightly sampling.

In order to establish the appropriateness of the factor analysis adoption the criteria of KMO and MSA were calculated. In accordance with them the adoption of factor/factorial analysis is substantiated. The results of statistical tests for the appropriateness of factor analysis adoption:

- MSA criterion: Na – 0.86, Mg – 0.73, Al – 0.83, Ca – 0.81, Cu – 0.91, Sb – 0.95, Ba – 0.93, Pb – 0.87, Cd – 0.9, Cr – 0.89, As – 0.91, Mo – 0.88, V – 0.86, Mn – 0.88, Fe – 0.92, Ni – 0.88, Zn – 0.91, PM_{10} – 0.83 » particular characters are predicated with the other ones very precisely,
- KMO criterion: KMO = 0.88 – a very good correlation of characters,
- Bartlett Sphericity Test: Criterion = 2501.7, Degrees of variance = 153, P = 0.000.

The calculated significance level of P is significantly lower than the given level of $\alpha = 0.05$, that is why the PCA may be applied on this set of data, readings [21].

Whereas, at the factor analysis it is deemed to be necessary to specify the number of factors and then the calculation may be run, during the first step the analysis of principal components was performed. As a result of which we could conclude the possible number of principal components which, to a sufficient measure, specify the variability, variety of characters. As observed in the Fig. 1 we are able to select the number of principal components 3. The three principal components define 79.66 % of the total variability of the original characters [21].

There were 3 factors selected for the factor analysis. The used model of factors rotation was Varimax. In the Table 2 the factor loadings of characters are quoted in relation to factors. They may be explained as the correlation between the factors and characters. They represent the most important unit of information the interpretation of factors is based on.

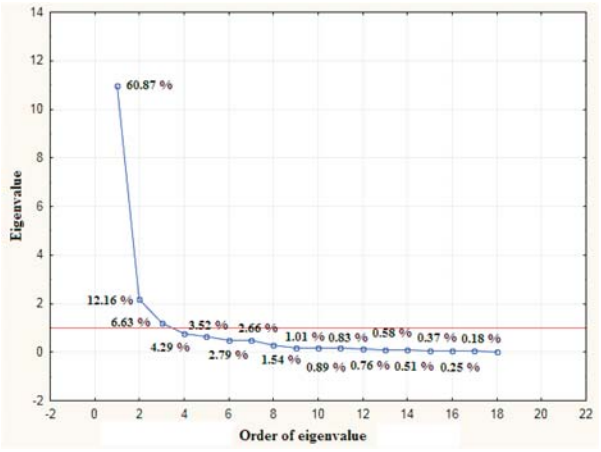

Fig. 1 Eigenvalues of Correlation Matrix Chart [21]

Each factor is contributed by several elements (characters). As the most decisive factor of loads the values close to or greater than 0.7 were selected. Based on the representation and presence of elements in particular, selected factors, the following factors may be named.

Factor 1.: Na, Pb, Cd, Zn, PM_{10}
Factor 2.: Cu, Sb, Ba, Mo, Fe **Factor 3.:** Mg, Ca

Values of factor loads and their transformation into the factor equations (Factor 1 to Factor 2, Factor 2 to Factor 3) [21] Table 2

Variable	Factor 1	Factor 2	Factor 3
Na	**0.731243**	0.239047	0.174231
Mg	0.131402	0.104391	**0.948492**
Al	0.079466	0.681083	0.564493
Ca	0.211769	0.390023	**0.857842**
Cu	0.523754	**0.744955**	0.227409
Sb	0.427920	**0.741372**	0.256502
Ba	0.273923	**0.783796**	0.486153
Pb	**0.856858**	0.239686	0.118103
Cd	**0.898693**	0.237152	0.047900
Cr	**0.699834**	0.339355	0.121727
As	0.395564	0.477598	0.199278
Mo	0.210323	**0.906938**	0.213498
V	0.244208	0.483371	0.619649
Mn	0.619768	0.670952	0.260199
Fe	0.314326	**0.892339**	0.092341
Ni	**0.680881**	0.399069	0.202344
Zn	**0.785544**	0.361700	0.215592

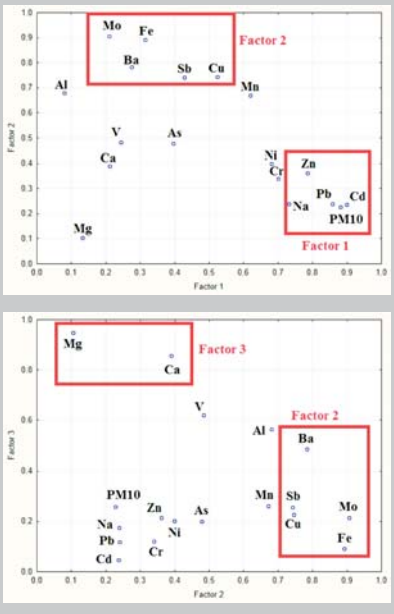

APCS Results:
Measurements of Multiple Regression Analysis

Results as of the multilayer regression analysis (PM_{10} is a dependant variable, independent variables absolute score for specific factors) [21] Table 3

Estimate	Parameter	Std. Error	t-value	p	Significance of the variable
(Non-specified)	9.40	2.13	4.42	$2.39e^{-5}$	***
APCSFactor1	33.78	1.00	32.76	$<2.00e^{-16}$	***
APCSFactor2	6.91	1.00	6.91	$3.98e^{-10}$	***
APCSFactor3	9.79	1.01	9.68	$3.49e^{-16}$	***

All the variables (factors) are within the model to be understood as significant ones (***) and to a greater extent contribute to PM10 concentrations (Table 3).

Determination coefficient describes a share of the overall distribution, which may be clarified by means of a linear relation. In this case it bears the value of $R^2 = 0.92$, which means that the linear relation clarifies a sufficient part of the overall variability.

The significance level is very small $P = 2.2e^{-16}$, the adoption of a given model thence sufficiently significant [21].

Absolute contributions of factors towards the mean concentration of PM10 [μg/m3] [21]:

	Unresolved	APCS1	APCS2	APCS3
APCS	**9.40**	**29.66**	**9.48**	**8.00**

Percentile contributions of factors towards the mean concentration of PM10 [%] [21]:

	Unresolved	APCS1	APCS2	APCS3
APCS	**16.62**	**52.45**	**16.77**	**14.16**

5. Discussion on the achieved results

In order to identify the origin of the particulate matter at the aforementioned monitoring station, the usage of factor analysis proved as the appropriate one. As resulted from the factor analysis, the original dataset may be explained using several factors. The four factors explain 79.66 % of the total variability of the original characters. Naming these factors is enabled based on the characters, which specify unique factors. This is, at the same time, conditioned by a supposition of the fact where separate elements – heavy metals – may originate from. The survey on the origin may be drawn from the former research surveys performed by various authors. In the monitored station, the primary cause of particulate matter originates as a consequence of the vehicular traffic. We follow the supposition that the observed metals are traced to specific automotive components and the road surface itself (Table 1). Based on the results of factor analysis and the supposed sources, the factors of 1 and 3 were named, designated in the following manner: Factor 1 – Tyre wear and tear and gritting materials. Factor 2 – Brake pads lining tear and wear, brake pads, car components and combustion of propulsive, propulsion fuels. Factor 3 – Road pavement wear – aggregate, road tar binders and road dust.

Using the APCS method while supported by adoption of the input data the following may be implicated: the contribution of the tyre tear and wear and gritting materials to the PM_{10} formation by **52.45 %**, brake pads lining tear and wear, brake pads, car components and combustion or propulsive, propulsion fuels by **16.77 %**, road pavement wear – aggregate, road tar binders and road dust by **14.16 %** and unresolved part by **16.62 %**. A detailed specification of contribution towards particular sources of PM_{10} formation may be narrowly specified by a number of chemical elements and compounds, based on which statistical analyses are performed. In our case, the analyses performed incorporated the selection of 17 heavy metals, which are typical for vehicular traffic and road transportation [21].

Acknowledgements

The paper originated thanks to being supported by means of a grant for the scientific research task VEGA 1/0508/2011 entitled Overall characteristics and chemical composition of particulates as created by the vehicular traffic.

References

[1] DECKY, M., DURCANSKA, D.: *Environmental impact objectification of traffic noise and air pollution.* In: Theoretical Foundation of Civil Engineering: XVII Polish-Russian-Slovak Seminar: proceedings: Warszawa – Wroclaw, 02.06-06.06.2008. In Zilina: University of Zilina, 2008. ISBN 978-80-8070-855-9. p. 383–388.

[2] DURCANSKA, D.: Monitoring of particulate matter in the air around roads. In: *Science journal of transportation:* international cooperation journals MADI - SWJTU - UTC. ISSN 1859-2724; 1993-8543; 1005-2429. Espec. iss. no. 03 (2011), p. 78–85.

[3] DURCANSKA, D., DECKY, M., LICBINSKY, R., HUZLIK, J.: Project SPENS – Sustainable Pavement for European New Members States, *Communications – Scientific Letters of the University of Zilina,* vol. 15, No. 2, 2013, ISSN 1335-4205.

[4] Act of the National Council of the Slovak Republic No. 137/2010 on the Air and Atmosphere.

[5] Public Notice, Decree No. 360/2010 of the Ministry of Agriculture and the Environment and the Regional Development of the Slovak Republic on the quality of air.
[6] DURZA, O.: The Utilization of Soil Magnetometry in the Environmental Geochemistry of Heavy Metals. *Acta Geologica Universitatis Comenianae*, No. 58, 2003, pp. 29–55 (in Slovak).
[7] STN EN 12341: 2001 Air quality. Determination of PM_{10} fraction of suspended particulate matter. Reference Method and Field test procedure to demonstrate reference equivalence of measurement methods.
[8] STN EN 14907: 2005 Air quality. Ambient Air quality. Standard gravimetric measurement method for the determination of the $PM_{2.5}$ mass fraction of suspended particulate.
[9] DURCANSKA, D.: Analysis of Particulate Matter Composition, *Communications – Scientific Letters of the University of Zilina,* vol. 12, No. 3A, 2010, pp. 17–22, ISSN 1335-4205.
[10] ADAMEC, V. et al.: *Traffic Dust and its Impact on the Atmospheric Emission Extent by the Suspended Particles.* Project Report of VaV 1F54H/098/520. Transport Research Institute, v.v.i., Brno, 2008 (in Czech).
[11] WEINBRUCH, S., EBERT, M.: *Source Apportionment of Atmospheric Aerosols Based on Electron Microscopy,* Technical University of Darmstadt, 2004.
[12] McCULLUM, K., KINDZIERSKI, W.: *Analysis of Particulate Matter Origin in Ambient Air at High Level.* Department of Civil and Environmental Engineering, University of Alberta, Edmonton, Alberta. 2001.
[13] GATARI, M. J., BOMAN, J., WAGNER, A., JANHALL, S., ISAKSON, J.: Assessment of Inorganic Content of $PM_{2.5}$ Particles Sampled in a Rural Area North East of Hanoi, Science of the Total Environment 368, 2006.
[14] VOJTESEK, M., MIKUSKA, P., VECERA, Z.: Presence, Sources and Classification of metals present in the Air (in Czech). *Chemical Letters (The J. of Chemistry)* 103, 2009, ISSN 1213-7103.
[15] HARRISON, R. M., THORPE, A.: Sources and Properties of Non-exhaust Particulate Matter from Road Traffic: A review. Science of Total Environment 400, 2008, pp. 270–282. Available at www.sciencedirect.com.
[16] STN EN 14902: 2005 Ambient air quality. Standard method for the measurement of Pb, Cd, As and Ni in the PM_{10} fraction of suspended particulate matter.
[17] BUJDOS, M., HAGAROVA, I., MATUS, P., CANECKA, L., KUBOVA, J.: Optimization of Determination of Platinum Group Elements in Airborne Particulate Matter by Inductively Coupled Plasma Mass Spectrometry. *Acta Chimica Slovenica,* vol. 59, No. 1, pp. 124–128, 2012, ISSN 1318-0207.
[18] MELOUN, M., MILITKY, J.: *Statistical Analysis of Experimental Data (in Czech)*, Academia 2004, p. 953, ISBN 80-200-1254-0.
[19] MELOUN, M., MILITKY, J., HILL, M.: *Computer Analysis of Multi-dimensional Data in Examples,* Academia: Praha, 2005, ISBN 80-200-1335-0 (in Czech).
[20] HUZLIK, J., LICBINSKY, R., MIKUSKA, P.: *Identification of Re-suspended Particle Matter Particles Sources by Statistical Methods.* Proc. of conference XII Annual Conference of Czech Aerosol Society. Cejkovice, 2011, pp. 69–74, ISBN 978-80-86186-31-3.
[21] JANDACKA, D.: R*oad Transport Impact on the Occurrence of Particulates, Dissertation thesis.* University of Zilina, 134 p., 2012.

Jan Mikolaj – Frantisek Schlosser – Lubos Remek *

LIFE-CYCLE COST ANALYSIS IN PAVEMENT MANAGEMENT SYSTEM

Pavement Management System (PMS) is a set of methods and tools which allow for optimal allocation of limited resources while keeping the road network in serviceable condition. The system evaluates the viability of all maintenance, rehabilitation and reconstruction (MR&R) actions; the evaluation is a comparison process between procurement cost of MR&R action and benefits, which are achieved by the new, more favourable, serviceability conditions attained as a result of this particular action. The investment cost − procurement costs of MR&R action − are evaluated in terms of economical effectiveness by means of Life-Cycle Cost Analysis (LCCA).

Keywords: Pavement management system, pavement evaluation, serviceability, structural analysis, user costs, cost benefit analysis.

1. Introduction

Within LCCA, different variants of MR&R actions are assessed in terms of impact on condition of the pavement, i.e. structural distress and surface distress. Different variants of MR&R actions have different impact on serviceability, and operational performance of treated road sections. In addition, each variant has different procurement costs, it influences directly maintenance costs of treated road section, and prolongs its service life by different amount. All these aspects come into consideration during the LCCA; in addition, the impact on road user costs, environmental costs, and accident costs are evaluated in detail [1]. Within the framework of LCCA, evaluation of economic efficiency is carried out with the use of Cost-Benefit Analysis (CBA), which evaluates the benefits yielded by improved operating parameters of particular road, in relation to procurement cost of applied MR&R actions. The Payback Period (PP), Internal Rate of Return (IRR) and Net Present Value (NPV) are economic indicators of the Cost-Benefit Analysis (CBA).

Utilization of LCCA started in the 90's and is closely described in [2]. Basic economic parameters were defined, and based on deterministic models, prediction trend lines were created. This article complexly describes the role of LCCA in the PMS in the context of diagnostics, pavement evaluation and structural assessment of the pavement. The result of structural assessment is the calculation of residual service life based on trend lines for complex modulus of elasticity, design of overlay, algorithm for selection of repair technologies, and Cost-Benefit Analysis.

2. Diagnostics and pavement evaluation

Diagnostics and pavement evaluation are performed on the basis of pavement serviceability and pavement structure assessment.

2.1. Road network inventory

Main part of this module is a database gathering data on the road network. In addition to data on traffic volume and physical characteristics of road sections, as well as physical characteristics of other road network assets such as bridges and culverts, substantial part of the database consists of data regarding surface characteristics of pavements i.e., pavement distress data. The PMS distinguishes following types of pavement distresses: Roughness, Rut depth, Skid resistance, Surface distress.

These distresses can be measured locally with laboratory equipment; however, in practice, variety of survey instruments for data collection is used for quicker, continuous, and foremost, price efficient measurement. For these reasons, Slovak Road Administration holds and manages a fleet of automated data collection vehicles. The fleet consists of PROFILOGRAPH GE, SKIDDOMETER BV 11, and VIDEO CAR [3] and [4].

2.2. Pavement structure assessment

Pavement Structure Assessment is aimed at provision of data regarding residual service life of particular pavement and required

* **Jan Mikolaj, Frantisek Schlosser, Lubos Remek**
Faculty of Civil Engineering, University of Zilina, Slovakia, E-mail: jan.mikolaj@fstav.uniza.sk

overlay thickness. The measurements are performed by dynamic deflectometer FWD KUAB 150 – more details attainable in [5] – it is a falling-weight loading system which transfers the impulse to the pavement construction, to create a temporary deflection, which is measured by series of velocity transducer sensors. The deflection bowl is used during calculations of Young's modulus of elasticity of particular layers, residual service life of the pavement and required overlay thickness. The calculation is, for the needs of RNMS, incorporated into software called Comprehensive Analysis of the Pavement Bearing Capacity – CANUV [6].

2.2.1. Residual service life calculation

The elastic modulus of asphalt layers recalculated to 11° C temperature, and elastic modulus of the sub-base and subgrade, as results from the backcalculation are used in this calculations. The residual life of the pavement is calculated according to two criterions. The first criterion is the cracks initiation at the bottom edge of the bound layers, and the second criterion is load bearing capacity of the subgrade.

Criterion of crack initiation at the bottom edge of the bound layers is considered satisfied, when equation (1) applies.

$$\frac{\sigma_{r,i}}{S_N \times R_{i,j}} \leq 1 \qquad (1)$$

$\sigma_{r,i}$ = radial stress on the bottom edge of the bound layer "i" [MPa];
R_i = maximal tensile stress produced at the point of failure after one loading cycle of the pavement layer "i" [MPa];
S = fatigue coefficient of the pavement layer material.

According to design methodology, the fatigue coefficient S is dependent on the number of repetitions of standard axle load (SAL) and it is derived from experimental measurements. It can be expressed as:

$$S = A - B \cdot \log N \qquad (2)$$

A, B = fatigue coefficients derived for a variety of asphalt and cement-bound materials;
N = residual service life of particular layer expressed in standard axles loads [SAL].

Consequently, after integrating (2) into (1), residual service life of layer i can be calculated according to equation (3).

$$\log N_i = \frac{A \times R_i - \sigma_{r,i}}{B \times R_i} \qquad (3)$$

N_i = residual service life of layer "i" in standard axles load [SAL];
$\sigma_{r,i}$ = calculated radial stress on the bottom edge of the pavement bounded layer "i" [MPa];
A, B = fatigue coefficients derived for a variety of asphalt and cement-bound materials. Their value lies within interval:

A, B for bituminous layers $A = 0.95 - 0.9$ $B = 0.11 - 0.12$
A, B for cement bounded layers $A = 0.90 - 1.0$ $B = 0.07 - 0.80$

Analysis of long-term measurements was carried out, based on methodology [7]. The aim of these measurements was to identify residual service life. Provided that those results have not proved significant changes, other methods are used to establish the tendency lines for residual service life.

Due to the fact that the radial stress calculation can be performed by means of a mathematical model – the layered elastic half-space model – and due to the fact that the resiliency of particular layers can be derived from laboratory measurements, the determining factor for the accuracy of residual service life calculation is the fatigue coefficient S. In this article, application of fatigue modelling theory is presented and supported with measured values. "Two-point bending test" was used for specification of the fatigue coefficient. This test is performed in accordance with national methodology [8] and current European standard [9]. The basic characteristics include elasticity modulus, deformation modulus, modulus of stiffness creep ratio and Poisson's ratio. Measurement of the complex stiffness modulus is performed at short-term alternating harmonic load. Complex stiffness modulus expresses the proportion of maximum amplitudes of excitation tension and deformation induced by this tension and phase shift of the amplitude. The stress, which varies sinusoidally in time, is applied on the element made of linear viscoelastic material. The strain – deformation – varies in time with the same frequency as the stress, but it lags behind by a phase. For the purpose of PMS, variety of measurements has been made on bitumen bound samples extracted directly from the test track of the CCT facility [10]. Following formulas for fatigue coefficient calculation were derived as results of tests on samples made from modified and unmodified asphalt.

Asphalt concrete AC11 and AC 22:

AC 11 $S = A - B.\log N$ $A = 1$ $B = 0.10$
range: 0.078 to 0.129
AC 22 $S = A - B.\log N$ $A = 1$ $B = 0.06$
range: 0.060 to 0.125

Stone Mastic asphalt:

SMA $S = A - B.\log N$ $A = 1$ $B = 0.08$

Ascertained fatigue values are higher than life expectancies of asphalt bound mixtures, which are stated in the design method. In accordance with the European standard [11], fatigue has to be defined by means of linear regression represented by a logarithmic function. This function has to be based on results, which represent the length of service life Ni for relative deformation ε_i chosen through the linear regression between the value of lg Ni and value lg ε_i according to formula (4)

$$\lg N_i = a + \left(\frac{1}{b}\right) \cdot \lg \varepsilon \qquad (4)$$

N_i = conventional fatigue life of sample i;
a = ordinate of the function;
$1/b$ = steepness of the function;
lg ε = average value of lg ε_i.

Example of Asphalt Mixture

Table 1

Mixture	Fatigue of asphalt mixture ($T = +10$ °C; $F = 25$ Hz)					Category
	Fatigue coefficients			Microstrain		
	A_o	A_1	b	$\varepsilon_6 * 10^{-6}$	$\varepsilon * 10^{-6}$	
ACo 11 PmB 45/80-75; I [1]	−13.69	−4.85	−0.206	87.44	117.75	ε_6 - 115

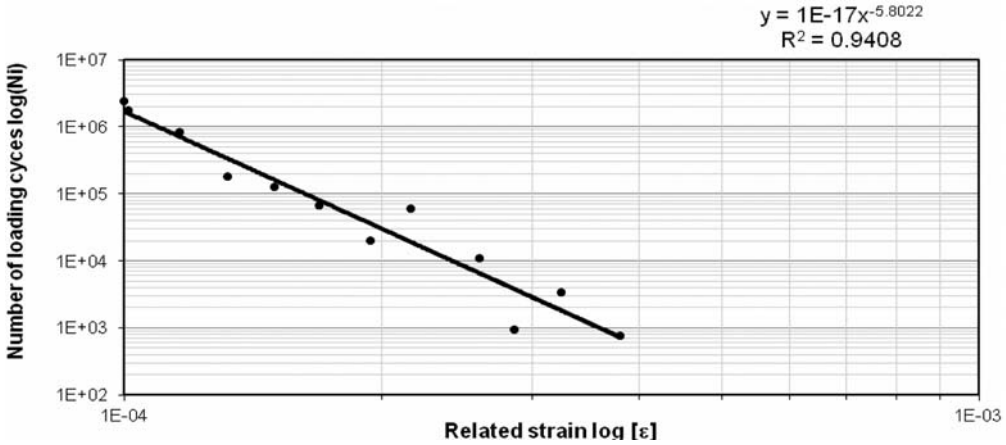

Fig. 1 Wohler diagram for ACo 11 PmB 45/80-75

In terms of fatigue, value of relative deformation ε_6 is an arbitrary one. It is derived from linear regression for 1 million of load cycles. As an example, in Fig. 1, we present relationship of the serviceability expressed by number of loading cycles N_i, to the relative deformation (ε_i) for asphalt concrete in Table 1.

3. Benefits gained by MR&R actions

Identification and calculation of benefits gained through repaired pavements is a key factor for economic efficiency calculation. Benefits are calculated as a difference in transportation costs before the MR&R action and decreased transportation costs stemming from improved pavement parameters as a result of the MR&R action. Benefits may be internal or external. Internal benefits are the road user costs which consist of vehicle operating costs and travel time costs. External benefits are monetized savings from emission reduction, noise emissions and accident rate reduction. Dust emissions and vibration are in the process of implementation into the system. The vehicle operating costs are the transportation costs, which include fuel consumption, lubricant consumption, car maintenance, wearing of tires, and transportation time of cargo and passengers.

4. Cost benefit analysis

The calculation of economic efficiency of chosen repairs is based on comparison of the benefits they will produce and their procurement and maintenance costs. In view of the fact that it is necessary to incorporate a huge amount of data from the pavement diagnostics, future maintenance costs, year in which the repair will take place, expected service life of the repair and calculated benefits, an algorithm of this procedure – decision making algorithm – was established to incorporate all the relevant data. Diagram of the algorithm is shown in Fig. 2. The procurement costs for particular MR&R method are included in the library of technologies, which is annually updated with new market prices, paid by the administrator. Following are the economic indicators of CBA: Internal Rate of Return (IRR), Net Present Value (NPV), Benefit-Cost Ratio (B/C), Payback Period (PP).

5. Results

The application of LCCA provides us with fund allocation strategies and creation of site specific plans for MR&R actions, i.e. plans for meeting the performance objective. The application proved that the resources are allocated to road sections which have the highest demand for repairs, thus financial funds are used effectively. The saved funds are in turn used as additional resources for further repairs. Another important fact is that this systematic approach increased the discipline of subcontractors of repair works, employed by road administrators [12]. The road network administrator has, by means of LCCA, a huge number of results, enabling him to optimize his activities; for example, the trend lines of roughness, skid resistance or surface damage.

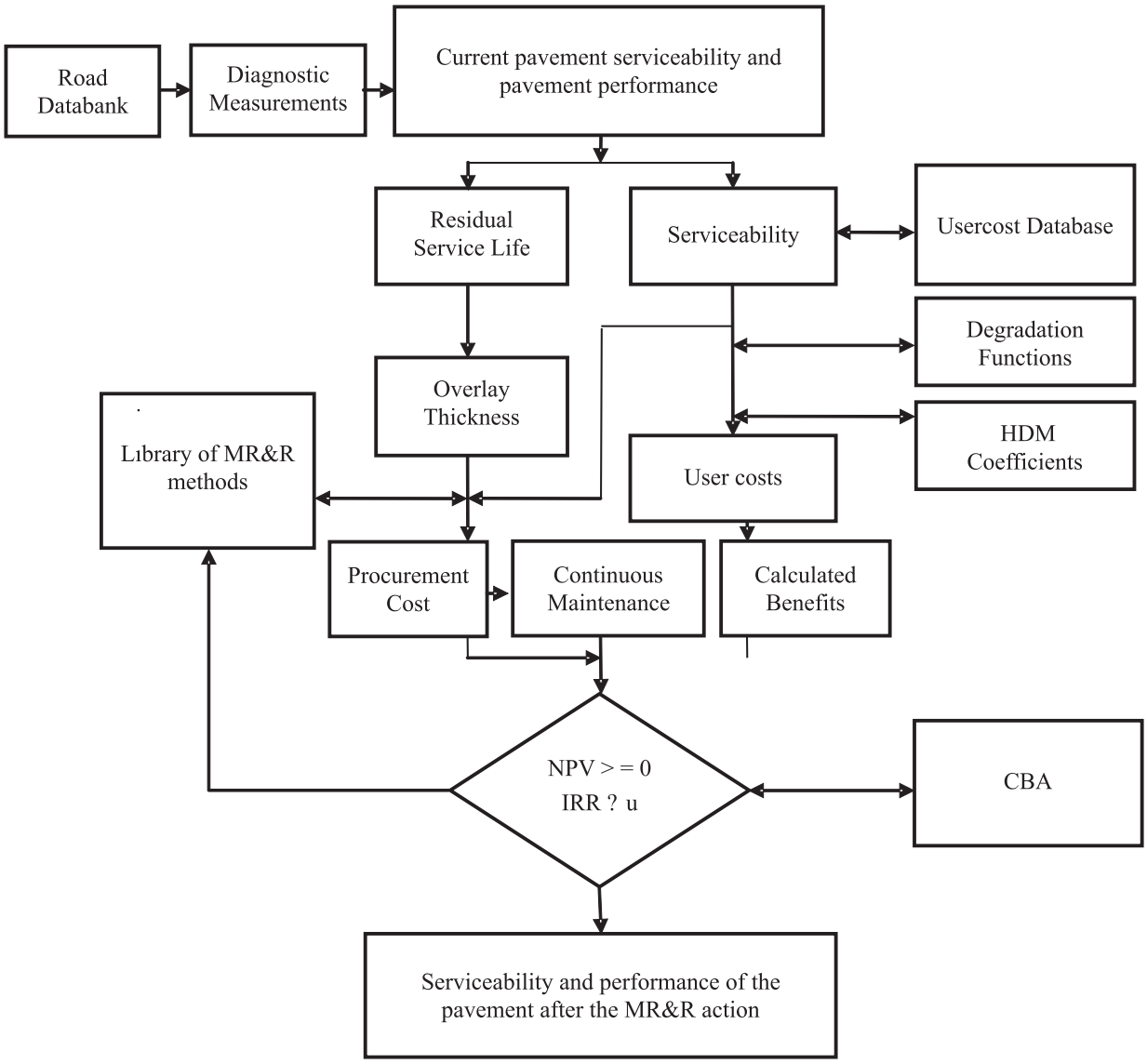

Fig. 2 Algorithm for selection of appropriate MR&R method

Application of LCCA allows for different variants of financing. As seen in [13], the economic calculations have also enabled us to increase value of money spent for repairs by financing through European Investment Bank loans or Public Private Partnerships between road administrator, construction subcontractor, and a bank.

In further development of the program, it will be necessary to focus on the completion of calculations performed in the CBA in regards to investment into new infrastructure; it will be also necessary to incorporate other factors like environmental impacts – noise, dust, vibration, exhaust emissions. Currently, as seen in [12] and [13], these factors are calculated only outside of the computational program.

Acknowledgement

This contribution is the result of the project implementation: "Independent Research of Civil Engineering Construction for Increase in Construction Elements Effectiveness" (ITMS: 26220220112) supported by the Research & Development Operational Programme funded by the ERDF.

References

[1] MIKOLAJ, J.: The Road Network Management System in Slovakia. *Transport Reviews,* Taylor and Francis Ltd. London, vol. 16, No. 4, pp. 313–321, 1996.

[2] FEDERAL HIGHWAY ADMINISTRATION: *Life-Cycle Cost Analysis in Pavement Design.* U.S. Department of Transportation, Federal Highway Administration. Publication No. FHWA-SA-98-079

[3] BENKO, Z.: *Pavement Management Systems Employed by Slovak Road Administration.* Proc. of Q-2012 Conference Construction, Financing and Management of Roads and Motorways, University of Zilina, pp. 44–482012, ISBN 978-80-554-0572-8.

[4] CELKO, J., KOVAC, M., DECKY, M.: Analysis of Selected Pavement Serviceability parameters. *Communications - Scientific Letters of the University of Zilina,* No. 3, 2011, ISSN 1335-4205.

[5] ENGINEERING AND RESEARCH, Inc.: Eri Kuab – Falling Weight Deflectometer, 2013, <http:www.erikuab.com>.

[6] KOMACKA, J., CELKO, J.: CANUV – Computer Program for Analysis of the Bearing Capacity on the Deflection Bowl Basis. *Studies of University of Transport and Communications in Zilina,* vol. 19, pp. 63–70, Zilina, 1996.

[7] KOMACKA, J.: Change of Bearing Capacity Characteristics of Asphalt Pavement *Communications - Scientific Letters of the University of Zilina,* No. 3, 2011, ISSN 1335-4205.

[8] Slovak Office of Standards SUTN: STN 73 6160 Evaluation of Asphalt Bituminous Mixtures, 1986

[9] European Standardisation Organisation CEN, EN12697-26: Bituminous Mixtures – Test Methods for hot mix asphalt – part 26: Stiffness

[10] SCHLOSSER, F. et al.: *Rheological Characteristics of Asphalt Mixtures Extracted from Circular Test Track: Testing of Bituminous Mixtures,* VU report No. 93/SvF/98. University of Zilina, 1998

[11] European Standardisation Organisation CEN, EN12697-24: Bituminous Mixtures – Test Methods for Hot-mix Asphalt – part 24. Resistance to fatigue, 2003

[12] TROJANOVA, M., ZGUTOVA, K., PEPUCHA, L., PITONAK, M.: Inter-laboratory Comparison of Accredited Laboratories in Terms of Benchmarking in Slovakia, *Communications - Scientific Letters of the University of Zilina,* No. 3a, 2010.

[13] MIKOLAJ, J., VALUCH, M., PEPUCHA, L.: *Innovative Road Management Arrangement in Slovakia / Dispositifs Novateurs de Gestion de la Route en Slovaquie,* Proc. of XXIV World Road Congress Roads for a better life Mobility, sustainability and development, September 2011, Mexico City, DVD 12s.

Patricia Duratna – Jan Bujnak – Abdelhamid Bouchair – Frantisek Bahleda *

BEHAVIOUR AND STRENGTH OF HEADED SHEAR STUD CONNECTORS

Headed stud shear connectors are commonly used to transfer longitudinal shear forces across the steel-concrete interface in composite structures. This paper is focused on the experimental and numerical study on the behaviour of this type of connectors. The push-out tests of headed studs, 10 mm in diameter and 50 mm in length, in normal C25/30 concrete with transverse reinforcement were carried out. The experimental study also treated the influence of the connectors spacing, in the longitudinal and transversal directions, and the thickness of the concrete slab on the shear resistance.

Keywords: *Shear connectors, shear resistance, finite element analysis, push-out test.*

1. Introduction

Headed stud shear connectors are the most widely used shear connectors in steel-concrete composite structures. The most important characteristics for the design of the composite structures are the shear capacity and the load-slip relations of these connectors. The most exact method to determine these characteristics is a full-scale composite beam test but it might be time-consuming and costly, therefore the push-out tests are adopted.

In the second half of the 20th century, the first parametric studies to investigate the behaviour of the connectors were realized. The first analysis of headed stud connectors with different parameters was carried out by Viest [1], followed by Slutter and Driscoll [2] and [3], Goble [4]. The behaviour of connectors was analysed by the authors in [5][6][7]. Lam and El-Lobody [8] developed a numerical model of push-out tests, which they compared to the experimental results and the design standards – British BS5950 [9], European EC4 [10] and American AISC [11]. Design of the connection in the composite structures according to EC4 is described also in [12].

However, the full-scale push-out test remains also the time-consuming and costly option, therefore the numerical analysis is adopted, once the verification of the numerical model with experimental results was established.

The main objective of this investigation is to carry out the full-scale push-out tests and to develop a three-dimensional finite element model using the software ATENA to simulate the behaviour of headed shear stud connectors and to use it for subsequent parametric study. The results of this model were compared with the experimental results. The push-out tests with different configurations of connectors, 10 mm in diameter and 50 mm in length, in normal C25/30 concrete with transverse reinforcement were carried out.

2. Push-out test specimens

Five series of three push-out specimens called SP1, SP2, SP3, SP4 and SP5, were tested (Fig. 1). Each specimen consists of a short piece of steel beam HEB 260 connected on both sides to concrete slabs using shear connectors. The concrete slabs dimensions are 650 mm length and 600 mm width for all the specimens. However, the thickness of the specimen SP1 (150 mm) is different from that of specimens SP2 to SP5 (100 mm). Concrete slabs were produced from concrete C25/30. For each mix, three cylindrical specimens of concrete were prepared and tested to obtain the concrete strength. The connectors are made of steel S235J2. The specimens SP1-SP2 are realized with four connectors and the specimens SP3-SP5 with six connectors welded on each beam flange. The diameter of the connectors is 10 mm and their height 50 mm. The longitudinal distance between the connectors is 250 mm (SP1-SP2), 60 mm (SP3, SP5) or 40 mm (SP4) and transversal distance is 100 mm (SP1-SP4) and 32 mm (SP5).

Slip between the concrete slabs and the steel beam is measured continuously using potentiometric displacement transducers. The average value of slip between the two interfaces concrete-steel is plotted against the load per connector and used to compare the different configurations. Fig. 2 shows the tested configurations of push-out specimens.

* **Patricia Duratna[1,2], Jan Bujnak[1], Abdelhamid Bouchair[2], Frantisek Bahleda[1]**
[1] Department of Structures and Bridges, Faculty of Civil Engineering, University of Zilina, Slovakia, E-mail: patricia.duratna@fstav.uniza.sk, patricia.duratna@polytech.univ-bpclermont.fr
[2] Clermont Université, Université Blaise Pascal, Institut Pascal, Clermont-Ferrand, France

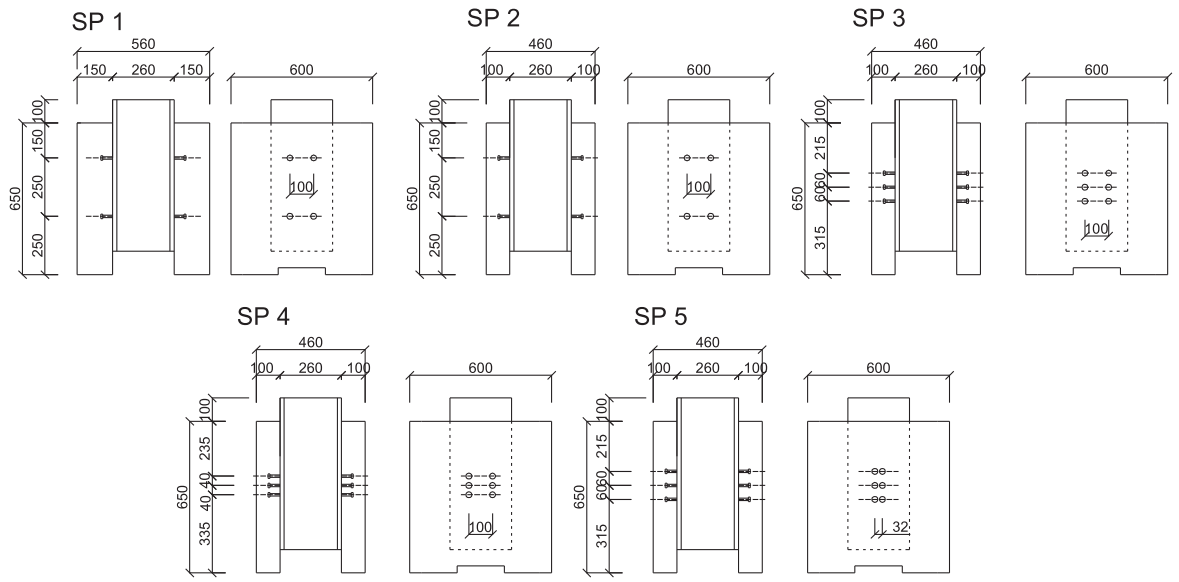

Fig. 1 Details of the push-out test specimens

The procedure of testing was carried out in accordance with Eurocode 4 [10]. The load was applied in increments from 0 to 40 % of the expected failure load, and then returned to 5% of the expected failure load. After that, the loading cycle between the values of 5 and 40 % was repeated 25 times. The slip controlled load continued up to the failure so that it did not occurred earlier than in 15 minutes. At each load increment, values of slip between the steel beam and the concrete were recorded. For each specimen, 8 transducers (4 for each steel-concrete interface) were used to measure the relative displacement, vertical displacement between steel and concrete, representing the slip, and 4 (2 for each steel-concrete interface) to measure the horizontal displacement representing the separation between steel and concrete.

3. Finite Element Model

Finite element (FE) model is developed using the software ATENA. It considers the nonlinear behaviour of materials and the large displacements. It is capable of simulating real behaviour of concrete material in structures including cracking, crushing and reinforcement yielding.

3.1. Finite Element Mesh

Three-dimensional linear four-node tetrahedral isoparametric element (IsoTetra4_3D) was used to model the specimens. Because of symmetry, only a quarter of the push-out configuration was modelled. Fig. 3 shows the FE mesh used to represent a quarter of the push-out test specimen. The element size is 0.05 m for the elements of concrete slab and steel beam and 0.005 m for the shear connectors (head and shank). The circular shape of the connector is approximated by a prism because of the problems with concentrated mesh in cylindrical form of the stud.

3.2. Boundary Conditions

To reproduce the testing conditions on the supports, all the nodes of the concrete slab on the opposite side of loading are fixed in the Z direction. All the nodes on the plane of symmetry of the specimen (steel beam web and bearing plate) are fixed in the X direction. For the second plane of symmetry (XZ), all the nodes of concrete, steel beam flange and steel beam web are fixed in the Y direction.

3.3. Application of the Load

A displacement controlled load is applied at the centre of the steel web, as shown in Fig. 3. Load is applied using the arc length method to improve the convergence process in the phases of large nonlinearities. An initial increment of displacement is given on the data line and the initial load proportionality factor is assigned to this initial increment using the automatic incremental scheme.

3.4. Materials behaviour

To describe the behaviour of the concrete slab in the push-out specimen, concrete is treated as an elastic-plastic material, as shown in Fig. 4a. From tests realized on cylinder specimens, the average measured value compressive strength (f'_{cu} = 28 MPa) was set-up and entered as known input concrete property and the other values have been calculated according to the parameters used by ATENA:

Fig. 2 Configuration of the push-out test

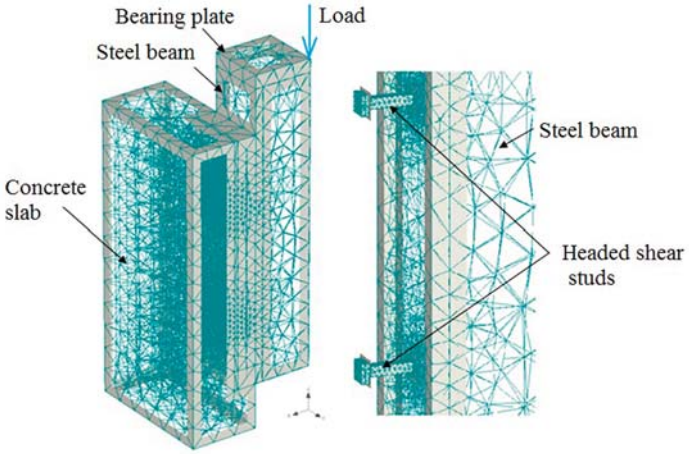

Fig. 3 Finite element mesh of the model

$$f_c' = 0.85 f_{cu}'; \; f_t' = 0.24 f_{cu}'^{2/3}; \qquad (1)$$
$$E_c = \left(6000 - 15.5 f_{cu}'\right)\sqrt{f_{cu}'}$$

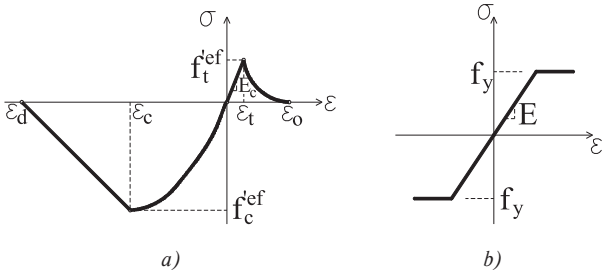

Fig. 4 Stress-strain law for (a) concrete; (b) steel beam, headed stud and reinforcement

The stress-strain curve of the headed stud is shown in Fig. 4b. The steel was modelled as elastic perfectly plastic. For stud and beam, the Young's modulus $E = 210000$ MPa is chosen and the yield stress is taken equal to $f_y = 360$ MPa for stud and to $f_y = 235$ MPa for the steel beam. For the steel reinforcement, the Young's modulus and yield stress chosen are: $E = 200000$ MPa and $f_y = 550$ MPa, respectively. Reinforcement was modelled by discrete bars loaded in tension and also in compression.

4. Results

Because of limited number of specimens the evaluation was not carried out statistically, but the characteristic resistance P_{Rk} and the characteristic ultimate slip δ_{uk} were determined in accordance with [10]. These values are presented in Table 1. The value $P_{u,min}$ is the value of minimal failure load, the characteristic resistance $P_{Rk,exp}$ is 0.9 $P_{u,min}$ and δ_{uk} is the maximal value of the slip measured at characteristic load. From these results, according to the Eurocode 4 requirements [10], it can be observed that the 10 mm studs tested with concrete C25/30 cannot be considered as ductile ($\delta_{uk} < 6$ mm). The failure modes observed were the shear failure of the studs or the combination of failures of stud and concrete bearing. The typical failures are shown in Fig. 5.

Push-out tests results — Table 1

Series	Strength per stud [kN]		Ductility [mm]
	$P_{u,min}$	$P_{Rk,exp}$	δ_{uk}
SP1	31.91	28.71	4.5
SP2	29.48	26.53	4.4
SP3	33.29	29.96	4.7
SP4	29.64	26.67	4.1
SP5	34.09	30.68	5.9

Figure 6 shows the mean force-slip curves for all the specimens taking into account the force corresponding to one connector. It can be observed that for all the tested configurations of push-out specimens, in the elastic domain, the behaviour of the studs is characterized by very close values of initial stiffness. When curves exceed the initial domain, a plastic plateau can be observed for the specimens SP1, SP3 and SP4. For the other specimens (SP2 and SP5), the plastic plateau is too short and passes directly to the decreasing branch. From Fig. 6 and Table 1, it can be stated that the resistance and ductility of 10 mm stud is not influenced by the

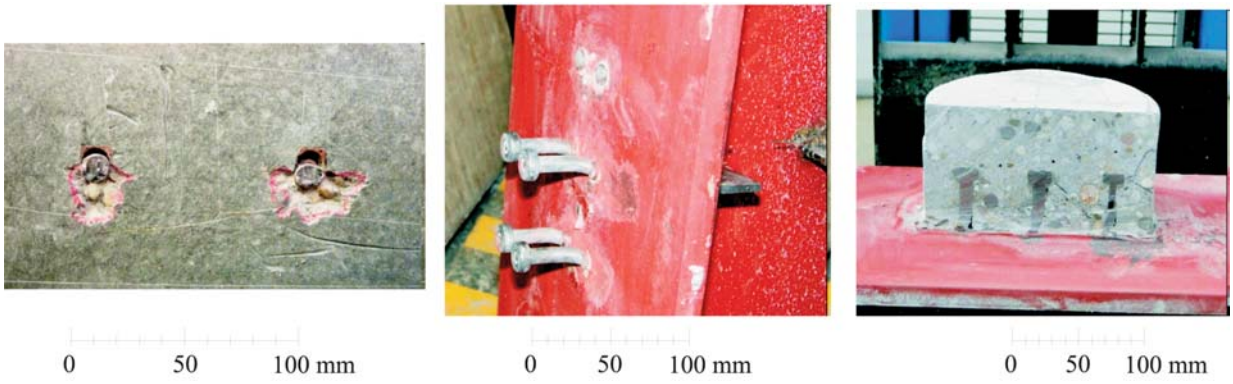

Fig. 5 Details of failures of the push-out test specimens

slab thickness, the longitudinal and transversal spacing of the connectors. However, for the SP1 specimen, where the transversal spacing is limited to 32 mm, the resistance and ductility of the stud is greater than the others with larger spacing. As the value of 32 mm is in the limit of the Eurocode 4 [10], it is supposed that it is caused by the proximity of the studs to the web of the steel beam where the stiffness is greater.

Fig. 6 shows also a comparison between the load-slip curves obtained experimentally and numerically using the finite element method. The model describes well the elastic domain of the stud; however for plastic domain it does not represent the descending branch of force-slip curve. This one could be explained by the damage evolution in the concrete or the connector welded basis.

Eurocode 4 specifies for the studs with 16-25 mm diameters two expressions (2) to determine their strength:

$$P_{Rk,1} = 0.8 f_u \pi d^2/4 \qquad P_{Rk,2} = 0.29 d^2 \sqrt{f_{ck} E_{cm}} \qquad (2)$$

With the nominal values of steel and concrete, the calculated resistances (without the partial safety factor) of the tested connectors are: $P_{Rk,1}$ = 32.04 kN and $P_{Rk,2}$ = 25.53 kN.

5. Conclusion

The behaviour of shear studs (d = 10mm, h = 50mm) with concrete C25/30 is analysed on the basis of 15 push-out tests. The tests showed insufficient ductility of these connectors, with slip lower than 6 mm, for all the configurations. The tests showed also a small influence of the slab thickness and transversal and longitudinal spacing of the studs on their resistance and ductility. A finite element model is developed to simulate the behaviour of the studs considering the nonlinear behaviour of materials (steel and concrete). The proposed model described well the behaviour of the tested specimens mainly in the elastic domain. Improvements of the model are in progress to represent the whole load-slip curves of the push-out test including the descendant branches.

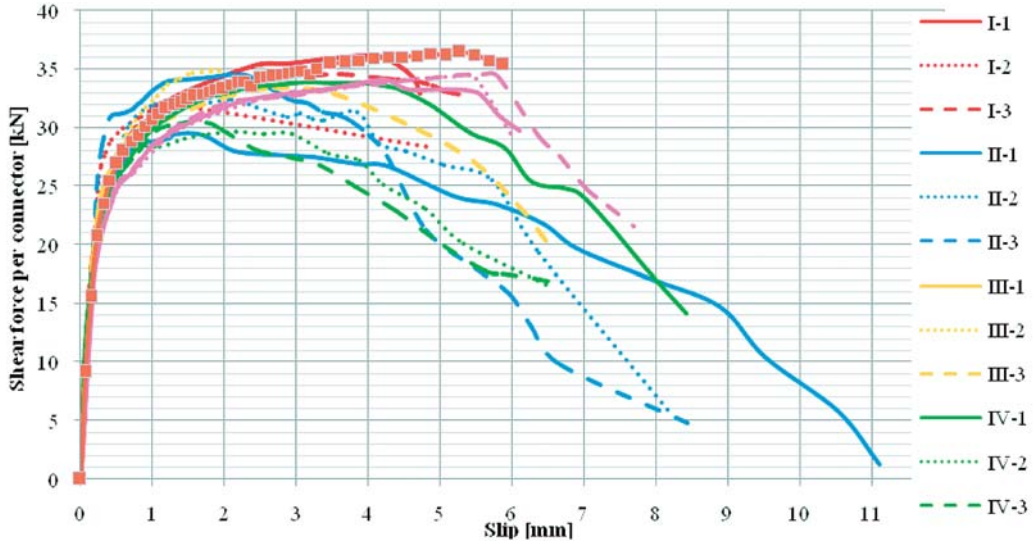

Fig. 6 Load-slip curves of the push-out tests

References

[1] VIEST, I. M.: *Test of Stud Shear Connectors - Parts I, II, III and IV,* Engrg. Test Data, Nelson Stud Welding. Lorain, Ohio, 1956.

[2] SLUTTER, R. G., DRISCOLL, G. C.: Flexural Strength of Steel-concrete Composite Beams. *J. of the Structural Division,* ASCE, No. 2, vol. 91, April 1965, pp. 71–99.

[3] DRISCOLL, G. C., SLUTTER, R. G.: *Research on Composite Design.* Proc. of National Engineering Conference, Lehigh University, AISC, May, 1961.

[4] GOBLE, G. G.: Shear Strength of thin Lange Composite Specimens. *Engineering J.*, AISC, No. 2, vol. 5, 1968. pp. 62–65.

[5] BUJNAK, J., FURTAK, K., ODROBINAK, J.: On Shear Connection Design in Composite Beams*. Communications - Scientific Letters of the University of Zilina,* 2002, No. 3, vol. 4, p. 13–16.

[6] ODROBINAK, J.,JUTILA, A.: Longitudinal Shear Flow at the Support Srea of Beam with an Overhanging Cantilever, *Communications - Scientific Letters of the University of Zilina,* 2002, No. 3, vol. 4, p. 17–20.

[7] BUJNAK, J., FURTAK, K.: Research on Shear Connection Design in Composite Beams. *Communications - Scientific Letters of the University of Zilina,* 2007, No. 3, vol. 9, p. 47–50.

[8] LAM, D., EL-LOBODY, E.: Behavior of Headed Stud Shear Connectors in Composite Beam. *J. of Structural Engineering*, ASCE, January 2005, pp. 96–107.

[9] British Standards Institution. *Code of Practice for Design of Simple and Continuous Composite Beams.* BS5950, Part 3: Section 3.1 Structural use of steelwork in building. London, 1990.

[10] CEN.Eurocode 4: *Design of Composite Steel and Concrete Structures,* Part 1: General rules and rules for building. Brussels: CEN, 2006.

[11] American Institute of Steel Construction: *Load and Resistance Factor Design Specification for Structural Steel Building,* Chicago, 1999.

[12] DURICOVA, A., ROVNAK, M.: *Design of Composite Steel and Concrete Structures According to STN EN 1994-1-1*, VEDA, Bratislava, 2008.

Josef Vican – Marian Sykora *

NUMERICAL ANALYSIS OF THE BRIDGE ORTHOTROPIC DECK TIME DEPENDENT RESISTANCE

Resistance of the stiffened plated orthotropic deck of bridge with ballast bed is affected by the environmental action effects due to unchecked corrosion process of steel bridge deck under ballast bed. Therefore, to observe the behaviour and resistance of those types of steel bridges, the probabilistic nonlinear finite element analysis using adequate sophisticated software is needed. The paper presents results of the parametric numerical analysis of the time dependent resistance of bridge with ballast bed on the orthotropic deck considering corrosion attack using ANSYS software support module PDS. Random variables entering calculations were described by means of parameters of probability density functions according to data determined experimentally. The model takes also into account the geometrical and material nonlinearities of bridge structure including the selected corrosion models.

Keywords: *Steel orthotropic plated structures, time-dependent corrosion effects, numerical simulations, time dependent resistance.*

1. Introduction

Steel bridges with ballast beds lying on the compression orthotropic plate decks are spatial structures with very complicated behaviour. The orthotropic deck of those bridges consists of thin-walled sheets stiffened by the system of longitudinal and transversal stiffeners. Its stress state is significantly influenced by the interaction of global and local buckling, shear-lag and effect of transversal load due to traffic action effects resulting from the deck performance. Moreover, the geometrical and material nonlinearities are necessary to take into account. Accurate prediction of the resistance of stiffened plated elements is a very important task for engineers. Therefore, the extensive work in predicting the compressive resistance of those type of structural elements has been conducted since 1970s. The results of the effort were presented in many papers and works, whose summary can be found e.g. in [1]–[5], and they were introduced into the last edition of Eurocodes [6]. Three types of methods could be normally used to estimate the resistance or stress state of stiffened plate, i.e. the experimental method, analytical method and numerical simulation such as the finite element method employing advanced numerical models [7].

The solution of the stress state of compression and transversally loaded bridge decks in the analytic form is practically impossible. Therefore, simplified procedures based on the assumptions of linear elasticity methods including stress superposition have been preferred and involved into the Eurocodes because of their general simple use. However, those methods are applicable for routine design and they do not provide appropriate outputs convenient for research concerning with the time dependent reliability verification due to e.g. degradation effects. To obtain more accurate results, the numerical simulations should be used.

However, many factors influencing the resistance of the bridge orthotropic deck are random variables even random processes. Therefore an adequate probabilistic model of resistance determination is necessary to develop from the viewpoint of structural reliability assessment due to significant uncertainties of the initial performance, effects of deterioration caused by environmental actions like corrosion and because of stochastic nature of all factors affecting the resistance (geometric parameters and material properties).

It is necessary to notice that numerical calculations based on the finite element method using nonlinear analysis considering both geometrical and material nonlinearities are quite time consuming. An increased interest in application of those types of structures (not only in the bridge engineering) and not sufficiently known way how to determine the actual resistance of the stiffened plate gives the possibility to employ an approach based on the artificial neural network enabling to derive a design formula predicting the resistance of stiffened plates by means of the response surface method using existing experimental data and numerical results.

As mentioned above, the actual bridge resistance could be changed by various factors like degradation of materials due to aggressive environment. In general, deteriorating structures are maintained in accordance with their condition states. Although many quality corrosion protection systems are available at present, due to limited available resources and incorrect maintenance deci-

* **Josef Vican, Marian Sykora**
Faculty of Civil Engineering, University of Zilina, Slovakia, E-mail: vican@fstav.uniza.sk

sions, phenomena of corrosion as the basic and most important degradation effect is significant all the time. Effects of this degradation cause material loss leading to the reduction of structural resistance. Corrosion effects influencing resistance can be obtained by means of structural model based on some corrosion models. Then, the corrosion effects could be expressed in the form of the time variant loss of the resistance. The parametric study of corrosion effects simulation was realized to observe the variation of the bridge deck resistance within the bridge service lifetime resulting from the generalized corrosion of the bridge stiffened deck plate.

A proper consideration and treatment of uncertainties enables a more sophisticated reliability assessment and ensures the quality and reality of the bridge global analysis. The methodology of the probabilistic approach to the bridge orthotropic deck reliability introduced in this paper is a part of the global study related to the remaining lifetime and durability of structures, which is a long-term subject of the research activities of the Department of structures and bridges [8], [9] and [10].

2. Bridge computational model

The simulations were performed by means of computational model (see Fig. 1) of the real bridge structure (Fig. 2) using the finite-element package ANSYS, taking into account the nonlinear structural behaviour. The Shell 181 element (four nodded shell element with six degrees of freedom at each node) suitable for large rotation and large deflection of nonlinear applications was chosen. Moreover, the model should include the same boundary conditions as those in the real structure and therefore should also respect the actual material properties and relevant initial imperfections.

The isotropic nonlinear plastic material behaviour was modelled using the von Misses yield criterion coupled with an isotropic work hardening assumption and a multi-linear approximation of the stress-strain curve. Due to absence of measured initial imperfections, the standard equivalent geometrical initial imperfection in the form of sinusoidal surface was incorporated into the computational model. The transverse displacement fields of imperfect plates are normally represented by a double Fourier series. For ratios of plate dimensions usually used on the bridge decks, the following equation was applied to take into account the initial imperfections

$$w_0 = f_0 \sin(\pi x/a)\sin(\pi x/b), \tag{1}$$

where f_0 is value of initial bow, a is the plate length (between adjacent cross-beams) and b is the plate width (between main girders) respectively. The amplitude of the longitudinal stiffener initial bow was considered by the value of $a/400$ in accordance with [6] and the initial bow of the deck sheet in transversal direction between longitudinal stiffeners was given in the form of "hungry horse" with the amplitude $b_0/200$, where b_0 is the axes distance of the adjacent longitudinal stiffeners (see Figs. 1 and 2).

Two numerical finite calculation models were created. Firstly, the deterministic model was developed. Secondly, the probabilistic model was created using deterministic one and software support module PDS (Probabilistic Design System) allowing for direct connection between FEM analysis and methods of the probability analysis. Based on the parameters of material characteristics as well as other random variable input values and their statistical models, PDS module enables to generate files of random variables and to calculate required probabilities. Basic input random variable characteristics were obtained from experimental measurements and can be found in [11].

Random character of the bridge geometric parameters (see Fig. 2) was considered in accordance with the Gaussian random process and the log-normal distribution was applied in the case of material characteristics (modulus of elasticity and yield strength). Random variables were described by means of parameters of probability density distribution according to data determined experimen-

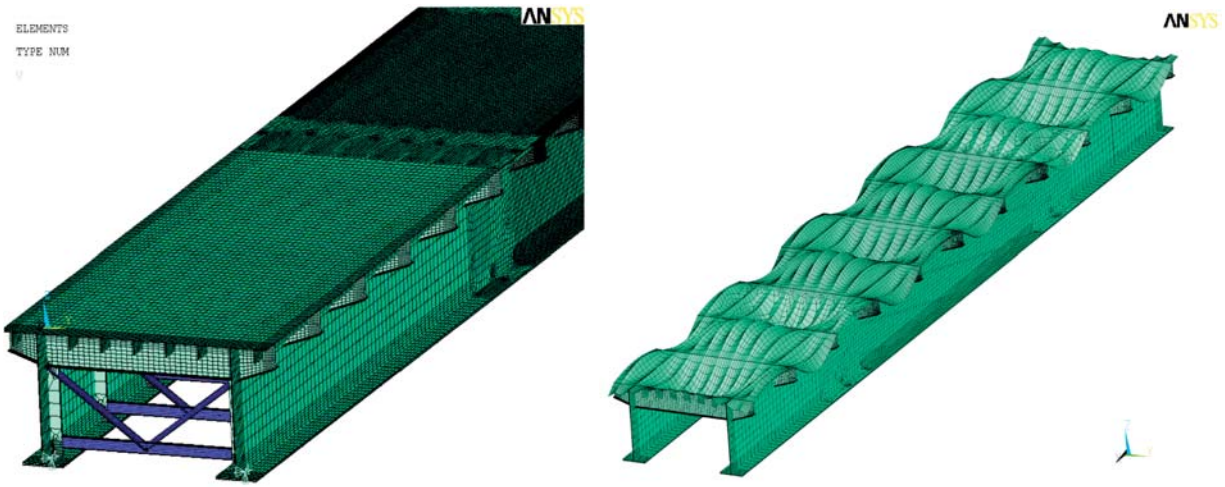

Fig. 1 Structural model of bridge with orthotropic plate deck – detail of finite element meshing and shape of initial imperfections (100 times multiplied)

tally. The traffic action on bridge was modelled by means of idealised uniformly distributed load representing the relevant load model of railway traffic action [12].

The developed models were calibrated using the results of experimental analysis accenting the structural behaviour of the real bridge shown in Fig. 2. The calculations were carried out using LHS simulation method for 40 steps of the data dispersion. The nonlinear calculation ran in every step determining random output parameters in the form of stresses and deformations of girder upper flanges in experimentally measured places (see Fig. 2). Comparative analysis of the results proved the very good agreement of the measured outputs with the calculation results obtained by means of the above described probabilistic numerical model.

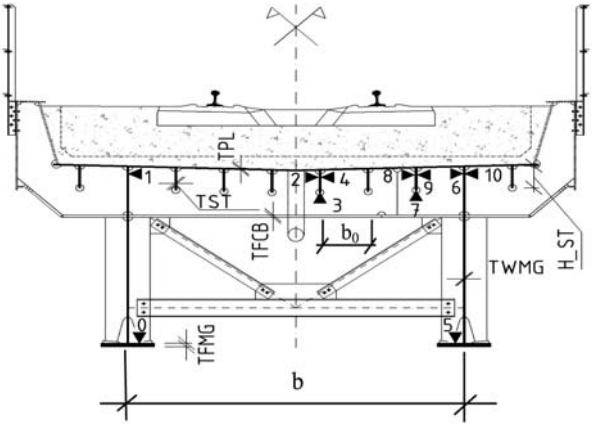

Fig. 2 Bridge cross-section with designated measured places and geometrical parameters

3. Corrosion degradation modelling

Corrosion of the bridge plated deck due to environmental conditions was taken into account. A lot of effort was done to evolve appropriate analytical models of corrosion mainly through extrapolation procedures processing the results of in-situ measurements. Many factors including the corrosion protection system and various operational parameters are influencing the corrosion rate and due to this complexity of the problem, it is difficult to express the time dependent loss of material. Although, several research long-time programmes were realized in the past and many factors influencing degradation process are known, models of corrosion loss in time are more or less simplified. Conventional models consider the constant measure of corrosion loss in time, which is leading to almost linear dependence of material loss on time. However, experimental measurements proved that nonlinear models are more appropriate. Because of random variable character of many parameters entering corrosion process, the probability theory and mathematic statistics should be the most appropriate approaches to describe it. At present, several corrosion models are known, which could be generally used for analysis of the corrosion influence on the structural reliability.

However, these corrosion models were developed for structural steel with general corrosion protection. Insulation system used for actual bridge structure under ballast bed is based on the epoxy resins extra resistant against the environmental actions. The passive stadium of the corrosion process, where insulation system is resisting to environmental actions, is unknown. Therefore, due to absence of the above mentioned actual corrosion model of the structural steel under ballast bed, the known corrosion prediction models of structural steel degradation were used for the corrosion modelling. The model of Akgul-Frangopol [13] was used to simulate the corrosion process under insulation of the bridge deck and the model of Qin-Cui [14] was applied for the modelling of the corrosion process on the lower part of the bridge deck. The corrosion losses were determined using relations expressing mean values and standard deviations. In the case of the Frangopol model, the following equations were used

$$\mu_{dcorr} = 0.03207t^{0.5}, \tag{2}$$

$$\sigma_{dcorr} = 0.00289t^{0.045} \tag{3}$$

and in the case of the Qin-Cui model, the following relations were applied

$$\mu_{dcorr} = 1.67[1 - \exp(-t/9.15)^{1.97}], \tag{4}$$

$$\sigma_{dcorr} = 0.0674[1 - \exp(-t/0.181)^{0.0294}], \tag{5}$$

where t is time in years, μ_{dcorr} and σ_{dcorr} are the mean value and standard deviation of the corrosion lost.

Corrosion effects was taken into account by means of thickness reduction d_{corr} calculated according to the above mentioned probability models using following relation

$$t_{pl,red} = t_{pl} - d_{corr}, \tag{6}$$

where t_{pl} is the plate thickness without corrosion effects.

For practical use, such approach was applied in which time variant problem of corrosion influence on the structural resistance is solved by means of time invariant problem in several discrete time points with resulting reduced cross-sectional characteristics due to corrosion effects.

4. Parametric study of the corrosion effects on the bridge deck resistance

The resulting bridge deck resistance due to corrosion effects depends on several factors. Firstly, it is necessary to observe the influence of slenderness of the bridge plate and longitudinal stiffeners creating the bridge deck. Moreover, the effect of the material mechanical properties plays also an important role. The effect

of the global bridge geometric parameters and the bridge arrangement are other equally important factors, which are manifested mainly in the form of stress distribution over the bridge cross-section due to influence of the shear-lag and plate buckling.

To determine the impact of time-varying corrosion effects on the bridge deck resistance, a parametric study was performed in which the variation of slenderness of steel plate was considered in range from 30 to 45 in increments of 5 and slenderness of longitudinal stiffeners varied from 30 to 60 in increments of 10. Thus, the study consisted of 16 types of bridge structures with plated orthotropic decks. The impact of changes in the quality of the material due to a considerable amount of study parameters was not considered and, therefore, only one type of material i.e. steel S355 was used in the study. The input geometric parameters of the parametric study are presented in Table 1, where t_{pl} means the thickness of the deck plate, β_p is the slenderness of the deck plate, a is the span of the longitudinal stiffener, b_0 is the axes distance of the adjacent longitudinal stiffeners, h_{st} is the depth of the longitudinal stiffener, t_{st} is the thickness of the longitudinal stiffener and λ_{st} is the slenderness of the longitudinal stiffener. Details of the study input parameters are presented in [8]. The above described parameters were considered as the random variables. The cross-beams of the bridge deck were modelled in the same way for all observed cases as $\perp$ cross-section with the web parameters of 14.30 $\times$ 550.00 mm and bottom flange parameters of 15.60 $\times$ 200 mm. The main bridge girders were also considered in the same way for all cases with the web parameters of 14.30 $\times$ 1 900 mm and the bottom flange parameters of 50.10 $\times$ 700 mm.

Input geometric parameters of the parametric study — Table 1

Case No.	t_{pl} [mm]	β_p	a [m]	b_0 [m]	h_{st} [m]	t_{st} [m]	λ_{st}
1	14.00	30.00	1.925	0.420	0.200	0.020	30.00
2	14.00	35.00	1.874	0.490	0.200	0.020	30.00
3	14.00	40.00	1.824	0.560	0.200	0.020	30.00
4	14.00	45.00	1.777	0.630	0.200	0.020	30.00
5	14.00	30.00	2.567	0.420	0.200	0.020	40.00
6	14.00	35.00	2.499	0.490	0.200	0.020	40.00
7	14.00	40.00	2.432	0.560	0.200	0.020	40.00
8	14.00	45.00	2.369	0.630	0.200	0.020	40.00
9	14.00	30.00	3.209	0.420	0.200	0.020	50.00
10	14.00	35.00	3.123	0.490	0.200	0.020	50.00
11	14.00	40.00	3.041	0.560	0.200	0.020	50.00
12	14.00	45.00	2.962	0.630	0.200	0.020	50.00
13	14.00	30.00	3.850	0.420	0.200	0.020	60.00
14	14.00	35.00	3.748	0.490	0.200	0.020	60.00
15	14.00	40.00	3.649	0.560	0.200	0.020	60.00
16	14.00	45.00	3.554	0.630	0.200	0.020	60.00

The resistance of the bridge structure was determined using incremental analysis in which the limit state was defined by the total structural collapse. In order to determine the collapse load in a more accurate way, the gradually increasing load with the defined time step of 1/200 was applied until structural failure. The time-dependent resistance of the structure was calculated within the structural design lifetime of 100 years for both above mentioned models of corrosion losses. Therefore, the structural resistance was determined at different time points with the time step of 5 years for the structural age until 25 years and then the time step was adjusted to 25 years. It was considered that the corrosion is affecting on the lower and upper part of the bridge deck respecting the assumption not perfectly functional isolation of the bridge deck under ballast bed for the whole design lifetime of the structure.

Results of the parametric study were presented in the form of curves expressing the decrease of the time dependent structural resistance in the measured points of the observed structure. The curves were determined as the ratio of the structural resistance including the corrosion effects at the bridge lifetime of 100 years to the resistance without the influence of the corrosion losses at the beginning of the bridge lifetime. The resistance was either defined in accordance with the elastic limit state due to attaining the yield strength in the most loaded point of bridge deck, or as the plastic limit state by means of achieving the plastic strain $2\varepsilon_y$ (ε_y means the strain corresponding to the yield strength) in the most loaded point of the bridge deck. Results of the structural resistance decreases measured in selected relevant points of structure (see Fig. 2) are presented in Figs. 3 - 5.

The above described approach to determine the resistance decrease is suitable for elastic phase of the bridge loading. This approach is not accurate in the elastic-plastic stage of the bridge behaviour due to elastic-plastic stress redistribution over the bridge cross-section. Therefore, the more accurate approach how to estimate the degradation effect of the corrosion process on the bridge deck resistance is determining the limit load corresponding to attaining the bridge deck limit state. Then the ratio of this load to the limit load at the beginning of bridge lifetime could also give the answer related to the resistance loss due to corrosion effects. Results of this approach are presented in Fig. 6.

5. Conclusions

From the comparison presented in Figs. 3–5, the decrease about 12.5 % of resistance is evident due to the corrosion attack on the bridge deck in the case of bridges with longitudinal stiffeners having slenderness less than 40 (cases 1–10). Concurrently, the resistance loss is successively decreasing to 18 % with the slenderness increasing. In time period till 25 years of bridge lifetime, the significant dynamic of the corrosion process with nonlinear courses is visible, that is connected with the development of the initial and transitive phase of the corrosion process.

The resistance decrease is slowing after stabilisation of corrosion process and creating the layers of corrosion product with pro-

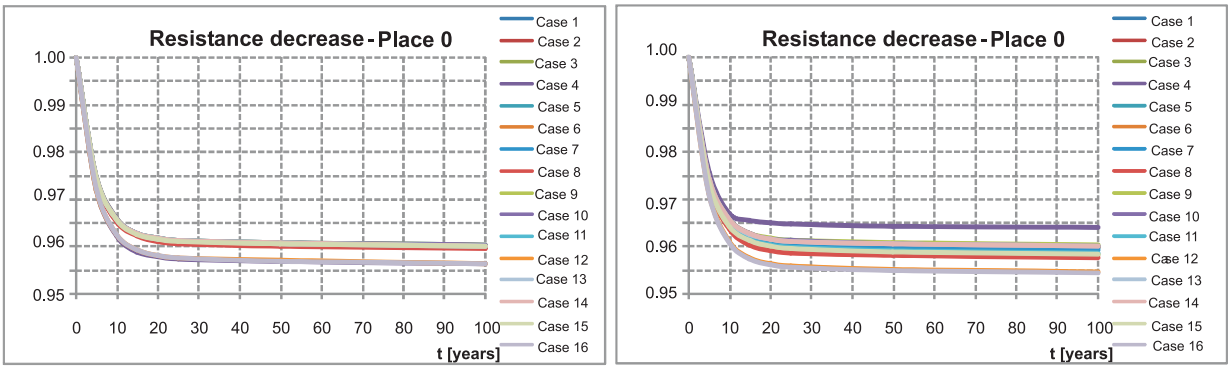

Fig. 3 Time dependent structural resistance decrease in the observed point 0 expressed in the form of limit state stress ratio (left - elastic limit state, right - plastic limit state defined by achieving $2\varepsilon_y$ in the most loaded point)

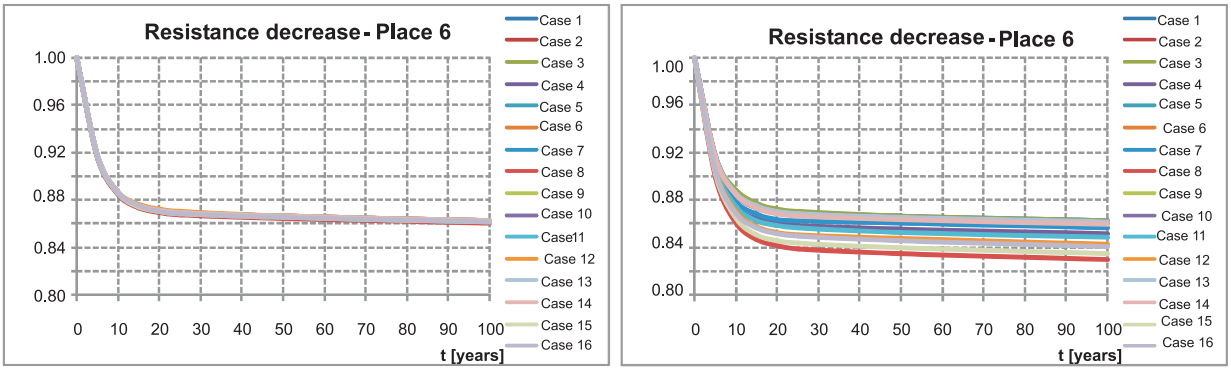

Fig. 4 Time dependent structural resistance decrease in the observed point 6 expressed in the form of limit state stress ratio (left - elastic limit state, right - plastic limit state defined by achieving $2\varepsilon_y$ in the most loaded point)

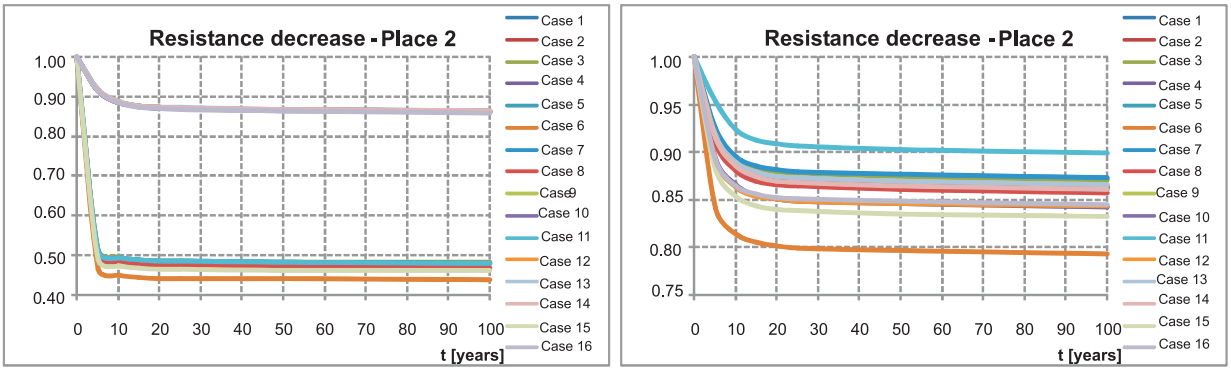

Fig. 5 Time dependent structural resistance decrease in the observed point 2 expressed in the form of limit state stress ratio (left - elastic limit state, right - plastic limit state defined by achieving $2\varepsilon_y$ in the most loaded point)

tective effect, so that the process is then approximating to a linear course. The equal conclusions are evident from the comparison of time dependent resistance decrease by means of the limit loads presented in Fig. 6.

Acknowledgement

This work was supported by the Slovak Research and Development Agency under contract No. APVV-0106-11 and by Research Project No. 1/0364/12 of Slovak Grant Agency.

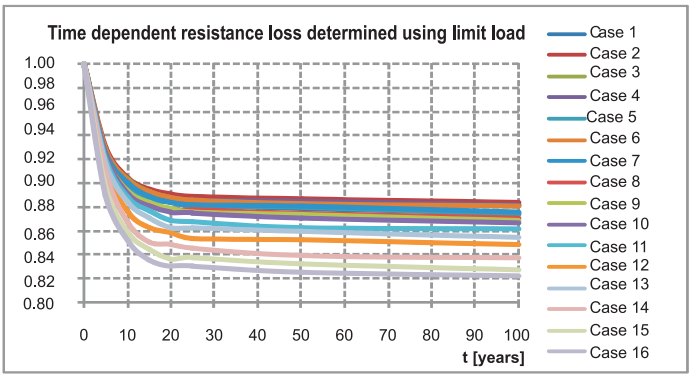

Fig. 6 Time dependent structural resistance decrease in the form of limit state load ratio

References

[1] MAQUOI, R., MASSONET, CH.: *Theorie non lineare de la resistance postcritique des grandes poutres en caisson raidies.* Memoires de I AIPC, vol. 31-II, Zurich 1971.

[2] BALAZ, I., DJUBEK, J.: Ultimate Strength of Compression Orthotropic Plate. *J. of Building Engineering,* vol. 26, 1978, No. 4, pp. 283–301.

[3] SKALOUD, M.: *Design of Plates and webs of Steel Structures,* Academia Praha, 1988.

[4] SERTLER, H., VICAN, J.: *The Real Behaviour of Steel Railway Bridges (in Czech).* Zilina, ES VSDS, 1995.

[5] KVOCAK, V.: *Stability of Plated Flanges.* Monograph, TU Kosice, 2012.

[6] EN 1993-1-5 Eurocode 3: *Design of Steel Structures. Part: 1-5: Plated structural elements,* CEN Brussels, 2003.

[7] KALA, Z., KALA, J.: *Resistance of Plate Girders under Combined Bending and Shear,* Latest Trends on Engineering Mechanics Structures, Engineering Geology, Athens : World scientific and engineering acad. and soc. 2010, pp. 166–171, ISBN 978-960-474-203-5.

[8] VICAN, J., SYKORA, M.: Design of Compression Members for Durability, *Communications - Scientific letters of the University of Zilina,* vol. 11, No. 4, 2009, pp. 9–14, ISSN 1335-4205.

[9] VICAN, J., GOCAL, J., MELIS, B., KOTES, P., KOTULA, P.: Real behaviour and Remaining Lifetime of Bridge Structures, *Communications - Scientific Letters of the University of Zilina*, vol. 10, No. 2, 2008, pp. 30–37, ISSN 1335-4205.

[10] DURATNA, P., BOUCHAIR, A., BUJNAK, J.: Analysis of the Behaviour of Steel-concrete Composite Truss, *Communications - Scientific Letters of the University of Zilina,* vol. 13, No. 4, 2011, pp. 46–50, ISSN 1335-4205.

[11] SYKORA, M.: *The Remaining Lifetime of Bridge Decks with Ballast Beds.* PhD thesis. University of Zilina, 2010.

[12] STN EN 1991-2 Eurocode 1: *Actions on Structures. Part 2: Traffic actions on bridges.* SUTN Bratislava 2006.

[13] AKGUL, F., FRANGOPOL, D. M.: Lifetime Performance Analysis of Existing Steel Girder Bridge Superstructures. *J. of Structural Engineering,* vol. 130, No. 12, pp. 1875-1888.

[14] QIN S., CUI W.: Effect of Corrosion Models on the Time-dependent Reliability of Steel Plated Elements, *Marine Structures,* Elsevier, 2003.

Vladislav Krivda – Ivana Mahdalova – Jan Petru *

USE OF VIDEO ANALYSIS OF CONFLICT SITUATIONS FOR MONITORING THE TRAFFIC ON URBAN ROAD INFLUENCED BY PARALLEL PARKING

The paper deals with problems of influence of parallel parking on urban roads for road traffic safety. It shortly refers to evaluation of normative principles related to parking of road vehicles in the Czech Republic.

It presents the results of analysis of traffic participant behavior on the particular section of inhabited area by use of video analysis of conflict situations. Thus it is pointed out to a possibility of application of this methodology in execution of safety inspections on roads, for example.

Keywords: *Road Transport, Video Analysis, Conflict Situation, Parking.*

1. Introduction

Lack of parking places in inhabited areas is thorny topic for majority of towns with developed individual road traffic. The drivers are forced to park in the places where it is prohibited by traffic signs or even by law – even at the risk of increase of dangerousness of this place. However, they often park in full accord with traffic signs, but the parking places marked by this way show their own deficiencies. Then the dangerous conflict situations can arise between parked vehicles (or also their drivers) and vehicles passing through this road. This paper refers to these conflict situations arising in concrete locality with parallel parking.

This paper shows only the selected conflict situations which are most important and which can arise also on other roads with similar cross arrangement.

In the process of observing the conflicts caused by parallel parking the video analysis of conflict situations was used – this method was described in [1]. The principle of this method is in provision of video record of the observed locality and subsequent evaluating the road traffic participant behavior. Conflict situations (i.e. the situations when a dangerousness degree can arise without incidence of traffic accident) are classified according to the situation type, place and way of incidence and above all according to their seriousness. On the basis of the conflict situation video analysis results we can then place proposals for modification of this place with a purpose to increase the traffic safety or traffic flow continuity. Other particular applications of this methodology can be found by the interested person e.g. in [2] or [3].

Fig. 1 Monitored locality with marked traffic survey points

* **Vladislav Krivda, Ivana Mahdalova, Jan Petru**
Department of Transport Constructions, Faculty of Civil Engineering, VSB – Technical University of Ostrava, Czech Republic,
E-mail: vladislav.krivda@vsb.cz

2. Description of the locality monitored

The detailed analysis of influence of parallel parking on traffic was made on the street "Nabreži Svazu protifasistickych bojovniku" ("Nabrezi SPB" for short) – see Fig. 1. It's a two-lane urban road which contains parallel parking from its greater part. On the road section monitored are also bus stops "Namesti B. Nemcove" (see Fig. 1 – A1 and A2) and "Nabrezi" (see Fig. 1 – B1 and B2). The part between the street "17. listopadu" and "Porubska" was monitored (see Fig. 1 – marked by yellow color).

Four traffic survey points were selected (see Fig. 1 – roman numerals I–IV), from which the video records were made for video analysis of conflict situations. From points I and II the records were made in both direction, as Fig. 1 shows. The views from each individual point are shown on photographs of Figs. 2-4. Parameters of traffic and parking lanes near point IV are shown in Fig. 5.

3. Sizes of parallel parking places according to czech norms

At present the norm CSN 73 6056 Parking Areas for Road Vehicles since March 2011 [4] is valid in the Czech Republic. Because the vast majority of parking places were built before the launching of this norm, let's see how this problem was solved earlier.

Fig. 2 Views from traffic survey point I

Fig. 3 Views from traffic survey point II

Fig. 4 Views from traffic survey point III (left photograph) and IV (right photograph)

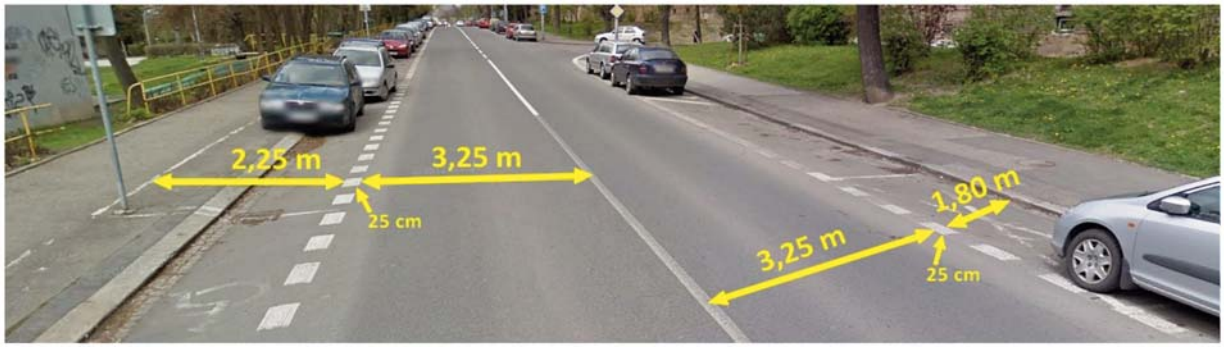

Fig. 5 Width of parking lanes and traffic lanes near point IV

The norm CSN 73 6056 since 1987 [5] (or its Amendment Z1 since 2001 [6]) was valid before 2011. This norm defined parallel parking places as follows. The width of parking place (see Fig. 6 – size a) for a small or middle passenger car was 2.00 m. The width of parking place for big passenger cars was 2.20 m. The length of the parking place (see Fig. 6 – size b) for a small or middle passenger car was 5.50 m and for a big passenger car then 6.50 m. These parameters were based on sizes of average vehicles (i.e. small or middle passenger cars with width 1.65 m and length 4.25 m and big passenger cars with width 1.80 m and length 5.00 m).

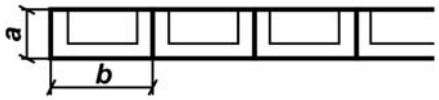

Fig. 6 Width (a) and length (b) of parallel parking place according to CSN 73 6056 since 1987 [5]

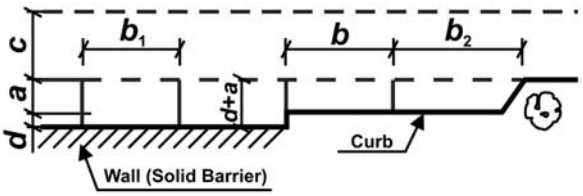

Fig. 7 Sizes of parallel parking places according to CSN 73 6056 since 2011 [4]

However, the Amendment Z1 in 2001 brought no modifications of parking places. The modifications were made in the norm since 2011 [4] which is a completely new norm for parking areas. This norm already respects bigger sizes of modern vehicles and it also adapts sizes of parking places to them. The sizes of vehicles according to the current norm are as follows – the width of the passenger car (without rear-view mirrors) is 1.75 m and its length is 4.75 m, the width of the van is then 2.00 m and length is 6.00 m.

Sizes of parking places are given in Table 1 and are connected with Fig. 7, where a or b is a basic width or length of the parking place, b1 or b2 is length of the parking place with free entry or near planted area, c is a width of adjacent traffic lane, d is distance between the parking place and solid obstacle and sum d+a is a real width of the parking place in case of solid obstacle in the level of front door.

Sizes of parallel parking places for passenger cars and vans and width of adjacent traffic lane (see Fig. 7) according to CSN 73 6056 since 2011 [4] Table 1

Vehicle	Parking way	a (m)	d (m)	b (m)	b_1 (m)	b_2 (m)	c (m)
car	driving forward	2.00	0.40	6.75	5.25	7.75	3.25
	reversing			5.75	–	6.75	3.75
Van	driving forward	2.25	0.40	8.25	6.50	9.00	3.50
	reversing			7.50	–	8.00	3.75

It's evident that modification of the norm was very desirable. Sizes of the vehicles were changed in the last 30 years – which is not only a trend in the Czech Republic, but also in other European states where there are also changes related to normative sizes of parking places (see e.g. [7]).

4. Video analysis of conflict situations

This chapter will describe conflict situations discovered by observations which are related to parallel parking of concrete locality. Individual video sequences can be found on the web page https://sites.google.com/site/krivdaspb [8].

The biggest problem during parking maneuvers into the parallel parking place is probably parking with the use of reversing. The driver has to stop in the traffic lane near a free parking place the length of which is considered by him as sufficient for parking of his vehicle. If this vehicle intending to park is followed by other vehicles, they either have to stop and wait for ending the parking

Fig. 8 Driving around vehicle parking by reversing (point II; see VIDEO 01 [8])

Fig. 9 Unsuccessful parking maneuver (point II)

maneuver (this however results in traffic flow continuity interruption) or drive around this vehicle (usually by driving into opposite direction – see Fig. 8). However, the driving into opposite direction is possible only in case of absence another vehicle which could be restricted or endangered.

If the length of parking place is reckoned by driver wrongly, the other car can be crashed (see Fig. 9 left). And it can also happen that the driver is forced to leave his / her car in an inappropriate position (see Fig. 9 on the right).

The time of parking maneuver by reversing depends then especially on the driver's experiences. In case of a longer time it occurs that a queue of vehicles is formed or other vehicles drive around this vehicle more frequently and they use opposite direction. The similar situation, when the parking maneuver into parallel parking place by reversing took approx 1.5 minute, can be seen in the VIDEO 02 [8].

If the driver decides to drive into parallel parking place by forward driving, he has to have free place of a sufficient length, because this maneuver needs more place (often in case of two or more free parking places in a row). In case of availability of only one free parking place the drivers usually don't use this maneuver. In opposite case the maneuver isn't usually successful and the vehicle isn't parked correctly or after all, the driver goes out from this parking place into the traffic lane and parks his/her car by reversing. Next vehicle can be restricted (or delayed) even in case of successful maneuver, i.e. driving into the parking place by forward driving for the first time – see Fig. 10.

Conflict situations caused by exiting the parking place don't usually arise, because the driver is able to find a needed space in the traffic flow of vehicles, which are going in the traffic lane, using the rear-view mirror.

Another situation is related to the width of traffic lanes and parking lanes (see Fig. 5), because the widths of parking lanes don't comply with present demands – see Chapter 3. The drivers going in the traffic lane drive closer to the middle of road probably

Fig. 10 Delayed vehicle after the vehicle entering the parking place by driving forward (point II; see VIDEO 03 [8])

Fig. 11 Crossing the bus into opposite direction due to inadequate width proportions (point I; see VIDEO 04 and VIDEO 05 [8])

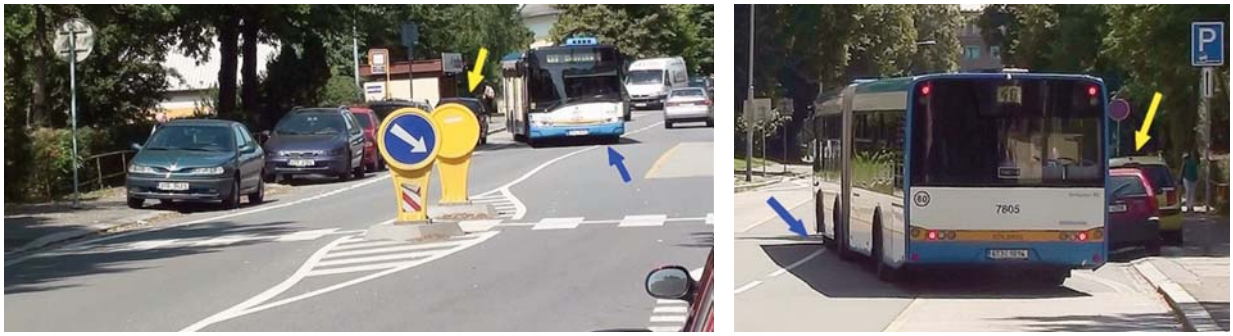

Fig. 12 Exiting the bus from the bus stop influenced by parallel parking places (yellow arrows) and subsequent driving into opposite direction (blue arrows); the left photograph from the point III (see VIDEO 06 [8]) and the right photograph from the point II (see VIDEO 07 [8])

due to keeping safety side distance from the vehicles parked. However it can cause collision with vehicles driving in opposite direction. This distance is respected by drivers of smaller vehicles (i.e. passenger cars), but especially by drivers of larger vehicles (i.e. trucks and buses). The larger vehicles then often have to cross the center dividing line relatively markedly into the opposite direction – see Fig. 11.

Fig. 12 describes another situation when the vehicle (this time it is a bus exiting the bus stop) must drive into opposite direction. It is primarily caused by a relatively small distance between the stop marker and the first parking place. The Photograph in Fig. 12 (or relevant videos) shows the same place from the point of view of different traffic survey points.

Unfortunately, numerous drivers also ignore the fact that parked vehicle can cause restriction of road traffic or even dangerous conflict situation caused again by driving another vehicle into opposite direction – see Fig. 13.

Leaving the parallel parking places has been already mentioned above. If the driver of such a vehicle decides to leave the place in opposite direction compared to the direction in which he/she arrived and in which he/she parked the car, he/she has to carry out a U-turn. In case of absence of other safer alternative (e.g. near roundabout) he/she usually makes it through traffic lanes. This maneuver, which does not have to be successful for the first time, can cause restriction or hazard to other road participants (see Fig. 14 and especially relevant video in which you can see this situation best).

As already mentioned, an array of drivers pass the vehicles parked in a certain safe distance, namely partly to avert damage of their own cars or other vehicles and partly to avert traffic accident in case of the parked vehicle crew's carelessness when they, for example, open the door into the traffic lane. Danger arises especially in such cases when the distance between the vehicle parked and the traffic lane isn't sufficient (it refers to majority of parking places in the observed locality). The crew of the vehicle can be endangered while they are getting out of the car and moving on the road (the driver has no other option, in fact). The same situation, but in reverse order, is shown in Fig. 15, when driver is coming to his/her vehicle (by walking along the traffic line) and opening the door which also sticks out into traffic lane (see also relevant video referred to Fig. 15).

On the road monitored there is another problem, namely inadequate sight proportions for exiting the vehicles from the minor

Fig. 13 Driving around a wrongly parked vehicle (yellow arrows) into opposite direction (blue arrows); point II (see VIDEO 08 and VIDEO 09 [8])

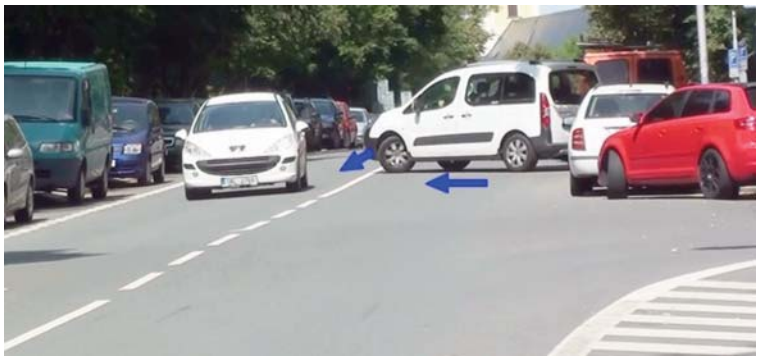

Fig. 14 Turning of the vehicle exiting the parking place (point IV – see VIDEO 10 [8])

Fig. 15 Open door sticking out into traffic lane and movement of pedestrian (driver) along vehicles parked (point IV – see VIDEO 11 [8])

road into the major road. Such drivers are forced to run into the major road traffic lane relatively noticeably to be able to see an arriving potential vehicle as much as possible – see the left photograph in Fig. 16, where the driver turning left stopped on the major road traffic lane. While turning right the vehicles can in the process of driving around the vehicles parked drive into the opposite direction– see right photograph in Fig. 16, where furthermore the vehicle marked by yellow arrow makes sight proportions worse and the vehicle marked by red arrow can endanger (also by influence of inadequate width of traffic lanes) the vehicle in opposite direction (see blue broken arrow which indicates tugging the steering wheel). Both situations from Fig. 16 are more noticeable from relevant videos.

Fig. 16 Conflict situations caused by wrong sight proportions (point IV - see VIDEO 12 and VIDEO 13 [8])

5. Conclusion

The above-described conflict situations are only a selection of all situations found out which happened on the road section monitored. It can be however noted that this list of the situations can be used as a general illustration of what can be expected on road with this cross arrangement. The project engineers designing this road didn't certainly mean to make a dangerous section of the road. They rather intended to increase the number of parking places in an inhabited area and maybe to make some traffic calming. Unfortunately, this solution results in above-mentioned problems. On the basis of these pieces of knowledge we can agree with a statement that whichever (even if a positive one) change can cause another problem or several problems (which are often much more serious than before).

The width of the parking place is 2.00 m according to the valid norm [4] (see Chapter 3 of this paper). If we take the passenger car width into account, which is 1.75 m, then only 25 cm remain. This space however isn't sufficient for the safe opening of the door, getting the driver out of the car and movement of driver along the vehicle. Besides, unless the driver parks closely to the curb, the distance between the vehicle parked and the traffic lane is decreased. The parking place width of 2.00 m is thus minimal and in order to ensure the traffic safety on the road with parallel parking it is appropriate to install a so- called maneuver lane between the parking lane and the traffic lane. This lane can serve not only for movement of pedestrians (drivers), but also for simplified parking maneuvers. In case of adequately wide maneuver lane we can expect no conflict situations which were described in Chapter 4 (see for example Fig. 8, 11 and 13).

The paper refers to the fact that the video analysis of conflict situations can be applied very well for detection of problems in road traffic which are relatively serious, but of which there are no (and there cannot be) any statistic information (compared to the statistics of traffic accidents) in existence. Video analysis of conflict situations is accepted as an instrument for the evaluation of traffic safety at intersections in the Czech Republic. The aim of the project was to prove the suitability of video analysis of conflict situations for the evaluation the safety of static transport. The methodology of the conflicts monitoring with the help of the by video apparatus proves to be a suitable instrument for safety inspections conducting on roads. Initiative for the adjustment the methodology of safety inspection will be prepared in this sense.

A separate question related to influence of parallel parking refers to problems of influencing the capacity of the road considered. That depends on volumes of traffic flows and on numbers of parking maneuvers. In the present Czech norms these problems are not mentioned too elaborately. Nevertheless, the Slovak norms, for example, deal with these problems in more details (see also [9] e.g.). The project results will also be used for the preparation of the initiative to revision of Czech technical standards.

The paper was created with the support of the Ministry of Education, Youth and Sports of the Czech Republic to support of creative activity according to indicator F which was allocated to VSB-TU Ostrava [10]. In this project and on the basis of the video analysis the authors of this article will be also interested in influence of parking maneuvers on capacity of sections between intersections under Czech traffic conditions, the solution of which is not sufficiently addressed in present norms. The video records were also made from financial resources of the research project of the Ministry of Transport "The Influence of Structural Elements Geometry on the Safety and Fluency of Operation in Roundabouts and Possibility of Rise Crashes Prediction" (Project No. CG911-008-910) [11].

References

[1] KRIVDA, V.: Video-Analysis of Conflict Situations on Selected Roundabouts in the Czech Republic. *Communications – Scientific Letters of the University of Zilina,* vol. 13, No. 3, p. 77–82, 2011, ISSN 1335-4205. Available in http://www.uniza.sk/komunikacie.

[2] KRIVDA, V., MAHDALOVA, I.: Use of Video Analysis of Conflict Situations by the Evaluation of Inappropriately Designed Building Elements on Roundabouts. *Transactions of the VSB – Technical University of Ostrava, Civil Engineering Series.* No. 2, 2011, vol. XI, paper #25 (8 p), DOI 10.2478/v10160-011-0025-8. Publisher Versita, Warsaw, ISSN 1213-1962 (Print) ISSN 1804-4824 (Online).

[3] KRIVDA, V.: Analysis of Conflict Situations on Roundabouts in Valasske Mezirici. *Transactions of the VSB – Technical University of Ostrava, Civil Engineering Series.* No. 1, 2010, vol. X, paper #8 (10 p), DOI 10.2478/v10160-010-0008-1. Publisher Versita, Warsaw, ISSN 1213-1962 (Print) ISSN 1804-4824 (Online).

[4] CSN 73 6056 *Parking Areas for Road Vehicles.* Praha: Office for Standards, Metrology and Testing, 2011 (in Czech)

[5] CSN 73 6056 *Parking Areas for Road Vehicles.* Praha: Office for Standards and Measurement, 1987 (in Czech)

[6] CSN 73 6056 *Parking Areas for Road Vehicles – Amendment Z1.* Praha: Czech Standards Institute, 2001 (in Czech)

[7] BRCIC, Davor, Marko SOSTARIC and Marko SEVROVIC. Analytic Determination of Reference Passenger Car Size for Parking Space Dimensioning in Croatia. *Promet – Traffic&Transportation.* University of Zagreb, Faculty of Transport and Traffic Sciences, Croatia, vol. 24, No. 3, 2012, pp. 215–222, ISSN 1848-4069 (ISSN 0353-5320 in Web of Science)

[8] KRIVDA, Vladislav, Ivana MAHDALOVA a Jan PETRU. *Video Analysis of Conflict Situations on Street "Nabrezi SPB" in Ostrava-Poruba.* 2012. Available in https://sites.google.com/site/krivdaspb (appendix of this paper)

[9] HUSZAROVA, K.: *Capacity Calculations of Urban Roads.* Thesis. Zilina: University of Zilina, 2011, 87 p., (in Slovak)

[10] KRIVDA, V. et al.: *Influence of Parallel Parking on Safety and Capacity of Road Section between Intersections.* Project supported from benefit s of Ministry of Education, Youth and Sports of the Czech Republic to support of creative activity according to indicator F which was allocated to VSB-TU Ostrava. Ostrava: VSB-TU Ostrava, Faculty of Civil Engineering. 2012

[11] MAHDALOVA, I. et al.: *The Influence of Structural Elements Geometry on the Safety and Fluency of Operation in Roundabouts and Possibility of Rise Crashes Prediction.* Project No. CG911-008-910. Project of the Ministry of Transport, Czech Republic. VSB-TU Ostrava, 2009-2010.

Tomas Lack – Juraj Gerlici *

WHEEL/RAIL CONTACT STRESS EVALUATION BY MEANS OF THE MODIFIED STRIP METHOD

The Strip Method is often used for rail/wheel contact area and contact normal stress evaluation. The paper deals with the computational time saving procedure when the computation accuracy is guaranteed. We included the local coordinate system with a presupposed semi-circular course of the normal stress for the purpose of the integral that is necessary for deformation in the middle of individual strips evaluation. The integral is solvable analytically. The input parameters for individual parts of splines and individual strips expression are possible to insert after analytical solution..

Keywords: *Wheel/rail contact, contact stress evaluation, modified Strip method, optimized computation procedure.*

1. Introduction

An important parameter influencing the power effect of a wheel on the rail is the size and shape of the contact area as well as the normal stress distribution which has the impact on it. Nowadays various methods are used to find out the size of contact areas and stresses [1, 2]. It is necessary to mention the Hertz method as one of the oldest up to date used methods. It provides acceptable results for a large area in spite of many simplifications. Another computational procedure is the Kalker variation method or the strip method which is, thanks to its results, close to reality and is used in the following calculations [3]. Nowadays, another group of calculation program systems (ANSYS, ADINA) is used in certain situations. The systems work on the base of finite elements method theory.

2. Strip method

The Strip Method presupposes quasi-static rolling [1]. The principal idea of the theory is to take into consideration slim contact areas in the *y*-direction. In Fig. 2 there are two bodies in contact. In fact the geometrical parameters (of railway wheel and rail) should be similar to the reality. The deformation zones are of the similar shapes too. In spite of this fact the parameters (the displacements w_1 and w_2) in Fig. 1 are rather different for better understanding of the theory.

In fact, the contact area should be a plane (parallel with the x-y plane).

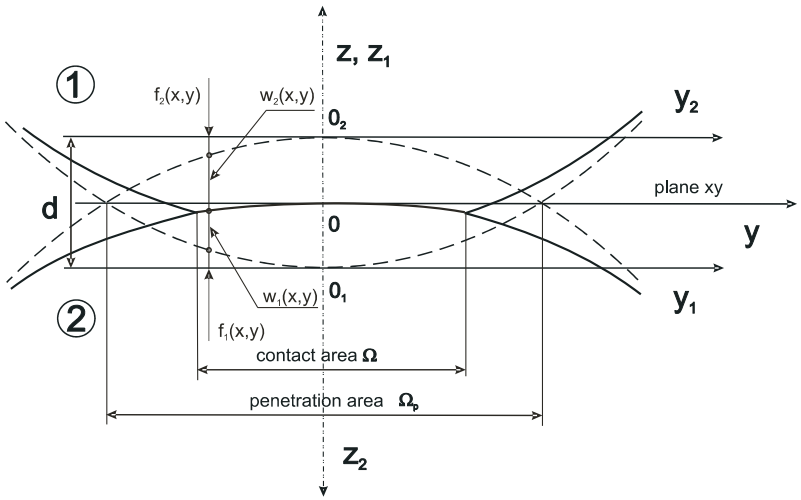

Fig. 1 Variation Coordinate body system at the contact

* **Tomas Lack, Juraj Gerlici**
Faculty of Mechanical Engineering, University of Zilina, Slovakia, E-mail: tomas.lack@fstroj.uniza.sk

The method presupposes the existence of two rotating bodies 1 and 2 with surfaces *S*1 and *S*2. The bodies touch in the point 0, which is at the same time the beginning of their spatial coordinate systems. The axes *x* and *y* determine the horizontal base. We will mark the horizontal coordinate as the *z* – axis. If there is no influence of a normal force *Q*, then there exclusively exists geometrical binding between the bodies.

If the bodies are pressed against each other by the normal force *Q*, a deformation and a contact area Ω instead of a contact point **arises** between the bodies.

- The geometrical profile shape of the first body surface will be marked $f_1(x,y)$, the geometrical profile shape of the second body surface will be marked $f_2(x,y)$.
- The elastic displacement in the *z*-axis direction caused by the deformation of the first body surface will be marked $w_1(x, y)$, the displacement in the z-axis direction caused by the deformation of the second body surface will be marked $w_2(x, y)$.
- The displacement of bodies centers against each other in the axis-z direction will be marked *d*.
- The perpendicular distance between the points of the deformed bodies surfaces will be marked $\delta(x, y)$.

3. Normal stress approximation over a strip

The stress evaluation over the k[th] strip (Fig. 2) is approximated in a standard way [4]:

$$p_k(x,y_k) = p_{0k} \cdot \sqrt{1 - \left(\frac{x}{x_{dk}}\right)^2} \tag{1}$$

where:
$p_k(x,y_k)$ normal stress in the *x* position,
p_{0k} maximum normal stress,
x_{dk} half length of the k[th] strip.

We aimed our interest at increasing the computational effort. To obtain the requested results, deformations and stresses in the middle of strips, we utilized the procedures introduced in the next text.

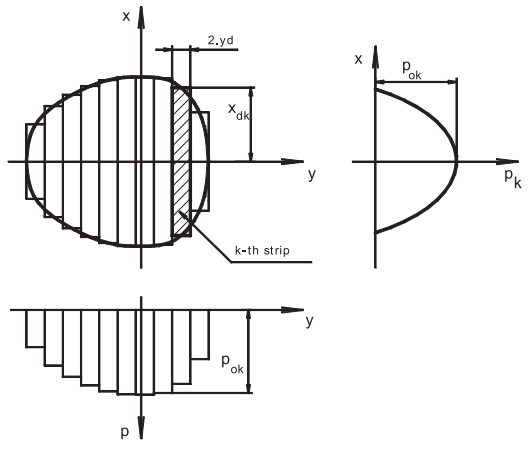

Fig. 2 Contact patch distribution into the strips, stress distribution over individual strips

4. Time optimized computational procedure for contact stresses assessment

The equation system assembly is necessary for the stress evaluation in the middle of strips [4, 5, 6]:

$$[M] \cdot \{p^{(0)}\} = \{w^{(0)}\} \tag{2}$$

where:
[*M*] influence coefficients matrix,
$\{p^{(0)}\}$ normal stresses in the middle of strips vector,
$\{w^{(0)}\}$ in the middle of strips strains vector.

The [*M*] matrix elements are of values:

$$M_{k,s} = H \cdot I_{k,s}^{(0)} \tag{3}$$

where:

$$H = \frac{1}{\pi} \cdot \left(\frac{1-\mu_1^2}{E_1} + \frac{1-\mu_2^2}{E_2}\right) \tag{4}$$

where:
μ_1 Poisson's ratio of a first body,
μ_2 Poisson's ratio of a second body.
E_1 modulus of stiffness of a first body.
E_2 modulus of stiffness of a second body.

The vector elements are:

$$w_k^{(0)} = z_{2k} - z_{1k} - D \tag{5}$$

where:
$w_k^{(0)}$ deformation in the middle of k[th] strip.
z_{1k} z- coordinate of a first body in the middle of k[th] strip,
z_{2k} z- coordinate of second body in the middle of k[th] strip,
D straightening up of bodies.

The aim is to compute the value $I_{k,s}^{(0)}$ in accordance with relation below:

$$I_{k,s}^{(0)} = 2 \cdot \int_0^{x_{dk}} \int_{y_{lk}}^{y_{rk}} \sqrt{\frac{1 - \left(\frac{x}{x_{dk}}\right)^2}{x^2 + (y_s - y)^2}} \cdot dy \cdot dx \tag{6}$$

when:

$$y_{lk} = y_k - y_d \tag{7}$$

$$y_{rk} = y_k + y_d \tag{8}$$

where:
x_{dk} half length of the kth strip,
y_k y-coordinate of kth strip,

y_s y-coordinate of sth strip,
y_d half width of strips.

This integral can be modified into one- dimension integral in the form:

$$I_{k,s}^{(0)} = -\frac{2}{|x_{dk}|} \cdot \int_0^{x_{dk}} \sqrt{x_{dk}^2 - x^2} \cdot Ln\{AA\} \cdot dx \quad (9)$$

$$AA = \frac{[AB] \cdot [AC]}{x^2} \quad (10)$$

$$AB = \sqrt{x^2 + (y_s - y_{rk})^2} + y_s - y_{rk} \quad (11)$$

$$AC = \sqrt{x^2 + (y_s - y_{lk})^2} - y_s + y_{lk} \quad (12)$$

It is unavoidable to solve the integral in the relation (9) numerically, because it has no analytical solution. This computation is very time consuming for separate strips in the relationship to other strips.

This is the reason for the new procedure development that is not dependent on a real strip length. We presuppose that a strip is of one unit length. Description of individual parameters in the x, y coordinate system is in Fig. 3 and a description of individual parameters in the *u*, *v* coordinate system is in Fig. 4.

For the value $I_{k,s}^{(0)}$ the relation is valid:

$$I_{k,s}^{(0)} = i_{k,s}^{(0)} \cdot x_{dk} \quad (13)$$

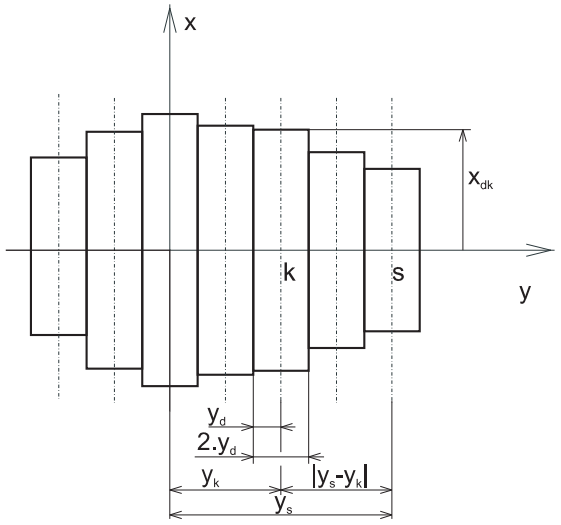

Fig. 3 Description of individual parameters in the coordinate system

We establish:
- the k[th] strip length in the *u, v* system has the value of 1
- the k[th] strip width in the *u, v* system has the value:

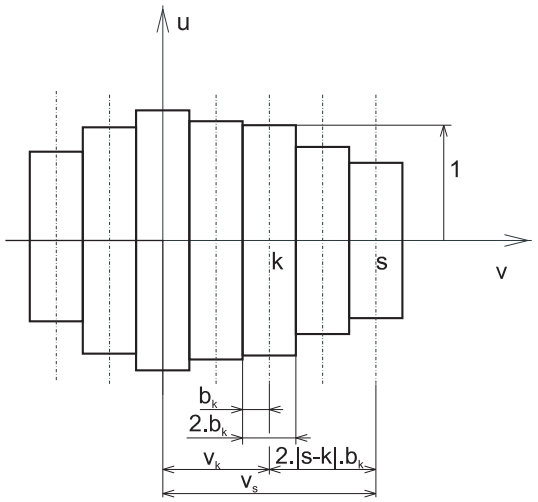

Fig. 4 Description of individual parameters in the coordinate system

$$b_k = \frac{y_d}{x_{dk}} \quad (14)$$

The relationship for the $I_{k,s}^{(0)}$ computation is valid:

$$I_{k,s}^{(0)} = 2 \cdot \int_0^1 \int_{-1}^1 \sqrt{\frac{1 - u^2}{u^2 + \left[\left(2 \cdot |s - k| - v\right) \cdot b_k\right]^2}} \cdot dv \cdot du \quad (15)$$

The value: "*i*" of this integral or value: "*E*" of decimal logarithm of integral are depicted in graphs in Figs. 5 – 10.

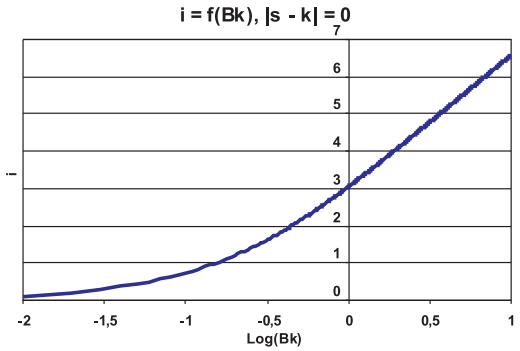

Fig. 5 The integral value "i" in dependence on Log(Bk) on condition that $|s - k| = 0$

The value of an integral decimal logarithm "*E*" can be expressed via the polynomial of 6-th grade:

$$E = \left\{\left\{\left\{\left\{\left\{\left[\left(a_6 \cdot L + a_5\right) \cdot L + a_4\right] \cdot \right\} \cdot L + a_3 \right\} \cdot L + a_2 \right\} \cdot L + a_1 \right\} \cdot L + a_0 \quad (16)$$

where:

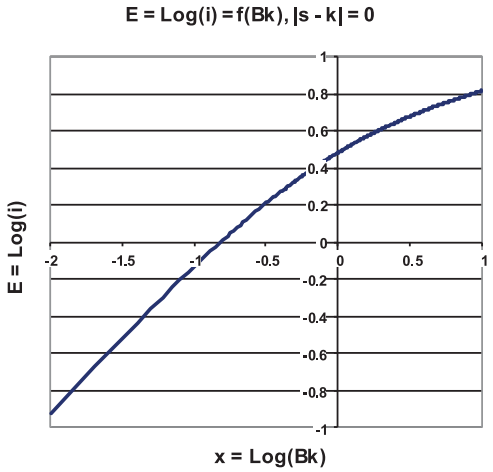

Fig. 6 The integral decimal logarithm value "E" in dependence on t Log(Bk), on condition that $|s-k| = 0$

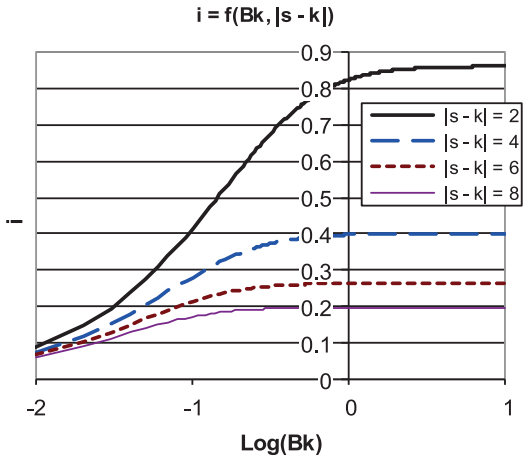

Fig. 7 The integral value "i" in dependence on Log(Bk) on condition that $|s-k| = <2;8>$

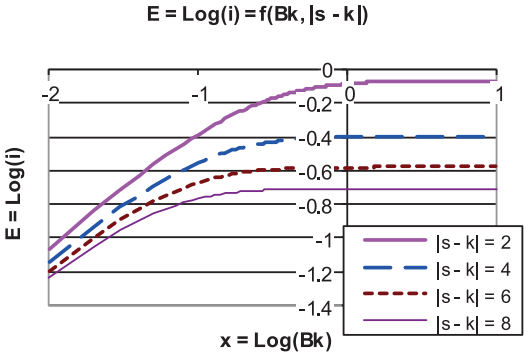

Fig. 8 The integral decimal logarithm value "E" in dependence on Log(Bk) on condition that $|s-k| = <2;8>$

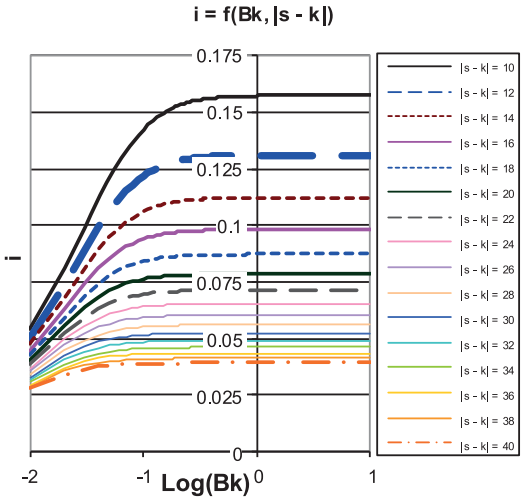

Fig. 9 The integral value "i" in dependence on Log(Bk) on condition that $|s-k| = <10;40>$

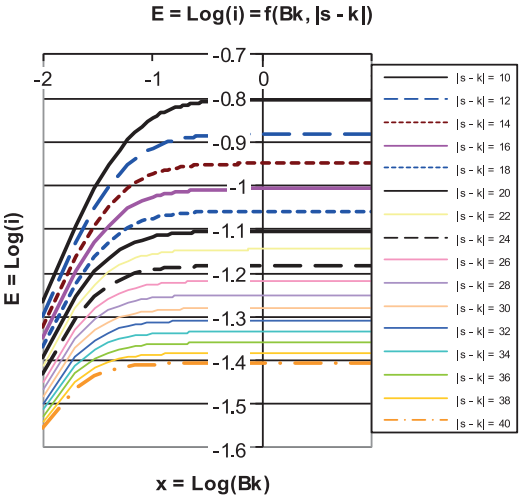

Fig. 10 The value of integral decimal logarithm in dependence on Log(Bk) on condition that $|s-k| = <10;40>$

$$L = Log(b_k) \tag{17}$$

Polynomial coefficients from a_6 to a_3 are in Table 1.

Polynomial coefficients from to are in Table 2.

The $i_{k,s}^{(0)}$ value can be expressed via this relation:

$$i_{k,s}^{(0)} \approx 10^{E} \tag{18}$$

Polynomial coefficients a_6 to a_3 Table 1

$\|s-k\|$	a_6	a_5	a_4	a_3
0	- 0.00255	- 0.001497	0.022573	0.009238
2	- 0.00756	- 0.026714	0.015249	0.105083
4	0.003839	- 0.008085	- 0.02931	0.068803
6	0.007608	0.004252	- 0.03718	0.037078
8	0.007902	0.009316	- 0.03513	0.019712
10	0.007030	0.01098	- 0.03057	0.010126
12	0.005830	0.011066	- 0.02574	0.004737
14	0.004628	0.010462	- 0.0213	0.001656
16	0.003549	0.009613	- 0.01744	- 0.00014
18	0.002611	0.008678	- 0.01415	- 0.00115
20	0.001806	0.007735	- 0.01138	- 0.00165
22	0.001127	0.006837	- 0.00907	- 0.00186
24	0.000534	0.005942	- 0.00714	- 0.00182
26	0.000064	0.005204	- 0.00551	- 0.00174
28	- 0.000320	0.00455	- 0.00417	- 0.00164
30	- 0.00063	0.003985	- 0.00305	- 0.00152
32	- 0.00087	0.003496	- 0.0021	- 0.00139
34	- 000102	0.003193	- 0.00132	- 0.00141
36	- 0.00128	0.002579	- 0.00064	- 0.00097
38	- 0.0014	0.002248	- 7,3E-05	- 0.00083
40	- 0.00151	0.001912	0.000334	- 0.00069

Polynomial coefficients a_2 to a_0 Table 2

$\|s-k\|$	a_2	a_1	a_0
0	- 0.16037	0.467393	0.483852
2	- 0.14821	0.079591	- 0.08251
4	- 0.04814	0.015369	- 0.39959
6	- 0.0153	0.005056	- 0.5794
8	- 0.0027	0.00233	- 0.7058
10	0.00236	0.001448	- 0.80338
12	0.004248	0.001116	- 0.88289
14	0.004707	0.000973	- 0.95
16	0.004506	0.000906	-1.00807
18	0.004019	0.000859	-1.05925
20	0.003431	0.000813	-1.10502
22	0.002834	0.000765	-1.1464
24	0.002282	0.000698	-1.18418
26	0.001758	0.000651	-1.21892
28	0.001302	0.000611	-1.25109
30	0.0009	0.000577	-1.28104
32	0.000545	0.000544	-1.30905
34	0.000223	0.000551	-1.33537
36	- 0.00002	0.000445	-1.36018
38	- 0.00026	0.000409	-1.38364
40	- 0.0004	0.000389	-1.40591

For a strip with the coordinate x deformation computation the following relation is valid:

$$w_k(x) = H \cdot \sum_{s=1}^{n} p_s^{(0)} \cdot I_{k,s}(x) \ , \tag{19}$$

where integral:

$$I_{k,s}(x_k) = \int_{-x_{dk}}^{x_{dk}} \int_{y_{lk}}^{y_{rk}} \sqrt{\frac{1\left(\frac{x}{x_{dk}}\right)^2}{(x_k - x)^2 + (y_s - y)^2}} \cdot dy \cdot dx \tag{20}$$

This integral can be modified into the one-dimensional integral in form:

$$I_{k,s}(x_k) = -\frac{1}{|x_{dk}|} \cdot \int_{-x_{dk}}^{x_{dk}} \sqrt{x_{dk}^2 - x^2} \cdot \cdot Ln\left\{\frac{\sqrt{(x - x_k)^2 + (y_s - y_{lk})^2} - y_s - y_{lk}}{\sqrt{(x - x_k)^2 + (y_s - y_{rk})^2} - y_s - y_{rk}}\right\} \cdot dx \tag{21}$$

This integral has no analytical solution, so it is unavoidable to compute this integral numerically. In relation to other strips, the mentioned solution for strip by strip computation is time consuming.

We establish:

- the k-th strip length in the *u, v* system has the value of 1
- the k-th strip width in the *u, v* system has the value:

$$b_k = \frac{y_d}{x_{dk}} \tag{22}$$

and

$$u_k = \frac{x_k}{x_{dk}}, \tag{23}$$

where:

x_k x – coordinate, in the *x, y* coordinate system on kth strip,
x_{dk} length of the kth strip,
u_k u – coordinate, in the *u, v* coordinate system on kth strip.

$$I_{k,s}(x_k) = i_{k,s}(u_k) \cdot x_{dk} \, , \tag{24}$$

$$i_{k,s}(u_k) = i_{k,s}^0 \cdot \frac{q_{k,s}(u_k) + q_{k,s}(-u_k)}{q_{k,s}^{(0)}}, \tag{25}$$

$$q_{k,s}^{(0)} = 2 \cdot \int_0^1 \int_{-1}^1 \frac{1 - u^2}{\sqrt{u^2 + \left[\left(2 \cdot |s - k| - v\right) \cdot b_k\right]^2}} \cdot dv \cdot du \tag{26}$$

$$q_{k,s}^{(0)}(\chi) = \int_0^1 \int_{-1}^1 \frac{1-u^2}{\sqrt{(\chi-u)^2 + \left[\left(2\cdot|s-k|-v\right)\cdot b_k\right]^2}} \cdot dv \cdot du \tag{27}$$

The $q_{k,s}^{(0)}$ integral values and $q_{k,s}(\chi)$ integral are utterably analytical.

Further, we compare the computational precision and computation speed gained by the Kalker's method with the results gathered by other methods.

4. Computation results obtained by different methods

In the following graphs are maximum stresses in contact courses against lateral shift of the wheel along a rail head movement from a wheel rim (Fig. 11), maximum stresses in contact courses against lateral shift of the wheel along a rail head movement to a wheel rim (Fig. 12) as well as the contact patch values courses against lateral shift of the wheel along a rail head movement from a wheel rim (Fig. 13) and contact patch area courses against lateral shift of the wheel along a rail head movement to a wheel rim (Fig. 14).

The computational time spent on the P5 computer, with 2GB RAMM, 3GHz frequency.

Utilized methods:

- *Strip method* level of tenth of second
- *Kalker method with input of strip method results* – level of second
- *Kalker variation method* – level of more than ten seconds.

7. Conclusions

The Strip Method is often used for rail/wheel contact area and contact normal stress evaluation. It presupposes quasi-static rolling. The principal idea of the theory is to take into consideration slim contact areas in the y-direction. The paper deals with the *computational time saving procedure* when the computation accuracy is guaranteed.

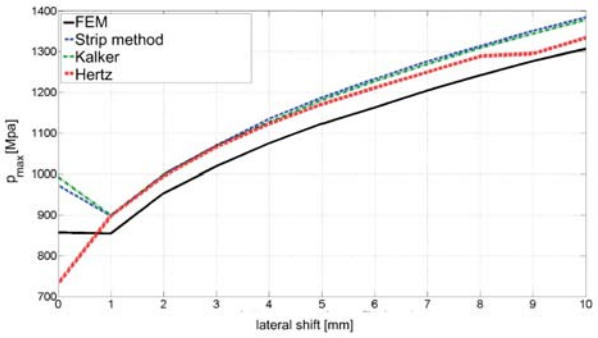

Fig. 11 Maximum stresses (pmax) in contact courses against lateral shift of the wheel tread along a rail head movement from a wheel rim

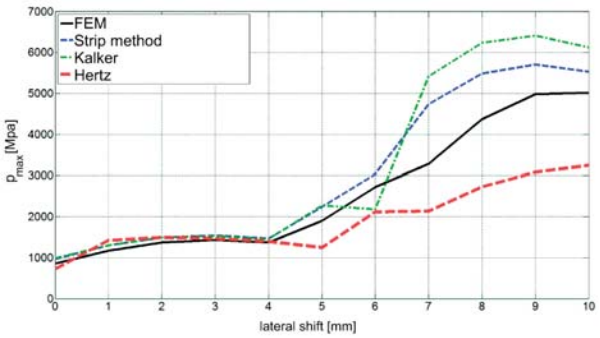

Fig. 12 Maximum stresses (pmax) in contact courses against lateral shift of the wheel tread along a rail head movement to a wheel rim

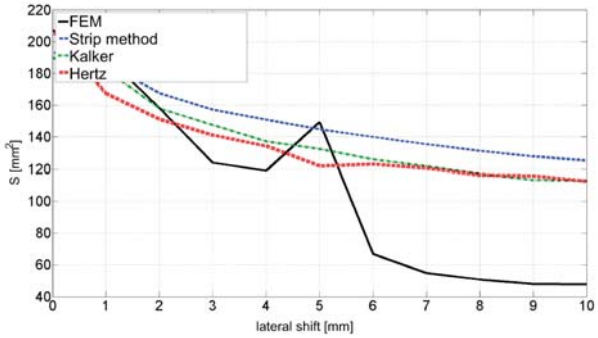

Fig. 13 Contact patch values (S) courses against lateral shift of the wheel tread along a rail head, movement from a wheel rim

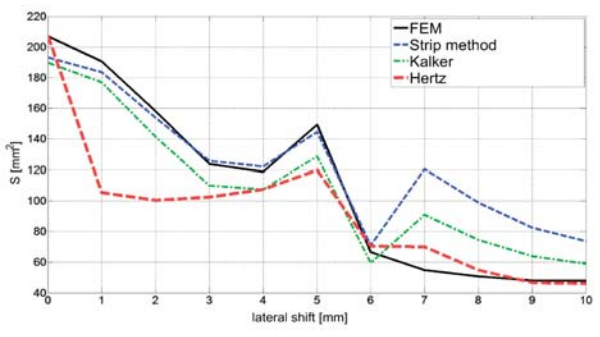

Fig. 14 Contact patch values (S) courses against lateral shift of the wheel tread along a rail head, movement to a wheel rim

The introduced method enables contact patches and contact stresses between railway wheel and rail [7] under decreased computational time consumption. Rules and procedures characteristic of the Strip method are preserved. The stress computation acceleration is in this case based on the algorithm for numerical solution of integrals. We included the local coordinate system with a presupposed semi-circular course of the normal stress for the purpose of the integral computation. This integral computation is needed for deformation in the middle of individual strips evaluation. The integral is solvable analytically. The input values for the separate spline parts and separate strips computation are possible to insert after analytical solution of the integral. The procedure application may bring the practical benefit for researchers and computation – analysis experts who are interested in the field of vehicle dynamics simulations, rail /wheel contact analysis, as well as new profiles on the base of geometric characteristics design [8].

Acknowledgements

This paper was created during the processing of the project "RAILBCOT - RAIL Vehicles Brake COmponents Test Stand", ITMS Code 26220220011 based on the support of Research and Development Operational Program financed by European Fund of a Regional Development. The work was also supported by the Scientific Grant Agency of the Ministry of Education of the Slovak Republic and the Slovak Academy of Sciences in project No. 1/0347/12: "Railway wheel tread profile wear research under the rail vehicle in operation conditions simulation on the test bench.", project No. 1/0383/12: "The rail vehicle running properties research with the help of a computer simulation." and the project No. APVV-0842-11: "Equivalent railway operation load simulator on the roller rig.

References

[1] GERLICI J., LACK, T. et al.: *Transport Means Properties Analysis - part I,* p. 214, EDIS: University of Zilina, 2005, ISBN 80-8070-408-2, 2005.

[2] LACK, T. GERLICI, J.: Contact Area and Normal Stress Determination on Railway Wheel / Rail Contact, *Communications - Scientific Letters of the University of Zilina,* vol. 7, No. 2, 2005, pp. 38–45.

[3] SHACKLETON, P., IWNICKY, S.: Comparison of Wheel–rail Contact Codes for Railway Vehicle Simulation: An Introduction to the Manchester Contact Benchmark and Initial Results. *Vehicle System Dynamics,* vol. 46, No. 1–2, 2008, pp. 129–149.

[4] GERLICI, J., LACK, T.: *Strip Method Modification for Stresses in a Wheel / Rail Contact Computation (in Slovak),* Proc. of the 7th Intern. Conference Dynamics of Rigid and Deformable Bodies, Usti nad Labem, September, 2009.

[5] LACK, T., GERLICI, J.: *Contact Stresses between Railway Wheel and Rail Computation by Means of Strip Method Optimized Procedure (in Slovak),* Proc. of the 9th Intern. Conference Dynamics of Rigid and Deformable Bodies 2011, Usti nad Labem, October, 2011.

[6] LACK, T., GERLICI, J.: *Modified Strip Method Utilization for Wheel /Rail Contact Stress Evaluation,* Proc. of the 9th Intern. Conference on Contact Mechanics and Wear of Rail/Wheel Systems (CM2012), Chengdu, China, 2012.

[7] GERLICI, J., LACK, T.: Contact Geometry Influence on the Rail / Wheel Surface Stress Distribution, Proc. *Engineering,* vol. 2, No. 1, pp. 2249–2257, 2010.

[8] GERLICI, J., LACK, T.: Railway Wheel and Rail Head Profiles Development Based on the Geometric Characteristics Shapes. *Wear,* vol. 271, No. 1-2, Special issue, pp. 246–258, 2011.

COMMUNICATIONS – Scientific Letters of the University of Zilina
Writer's Guidelines

1. Submitted papers must be unpublished and must not be currently under review for any other publication.
2. Submitted manuscripts should not exceed 8 pages including figures and graphs (in Microsoft WORD – format A4, Times Roman size 12, page margins 2.5 cm).
3. Manuscripts written in good English must include abstract and keywords also written in English. The abstract should not exceed 10 lines.
4. Submission should be sent: By e-mail – as an attachment – to one of the following addresses: komunikacie@uniza.sk or holesa@uniza.sk (or on CD to the following address: Zilinska univerzita, OVaV – Komunikacie, Univerzitna 1, SK-10 26 Zilina, Slovakia).
5. Uncommon abbreviations must be defined the first time they are used in the text.
6. Figures, graphs and diagrams, if not processed in Microsoft WORD, must be sent in electronic form (as JPG, GIF, TIF, TTF or BMP files) or drawn in high contrast on white paper. Photographs for publication must be either contrastive or on a slide.
7. The numbered reference citation within text should be enclosed in square brackets. The reference list should appear at the end of the article (in compliance with ISO 690).
8. The numbered references (in square brackets), figures, tables and graphs must be also included in text – in numerical order.
9. The author's exact mailing address, full names, E-mail address, telephone or fax number, the name and address of the organization and workplace (also written in English) must be enclosed.
10. The editorial board will assess the submitted paper in its following session. If the manuscript is accepted for publication, it will be sent to peer review and language correction. After reviewing and incorporating the editor's comments, the final draft (before printing) will be sent to authors for final review and minor adjustments
11. Submission deadlines are: September 30, December 31, March 31 and June 30.

COMMUNICATIONS

SCIENTIFIC LETTERS OF THE UNIVERSITY OF ZILINA
VOLUME 15

Address of the editorial office:
Zilinská univerzita
Office for Science and Research
(OVaV)
Univerzitna 1
SK 010 26 Zilina
Slovakia

E-mail: komunikacie@uniza.sk

Each paper was reviewed by two reviewers.

Journal is excerpted in Compendex and Scopus.

It is published by the University of Zilina in
EDIS – Publishing Institution of Zilina University
Registered No: EV 3672/09
ISSN 1335-4205

Published quarterly

Single issues of the journal can be found on:
http://www.uniza.sk/komunikacie

ICO 00397 563
August 2013